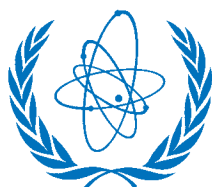


# ATOMIC AND PLASMA-MATERIAL INTERACTION DATA FOR FUSION

VOLUME 17



**IAEA**  
International Atomic Energy Agency

ATOMIC AND PLASMA–MATERIAL  
INTERACTION DATA FOR FUSION

The following States are Members of the International Atomic Energy Agency:

AFGHANISTAN	GEORGIA	OMAN
ALBANIA	GERMANY	PAKISTAN
ALGERIA	GHANA	PALAU
ANGOLA	GREECE	PANAMA
ANTIGUA AND BARBUDA	GUATEMALA	PAPUA NEW GUINEA
ARGENTINA	GUYANA	PARAGUAY
ARMENIA	HAITI	PERU
AUSTRALIA	HOLY SEE	PHILIPPINES
AUSTRIA	HONDURAS	POLAND
AZERBAIJAN	HUNGARY	PORTUGAL
BAHAMAS	ICELAND	QATAR
BAHRAIN	INDIA	REPUBLIC OF MOLDOVA
BANGLADESH	INDONESIA	ROMANIA
BARBADOS	IRAN, ISLAMIC REPUBLIC OF	RUSSIAN FEDERATION
BELARUS	IRAQ	RWANDA
BELGIUM	IRELAND	SAN MARINO
BELIZE	ISRAEL	SAUDI ARABIA
BENIN	ITALY	SENEGAL
BOLIVIA, PLURINATIONAL STATE OF	JAMAICA	SERBIA
BOSNIA AND HERZEGOVINA	JAPAN	SEYCHELLES
BOTSWANA	JORDAN	SIERRA LEONE
BRAZIL	KAZAKHSTAN	SINGAPORE
BRUNEI DARUSSALAM	KENYA	SLOVAKIA
BULGARIA	KOREA, REPUBLIC OF	SLOVENIA
BURKINA FASO	KUWAIT	SOUTH AFRICA
BURUNDI	KYRGYZSTAN	SPAIN
CAMBODIA	LAO PEOPLE'S DEMOCRATIC REPUBLIC	SRI LANKA
CAMEROON	LATVIA	SUDAN
CANADA	LEBANON	SWAZILAND
CENTRAL AFRICAN REPUBLIC	LESOTHO	SWEDEN
CHAD	LIBERIA	SWITZERLAND
CHILE	LIBYA	SYRIAN ARAB REPUBLIC
CHINA	LIECHTENSTEIN	TAJIKISTAN
COLOMBIA	LITHUANIA	THAILAND
CONGO	LUXEMBOURG	THE FORMER YUGOSLAV REPUBLIC OF MACEDONIA
COSTA RICA	MADAGASCAR	TOGO
CÔTE D'IVOIRE	MALAWI	TRINIDAD AND TOBAGO
CROATIA	MALAYSIA	TUNISIA
CUBA	MALI	TURKEY
CYPRUS	MALTA	TURKMENISTAN
CZECH REPUBLIC	MARSHALL ISLANDS	UGANDA
DEMOCRATIC REPUBLIC OF THE CONGO	MAURITANIA	UKRAINE
DENMARK	MAURITIUS	UNITED ARAB EMIRATES
DJIBOUTI	MEXICO	UNITED KINGDOM OF GREAT BRITAIN AND NORTHERN IRELAND
DOMINICA	MONACO	UNITED REPUBLIC OF TANZANIA
DOMINICAN REPUBLIC	MONGOLIA	UNITED STATES OF AMERICA
ECUADOR	MONTENEGRO	URUGUAY
EGYPT	MOROCCO	UZBEKISTAN
EL SALVADOR	MOZAMBIQUE	VANUATU
ERITREA	MYANMAR	VENEZUELA, BOLIVARIAN REPUBLIC OF
ESTONIA	NAMIBIA	VIET NAM
ETHIOPIA	NEPAL	YEMEN
FIJI	NETHERLANDS	ZAMBIA
FINLAND	NEW ZEALAND	ZIMBABWE
FRANCE	NICARAGUA	
GABON	NIGER	
	NIGERIA	
	NORWAY	

The Agency's Statute was approved on 23 October 1956 by the Conference on the Statute of the IAEA held at United Nations Headquarters, New York; it entered into force on 29 July 1957. The Headquarters of the Agency are situated in Vienna. Its principal objective is "to accelerate and enlarge the contribution of atomic energy to peace, health and prosperity throughout the world".

ATOMIC AND PLASMA–MATERIAL  
INTERACTION DATA FOR FUSION

VOLUME 17

INTERNATIONAL ATOMIC ENERGY AGENCY  
VIENNA, 2017

## COPYRIGHT NOTICE

All IAEA scientific and technical publications are protected by the terms of the Universal Copyright Convention as adopted in 1952 (Berne) and as revised in 1972 (Paris). The copyright has since been extended by the World Intellectual Property Organization (Geneva) to include electronic and virtual intellectual property. Permission to use whole or parts of texts contained in IAEA publications in printed or electronic form must be obtained and is usually subject to royalty agreements. Proposals for non-commercial reproductions and translations are welcomed and considered on a case-by-case basis. Enquiries should be addressed to the IAEA Publishing Section at:

Marketing and Sales Unit, Publishing Section  
International Atomic Energy Agency  
Vienna International Centre  
PO Box 100  
1400 Vienna, Austria  
fax: +43 1 2600 29302  
tel.: +43 1 2600 22417  
email: [sales.publications@iaea.org](mailto:sales.publications@iaea.org)  
<http://www.iaea.org/books>

For further information on this publication, please contact:

Nuclear Data Section  
International Atomic Energy Agency  
Vienna International Centre  
PO Box 100  
1400 Vienna, Austria  
Email: [Official.Mail@iaea.org](mailto:Official.Mail@iaea.org)

ATOMIC AND PLASMA-MATERIAL INTERACTION DATA FOR FUSION, VOLUME 17  
IAEA, VIENNA, 2017  
STI/PUB/023/APID/17  
ISBN 97892-0-105817-1  
ISSN 1018-5577

© IAEA, 2017

Printed by the IAEA in Austria  
September 2017

## FOREWORD

Fusion energy plasma has the natural constituents hydrogen (isotopes deuterium and tritium) and helium, but inevitably impurities are introduced, for example due to plasma interaction with material walls. Light impurities are easily ionized to the level at which they are fully stripped of electrons, but heavier impurities retain some electrons, even in the hot core plasma, and they radiate strongly because they are only partially stripped. This radiation, which constitutes a loss of energy, also provides diagnostic opportunities.

The mission of the IAEA Nuclear Data Section in the area of atomic and molecular data is to provide internationally recommended atomic, molecular, plasma–material interaction and material properties databases. One mechanism by which the IAEA pursues this mission is the Coordinated Research Project (CRP). The present volume of Atomic and Plasma–Material Interaction Data for Fusion contains contributions from participants in the CRP “Atomic Data for Heavy Element Impurities in Fusion Reactors” (2005–2009). In accordance with priorities in fusion energy research, much of the work in this CRP focused on the noble gases argon, krypton and xenon, on the likely wall material tungsten, and on other possible impurities such as chlorine, iron and silicon. R.E.H. Clark of the Nuclear Data Section was scientific secretary of the CRP.

Participants’ contributions for this volume were collected and refereed after conclusion of the CRP. The IAEA takes this opportunity to thank the CRP participants for their dedicated efforts during the CRP and for their contribution to this volume. The IAEA officer responsible for this volume was B.J. Braams.

## EDITORIAL NOTE

*This publication has been prepared from the original material as submitted by the contributors and has not been edited by the editorial staff of the IAEA. The views expressed remain the responsibility of the contributors and do not necessarily represent the views of the IAEA or its Member States.*

*Neither the IAEA nor its Member States assume any responsibility for consequences which may arise from the use of this publication. This publication does not address questions of responsibility, legal or otherwise, for acts or omissions on the part of any person.*

*The use of particular designations of countries or territories does not imply any judgement by the publisher, the IAEA, as to the legal status of such countries or territories, of their authorities and institutions or of the delimitation of their boundaries.*

*The mention of names of specific companies or products (whether or not indicated as registered) does not imply any intention to infringe proprietary rights, nor should it be construed as an endorsement or recommendation on the part of the IAEA.*

*The authors are responsible for having obtained the necessary permission for the IAEA to reproduce, translate or use material from sources already protected by copyrights.*

*The IAEA has no responsibility for the persistence or accuracy of URLs for external or third party Internet web sites referred to in this publication and does not guarantee that any content on such web sites is, or will remain, accurate or appropriate.*

## Contents

Introduction and Summary .....	1
Atomic data for optical diagnostics and modeling of fusion plasmas: transition probabilities of Ar and Xe species .....	3
<i>K. Katsonis, Ch. Berenguer, R.E.H. Clark, M. Cornille, Bin Duan, Jun Yan</i>	
Electron-ion recombination and electron-ion impact ionization data from laboratory experiments .....	17
<i>A. Borovik (Jr), S. Schippers, A. Müller</i>	
Theoretical studies on charge exchange and electron excitation in collisions between alpha particles, helium atoms and multiply charged heavy element ions .....	41
<i>V.K. Nikulin, N.A. Guschina</i>	
Spectral properties of heavy elements of fusion interest .....	65
<i>W.L. Wiese, M.A. Ali, I.N. Draganic, J.R. Fuhr, J.D. Gillaspy, R. Ibacache, D.E. Kelleher, A. Kramida, L.I. Podobedova, Yu. Ralchenko, J. Reader, E.B. Saloman, P.M. Stone</i>	
Electron-impact inner shell ionization cross-section measurements for heavy element impurities in fusion reactors .....	85
<i>J. J. Zhu, Y. Wu, Z. An</i>	
Collisional data for the Si, Cl and Ar isonuclear sequences using the Los Alamos atomic collision codes .....	99
<i>J. Colgan, H.L. Zhang, C.J. Fontes</i>	
Radiative recombination and photoionization of heavy element impurities in plasmas .....	105
<i>M.B. Trzhaskovskaya, V.K. Nikulin, R.E.H. Clark</i>	
Plasma diagnostics by the intensity ratios of emission lines of Fe ions and recommended excitation rate coefficients .....	129
<i>I. Murakami, N. Yamamoto, H.A. Sakaue, S. Morita, D. Kato, T. Kato</i>	
EUV spectra of high z impurities from large helical device and atomic data .....	161
<i>T. Kato, G. O'Sullivan, C. Suzuki, C. Harte, J. White, R. D'Arcy, H. Funaba, K. Sato, H. Tanuma, I. Murakami, D. Kato, H. Sakaue, N. Nakamura</i>	
Convergent close-coupling calculations of electron-impact ionization of intermediate and highly charged ions .....	193
<i>I. Bray, C. J. Bostock, D. V. Fursa, A. C. Renwick</i>	



## Introduction and Summary

During the years 2005–2009 the IAEA Atomic and Molecular Data Unit managed a coordinated research project (CRP) on Atomic Data for Heavy Element Impurities in Fusion Reactors. The CRP was concerned with provision of data for collisional and radiative processes that are important for fusion plasma modelling. Collisional processes include excitation, ionization and recombination due to electron and ion impact as well as charge transfer in the collision of two heavy particles. The processes are interlinked as excitation can lead to autoionization and dielectronic recombination and as recombination of ions with electrons is the inverse process of ionization. Radiative processes include bound-bound absorption as well as photoionization. The dual processes of line emission and radiative recombination are vital in the modeling of the spectral features of the plasma impurities. Data for all of these processes are needed for heavy elements occurring in present experiments or likely to be found in ITER or in a reactor, including tungsten as a plasma-facing material and inert gases such as argon and krypton as deliberately introduced impurities.

The CRP reflected advances in theoretical methods for generating such data with strong reliance on increased computational facilities. In addition, experimental techniques have increased in sensitivity, allowing cross sections for more highly ionized species to be measured. (The cross sections fall rapidly with increasing ionization.)

The paper by Katsonis, Berenguer *et al.* provides transition probabilities and electron collision excitation cross-sections for Ar and Xe atoms and their low ionization stages for use in collisional-radiative models for diagnostics and modeling of plasmas. The experimental paper by Borovik, Schippers and Müller presents colliding beams measurements of cross sections for electron impact ionization of Xe ions and of rate coefficients for electron-ion recombination of selected ions of Si, Fe and Ni. Nikulin and Guschina present charge exchange data and excitation cross-sections calculated in the framework of the close-coupling equation method for collisions of relevant impurity ions with helium atoms in the ground state and in metastable states. Partial cross-sections for quasi-resonant double electron capture into the ground He( $1s^2$ ) and metastable He( $1s2l$ ) states in the He $^{2+}$  + He collisions are also reported.

The paper by Wiese *et al.* provides a survey of spectroscopic work at NIST including EBIT studies of highly charged ions of tungsten, comprehensive critical compilations of the spectra of tungsten and other heavy elements of interest to fusion energy science (Al, Si, S, Ar, Cl, Fe, Kr and Xe) and calculations of ionization and excitation cross-sections for tungsten and molybdenum. Zhu, Wu and An of Sichuan University present measurements of electron-impact inner shell ionization cross-sections and x-ray production cross-sections of some heavy elements including the K-shell ionization cross-sections for S, Cl, Ca, Zn elements and the L-shell x-ray production cross-sections for W-L $_{\alpha}$ , L $_{\beta}$ , Bi-L $_{\alpha}$ , L $_{\beta}$ , Ba-L $_{\alpha}$  and Gd-L $_{\alpha}$ . The thin-target and the thick-target method of measurement and the associated data analysis are reviewed.

The paper by Colgan, Zhang and Fontes describes level-resolved electron-impact excitation and ionization data for all ions in the Si, Cl and Ar isonuclear sequences calculated using the Los Alamos suite of codes and employing first-order many body perturbation theory for excitation processes and distorted wave theory for ionization. The paper by Trzhaskovskaya, Nikulin and Clark presents a new unified database of atomic data for radiative recombination and photoionization cross-sections for ions of Si, Cl, Ar, Ti, Cr, Fe, Ni, Cu, Kr, Mo, Xe, and W as well as radiative rates for 9 tungsten ions calculated in the framework of the fully relativistic Dirac-Fock equation. Subshell photoionization cross-sections were fitted by a simple analytical expression and the fit parameters are provided.

The paper of Murakami *et al.* describes analysis of EUV spectra of iron ions obtained in the Large Helical Device (LHD) at the National Institute for Fusion Science. Experimental results are compared with collisional radiative modelling and recommended collision strengths are provided. The related paper by Kato *et al.* describes experiments on high Z impurity injection in LHD. EUV spectra from Xe, Sn and W ions are dominated by resonance

transitions to the ground state of the emitting ions and this is contrasted with charge exchange spectra of the same ions. Various new assignments and strong lines are tabulated. Finally, the paper by Bray *et al.* describes provides electron-impact total ionisation cross-sections for H-, Na- and Mg-like ions calculated using the convergent close-coupling (CCC) method including a relativistic Breit or Møller correction for higher charge states.

# ATOMIC DATA FOR OPTICAL DIAGNOSTICS AND MODELING OF FUSION PLASMAS: TRANSITION PROBABILITIES OF Ar AND Xe SPECIES

K. KATSONIS<sup>1</sup>, CH. BERENGUER<sup>1</sup>, R.E.H. CLARK<sup>2</sup>, M. CORNILLE<sup>3</sup>, BIN DUAN<sup>4</sup>, JUN YAN<sup>4</sup>

<sup>1</sup>Laboratoire de Physique des Gaz et des Plasmas,  
Université Paris-sud, Orsay, France

<sup>2</sup>Nuclear Data Section,  
International Atomic Energy Agency,  
Vienna, Austria

<sup>3</sup>LUTH, Observatoire de Paris, CNRS,  
Université Paris Diderot, Meudon, France

<sup>4</sup>Institute of Applied Physics and Computational Mathematics,  
Beijing, China

## Abstract

The transition probabilities ( $A_{ij}$ ) along with electron collision excitation cross-sections ( $\sigma_{ji}$ ) are the main determinants of the theoretical spectra calculated using detailed Collisional-Radiative (C-R) models. Such models are necessary for optical diagnostics of emission lines of plasmas and their modeling when they cannot be assumed to be in local thermodynamic equilibrium (LTE). Here we present typical evaluations of  $A_{ij}$  pertaining to Ar and Xe atoms and their low ionization stages, which we accomplished in the context of the CRP. Their results have been used in developing C-R models for diagnostics and modeling of plasmas of fusion interest. Results of the subsequent calculation of the corresponding  $\sigma_{ji}$  are presented elsewhere. Extension of the applicability of our ‘zero-dimension’ codes to treat the bulk of the plasma state and properties calls for their coupling with detailed kinetic codes as EIRENE.

## 1. INTRODUCTION

Generation of a huge number of atomic data has been necessary for making detailed C-R models. Production of these data is based on calculations from various theoretical methods and was often the result of collaborative efforts supported by the present CRP. We address here the calculation of transition probabilities  $A_{ij}$  and we present in § 3 typical examples of results, after giving in § 2 a description of the main theoretical results which we have used in the present work. In § 4, we report on selected experimental devices which have been used for benchmark studies of the rare gas spectra. Experimental spectra obtained with two of these devices were presented and compared with the theoretical results coming from our C-R models during the CRP.

Our fusion oriented C-R models include spectra up to Ar IX and Xe IX. Developing these models allowed for covering the population calculations for levels belonging to the entire range of the outer  $p^6$  and  $s^2$  shells of the rare gases. Work is in progress on completing the validation of some of these models and on their application to rare gas plasmas encountered in fusion research. During the validation process the spectra from several laboratory devices were acquired and studied, including a new set of spectral measurements in the WEGA Stellarator in Greifswald, optical diagnostics of the DIVA plasma reactor in LPGP, a study of Xe ions in the VUV region in IPNAS and dedicated experiments specifically conceived for the validation of these models.

To obtain correct theoretical spectra, knowledge of accurate data sets for the corresponding  $A_{ij}$  and electron collision excitation cross-sections  $\sigma_{ji}$  values is necessary. To evaluate the later, we used extensively the first order many body theory (FOMBT) and the

distorted wave (DW) approximation through the code ACE [1], available at LANL. Since here we are focusing on  $A_{ij}$  calculations, results of our  $\sigma_{ji}$  evaluations are reviewed elsewhere. To complete the C-R models, calculations of cross-sections for ionization and recombination processes were also carried out, allowing for the determination of the dynamic equilibrium between the ionization stages included in the model. Development of detailed C-R models is necessary for the diagnostics of the ionized plasmas which are out of local thermodynamic equilibrium (LTE), such as those often encountered in fusion devices. The developed models can also serve as the basis for a realistic modeling of such plasmas, after extending the “zero-dimension” C-R code to non-stationary and inhomogeneous plasmas.

$A_{ij}$  and  $\sigma_{ji}$  play an important role in the global ionization and recombination balance of each species: Population of the excited states greatly influences the ionization – recombination equilibrium, hence the species abundances; also, the  $A_{ij}$  determine which states will be metastable. Note that a significant simplification is possible in the case of plasmas in coronal equilibrium. The sole important processes in this case are ionization originating from the ground state(s) and recombination leading to the ground state(s), the ratios of the excited levels intensities being invariable. The influence of  $A_{ij}$  and  $\sigma_{ji}$  can then be neglected.

Besides being important for the validation of our models, the applications which will be reviewed in § 4 also allow to judge the quality of the used atomic data sets. The bulk of the data used here have been measured, calculated and evaluated by our collaborators and by us. We have also made extensive use of databases available in the web, notably those available by NIST [2, 3]. We are grateful to Dr. Saloman, who provided us with a printed copy of his compilation pertaining to Xe structure and spectra.

**C-R** models are “zero-dimension” codes: The provided populations are valid for a specific point of the plasma. In order to be applied in real plasmas the latter must fulfill the following conditions:

- The plasma has to be near a homogeneous and stationary (H-S) state, as the left hand side (LHS) of the Boltzman statistical equations has been put equal to zero, neglecting any variation on space and in time, thusly ignoring any transport of the plasma species. Approximate solutions for slightly transitory plasmas have been given in the past taking into account the kinetics of the most populated states, e.g., the ground level, by resolving the corresponding differential equations scheme instead of the linear system describing the H-S case [4, 5].
- The electron distribution and those of the various present heavy species have to be determined by successive calculations of the code or given from the beginning. In the latter case they are usually taken as Maxwellian.

In order to obtain global models taking into account both the atomic properties of the plasma and the plasma geometry and kinetics, we need to link together the kinetic and the C-R codes. This has been obtained in simplified cases as in the study of reentry [6] and is in progress for the case of prototype Ar and Ne plasma thrusters. In these cases, simplified models have been used both for the kinetics of the species and for the C-R part [7]. For the fusion modeling and diagnostics needs, extended kinetic codes as EIRENE [8] have to be used together with full C-R type models. Such work has been already done in the case of H and He plasmas. We are looking forward to implement such a global model for the case of Ar plasmas as explained in §4. Finally, the main conclusions of the fusion-oriented part of our atomic data work is given in §5.

In the spectra of interest, the resonant lines of the plasma, constituting a significant part of the plasma radiation, are due to allowed transitions from the levels of the  $4/6s$ ,  $5/7s$ , and  $3/5d$ ,  $4/6d$  and  $5/7d$  configurations which populate the levels of the  $3/5p$  ground configurations, the smaller principal quantum numbers corresponding to Ar and the ones after the slashes to Xe plasmas. Depending on the ionization stage, the ground level compound consists of one (Ar/Xe I, VII), two (Ar/Xe II, Ar/Xe VI) or five (Ar/Xe III, IV, V) levels. There are also a number of metastable levels belonging to the  $s$  and  $p$  configurations, because some of the  $p-s$ ,  $p-d$  transitions are forbidden and the  $p$  configurations cannot directly decay to the ground level configuration. We observe that the resonant lines belong to a relatively constricted wavelength region in comparison with those coming from transitions between low

lying multiplets. They appear mostly in the 40–200 nm UV region, while transitions between low lying excited states are mainly in the visible to infrared region, with the longest wavelengths corresponding to the neutral and for the lower ionized Ar/Xe species.

## 2. COMMON THEORETICAL METHODS FOR $A_{ji}$ CALCULATION

Because of the extensive number of the transitions of interest to various applications, experimental determination of all the needed transition probabilities is not feasible, and reliable theoretical methods have been developed to complement the measurements. Among them, the Coulomb Approximation (CbA) was introduced early by Bates and Damgaard [9] in an effort to obtain transition probabilities of atoms and ions without extensive calculations. These authors in their original paper provided tables giving the approximate values of the radial part  $P$  of the line strength integral  $S_i = PS_w$  to be used for each  $A_{j \rightarrow i}$ . The necessary 6- $j$  symbol values for evaluating the angular part  $S_w$  have been made available in the book by Rotenberg et al. [10]. A more precise evaluation of  $P$  was devised later [11] by Friedrich et al., with a revised FORTRAN subroutine edition. With the increased use of electronic computers, various codes have been developed for direct calculation of  $A_{j \rightarrow i}$  on the Coulomb approximation. Calculations of  $A_{j \rightarrow i}$  based in the CbA have often been published, in particular for noble gases and their ions [12–16]. They were often compared to other available theoretical and experimental results and were also extensively used in applications where complete sets of  $A_{j \rightarrow i}$  for numerous multiplets are needed, as is the case for Collisional-Radiative (C-R) models [17–19].

The available experimental data of interest to fusion applications are far from complete. Accordingly, we have used common theoretical codes in an effort to evaluate  $A_{ji}$  of the multiplets containing the more prominent transitions of Argon [20] and Xenon [21] species. These include low radiative and metastable levels, and multiplets containing the most prominent lines in the Ar/Xe neutral and ion spectra.

A common numerical code using experimental energy levels values, which we used routinely is:

### 2.1. The Quasi-Classical Approximation CbA code

This CbA code, based in the aforementioned approximation by Bates and Damgaard [9], was developed previously by K. Katsonis. We have used this code systematically to obtain transition probabilities of multiplets belonging to neutral and ionized species of rare gases, whenever the corresponding energy levels are experimentally available.

Concerning the *ab initio* quantum methods an impressive number of codes is available. They have been developed with the intent of giving more exact values, also for cases when the values of the experimental energies and/or the corresponding quantum descriptions are not sufficiently well known. According to these methods, once the necessary wavefunctions are written down the codes, based on *ab initio* methods are able to calculate  $A_{j \rightarrow i}$  for the expected spectral lines of various neutral and ionized species, giving at the same time theoretical values of the energy levels. Such codes have been used in preference to large models of C-R type developed elsewhere. Those which we have used include.

### 2.2. The CATS Code

In calculating  $A_{j \rightarrow i}$  and connected parameters we used the Los Alamos National Laboratory (LANL) codes available through the Internet [22], as described by Abdallah et al. [23]. These constitute an extension of the H-F RCG Mod 4 program [24] to include configuration interaction and magnetic dipole plus electric quadrupole transitions [25]; these results are hereafter labeled LANL. This code calculates the transition probabilities of any selected multiplet together with its atomic structure. As it is an “*ab initio*” code, there is the possibility to select a list of configurations for a specified ion.

### 2.3. The GRASP2 Package

Additional comparison of the transition probabilities has been performed on the basis of calculations made using the relativistic multi-configuration Dirac-Fock (MCDF) GRASP2 package, which was in time available to download e.g. by P. Norrington through URL <http://www.am.qub.ac.uk/user/p.norrington>. Whenever the wavefunctions were sufficiently optimized, this code produced energy levels and transition probabilities often in satisfactory agreement with available experimental data, thus leading in principle to more realistic theoretical spectra [26]. The GRASP package, described in [27], has been superseded by various versions, as GRASP92. Note that such packages are now available e.g. by ResearchGate and by Computer Physics Communications Program Library.

### 2.4. The SUPERSTRUCTURE Code

We calculated wavefunctions, energy levels and radiative transition probabilities (electric and magnetic dipole and quadrupole) using the code contained within the SUPERSTRUCTURE package (noted SST thereafter). This code, currently used in Meudon Observatory for transition probability calculations was developed at University College (UCL) by Eissner and collaborators [28]. In the first step, this program determines a set of non-relativistic wavefunctions by diagonalization of the non-relativistic Hamiltonian using orbitals calculated in scaled Thomas-Fermi-Dirac-Amaldi (TFDA) potentials  $V_{\lambda(l)}(r)$ . The scaling parameters  $\lambda(l)$  are obtained through a self-consistent energy minimization procedure. In the second step, the program diagonalizes the relativistic Breit-Pauli Hamiltonian; the multi-configurational wavefunctions obtained contain both the correlation and the relativistic effects in the configuration mixing coefficients.

### 2.5 The FAC Code

The Flexible Atomic Code (FAC) developed by Gu [29], has been installed at Meudon Observatory; it calculates transition probabilities and excitation cross-sections used for evaluation of the atomic data needed for our C-R model. Note that calculations of these atomic data in FAC are provided with construction of C-R models in mind.

In relation to the two last codes, the SUPERSTRUCTURE code was proven to be useful after adequate optimizations, whenever the used basis could be restricted to 18 configurations or less. For the lower ionized species, calculations using the FAC code were not satisfactory.

## 3. EXAMPLES OF $A_{ij}$ EVALUATION FOR MULTIPLETS OF Ar AND Xe SPECIES

A considerable effort is devoted to determine various types of rare-gas atomic data which are subsequently used in evaluating C-R models. Among them, structure data and  $A_{ij}$  of Ar and Xe atoms and ions have been measured, calculated by various codes and evaluated. These data are validated by comparison of theoretical spectra coming from the corresponding C-R models with the experimental ones. We are presenting here as typical examples  $A_{ij}$  values of the lower  $s$ - $p$  multiplets transitions of Ar III and Xe III from various sources and their systematic evaluation. The corresponding values of the two elements present evident similarities coming from the common external shell of four equivalent electrons.

### 3.1. Evaluation of $A_{ij}$ for the $4s4p$ multiplet of Ar III

In order to make an interesting comparison of the CbA results with the *ab initio* quantal calculations, we present here only the  $4s \leftarrow 4p$  case, because this is the simpler and shorter non-resonant multiplet of Ar III. An extensive set of Ar III  $A_{j \rightarrow i}$  values is available directly from the authors or can be found in the ALADDIN database on the web site of the IAEA A+M Unit [30]. In Table 1 we present our results for  $4s \leftarrow 4p$ , together with most of

the other available data concerning this multiplet, separately for each core for which we give the parent term; all numerical  $A_{j \rightarrow i}$  values are given in  $10^7 \text{ s}^{-1}$ . Where a 0.00 value appears, it means that our calculations give non-zero values but too small to be significant for the present comparison (less than  $0.01 \times 10^7 \text{ s}^{-1}$ ).

Throughout the CbA calculations experimental energy levels have been used, taken from the NIST database. The used values are included in Table 1 together with the wavelengths and the appropriate quantum parameters, in order to clearly identify each transition. Our own  $A_{j \rightarrow i}$  calculations following CbA, SST and LANL CATS codes are compared with previous theoretical results [31] (marked CEYZ) and with experimental data [32] (marked NAND). We include also the  $A_{j \rightarrow i}$  values given in the following specialized databases:

**NIST** [http://physics.nist.gov/cgi-bin/AtData/main\\_asd](http://physics.nist.gov/cgi-bin/AtData/main_asd) by Wiese, W.,

**KURUCZ** <http://cfa-www.harvard.edu/amdata/ampdata/kurucz23/sekur.html> ,

**ATLL** Atomic Line List <http://www.pa.uky.edu/~peter/atomic/> and

**MCHF** Multi-configuration Hartree-Fock <http://atoms.vuse.vanderbilt.edu/> by Fischer. Ch.F.,

We note that these databases can all be searched through a single search engine, GENIE, available through the aforementioned A+M web page [30].

Our SST calculations for the Ar III  $4s \leftarrow 4p$  multiplet, lead to scaling parameters  $\lambda(s) = 1.1366$ ,  $\lambda(p) = 1.0771$  and  $\lambda(d) = 1.1358$  obtained from the self-consistent energy minimization procedure on all the term energies of the five following configurations:  $1s^2 2s^2 2p^6 3s^2 3p^4$  and  $1s^2 2s^2 2p^6 3s^2 3p^3 3d$ ,  $4s$ ,  $4p$  and  $4d$ . Relativistic corrections (spin-orbit, mass, Darwin and one-body) are introduced to the Breit [33] approach. In the relativistic theory,  $L$  and  $S$  are no longer sufficiently “good” quantum numbers, but the inner quantum number is [34]. This suggests the introduction of the coupling scheme known as  $LSj$ , allowing for more transitions than the  $LS$  (and  $jK$ ) one. More generally, the Intermediate Coupling ( $IC$ ) scheme has been introduced, allowing for a continuous variation from one scheme to another [35], in which all transitions could in principle be allowed, but practically are cut-off by a lower limit imposed to the  $A_{j \rightarrow i}$  (here  $0.01 \times 10^7 \text{ s}^{-1}$ ). From our  $A_{j \rightarrow i}$  results obtained with the LANL code, only the  $LS$  allowed part of the  $4s \leftarrow 4p$  multiplet appears in Table 1. Transitions in  $IC$  for which non-zero  $A_{j \rightarrow i}$  values are obtained by this code, are excluded from this table whenever forbidden in  $LS$  coupling. This is also the case for  $LS$  forbidden  $IC$  transitions obtained with the SST code. Similarly, to the CbA and SST calculations, the LANL code gives significant  $A_{j \rightarrow i}$  values for all the cores of the multiplet. Considered terms include those of the SST calculation plus  $5s$ ,  $6s$  and  $7s$ , because they are directly communicating with  $4p$  and are situated in peculiar places in the energy level diagram of Ar III, corresponding to significant quantum defect values.

We see then that not all of the  $A_{j \rightarrow i}$  obtained in  $IC$  by each quantal method are given in Table 1; only the 46  $LS$  allowed transitions (those for which CbA calculations in  $LS$  scheme give nonzero values) are shown. Although also calculated with the CbA code, no  $jK$  values are given, since we estimated that the  $LS$  coupling scheme is most applicable in this case. Besides, the relation between  $LS$  and  $jK$  values and the corresponding  $S_w$  have been adequately described and given elsewhere [36]. One reason for including only  $LS$  allowed transitions is that the remaining  $A_{j \rightarrow i}$  values are rather small in this case. Another is that no individual comparison can be made for  $IC$  for these values, as they are forbidden in the  $LS$  scheme of our CbA calculations, which is mostly true also for the ones in  $jK$ .

TABLE 1. Ar III LS ALLOWED  $4s \leftarrow 4p$  TRANSITION PROBABILITIES  $A_{j \rightarrow i}$  IN  $10^7 s^{-1}$ 

$E_i$ (cm $^{-1}$ )	Term	$E_j$ (cm $^{-1}$ )	Term	$\lambda$ [Å]	$L_i$	$J_i$	$l_{i1}$	$l_{i2}$	$J_j$	$S_j$	CbA (T)	CEYZ (T)	NAND (E)	SST (T)	LANL (T)	NIST	MCHF (T)	ATLL (T)	KURU (T)
<b>4s, 4p core <math>^4S_{3/2}</math> (+ e<math>^-</math> <math>\rightarrow</math> triplet, quintet)</b>																			
174378.50	$^5S_2$	204569.95	$^5P_1$	3312.20	0	2	0	1	1	2	20.41			23.36	22.75	20.00		22.20	
		204655.80	$^5P_2$	3302.80	0	2	0	1	2	2	20.59			23.57	22.89	20.00		22.40	
		204803.34	$^5P_3$	3286.79	0	2	0	1	3	2	20.89	20.00	21.50	23.95	23.19	20.00		22.80	
180678.31	$^3S_1$	209126.16	$^3P_1$	3515.20	0	1	0	1	1	1	18.51			15.07	20.19			19.20	
		209150.88	$^3P_0$	3512.15	0	1	0	1	2	1	18.56			15.93	20.14			19.20	
		209165.61	$^3P_0$	3510.34	0	1	0	1	0	1	18.59			16.09	20.24			19.30	
<b>4s, 4p core <math>^2D_{5/2}</math> (+ e<math>^-</math> <math>\rightarrow</math> triplet)</b>																			
196590.64	$^3D_1$	225149.20	$^3D_2$	3501.58	2	1	2	2	2	1	2.62			1.13	0.90	2.60		2.69	
		225156.59	$^3D_1$	3500.67	2	1	2	2	1	1	13.12			10.10	10.19	13.00		13.50	
		226357.02	$^3F_2$	3359.50	2	1	2	3	2	1	16.64	20.00		19.15	20.64	16.00		18.40	
		231342.16	$^3P_2$	2877.57	2	1	2	1	2	1	0.31			0.49	0.32		0.30	0.32	0.31
		231627.38	$^3P_1$	2854.15	2	1	2	1	1	1	8.01		7.90	12.58	9.35		8.00	8.27	7.84
		231754.83	$^3P_0$	2843.80	2	1	2	1	0	1	32.36		10.90	50.21	38.39		31.27	33.40	31.94
196615.20	$^3D_2$	225149.20	$^3D_2$	3504.59	2	2	2	2	2	1	12.11		12.90	12.81	14.45	12.00		12.40	
		225156.59	$^3D_1$	3503.68	2	2	2	2	1	1	4.36			3.43	3.39	4.30		4.48	
		225404.11	$^3D_3$	3473.56	2	2	2	2	3	1	1.99			0.50	0.25	2.00		2.04	
		226357.02	$^3F_2$	3362.27	2	2	2	3	2	1	3.07			1.67	1.37	3.00		3.41	
		226504.16	$^3F_3$	3345.72	2	2	2	3	3	1	17.83	20.00	15.60	20.29	21.72	18.00		19.80	
		231342.16	$^3P_2$	2879.61	2	2	2	1	2	1	4.68			0.49	5.31		4.76	4.83	4.62
		231627.38	$^3P_1$	2856.15	2	2	2	1	1	1	23.98			12.58	28.40		22.99	24.80	23.63
196680.84	$^3D_3$	225149.20	$^3D_2$	3512.67	2	3	2	2	2	1	2.70			2.77	2.95	2.60		2.77	
		225404.11	$^3D_3$	3481.50	2	3	2	2	3	1	15.82	17.00	16.70	16.44	18.31	16.00		16.20	
		226357.02	$^3F_2$	3369.71	2	3	2	3	2	1	0.09				0.00	0.085			
		226504.16	$^3F_3$	3353.08	2	3	2	3	3	1	2.22			0.68	0.36	2.20		2.45	
		226646.69	$^3F_4$	3337.13	2	3	2	3	4	1	20.23	20.00	22.00	21.18	22.32	20.00		22.40	
		231342.16	$^3P_2$	2885.06	2	3	2	1	2	1	26.11	31.00	10.00	42.73	30.91		25.47	26.90	25.87
<b>4s, 4p core <math>^2D_{3/2}</math> (+ e<math>^-</math> <math>\rightarrow</math> singlet)</b>																			
199763.41	$^1D_2$	223663.16	$^1P_1$	4184.14	2	2	2	1	1	0	10.59			6.95	9.05			0.88	
		227244.17	$^1F_3$	3638.91	2	2	2	3	3	0	16.24			14.71	17.95			0.09	
		236064.63	$^1D_2$	2754.73	2	2	2	2	2	0	36.66			34.56	39.02		34.53	1.22	
<b>4s, 4p core <math>^2P_{3/2}</math> (+ e<math>^-</math> <math>\rightarrow</math> triplet)</b>																			
207233.00	$^3P_2$	239194.05	$^3S_1$	3128.81	1	2	1	0	1	1	13.09			10.01	12.04			3.69	
		240152.02	$^3D_1$	3037.76	1	2	1	2	1	1	0.71			0.47	0.41	0.70		0.37	
		240258.45	$^3D_2$	3027.97	1	2	1	2	2	1	6.50			4.48	4.33	6.40		3.36	
		240292.38	$^3D_3$	3024.86	1	2	1	2	3	1	26.06	26.00	9.30	20.67	21.57	26.00		13.50	
		243147.06	$^3P_1$	2784.42	1	2	1	1	1	1	13.83				11.38		8.80	9.24	13.72
		243425.80	$^3P_2$	2762.98	1	2	1	1	2	1	25.46			10.43	21.68		18.16	17.00	3.74
207532.33	$^3P_1$	239194.05	$^3S_1$	3158.39	1	1	1	0	1	1	7.67			6.27	6.31			2.15	
		240152.02	$^3D_1$	3065.63	1	1	1	2	1	1	10.47			8.39	8.60	10.00		5.39	
		240258.45	$^3D_2$	3055.66	1	1	1	2	2	1	19.04		8.50	15.58	17.10	19.00		9.80	
		242924.58	$^3P_0$	2825.48	1	1	1	1	0	1	31.93			36.33	28.63		21.30	21.20	
		243147.06	$^3P_1$	2807.83	1	1	1	1	1	1	8.13			9.27	7.98		5.84	5.40	16.99
		243425.80	$^3P_2$	2786.02	1	1	1	1	2	1	8.31			7.93	5.82		5.40	5.53	29.87
207674.19	$^3P_0$	239194.05	$^3S_1$	3172.60	1	0	1	0	1	1	2.53			2.17	2.07			0.71	
		240152.02	$^3D_1$	3079.02	1	0	1	2	1	1	13.81			11.49	11.93	14.00		7.10	
		243147.06	$^3P_1$	2819.06	1	0	1	1	1	1	10.73				8.50		7.53	7.12	0.93
<b>4s, 4p core <math>^2P_{1/2}</math> (+ e<math>^-</math> <math>\rightarrow</math> singlet)</b>																			
211063.77	$^1P_1$	241807.19	$^1P_1$	3252.73	1	1	1	1	1	0	22.05			14.86	16.31			11.30	
		244358.08	$^1D_2$	3003.52	1	1	1	2	2	0	27.90			26.08	23.79			22.00	
		255107.83	$^1S_0$	2270.45	1	1	1	0	0	0	59.28			79.99	54.40			40.20	

The mean values  $\langle A \rangle = \sum g_j A_{j \rightarrow i} / \sum g_j$  of each set of  $A_{j \rightarrow i}$  values for each of the 4s cores separately and also for the whole multiplet are given in Table 2 (odd, thick rows), calculated for all of the values appearing in Table 1. When the multiplicities of the upper 4p levels for the total of the 46 *LS* allowed transitions are added, we get for the studied multiplet  $\sum g_j = 198 (= 24+95+15+55+9)$ ; this is to be compared with the total multiplicity of the 4p term composed of 28 levels which is  $\sum T = 120 (= 24+45+15+27+9)$ , each level entering only once. Table 1 shows that, according to *LS* coupling, to the  $^2D_{5/2}$  and  $^2P_{3/2}$  parent terms correspond 4p levels which may fall to more than one 4s level. The  $\sum g_j A_{j \rightarrow i} / 120$  values for the whole multiplet and the partial values corresponding to each data set (where the partial sums are divided by 24, 45, 15, 27, 9) are also given in Table 2 (even, thin rows) as a measure of the part of 46 multiplet transitions given into each column set and also separately for each of the five parent cores.

TABLE 2. TRANSITION MEAN VALUES IN  $10^7 s^{-1}$  FOR THE FIVE PARENT CORES OF 4s, 4p SEPARATELY AND FOR THE WHOLE Ar III 4s ← 4p MULTIPLET

Mean Value	CbA (T)	CEYZ (T)	NAND (E)	SST (T)	LANL (T)	NIST (T)	MCHF (T)	ATLL (T)	KURU (T)	CORE
$\langle A_{j \rightarrow i} \rangle = \sum (g_j A_{j \rightarrow i}) / \sum g_j$	477.33/24	140.00/7	150.50/7	496.53/24	526.54/24	300.00/15		511.10/24		$^4S_{3/2}$
	<b>19.89</b>	<b>20.00</b>	<b>21.50</b>	<b>20.69</b>	<b>21.94</b>	<b>20.00</b>		<b>21.30</b>		
$\sum (g_j A_{j \rightarrow i}) / 24$	<b>19.89</b>	<b>5.83</b>	<b>6.27</b>	<b>20.69</b>	<b>21.94</b>	<b>12.50</b>		<b>21.30</b>		
$\langle A_{j \rightarrow i} \rangle = \sum (g_j A_{j \rightarrow i}) / \sum g_j$	969.51/95	694.00/33	573.20/37	1028.48/90	1061.99/90	680.73/73	276.89/22	1030.18/90	280.35/22	$^2D_{5/2}$
	<b>10.20</b>	<b>21.03</b>	<b>15.49</b>	<b>11.43</b>	<b>11.80</b>	<b>9.33</b>	<b>12.59</b>	<b>11.45</b>	<b>12.74</b>	
$\sum (g_j A_{j \rightarrow i}) / 45$	<b>21.55</b>	<b>15.42</b>	<b>12.74</b>	<b>22.86</b>	<b>23.60</b>	<b>15.13</b>	<b>6.15</b>	<b>22.90</b>	<b>6.23</b>	
$\langle A_{j \rightarrow i} \rangle = \sum (g_j A_{j \rightarrow i}) / \sum g_j$	328.75/15			296.62/15	347.90/15		172.65/5	9.37/15		$^2D_{3/2}$
	<b>21.92</b>			<b>19.77</b>	<b>23.19</b>		<b>34.53</b>	<b>0.62</b>		
$\sum (g_j A_{j \rightarrow i}) / 15$	<b>21.92</b>			<b>19.77</b>	<b>23.19</b>		<b>11.51</b>	<b>0.62</b>		
$\langle A_{j \rightarrow i} \rangle = \sum (g_j A_{j \rightarrow i}) / \sum g_j$	753.81/55	182.00/7	107.60/12	517.33/49	631.93/55	383.10/26	205.61/20	417.66/55	262.97/19	$^2P_{3/2}$
	<b>13.71</b>	<b>26.00</b>	<b>8.97</b>	<b>10.56</b>	<b>11.49</b>	<b>14.73</b>	<b>10.28</b>	<b>7.59</b>	<b>13.84</b>	
$\sum (g_j A_{j \rightarrow i}) / 27$	<b>27.92</b>	<b>6.74</b>	<b>3.99</b>	<b>19.16</b>	<b>23.40</b>	<b>14.19</b>	<b>7.62</b>	<b>15.47</b>	<b>9.74</b>	
$\langle A_{j \rightarrow i} \rangle = \sum (g_j A_{j \rightarrow i}) / \sum g_j$	264.93/9			254.97/9	222.28/9			184.10/9		$^2P_{1/2}$
	<b>29.44</b>			<b>28.33</b>	<b>24.70</b>			<b>20.46</b>		
$\sum (g_j A_{j \rightarrow i}) / 9$	<b>29.44</b>			<b>28.33</b>	<b>24.70</b>			<b>20.46</b>		
$\langle A_{j \rightarrow i} \rangle = \sum (g_j A_{j \rightarrow i}) / \sum g_j$	2794.33/198	1016/47	831.30/56	2593.93/187	2790.64/193	1363.83/114	655.15/47	2152.41/193	543.32/41	TOTAL
	<b>14.11</b>	<b>21.62</b>	<b>14.84</b>	<b>13.87</b>	<b>14.46</b>	<b>11.96</b>	<b>13.94</b>	<b>11.15</b>	<b>13.25</b>	
$\sum (g_j A_{j \rightarrow i}) / 120$	<b>23.29</b>	<b>8.47</b>	<b>6.93</b>	<b>21.62</b>	<b>23.26</b>	<b>11.37</b>	<b>5.46</b>	<b>17.94</b>	<b>4.53</b>	

We first observe that the totality of the *LS* allowed transitions is present only for the CbA case of our calculations, the LANL code giving one  $A_{j \rightarrow i}$  value just less than  $0.01 \times 10^7 s^{-1}$  and the SST missing two values. Second, set aside our own data, complete  $A_{j \rightarrow i}$  data sets for all the five parent cores of 4s, 4p are not present in the other columns of Table 1, where the existing data are given, except for the ATLL data column. Consequently, the indicative mean values given in the even rows of the Table 2 (where, independently of the given transitions, all the sums are divided by 24, 45, 15, 27 and 9 for each core separately and by 120 for the whole multiplet) are systematically notably lower than those of our calculations (CbA, SST and LANL), except of those given by ATLL for the  $^4S_{3/2}$ ,  $^2D_{5/2}$  cores. The latter are individually (Table 1) very close to ours for the first core and even more for the second, especially for the CbA calculations; in general, they are falling between our results for these two cores and are very different from ours for the remaining three cores.

Inspecting the odd rows of the Table 2 corresponding to the same two first  $^4S_{3/2}$ ,  $^2D_{5/2}$  cores, we see that the experimental results from Nandi et al., which are mostly pertaining to short lifetimes, are resulting to big mean values, even bigger than our mean values in the  $^2D_{5/2}$

core case. Nevertheless, for the two first cores the values given by the experiment are in very good agreement with our calculations, especially for the CbA results, with two notable exceptions for the  ${}^3D_1 \leftarrow {}^3P_0$  and  ${}^3D_3 \leftarrow {}^3P_2$  transitions.

Mean (effective)  $A_{j \rightarrow i}$  values of the odd rows of Table 2, where the multiplicities of only the nonzero values of the Table 1 data are summed in calculating the divider (as it can be seen in the inset in the upper part of the row) are occasionally bigger than ours. This is the case with the  ${}^2D_{5/2}$ ,  ${}^2P_{3/2}$  cores (and the total multiplet mean value) in the calculations of Ceyzériat et al., who apparently have chosen only intense lines to calculate. Note that, although calculated within the Coulomb approximation, the values which these authors calculated for the  ${}^2D_{5/2}$  core are closer to our *ab initio* calculations, whenever a difference with CbA exists (transitions  ${}^3D_1 \leftarrow {}^3F_2$ ,  ${}^3D_2 \leftarrow {}^3F_3$  and  ${}^3D_3 \leftarrow {}^3P_2$ ).

$A_{j \rightarrow i}$  values in the last column of the Table 1 (KURU) are in a very good agreement with our CbA results whenever given, but only for the  ${}^2D_{5/2}$  core, diverging totally for the  ${}^2P_{3/2}$  core except in the  ${}^3P_2 \leftarrow {}^3P_1$  case.

MCHF  $A_{j \rightarrow i}$  values are practically identical with those of ATLL with a very significant exception for the sole  ${}^2D_{3/2}$  transition, where a value near ours is given; note that values are given only whenever NIST column is empty. Consequently, there is an excellent agreement with our values for the  ${}^2D_{5/2}$  core, when data are given.

NIST database gives selected  $A_{j \rightarrow i}$  values for three of the multiplet parent cores and none for the two smaller ones leading to singlets. The provided values are practically identical with our CbA results which, as previously noted, are based on the NIST experimental wavelengths.

It is well known [36] that the sum of the Racah coefficients expressed by the 6-*j* Wigner symbols is the same both in the *LS* and in the *jK* coupling scheme, as is the case for the total statistical weight  $\Sigma T$  of the term. Therefore, the difference between say  $A_{CbA}$  and  $A_{LANL}$  gives a measure of how good the *LS* coupling scheme is in describing the transitions of the  $4s \leftarrow 4p$  Ar III multiplet. Moreover, in comparing with the experiment the  $A_{j \rightarrow i}$  values in the CbA approximation have to be reduced by a factor  $\langle A_{j \rightarrow i} \rangle_{LANL} / \langle A_{j \rightarrow i} \rangle_{CbA}$  roughly about 1.025 to compensate for the inter-combination contributions missing in the *LS* scheme.

It has to be stressed that the mean values given in Table 2 are by no means an intrinsic qualitative measure. Still they do give a useful measure of the completeness of the data, in view of their subsequent use in the determination of the whole multiplet value, together with an estimate of the contribution of the neglected *IC* transitions. It also becomes evident from Table 2 that CbA, SST and LANL results are complete enough to describe the radiative contribution of the  $4s \leftarrow 4p$  multiplet in a complete C-R model. Determination of the collisional rate coefficients will be addressed elsewhere. Leading transitions towards the levels of each of the  $4s$  core are the same in CbA, LANL and SST calculations, as for ATLL, and mostly for MCHF and KURUCZ whenever values are given.

As a conclusion, we observe that our CbA and *ab initio*  $A_{j \rightarrow i}$  calculations give sufficiently agreeing results, provided exact experimental wavelengths and the prevailing coupling are considered for the former and leading terms are included in the base of the latter. The drawback of the CbA is that a coupling scheme has to be chosen from the beginning, which could be e.g., *jK* in the neutral Ar I and Xe I cases [6] instead of the *LS* used here for the Ar III; occasionally, a blend of couplings may also be necessary. Also, no inter-combination lines outside the chosen scheme could be calculated with CbA. On the other side, for *ab initio* calculations a selection of the terms to consider has to be made, which is often intuitive. Both methods give  $A_{j \rightarrow i}$  results near the experimental ones; inclusion of our calculated data in a C-R model could further validate them by comparison of the so obtained spectra with the experimental ones. Similar work has been made for various Ar plasmas [37] and also for Xe plasmas [38].

Standard diagrams showing the  $A_{ij}$  data spread have frequently been used in order to get a glimpse of an expected data agreement. In Fig. 1 our  $A_{j \rightarrow i}$  calculations following CbA ( $A_{ijCbA}$ ) codes and are compared with data given by NIST database, and our results from LANL CATS ( $A_{ijCATS}$ ) codes and our MCHF Multi-configuration Hartree-Fock calculations in the Coulomb (GRP C). The agreement is perfect for data contained in the

NIST base. For the first two cores the results are in quite satisfactory agreement, but this is evidently not the case for the last three cores. In order to get a recommended set of  $A_{j \rightarrow i}$  values to be used in various applications, we are in the process to study recently measured experimental spectra of lightly ionized Ar plasmas.

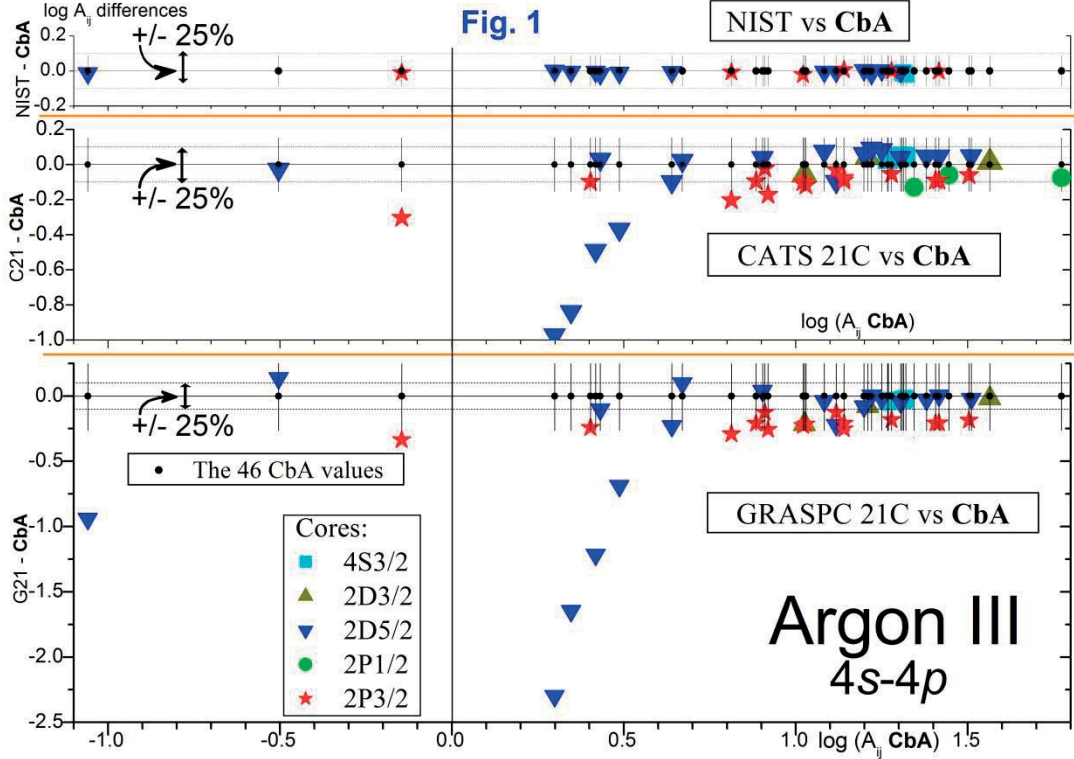


FIG. 1. Comparison of Ar III  $4s-4p$  transition probabilities calculated with three different codes (CbA, CATS, GRASP) with those available in NIST database".

### 3.2. Calculation of $A_{ij}$ for the $6s6p$ multiplet of Xe III

In the case of Xe III, our  $A_{j \rightarrow i}$  calculations for the Xe III  $6s \leftarrow 6p$  multiplet, corresponding to the  $4s \leftarrow 4p$  multiplet of Ar III studied previously, lead to totally analogous results, suggesting also the  $LS$  coupling scheme for the Xe III species and giving slightly smaller  $A_{j \rightarrow i}$  values than for Ar III, as expected. The set of Xe III  $A_{j \rightarrow i}$  values is also available from the authors or can be found in the ALADDIN database. In Table 3 we present our results for the  $6s \leftarrow 6p$  transitions, together with most of the other available data concerning this multiplet, separately for each of the five cores, of which we give the parent term; all numerical  $A_{j \rightarrow i}$  values are given in  $10^7 \text{ s}^{-1}$ . Here also, experimental energy levels have been used throughout CbA calculations, taken from the NIST database. The used values are included in Table 3 together with the wavelengths in Angstroms (Ang NIST) and the appropriate quantum parameters which allow for unambiguous identification of each transition. Our  $A_{j \rightarrow i}$  calculations following CbA ( $A_{ijCbA}$ ) and LANL CATS ( $A_{ijCATS}$ ) codes are compared with our results from MCHF Multi-configuration Hartree-Fock calculations in the Coulomb (GRP C) and Babushkin (GRP B) gauge. For the first two cores the results are in quite satisfactory agreement. This is evidently not the case for the last three cores. We are in the process to study experimental spectra of lightly ionized Xe plasmas which we measured recently, in order to get a recommended set of  $A_{j \rightarrow i}$  values to be used in various applications.

TABLE 3. Xenon III 6s-6p

$4S_{3/2}$											
C icm <sup>-1</sup>	C jcm <sup>-1</sup>	Ang CATS	AijCATS	NISTicm <sup>-1</sup>	NISTjcm <sup>-1</sup>	Ang NIST	TERM i	TERM j	AijCbA	GRP C	GRP B
121790	146770	4003.203	17.83	121475.9	146781.5	3951.704	5.S2.0	5.P1.0	16.89	12.87	14.85
121790	146970	3971.406	17.33	121475.9	146962.4	3923.649	5.S2.0	5.P2.0	17.25	13.75	15.35
121790	148480	3746.722	23.54	121475.9	149061.6	3625.076	5.S2.0	5.P3.0	21.63	17.95	20.04
121790	150240	3514.938	2.2	121475.9	150301.1	3469.191	5.S2.0	3.P1.0		1.58	1.72
121790	151690	3344.482	4.07	121475.9	152057.7	3269.921	5.S2.0	3.P2.0		2.92	3.29
121790	152360	3271.181		121475.9	152808.2	3191.602	5.S2.0	3.P0.0			
125840	146770	4777.831	0.89	125617.1	146781.5	4724.911	3.S1.0	5.P1.0		0.44	0.44
125840	146970	4732.608	1.37	125617.1	146962.4	4684.859	3.S1.0	5.P2.0		0.64	0.71
125840	148480	4416.961		125617.1	149061.6	4265.391	3.S1.0	5.P3.0			
125840	150240	4098.361	16.06	125617.1	150301.1	4051.201	3.S1.0	3.P1.0	16.65	14.04	14.04
125840	151690	3868.472	17.29	125617.1	152057.7	3782.054	3.S1.0	3.P2.0	20.24	11.78	12.9
125840	152360	3770.739	22.45	125617.1	152808.2	3677.673	3.S1.0	3.P0.0	21.88	9.74	11.4
$2D_{3/2}$											
C icm <sup>-1</sup>	C jcm <sup>-1</sup>	Ang CATS	AijCATS	NISTicm <sup>-1</sup>	NISTjcm <sup>-1</sup>	Ang NIST	TERM i	TERM j	AijCbA	GRP C	GRP B
144040	166870	4380.201	4.35	143048.2	164438.6	4674.986	1.D2.0	1.F3.0	11.66	9.53	10.22
144040	165030	4764.173	1.91	143048.2	164511.7	4659.083	1.D2.0	1.P1.0	11.77	11.03	9.66
144040	172130	3559.986	14.41	143048.2	171989.8	3455.232	1.D2.0	1.D2.0	27.11	13.08	17.35
$2D_{5/2}$											
C icm <sup>-1</sup>	C jcm <sup>-1</sup>	Ang CATS	AijCATS	NISTicm <sup>-1</sup>	NISTjcm <sup>-1</sup>	Ang NIST	TERM i	TERM j	AijCbA	GRP C	GRP B
135450	160040	4066.694	10.08	134667.4	158997	4110.226	3.D2.0	3.D1.0	3.54	5.55	5.77
135450	161590	3825.555	8.60	134667.4	160691.3	3842.625	3.D2.0	3.F2.0	2.69	8.49	9.43
135450	162790	3657.644	13.29	134667.4	162260	3624.167	3.D2.0	3.D2.0	14.22	5.68	5.58
135450	163110	3615.329	16.99	134667.4	162594.8	3580.714	3.D2.0	3.F3.0	18.84	11.61	13.23
135450	166200	3252.033		134667.4	165941.7	3197.517	3.D2.0	3.P0.0			
135450	166960	3173.596		134667.4	166554.8	3136.035	3.D2.0	3.F4.0			
135450	165340	3345.601	0.72	134667.4	166699.1	3121.908	3.D2.0	3.D3.0	3.45	3.32	3.72
135450	167550	3115.265	1.79	134667.4	167066.3	3086.524	3.D2.0	3.P2.0	4.79	2.01	2.29
135450	168250	3048.78	1.65	134667.4	168086	2992.348	3.D2.0	3.P1.0	25.99	8.42	11.39
136820	160040	4306.632	0.38	138145.5	158997	4795.82	3.D1.0	3.D1.0	7.03	4.87	4.6
136820	161590	4037.142	2.22	138145.5	160691.3	4435.414	3.D1.0	3.F2.0	9.97	2.64	3.33
136820	162790	3850.597	2.27	138145.5	162260	4146.886	3.D1.0	3.D2.0	2.17	10.43	11.68
136820	163110	3803.728		138145.5	162594.8	4090.093	3.D1.0	3.F3.0			
136820	166200	3403.676	0.57	138145.5	165941.7	3597.614	3.D1.0	3.P0.0	21.86	13.78	17.45
136820	166960	3317.85		138145.5	166554.8	3519.97	3.D1.0	3.F4.0			
136820	165340	3506.311		138145.5	166699.1	3502.183	3.D1.0	3.D3.0			
136820	167550	3254.149	0.50	138145.5	167066.3	3457.715	3.D1.0	3.P2.0	0.24	0.20	0.31
136820	168250	3181.674	0.09	138145.5	168086	3339.957	3.D1.0	3.P1.0	6.71	4.37	5.21
139660	160040	4906.771		138658.2	158997	4916.716	3.D3.0	3.D1.0			
139660	161590	4559.964	0.91	138658.2	160691.3	4538.626	3.D3.0	3.F2.0	0.05	0.60	0.67
139660	162790	4323.39	0.04	138658.2	162260	4236.97	3.D3.0	3.D2.0	2.13	0.43	0.30
139660	163110	4264.392	1.00	138658.2	162594.8	4177.701	3.D3.0	3.F3.0	1.59	2.84	3.21
139660	166200	3767.898		138658.2	165941.7	3665.22	3.D3.0	3.P0.0			
139660	166960	3663.004	17.83	138658.2	166554.8	3584.664	3.D3.0	3.F4.0	22.23	16.06	18.41
139660	165340	3894.081	11.89	138658.2	166699.1	3566.218	3.D3.0	3.D3.0	20.05	7.68	8.22
139660	167550	3585.515	14.21	138658.2	167066.3	3520.12	3.D3.0	3.P2.0	19.65	13.96	16.81
139660	168250	3497.726		138658.2	168086	3398.147	3.D3.0	3.P1.0			
$2P_{1/2}$											
C icm <sup>-1</sup>	C jcm <sup>-1</sup>	Ang CATS	AijCATS	NISTicm <sup>-1</sup>	NISTjcm <sup>-1</sup>	Ang NIST	TERM i	TERM j	AijCbA	GRP C	GRP B
160510	184130	4233.7	8.58	159388.2	184009.1	4061.587	1.P1.0	1.D2.0	17.88	5.66	7.00
160510	185340	4027.386	16.08	159388.2	185888	3773.606	1.P1.0	1.P1.0	21.88	7.85	8.50
160510	190470	3337.784	23.39	159388.2	190491.2	3215.126	1.P1.0	1.S0.0	32.79	24.34	28.34
$2P_{3/2}$											
C icm <sup>-1</sup>	C jcm <sup>-1</sup>	Ang CATS	AijCATS	NISTicm <sup>-1</sup>	NISTjcm <sup>-1</sup>	Ang NIST	TERM i	TERM j	AijCbA	GRP C	GRP B
152810	175760	4357.298	3.21	150505.3	175231.2	4044.352	3.P0.0	3.D1.0	7.99	2.68	2.94
152810	178200	3938.558		150505.3	177955.9	3642.905	3.P0.0	3.D2.0			
152810	178100	3954.132	6.60	150505.3	178029.3	3633.19	3.P0.0	3.P1.0	6.58	7.58	8.19
152810	178450	3900.156		150505.3	178054.5	3629.867	3.P0.0	3.P0.0			
152810	182160	3407.155	1.74	150505.3	182134.1	3161.672	3.P0.0	3.S1.0	3.25	0.31	0.17
152810	183500	3258.39		150505.3	184594.5	2933.486	3.P0.0	3.D3.0			
152810	186220	2993.116		150505.3	186320.9	2792.082	3.P0.0	3.P2.0			
152400	175760	4280.822	3.08	151482.4	175231.2	4210.753	3.P1.0	3.D1.0	5.38	4.69	5.25
152400	178200	3875.969	6.51	151482.4	177955.9	3777.362	3.P1.0	3.D2.0	13.38	10.14	11.61
152400	178100	3891.051	2.12	151482.4	178029.3	3766.918	3.P1.0	3.P1.0	4.50	3.83	4.29
152400	178450	3838.772	16.67	151482.4	178054.5	3763.346	3.P1.0	3.P0.0	18.04	14.4	16.51
152400	182160	3360.215	1.87	151482.4	182134.1	3262.461	3.P1.0	3.S1.0	9.04	0.07	0.16
152400	183500	3215.434		151482.4	184594.5	3020.051	3.P1.0	3.D3.0		0.11	0.05
152400	186220	2956.83	1.37	151482.4	186320.9	2870.392	3.P1.0	3.P2.0	9.52		
159050	175760	5984.44		158928.1	175231.2	6133.822	3.P2.0	3.D1.0	0.13	0.03	0.01
159050	178200	5221.932	0.04	158928.1	177955.9	5255.46	3.P2.0	3.D2.0	1.85	0.85	0.73
159050	178100	5249.344		158928.1	178029.3	5235.265	3.P2.0	3.P1.0	3.12	0.47	0.26
159050	178450	5154.639		158928.1	178054.5	5228.367	3.P2.0	3.P0.0			
159050	182160	4327.131	9.00	158928.1	182134.1	4309.223	3.P2.0	3.S1.0	7.47	15.88	16.17
159050	183500	4089.98	13.74	158928.1	184594.5	3896.152	3.P2.0	3.D3.0	18.04	3.65	5.94
159050	186220	3680.53	18.64	158928.1	186320.9	3650.597	3.P2.0	3.P2.0	16.27	11.38	13.73

Here also, the spread of data corresponding to *ab initio* results obtained with the GRASP and CATS codes in comparison to those calculated with the CbA code on the basis of the experimental energy levels available by NIST is illustrated by the standard diagram of the Fig. 2.

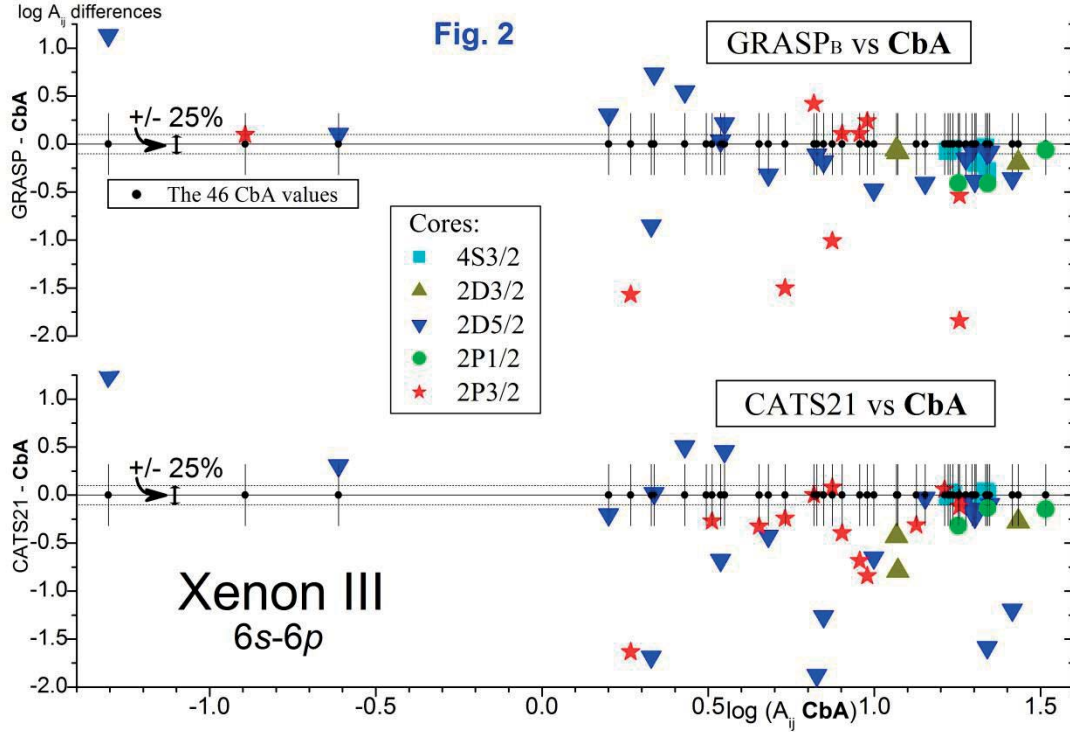


FIG. 2. Comparison of Xe III 6s-6p transition probabilities calculated with three various codes (CbA, GRASP, CATS)

#### 4. FUSION ORIENTED MULTI-DIMENSIONAL CODES FOR MODELING AND DIAGNOSTICS

Atomic data are important for the optical diagnostics of plasmas encountered in most applications. The low density plasmas in fusion devices are not in local thermodynamic equilibrium (LTE), therefore a huge amount of atomic data must be used, which describe the plasma properties in each point by a “zero dimension” Collisional-Radiative (C-R) model. This model takes account of the main collisional and radiative processes by means of the corresponding transition probabilities and cross-sections integrated over the prevailing distributions, often taken as maxwellian. Atomic data are entering the right hand side (RHS) of the statistical equations constituting the C-R model [17]. “Zero dimension” refers to the fact that the level populations expressed by the C-R model and obtained by resolving locally the set of the statistical equations are only valid in the considered point. Transport of the species is neglected in this case, an assumption valid only for homogeneous plasmas. Moreover, in case that each of the left hand side (LHS) part of the statistical equations is set to zero the code is valid only for stationary plasmas. It is possible to introduce the transport effect of all ion species by an additional transport code, which takes into account the particle transfer. Such a code constitutes a type of integrated numerical experiment including plasma physics, atomic and molecular processes and plasma-wall interaction. Although we are in the process of implementing some of our atomic models into various codes, we are primarily considering to use codes of simplified hydrodynamic, plasma in cell (PIC) or hybrid type

together with a C-R model containing a reduced number of ionization stages and excited levels, whenever the temperature is sufficiently low. In order to reduce the computational effort in such a scheme, we have to keep the total number of the considered levels to a strict minimum. Such global models can be also useful in electric propulsion, reentry and plasma reactors studies.

A collisional-radiative model, taking into account the atomic properties of all the plasma constituents, allows for calculation of the parameters which are necessary for the local optical diagnostics and for validation of the model itself. Such a model, a prerequisite for the detailed optical study of rare gas plasmas, once coupled with a convenient transport code, taking into account the geometry of the plasma and the circulation of the present species, may lead to a realistic multi-dimensional model contributing to the study of various confined plasma devices. Over the last 25 years, the Kern Forschung Zentrum in Juelich has developed, supported and applied such a transport code, the 3D Monte Carlo code EIRENE [8] with Linear and Nonlinear Applications. This code has gained a near world-wide monopoly for applications related to particle (and radiation) transport in fusion devices. Code characteristics, maturity and in particular its parallel performance are currently being re-assessed within dedicated EU projects. Special attention was paid to performance of Monte Carlo transport algorithms in iterative mode to cope with cases of non-linearity. Very few results seem to exist for this type of algorithm (dealing with statistical Monte Carlo noise) in computational science, despite the fact that such iterative schemes are increasingly important in many applications in science in general.

## 5. CONCLUSION

The typical examples given in Section 3 illustrate the fact that the CbA approximation calculations compared with results obtained by *ab initio*  $A_{ij}$  calculations, produce results which are shown to be satisfactory for most of the applications, especially for diagnostics and modeling of Tokamak plasmas near the edge. It is evident that the results can be improved whenever experimental  $A_{ij}$  values are available, therefore experiments are needed to improve the recommended  $A_{ij}$  sets.

## ACKNOWLEDGMENT

Two of us (KK and CB) gratefully acknowledge the unknown referee for the proposed style improvements.

## REFERENCES

- [1] CLARK, R.E.H., ABDALLAH JR., J., CZANAK, G., MANN, J.B., COWAN, R.D., 1988, ACE: Atomic Collisions with Electrons, Report LA-11436-M, vol. II.
- [2] SALOMAN, E.B., Energy levels and observed spectral lines of xenon, Xe I through Xe LIV, J. Phys. Chem. Ref. Data **33** (2004) 765.
- [3] SANSONETTI, J.E., MARTIN, W.C., Handbook of basic atomic spectroscopic data, J. Phys. Chem. Ref. Data **34** (2005) 1559.
- [4] DRAWIN, H.W., EMARD, F., KATSONIS, K., Calculation of population densities of helium atoms in non-LTE plasmas, Zeitschrift für Naturforschung A **28** (1973) 1422.
- [5] KATSONIS, K., 1976, Statistical and Kinetic Study of Ar non-LTE Plasmas, Doctorat d'Etat Thesis, EUR-CEA-FC 820, Fontenay-aux-Roses, France.
- [6] KATSONIS, K., BERENQUER, CH., KAMINSKA, A., IZRAR, B., LOPEZ, B., DUDECK, M., Ar(4s) and Ar(4p) excited states in an arc-jet used for planetary re-entry plasma simulations, EUCASS 3, 6-9 July 2009, Versailles, France.
- [7] BERENQUER, CH., KATSONIS, K., COHEN, S., TSEKERIS, P., CORNILLE, M., A Collisional-Radiative Model for Low Temperature Ne Plasmas, IEPC09, 20-25 September 2009, Ann Arbor, MI.

- [8] A Monte Carlo Transport Solver [www.eirene.de](http://www.eirene.de)
- [9] BATES, D.R., DAMGAARD, A., The Calculation of the Absolute Strengths of Spectral Lines, *Phil. Trans. Roy. Soc. (London)* **A242** (1949) 101.
- [10] ROTENBERG, M., BIVIUS, R., METROPOLIS, N., WOOTEN JR., J.K., 1959 *The 3-j and 6-j Symbols*, The Technology Press-MIT, Cambridge Mass.
- [11] FRIEDRICH, H., KATTERBACH, K., TREFFTZ, E., On the accuracy of machine programs for calculating oscillator strengths by Coulomb approximation, *J. Quant. Spectrosc. Radiat. Transfer* **10** (1970) 11.
- [12] ZURRO, B., CAMPOS, J., SÁNCHEZ DEL RIO, C., Lifetimes of some excited levels of Ar I, *Phys. Lett. A* **43** (1973) 527.
- [13] KATSONIS, K., DRAWIN, H.W., Transition probabilities for argon(I), *J. Quant. Spectrosc. Radiat. Transfer* **23** (1980) 1.
- [14] SEATON, M.J., Oscillator strengths in Ne I, *J. Phys. B* **31** (1998) 5315.
- [15] KATSONIS, K., CLARK, R.E.H., CORNILLE, M., SISKOS A, NDIAYÉ A, ABDALLAH JR., J., 2005, Rare Gases Transition Probabilities for Plasma Diagnostics, Plasma Conference Opole 2005, Opole, Poland.
- [16] KATSONIS, K., BERENQUER, CH., CLARK, R.E.H., CORNILLE, M., YAN, J., Transition Probabilities in the Third Spectrum of Rare Gases Ar III and Xe III, ICAMDATA 06, 28-31 October 2008, Beijing, China.
- [17] KATSONIS, K., DZIERZEGA, K., PELLERIN, S., *HTMP* **7** (1973) 559.
- [18] BERENQUER, CH., KATSONIS, K., DANAKAS, S., COHEN, S., TSEKERIS, P., CORNILLE, M., Study of the First Three Ar I, II, III Spectra Using a C-R Model, ICAMDATA 06, 28-31 October 2008, Beijing, China.
- [19] BERENQUER, CH., KATSONIS, K., CLARK, R.E.H., Ne I excitation rate coefficients for C-R models applied to electric propulsion, EGAS41, 8-11 July 2009, Gdansk, Poland.
- [20] KATSONIS, K., BLIMAN, S., CHAPELLE, J., DE IZARRA, CH., DZIERZEGA, K., PELLERIN, S., SISKOS, A., Modeling and Optical Diagnostics of an Argon Plasma under Plasma Thruster Conditions, IEPC 2003, poster 334, Toulouse, March 2003.
- [21] KATSONIS, K., CLARK, R.E.H., CORNILLE, M., BERENQUER, CH., HUMBERT, D., NDIAYE, A., MAYNARD, G., Atomic Data for Collisional-Radiative Models Used in Fusion Reactor Plasma Diagnostics, ICPEAC 2007.
- [22] Los Alamos Atomic Physics Codes <http://aphysics2.lanl.gov/tempweb/>
- [23] ABDALLAH JR, J., CLARK, R.E.H., COWAN, R.D., CATS: The Cowan Atomic Structure Code, Report LA-11436-M, Vol. I (1988).
- [24] COWAN, R.D., Theoretical calculation of atomic spectra using digital computers, *J. Opt. Soc. Am.* **58** (1968) 808.
- [25] COWAN, R.D., 1981 *The Theory of Atomic Structure and Spectra*, Univ. of California Press, Berkeley CA.
- [26] KATSONIS, K., BERENQUER, CH., CLARK, R.E.H., CORNILLE, M., DUAN, B., YAN, J., Transition Probabilities of Ar and Xe Species for Optical Diagnostics and Modeling of Fusion Plasma, RCM Meeting, 4-6 March 2009, IAEA, Vienna (Austria).
- [27] GRANT, I.P., MCKENZIE, B.J., NORRINGTON, P.H., MAYERS, D.F., PYPHER, N.C., An Atomic Multi-Configurational Dirac-Fock Package, *Compt. Phys. Commun.* **21** (1980) 207.
- [28] EISSNER, W., JONES, M., NUSSBAUMER, H., Techniques for the calculation of atomic structures and radiative data including relativistic corrections, *Compt. Phys. Commun.* **8** (1974) 270.
- [29] GU, M.F., Indirect X-Ray Line-Formation Processes in Iron L-Shell Ions, *Astrophys. J.* **582** (2003) 1241 and URL <http://kipac-tree.Stanford.edu/fac>
- [30] IAEA Atomic and Molecular Data Unit Activities <https://www-amdis.iaea.org/>
- [31] CEYZÉRIAT, P., DENIS, A., DUFAY, M., Transition Probabilities and Lifetime in Ar III, *J. Opt. Soc. Am.* **61** (1971) 641.

- [32] NANDI, T., KURUP, M.B., PRASAD, K.G., MEENAKSHI, P., RAO, R., PADMANABHAN, S., KRISHNAMURTY, G., MISHRA, A.P., Lifetimes and Excitation-Functions of Levels in Ar II—Ar IV, *J. Quant. Spectrosc. Radiat. Transfer* **49** (1993) 389.
- [33] BREIT, G., The fine structure of HE as a test of the spin interactions of two electrons, *Phys. Rev.* **36** (1930) 383.
- [34] BETHE, H.A., SALPETER, E.E., 1957 *Hanbuch der Physik XXXV*, Quantum Mechanics of One- and Two-Electron Systems, Springer-Verlag, Berlin.
- [35] SOBEL'MAN, I.I., 1972, *Introduction to the Theory of Atomic Spectra*, Pergamon Press, Oxford.
- [36] KATSONIS, K., DRAWIN, H.W., 1976, *Transition Probabilities of Ar I*, Rept. EUR-CEA-FC-835, Fontenay-aux-Roses, France.
- [37] KATSONIS, K., BOISSE-LAPORTE, C., BONNET, J., LETOUT, S., SISKOS, A., C-R Modeling and Spectroscopic Diagnostics of SPT Plasmas, 4<sup>ème</sup> ISPC, Sardinia, Italie, 2-9 juin 2004.
- [38] KATSONIS, K., CORNILLE, M., SISKOS, A., TANGUY, M., Low Temperature Validation of a Xe Plasma C-R Model, 4<sup>ème</sup> ISPC, Sardinia, Italie, 2-9 juin 2004.

# ELECTRON-ION RECOMBINATION AND ELECTRON-ION IMPACT IONIZATION DATA FROM LABORATORY EXPERIMENTS

A. BOROVIK (JR), S. SCHIPPERS, A. MÜLLER

Institut für Atom- und Molekülphysik,  
Justus-Liebig-Universität Gießen,  
Leihgesterner Weg 217, 35392 Gießen, Germany

## Abstract

Colliding-beams measurements of cross sections for electron-impact single and multiple ionization of  $Xe^{q+}$  ions and of rate coefficients for electron-ion recombination of  $Si^{3+}$ ,  $Fe^{q+}$ , and  $Ni^{25+}$  ions are reported. Charge states  $q$  between 7 and 22 have been investigated for recombination of iron ions using the heavy-ion storage ring in Heidelberg. Ionization of xenon ions was studied for  $q$  between 1 and 25 employing our crossed-beams apparatus in Giessen. The energy ranges of the measurements vary from threshold up to 1000 eV in the ionization experiments and cover the most important dielectronic resonances above 0 eV in the recombination measurements. The latter comprise data up to several hundred eV depending on the system and the core transitions investigated.

## 1. INTRODUCTION

The present work was partly motivated by the International Atomic Energy Agency (IAEA) coordinated research project (CRP) on Atomic Data for Heavy Element Impurities in Fusion Reactors. Within this CRP the measured data presented here provide a substantial contribution to the objectives of the CRP which included the collection and generation of new data relevant to heavy element modeling in fusion reactors, the improvement of data describing collisional and radiative processes, and the provision of data to calculate total power radiated from a plasma as well as undertaking spectral analysis. In particular, data on the recombination of iron ions in a wide range of charge states have been addressed, and parameterized plasma rate coefficients for dielectronic recombination deduced from heavy ion storage ring experiments are presented for a temperature range from below  $10^3$  K to above  $10^8$  K. Iron is a ubiquitous element in plasmas, it occurs with a relatively large abundance in astrophysical environments and it is a likely impurity in a fusion plasma. Sets of recombination data are also made available for the recombination of sodium-like  $Si^{3+}$  ions and lithium-like  $Ni^{25+}$  ions. Silicon is also a relevant impurity in the present context.

The second large subtopic discussed in this contribution is single and multiple ionization of xenon ions by electron-impact. Injecting xenon into a fusion plasma has been discussed for both diagnostic purposes and for draining energy from the plasma to maintain tolerable levels of heat loads on the plasma limiters and divertor surfaces.

Strong additional motivation for studying the processes investigated here for iron and silicon ions arises from data needs in astrophysics and particularly from the problem to understand and to model photoionized plasmas and their electromagnetic emission spectra. Xenon ions are of particular interest also for the generation of intense light of 13.5 nm wavelength envisaged for VUV lithography of the next generation of semiconductor nano devices employed, e.g., in computer chips. Moreover, accelerated xenon ions produced by electron-impact ionization provide the propulsion of micro thrusters for modern space craft.

## 2. ELECTRON-IMPACT IONIZATION OF XENON IONS

Cross-section measurements for electron-impact single and multiple ionization of a number of xenon ions in different charge states have been published previously. A comprehensive theoretical study of electron-impact single ionization covering all charge

states of the xenon atom has recently been reported by Loch et al. [1]. However, prior to the present study no comprehensive systematic experimental investigation had been undertaken. The highest xenon ion charge state for which experimental data from crossed-beams experiments had been available in the literature is  $\text{Xe}^{10+}$ . In contrast, the present study covers all xenon ion charge states from  $q=1$  to  $q=25$ . This substantial extension of accessible  $\text{Xe}^{q+}$  ions was made possible by using an optimized electron-ion crossed beams setup including a 10 GHz electron cyclotron resonance ion source. In this context it has to be mentioned that an experimental study of the ionization of  $\text{Xe}^{43+}$  ions has been carried out at an electron beam ion trap [2] resulting in the determination of relative cross sections that were put to an absolute scale by normalization.

## 2.1. Crossed Beams Experiments

The apparatus employed in this work has been successfully used in a number of experiments on electron-impact ionization of various ions such as  $\text{C}^{3+}$  [3],  $\text{Ti}^{3+}$  [4],  $\text{Mg}^+$  [5], and  $\text{Li}^+$  [6]. Details of the experimental setup were provided in publications on single and multiple ionization of  $\text{Sc}^+$  [7, 8] and recently on single ionization of ground-state  $\text{Li}^+(1s^2^1\text{S})$  and metastable  $\text{Li}^+(1s 2s^3\text{S})$  ions [6]. Therefore, only a short description of the experimental arrangement is provided. The  $\text{Xe}^{q+}$  parent ions were produced in a 10 GHz all-permanent-magnet electron-cyclotron-resonance (ECR) ion source [9]. Microwave power levels up to 100 W were used. Ions produced in the ECR plasma were extracted and accelerated by a voltage of 12 kV. A charge state spectrum of xenon ions extracted from the ECR source is shown in Fig.1. After selection of a suitable (background-free) isotope of 12 q keV  $\text{Xe}^{q+}$  ions (mostly  $A=132$ ) using a  $90^\circ$  dipole magnet and subsequent charge cleaning by an electrostatic  $90^\circ$  spherical deflector, the ion beam was collimated by two pairs of slits in front of the interaction region, where it was crossed by an intense ribbon-shaped electron beam. The electron beam which was employed in the present experiments is space-charge limited and reaches a current of up to 450 mA at 1 keV energy thus providing an electron density unsurpassed in other electron-ion crossed beams arrangements [10]. Products of electron-ion collisions were separated from the primary ion beam by a second  $90^\circ$  dipole magnet and were registered by a single particle detector [11] after passing an electrostatic  $180^\circ$  spherical deflector. The additional deflection of the product ions minimized background of stray electrons released by ions hitting surfaces. The signal detection efficiency was determined to be  $(97 \pm 3)\%$ . The primary ion beam was collected in a movable Faraday cup positioned at an appropriate location inside the second-magnet chamber. An overview of the whole apparatus used in the present experiment is provided in reference [7]. Absolute electron-impact single ionization cross sections of  $\text{Xe}^{q+}$  ions were measured in the energy range from threshold to a maximum of 1000 eV employing the well established animated-beams method [12,10]. The high-current electron gun is mounted on a linear translation feedthrough with its axis perpendicular to the ion beam direction. For the measurement of absolute cross sections, the gun is moved vertically across the ion beam from no overlap via optimum overlap of the electron and ion beams again to no overlap on the opposite side. At positions with no overlap this technique allows for a separate measurement of the background count rate while in the overlap region a position-dependent ionization signal on top of that background is recorded. The integral of the signal peak directly provides the cross section without additional measurement of any overlap form factors [10]. A rectangular aperture of 4 mm width and 16 mm height defines the entrance and exit geometry for the ion beam crossing the electron gun.

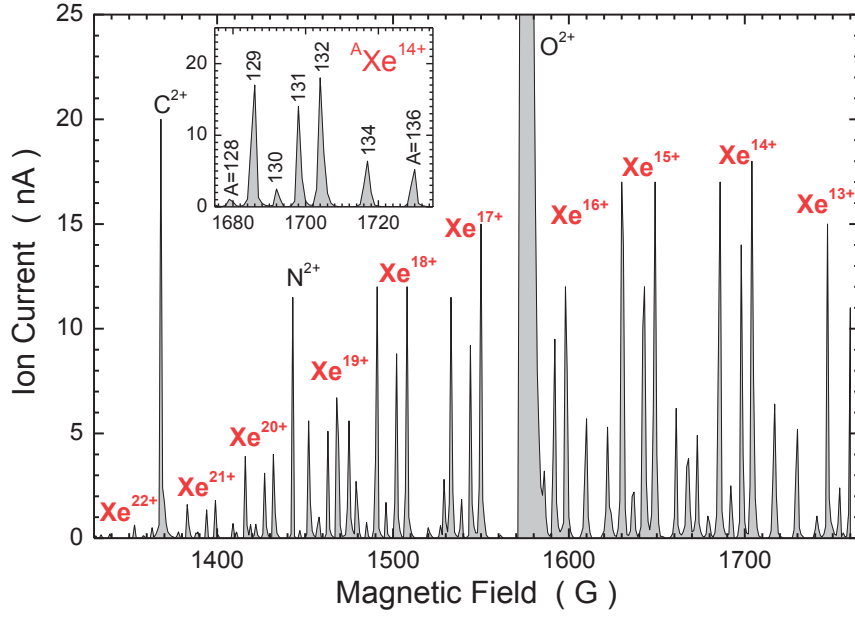


FIG. 1. Charge state spectrum of xenon ions measured in a Faraday cup behind the analyzing magnet down-beam from the ion source. The acceleration voltage was 12 kV. The Xe isotopes are resolved as evidenced in the inset for  $Xe^{14+}$ .

For the absolute measurements carried out with  $Xe^{q+}$  ions the ion beam was collimated to a typical size of 0.7mm x 0.7mm by two sets of movable four-jaw slits about 18.5 cm apart from one another. Ion currents were of the order of several nA. Tight collimation ensured complete transmission of both the parent  $Xe^{q+}$  ion beam to the Faraday cup and the product  $Xe^{(q+n)+}$  ( $n$ -fold ionized) ions to the detector. In the experiments the negative space charge of the electrons was offset by trapped positive ions formed from purposely introduced Kr background gas in the collision region [13]. In addition to the animated-beams technique employed for the measurement of independently absolute cross sections a high-resolution energy-scan technique was used to access details in the energy dependence of the cross sections [14]. Measurements covering a maximum electron energy range of 200 eV in a single sweep with up to 1000 energy steps were carried out at optimum overlap of the electron and ion beams. The dwell time on each energy step was chosen to be 3 ms. With a settling time as low as 0.3 ms for each energy a sweep over 1000 steps took only 3.3 s. Slow fluctuations of experimental conditions with a time constant of 0.1 s and up were therefore averaged over wide ranges of the energy-dependent spectrum measured. Real changes in the cross-section function due to fine energy-dependent structures are thus conserved and made accessible to experimental observation. The number of sweeps was chosen such that statistical uncertainties were reduced to below a desired level. The resulting relative cross sections were then normalized to the absolute cross sections determined by the animated-beams method. The systematic uncertainty of these normalized energy-scan cross sections is therefore almost identical with that of the cross sections obtained with the animated-beams method.

The electron-ion collision energy is predominantly determined by the electron energy in the laboratory frame because the xenon ions are slower than 1-eV electrons. Nevertheless, the kinetic energy of the ions was considered as well as possible contact potentials between the electrodes of the voltage power supplies and the electrodes of the electron gun which are connected via different cables, wires and vacuum feedthroughs. Moreover, space-charge potentials inside the electron beam can lower the actual electron energy. This effect is offset

by introducing Kr gas into the collision region at a pressure of about  $10^{-7}$  hPa. The electron beam produces slow positive ions from that gas and traps them within its own negative space charge potential well present inside the interaction region. Electron optics calculations of the present electron gun have shown that the maximum potential depression by uncompensated electron space charge inside the interaction region is 4% of the acceleration voltage applied between cathode and interaction region. At 1000 eV this would imply a 40 eV energy spread in the electron beam. In experiments with multiply charged barium ions [15] resonances have been observed even near 1000 eV with a width of 3 eV. Even if one would assume that the space charge depression of the potential inside the electron beam alone is responsible for this energy spread, the comparison with the theoretically expected 40 eV spread would require more than 90% compensation of the electron space charge by slow trapped ions. At lower electron energies, resonances with smaller widths have been observed. For example, 0.5 eV energy spread at about 50 eV have been found in the ionization of  $\text{Mg}^+$  ions [5]. Hence, electron space charge cannot significantly change the electron energy scale.

For the determination of possible potential shifts caused by contact potentials the well known 54.42 eV threshold for ionization of  $\text{He}^+$  ions was scanned. The set energies were transformed to the electron-ion center-of-mass (c.m.) frame which takes the velocity of the ions into account. Assuming laboratory energies  $E_e$  and  $E_i$  of the electrons (mass  $m_e$ ) and ions (mass  $m_i$ ), respectively, the c.m. energy  $E_{cm}$  in a colliding-beams experiment with the angle  $\theta$  between the beams was obtained from Ref. [16]

$$E_{cm} = m_i c^2 (1 + m_e / m_i) \left[ \sqrt{1 + \frac{2m_e / m_i}{(1 + m_e / m_i)^2} (G - 1)} - 1 \right] \quad (1)$$

With

$$G = \gamma_i \gamma_e - \sqrt{(\gamma_i^2 - 1)(\gamma_e^2 - 1)} \cos \theta \quad (2)$$

where the Lorentz factors are

$$\gamma_i = 1 + \frac{E_i}{m_i c^2}, \quad \gamma_e = 1 + \frac{E_e}{m_e c^2}. \quad (3)$$

The scan spectrum was then plotted as a function of the nominal c.m. energy determined from the above equations. By comparison with the known ionization threshold of H-like  $\text{He}^+$  the contact potential shift could be determined to be 0.9 V, i.e., the nominal laboratory energies had to be corrected by subtracting 0.9 eV. The resulting energy scale is estimated to be correct within  $\pm 0.3$  eV at least for the energy range up to 100 eV.

The systematic uncertainty of the absolute cross-section determination is the quadrature sum of the systematic uncertainties of the parameters that enter the cross-section determination [10] and this was determined to be 8%. On top of that an additional uncertainty has to be added (also in quadrature) which is due to the limited knowledge of the transmission of electrons through the interaction region. For the determination of cross sections, the electron current was obtained by subtracting the measured electron current  $I_{rods}$  to the acceleration electrodes from the measured electron current  $I_{cath}$  emitted by the cathode. A conservative estimate of the uncertainty of the resulting effective electron current  $I_{eff} = I_{cath} - I_{rods}$  is  $\pm I_{rods}$ . Thus, the energy dependent determination of the electron current through the interaction region has a possible error of about 15% at 20 eV and less than 1% for energies greater than 120 eV. Total uncertainties of cross-sections were determined from the square root of the squared individual uncertainties listed above plus the squared statistical uncertainty.

## 2.2. Results for Electron-Impact Ionization of Xenon Ions

Within the present project cross sections for electron-impact single and multiple ionization of xenon ions have been measured. The energy ranges covered are limited by a maximum of 1000 eV. For  $\text{Xe}^{1+}$  ions n-fold ionization was studied with  $n = 1, 2, 3, \dots, 9$ . Triple and quadruple ionization were also measured for  $\text{Xe}^{6+}$  and  $\text{Xe}^{7+}$ . Single ionization was studied for  $\text{Xe}^{q+}$  with all charge states  $q = 1, 2, \dots, 25$ . Cross sections for double ionization were measured for  $\text{Xe}^{q+}$  with all charge states  $q = 1, 2, \dots, 17$ . The data are still under final analysis.

From previous experiments cross sections are available for single ionization of  $\text{Xe}^{1+}$  ions [17–20]. The early data measured by Müller et al. [17] relied on calculated electron current densities in their electron gun rather than measured electron-ion beam overlap form factors. The resulting cross sections are now known to be too low by roughly 25%. In the measurements by Achenbach et al. [18] the electron-ion beam overlap was determined with tightly collimated  $\text{He}^+$  ion beams by comparing apparent cross sections from the experiment with well established cross sections for this hydrogen-like ion. By equally collimating their other ion beams and thus probing identical density regions of the electron beam Achenbach et al. [18] measured cross sections for a number of xenon ions. Their data are typically within 10% of the present measurements. Both their electron gun as well as the whole experimental arrangement was different from the present set-up. The cross sections obtained by Bell et al. [20] are in almost perfect agreement with the present measurements while the data of Man et al. [19] are 10% lower.

Double ionization of  $\text{Xe}^{1+}$  ions has been measured by Achenbach et al. [21] and cross sections for double, triple and quadruple ionization of  $\text{Xe}^{1+}$  ions were published by Müller et al. [22]. Except for triple ionization, where the older cross sections are about 15% too low, the previous and the present data are in very good agreement.

Electron-impact single ionization of  $\text{Xe}^{2+}$  ions was studied by Achenbach et al. [18], by Griffin et al. [23], by Danjo et al. [24], by Matsumoto et al. [25], and by Man et al. [26]. The data of Achenbach et al. [18] have large uncertainties at the lower energies. The threshold energy is apparently below that of the data of Griffin et al. [23] and Man et al. [26] and the measured cross sections are substantially above those of Griffin et al. [23] and Man et al. [26] at energies below about 80 eV. It was concluded previously that the  $\text{Xe}^{2+}$  ion beams of Achenbach et al. [18] contained substantial fractions of excited states. The cross sections measured by the Japanese group also indicate the presence of long-lived excited ions in their parent ion beam, however, their overall data are well below those of Achenbach et al. [18].

The present data on ionization of  $\text{Xe}^{2+}$  ions are of vastly increased statistical quality. They resemble the shape of the energy dependence of the data obtained by Man et al. [26] and by Danjo et al. [24] and Matsumoto et al. [25], however, the size of the cross sections around the maximum is roughly that of the Achenbach et al. [18] data. It is interesting to note that Griffin et al. [23] provided a distorted wave calculation also reaching a cross-section size at about 85 eV comparable to that measured in the present work (see Fig. 2.). At energies below 80 eV the calculation significantly underestimates the measured cross section. There are several reasons that can be responsible for this discrepancy and partly also for the differences between the different experiments. Already the  $(4d^{10}5s^25p^4)$  ground state configuration of  $\text{Xe}^{2+}$  comprises long lived excited states with excitation energies up to about 4.5 eV [27]. The present measurements as well as the data of the Japanese group indicate the presence of initial states excited by up to about 15 eV. Configurations with such states comprise  $(4d^{10}5s^25p^4)$ ,  $(4d^{10}5s5p^5)$ ,  $(4d^{10}5s^25p^35d)$ , and  $(4d^{10}5s^25p^36s)$ . There is no experimental access to the fractions of the many different states that can be present in the parent ion beam. Calculations for direct single ionization of these excited states using the Los Alamos Atomic Physics Codes (<http://aphysics2.lanl.gov/tempweb/lanl/>) compared with the experimental observations yield metastable contents of the primary ion beam of the order of 10 to 15%. Using the same codes one finds that excitation of a 5s electron in  $(4d^{10}5s^25p^35d)$  produces autoionizing states with large collision strengths at energies just above the ground state ionization threshold.

Such excitations can partly fill up the gap between the measured and calculated cross sections shown in Fig. 2.

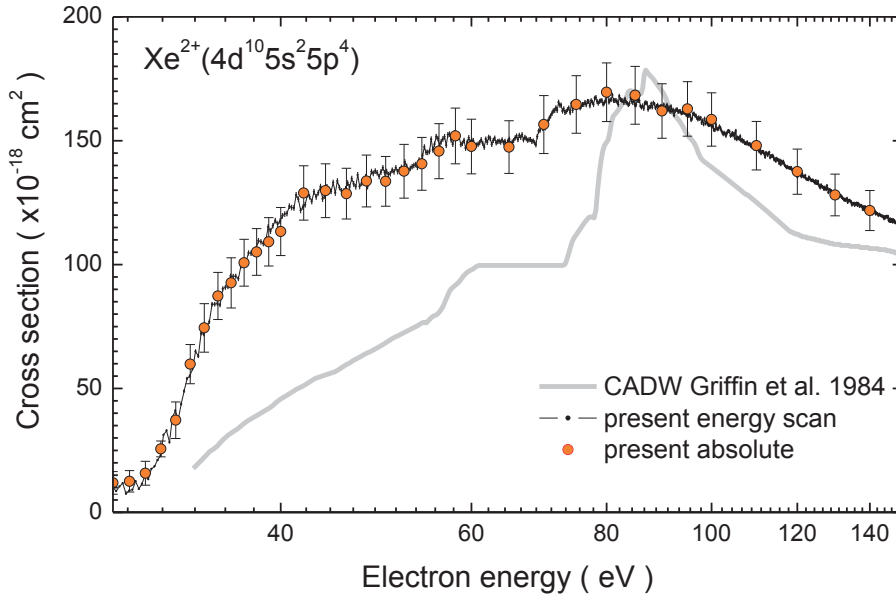


FIG. 2. Cross sections for electron-impact single ionization of  $Xe^{2+}$  ions. The solid gray line is the configuration averaged distorted wave (CADW) calculation carried out by Griffin et al. (1984). The circles are the present absolute measurements and the dots connected by thin solid lines represent the energy scan data.

Another reason that might be responsible for the differences between theory and experiment in Fig. 2. is that resonances in the different excitation channels have not been taken into account. It is well known, that electron-impact excitation is often dominated by resonances [16].

Multiple ionization of  $Xe^{2+}$  ions has been addressed previously by Achenbach et al. [21] and Müller et al. [22]. Their data for electron-impact double ionization of  $Xe^{2+}$  ions agree with the present measurements within the error bars.

Electron-impact single ionization of  $Xe^{3+}$  ions was studied by Gregory et al. [28] and by Achenbach et al. [18]. Both data sets were in agreement with one another within their error bars. Recently, Emmons et al. [29] reported new cross-section measurements. They concentrated their effort on fine details in the cross section and only measured an energy scan which was then normalized to the absolute measurements of Gregory et al. [28]. The present data are about 25% above the measurements of Achenbach et al. [18]. The difference is reduced for double ionization of  $Xe^{3+}$  ions where the present data are about 15% above those of Achenbach et al. [21] and Müller et al. [22]. Electron-impact triple ionization of  $Xe^{3+}$  has only been investigated by Müller et al. [22].

Electron-impact single ionization of  $Xe^{4+}$  ions was measured by Achenbach et al. [18] and by Griffin et al. [23]. Both data sets agree with one another within the error bars. The present data are about 10% above the measurements of Achenbach et al. [18]. Double ionization of  $Xe^{4+}$  ions was previously measured by Achenbach et al. [21], Müller et al. [22] and Pindzola et al. [30]. These data sets agree with one another within the uncertainties. The present measurement agrees well with the results of Müller et al. [22] but is slightly higher.

Electron-impact single ionization of  $Xe^{5+}$  ions has been measured previously by Griffin et al. [23]. The present data are 5 to 10% higher which is within the uncertainties of both experiments. Double ionization cross sections are only available from the present study.

Electron-impact single ionization of  $\text{Xe}^{6+}$  ions was first investigated by Gregory and Crandall [31] using a Penning type ion source. The present data exceed the older cross sections by about 20%. An obvious reason for the observed difference is the population of ( $5s5p\ ^3P$ ) metastable states in the electron cyclotron resonance (ECR) ion source employed in the present experiments. Howald et al. [32] published experimental cross sections for double and triple ionization of  $\text{Xe}^{6+}$  ions. The present data are in reasonable agreement with their findings.

The next charge state for which comparisons can be made with literature ionization data is  $\text{Xe}^{8+}$ . Electron-impact single ionization of  $\text{Xe}^{8+}$  ions was first investigated by Bannister et al. [33]. Measurements using different electron guns were published by Hofmann et al. [34] and later, data were obtained by Stenke et al. [35]. The different data sets have a spread of about 40% between the smallest and the largest cross sections at the maximum occurring at about 350 eV. The differences are readily associated with different fractions of metastable components in the parent ion beam leading to (different) signal levels between about 100 eV and the ground-state threshold near 180 eV. The present data are between the cross sections obtained by Bannister et al. and by Stenke et al. with a difference of about 10% with respect to each of the two previous measurements.

Electron-impact double ionization of  $\text{Xe}^{8+}$  ions was first investigated by Mueller et al. [36]. Hofmann et al. [34] published cross sections that showed good agreement with those of Mueller et al. and the present measurements agree very well with both previous data sets. Data for triple ionization of  $\text{Xe}^{8+}$  ions are also available from the work of Hofmann et al. [34].

Electron-impact single and triple ionization of  $\text{Xe}^{9+}$  ions was investigated by Hofmann et al. [34]. Their collision energies range from about 350 eV to 5 keV. In the overlap region up to 1000 eV the present data for single ionization of  $\text{Xe}^{9+}$  agree well with the previous cross-section measurements.

The highest charge state of xenon ions that was experimentally investigated prior to the present study was  $\text{Xe}^{10+}$ . Data for single and triple ionization were published by Hofmann et al. [34]. Their results for single ionization are compared in Fig. 3 with a number of different measurements that were carried out with the apparatus used here. Data sets with isotopes Xe-132 and Xe-129 were measured about 6 years ago. The perfect agreement shows that contaminations of the parent beam with ions other than  $\text{Xe}^{10+}$  was negligible. The present data are right on top of those previous measurements. The cross-section measurements of Hofmann et al. [34] cover higher energies. The electron gun used in those experiments delivered rapidly decreasing currents when the electron energy was reduced. Within the relatively large error bars that resulted from the low electron density at energies below 1 keV, the data of Hofmann et al. [34] agree with the present measurements. Moreover, the trend of the energy dependence of the cross sections measured at energies above 1 keV nicely matches that to be expected on the basis of the present data set. The comparison with a distorted-wave calculation for direct single ionization of ground state  $\text{Xe}^{10+}$  employing the Los Alamos Atomic Physics Code package (<http://aphysics2.lanl.gov/tempweb/lanl/>) makes it obvious - as in many other charge states of xenon ions - that indirect ionization processes [16] play a decisive role. The fact that there is an apparent non-zero cross section below the ground-state ionization threshold is an indication for the presence of long-lived excited states in the parent ion beam.

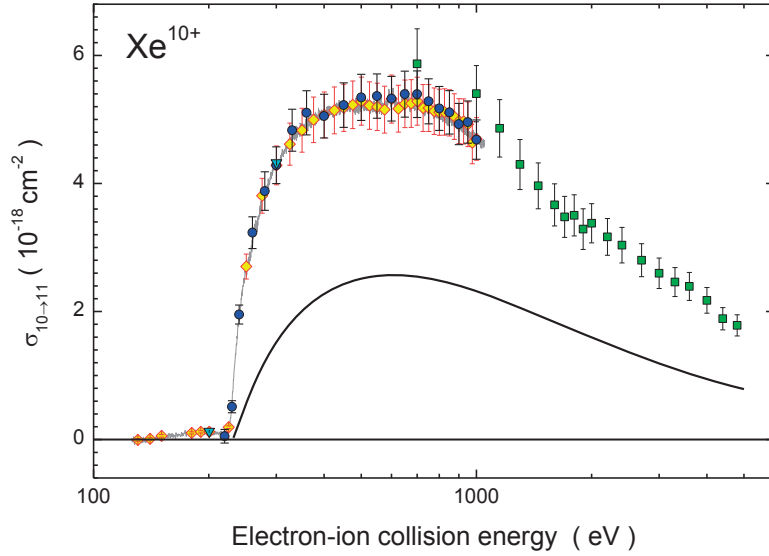


FIG. 3. Cross-section measurements for single ionization of  $Xe^{10+}$  ions by electron-impact. The squares were obtained by Hofmann et al. [34], the diamonds were measured with the isotope Xe-132 by Brandau et al. [37] using the present apparatus. As a test the triangles were measured with Xe-129 and an energy scan measurement (gray solid line) revealed the presence of metastable ions in the parent  $Xe^{10+}$  ion beam [37]. The circles were measured several years later using again the present apparatus. The solid black line is a distorted wave calculation for direct ionization of  $Xe^{10+}$  using the Los Alamos Atomic Physics Codes package (<http://aphysics2.lanl.gov/tempweb/lanl/>) applied to the  $(4p^6 4d^8)$  ground-state configuration.

Fig. 4 shows an enlarged view of the threshold region for ionization of  $Xe^{10+}$ . The energy scan data (the gray solid line in Fig. 3.) clearly reveal two thresholds: One at about 140 eV, the other at 225 eV. According to the NIST Atomic Spectra Database Levels Data [27] the ground state of  $Xe^{10+}$  is  $(4p^6 4d^8 \ ^3F_4)$  with an ionization potential of 229.02 eV. The ground state configuration also contains several fine structure manifolds. It is likely that the ion beam contains a substantial fraction of  $(4p^6 4d^8 \ ^3P)$  states with about 4 eV excitation energy. The threshold at 140 eV can be associated with states where a  $4p$  electron is excited to the  $4d$  subshell. The states within the resulting  $(4p^5 4d^9)$  configuration have excitation energies between 84 and 89 eV. Hence, the threshold of such excited states is to be expected at  $229 \text{ eV} - 89 \text{ eV} = 140 \text{ eV}$ , just where the first threshold can be recognized in the present data. Obviously the  $Xe^{10+}$  parent ion beam contained a fraction of ions in  $(4p^5 4d^9)$  states. Assuming that the threshold for ionization of  $Xe^{10+}(4p^5 4d^9)$  ions is at 140 eV one can calculate the cross section for direct ionization by using the Lotz formula [38]. By scaling down the result of that calculation one can fairly well represent the shape of the measured cross section obtained in the energy range 140 to 225 eV. Then an additional cross-section contribution appears above an onset energy of 225 eV. This contribution can be modeled by another Lotz calculation using a threshold energy of 225 eV. The sum of the two model cross sections is given in Fig. 4 by the solid red line. It matches the experimental data at energies up to 229 eV. Above that energy, which is the  $(4p^6 4d^8 \ ^3F_4)$  ground state ionization energy, the experimental data begin to exceed the model calculation indicating the onset for ionization of the parent ion fraction residing in the ground state.

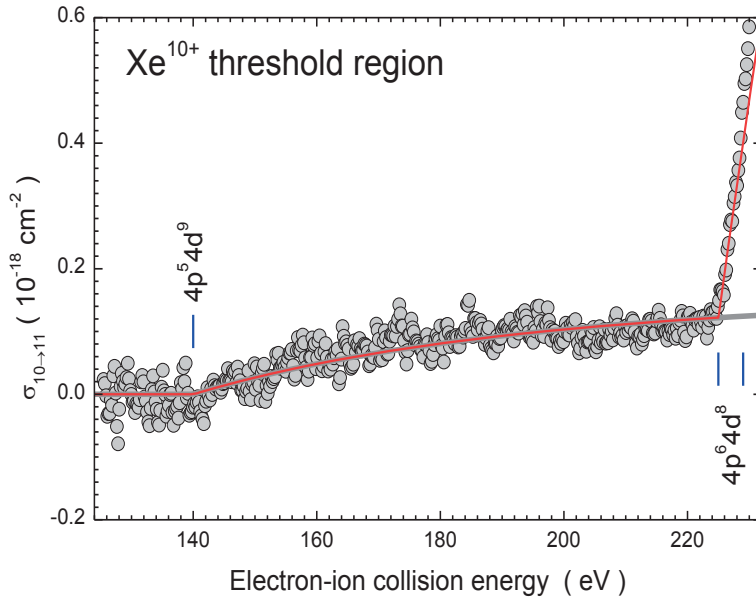


FIG. 4. Threshold energy scan for the electron-impact single ionization of  $\text{Xe}^{10+}$  ions from Fig. 3 (gray shaded circles). Vertical bars at 225 eV and 229 eV indicate the ionization thresholds of the  $^3F_4$  ground state and the  $^3P$  metastable state within the  $(4p^6 4d^8)$  ground-state configuration. The vertical bar at 140 eV represents the  $(4p^5 4d^9)$  ionization threshold. The solid curves are model cross sections based on the Lotz [38] formula employing the thresholds mentioned above and scaled to match the experimental data.

As an example of the data obtained within the present project for higher xenon charge states Fig. 5 shows the cross section for electron-impact single ionization of  $\text{Xe}^{22+}$  ions. The experimental data are compared with theoretical results of Mandelbaum et al. [39]. The most important contributions of excitation-autoionization (EA), i.e., non-resonant excitation of an electron from the  $3d$  and  $3p$  subshells with subsequent autoionization have been taken into account. The cross sections calculated for EA channels greatly exceed those for direct ionization. Given the present state of the analysis, conservative error bars are provided for the absolute experimental data points. The comparison shown in Fig. 5 indicates a substantial discrepancy between theory and experiment. Considering the rich resonance structure found in the experimental energy-scan data, this discrepancy might be explained by the contribution of indirect ionization proceeding via resonant excitation of an inner shell electron (with simultaneous capture of the incident electron) and subsequent emission of two electrons.

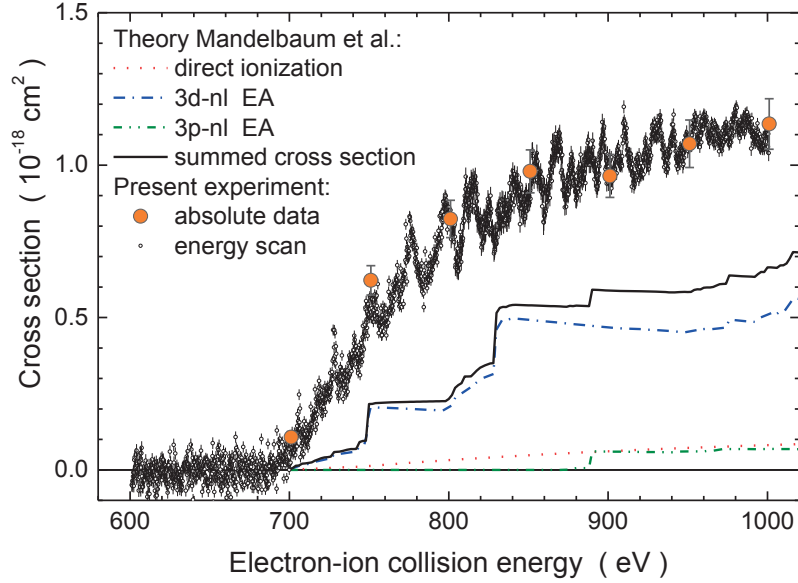


FIG. 5. Electron-impact ionization of  $Xe^{22+}$  ions: present preliminary experimental results with conservative error bars and theoretical calculations by Mandelbaum et al. [39] including indirect ionization through non-resonant excitation of the 3p and 3d subshells.

Summarizing the present investigation of electron-impact single and multiple ionization of xenon ions we find good to fair agreement of the measured cross sections with most of the previous experiments where available. The range of charge states that have been accessible so far to crossed beams electron-impact ionization studies has been significantly extended. The experimental results though preliminary in the present state of the investigation tend to substantially exceed theoretical predictions based on the separate treatment of direct ionization and excitation-autoionization contributions. The distinct threshold step features obtained by theory for excitation-autoionization are almost never seen in the experiments (see e.g., Fig. 2) where steps appear to be washed out to an extent that makes them mostly undetectable. This effect cannot be explained by limited energy resolution of the experiments. The present setup is characterized by energy spreads of less than 0.5 eV below 100 eV electron energy and less than 3 eV below 1 keV. With this low energy spread detailed scan measurements were carried out for all cross sections measured. Especially for the highest charge states large resonance features have been found. The large number of resonances that can be expected in ions as complex as the ones studied here, certainly cannot be individually distinguished even with the relatively good resolution of the present experiment. The resonance features seen in the measured cross sections must rather be regarded as the remaining structure obtained when large numbers of individual resonances are smeared out with a given energy distribution function. The individual resonances only leave a trace in this convolution because they are not evenly distributed across the collision energy axis and because they have vastly different widths and sizes. What the experiment can resolve must therefore be the "tips of icebergs". Thus, the resonance contributions may be of much greater

importance for electron-impact ionization than usually expected. The situation could be similar to the findings for electron-impact excitation of ions where resonances often completely dominate the cross section. If this is true, the theoretical efforts to reliably predict ionization cross sections for highly charged complex ions have to be greatly extended. So far it has been assumed that distorted wave calculations should deliver increasingly better results as the charge state of the ions increases. This expectation may have to be revised after the present experimental study. Another complex task arising in the theoretical modeling of experimental data on ionization of ions is due to the presence of unknown fractions of metastable ions in the parent ion beams used in the experiments. There is no general solution of this problem. Even in ion storage rings or traps, highly excited states may survive accessible storage times and contribute to the signals measured.

### 3. ELECTRON-ION RECOMINATION RATE COEFFICIENTS FROM STORAGE-RING EXPERIMENTS

During the past two decades electron-ion recombination experiments at heavy-ion storage rings have generated numerous recombination rate coefficients for plasma physical applications. A research program aiming at providing reliable electron-ion recombination rate coefficients for astrophysical applications is being carried out at the heavy-ion storage ring TSR of the Max-Planck-Institute for Nuclear Physics in Heidelberg, Germany. The status of these activities, which so far have been particularly focused on iron ions, has been reviewed repeatedly [16, 40–48]. Here the experimental procedure for obtaining absolute electron-ion recombination rate coefficients is briefly outlined and the derivation of plasma rate coefficients from the measured results is sketched. Finally, coefficients for a convenient representation of our experimentally derived DR plasma rate coefficients are listed for  $\text{Si}^{3+}$ ,  $\text{Ni}^{25+}$ , and  $\text{Fe}^{q+}$  with  $q=7-10, 13-22$ .

#### 3.1 Dielectronic Recombination

Dielectronic recombination (DR) is an atomic collision process where an initially free electron excites an electron which is initially bound in the primary ion and thereby loses energy such that it becomes bound, too. The DR process is completed if in a second step the thus formed intermediate doubly excited state decays radiatively to a state below the ionization threshold of the recombined ion.

The initially bound core electron may be excited from a state with principal quantum number  $N$  to a state with principal quantum number  $N'$ . In principle, there is an infinite number of excitation channels. In practice, however, only the smallest excitation steps with  $N'=N$  ( $\Delta N=0$  DR),  $N'=N+1$  ( $\Delta N=1$  DR) and sometimes also  $N'=N+2$  ( $\Delta N=2$ ) DR contribute significantly to the total DR rate coefficient. In the measurements reported here only  $\Delta N=0$  DR and  $\Delta N=1$  DR have been considered.

#### 3.2 Experimental Procedure

Heavy-ion storage rings equipped with electron coolers serve as an excellent experimental environment for electron-ion collision studies [49]. In these experiments a fast moving ion beam is collinearly merged with a magnetically guided electron beam with an overlap length  $L$  of the order of 1–2 m. Recombined ions are separated from the primary beam in the storage-ring's first bending magnet downstream of the interaction region and directed onto a single particle detector. Since the reaction products are moving fast and are confined in a narrow cone they can easily be detected with an efficiency  $\eta$  of nearly 100%. From the measured count rate  $R$ , the stored ion current  $I_i$ , and the electron density  $n_e$  of the electron beam the merged-beams recombination rate coefficient is readily derived as [50]

$$\alpha_{MB}(E_{cm}) = R \frac{eqv_i}{(1 - \beta_i \beta_e) I_i n_e L \eta} \quad (4)$$

Here  $eq$  is the charge of the primary ion,  $v_i = c\beta_i$  and  $v_e = c\beta_e$  are the ion and electron velocities, respectively, and  $c$  denotes the speed of light in vacuum. The center-of-mass energy  $E_{cm}$  can be calculated from the laboratory ion and electron energies using equations 1 to 3 with  $\theta = 0^\circ$ . In a storage-ring experiment the ion energy is kept fixed and  $E_{cm}$  is varied by changing either the cathode voltage at the electron gun or the voltage on a drift tube that is surrounding the electron-ion interaction region. As an example for a measured recombination spectrum Fig. 6 shows results for the recombination of  $\text{Ni}^{25+}$  ions [51].

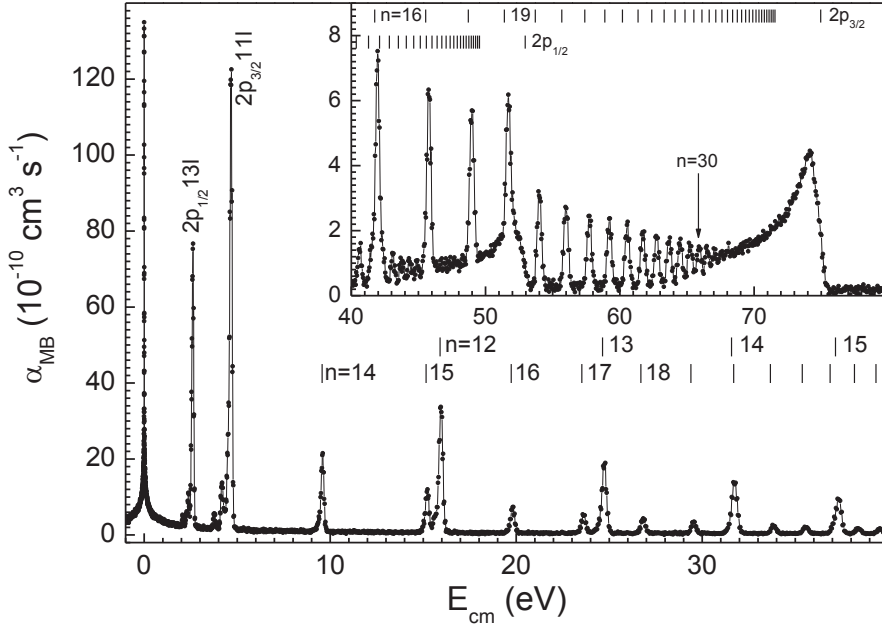


FIG. 6. Measured merged-beams rate coefficient for the recombination of Li-like  $\text{Ni}^{25+}$  ions with free electrons [51]. Two Rydberg series of  $2p_{1/2} nl$  and  $2p_{3/2} nl$   $\Delta N=0$  DR resonances are discernible converging to the respective series limits at 52.92 eV and 74.96 eV [27]. The sharp structure at  $E_{cm} = 0$  is due to radiative recombination. Positive (negative) energies correspond to electron velocities larger (smaller) than the ion velocity.

Further details of the various aspects of the experimental approach and the data reduction procedures at the Heidelberg heavy-ion storage ring TSR have been given by Kilgus et al. [52], Lampert et al. [53], Pastuszka et al. [54], Schippers et al. [51, 55, 56], Wolf et al. [57], Lestinsky et al. [58], and Schmidt et al. [59]. The systematic experimental uncertainty of the measured merged-beams recombination rate coefficient is typically 20% at 90% confidence level [60].

### 3.3 Derivation and Parameterization of DR Plasma Rate Coefficients

The plasma recombination rate coefficient (PRRC) is derived by convoluting the measured merged-beams recombination rate coefficient (MBRRC) with a Maxwell-Boltzmann electron energy distribution. As detailed in Schippers et al. [55, 56], there are three issues that require special consideration: The experimental energy spread, the recombination rate enhancement at low energies, and field ionization of high Rydberg states in the storage-ring bending magnets.

The experimental energy spread  $\Delta E_{cm}$  influences the outcome of the convolution for resonances with resonance energies  $E_{cm} \leq \Delta E_{cm}$ . This can be circumvented by extracting the

DR cross section, e.g., by a fit of individual DR resonances to the measured MBRRC at low energies [56].

An enhanced MBRRC is consistently observed in merged electron-ion beam experiments at very low energies below a few meV. There, the measured MBRRC exceeds the theoretical expectation by factors of typically 2–3 [61]. This excess rate coefficient is an artifact of the merged-beams technique, and hence it has to be subtracted from the measured MBRRC prior to the derivation of the PRRC.

Field ionization of the loosely bound high Rydberg electron in the recombined ions can result from the motional electric fields that the ions experience inside the storage-ring bending magnets [55]. For example, in the  $\text{Ni}^{25+}$  experiment, only DR involving capture into Rydberg levels with quantum numbers less than 80 contributed to the MBRRC (Fig. 7a). The missing DR resonance strength up to  $n_{\text{max}} = 1000$  (where the PRRC has converged) can be estimated from a theoretical calculation using, e.g., the AUTOSTRUCTURE code [62]. For high Rydberg quantum numbers this code reproduces the regular DR resonance structure close to the Rydberg series limits reasonably well (Fig. 7a) especially when slight “manual adjustments” are made to the autoionization transition rates and the core excitation energies that are relevant for the DR resonance calculations.

Fig. 7b displays the  $\text{Ni}^{25+}$  PRRC which has been derived from the measured MBRRC using these procedures. Its systematic uncertainty is basically the  $\pm 20\%$  uncertainty of the experimental MBRRC. In some cases, additional uncertainties arise from the subtraction of the non-resonant “background” due to radiative recombination from the measured MBRRC, from unresolved DR resonances at very low energies, from the theoretical estimate of the unmeasured high Rydberg resonances (especially for low charge states), or from the presence of a usually unknown fraction of primary ions in extremely long living metastable levels such as, e.g., the  $2s2p\ ^3P_0$  level in berylliumlike  $\text{Fe}^{22+}$  [60].

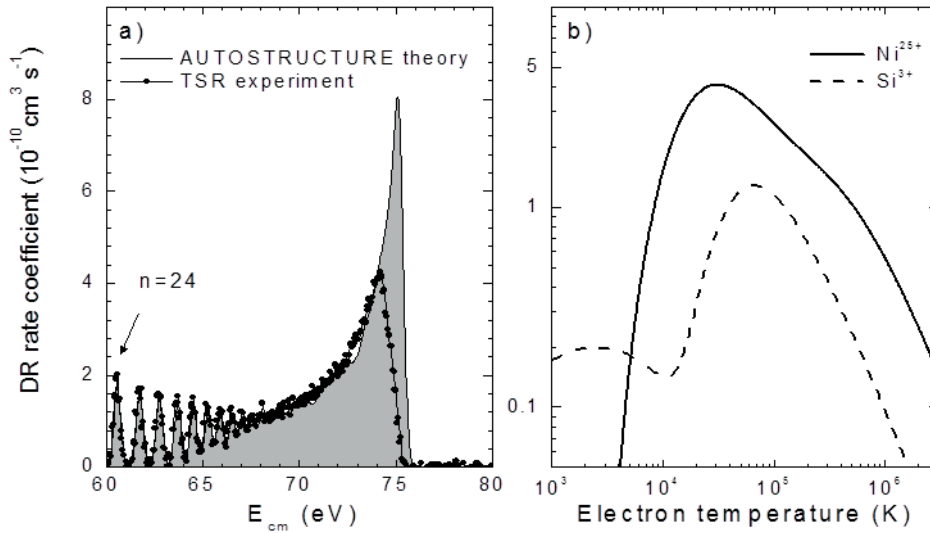


FIG. 7a. Comparison of the  $\text{Ni}^{25+}$  merged beams DR rate coefficient with a theoretical calculation using the AUTOSTRUCTURE code [62] at the  $2p_{3/2}$  series limit. The theoretical rate coefficient contains contributions by Rydberg resonances beyond the experimental field ionization cut-off at  $n=79$ . b) Full line: Experimentally derived  $\text{Ni}^{25+}$   $\Delta N=0$  DR plasma rate coefficient obtained by convoluting the AUTOSTRUCTURE–extrapolated experimental spectrum (Figures 6 and 7a) with an isotropic maxwellian. Dashed line: Experimentally derived  $\text{Si}^{3+}$  DR plasma rate coefficient [50].

A convenient parameterization of the plasma DR rate coefficient is

$$\alpha^{DR}(T) = T^{-3/2} \sum_i c_i \exp(-E_i/T) \quad (5)$$

where the parameters  $c_i$  and  $E_i$  are determined from a fit of equation 5 to the experimentally derived DR plasma rate coefficient. It should be noted that a given set of parameters can only be used in a limited temperature range  $[T_{\min}, T_{\max}]$ . Outside this range the fit may deviate strongly from the experimentally derived curve. In the temperature range  $[T_{\min}, T_{\max}]$  the deviation from the experimentally derived curve is usually less than 1.5% so that no significant additional uncertainty is introduced by the parameterization.

### 3.4 Results for $\text{Si}^{3+}$ , $\text{Fe}^{q+}$ ( $q=7-10, 13-22$ ) and $\text{Ni}^{25+}$

The experimentally derived DR plasma rate coefficients can be retrieved by using Eq. (5) and the tabulated parameters  $c_i$  and  $E_i$  (Tables 1–4, Figs. 7b, 8 and 9). Tables 1 and 2 contain the parameters for  $\text{Ni}^{25+}$  [51] and  $\text{Si}^{3+}$  [50], respectively. Table 3 lists the parameters for the Fe *L*-shell ions  $\text{Fe}^{16+}$  [63],  $\text{Fe}^{17+}$  [64],  $\text{Fe}^{18+}$  [65],  $\text{Fe}^{19+}$  [66],  $\text{Fe}^{20+}$  [67],  $\text{Fe}^{21+}$  [68], and  $\text{Fe}^{22+}$  [60] and Table 4 for the iron *M*-shell ions  $\text{Fe}^{7+}$  [59],  $\text{Fe}^{8+}$  [59],  $\text{Fe}^{9+}$  [68],  $\text{Fe}^{10+}$  [68],  $\text{Fe}^{13+}$  [69],  $\text{Fe}^{14+}$  [70], and  $\text{Fe}^{15+}$  [40].

It should be noted that in some of these references the parameters  $c_i$  and  $E_i$  were tabulated in units that differ from the units used here. In these cases, the respective coefficients have been converted to the present units. In Tables 1–4 also the temperature ranges of validity are given as well as the experimental uncertainties of the absolute DR plasma rate coefficients.

For  $\text{Ni}^{25+}$  and  $\text{Fe}^{15+}$  no fit parameters have previously been published. The tabulated parameters for these ions have therefore been newly derived for publication in the present work. The experimentally derived DR plasma rate coefficient for DR of neon-like  $\text{Fe}^{16+}$  [63] is in excellent agreement with the theoretical results of Zatsarinny et al. [71]. Therefore, no fit has been made to the experimental data and the theoretical fit parameters for  $\text{Fe}^{16+}$  are used.

TABLE 1. FIT PARAMETERS (CF. EQUATION 5) FOR THE  $\Delta N=0$  DR PLASMA RATE COEFFICIENT OF  $\text{Ni}^{25+}$  IONS. UNITS FOR  $c_i$  AND  $E_i$  ARE  $\text{cm}^3 \text{s}^{-1} \text{K}^{3/2}$  AND K, RESPECTIVELY. THE FIT IS VALID IN THE TEMPERATURE RANGE 4600 K TO  $10^8$  K. IN THIS RANGE, THE SYSTEMATIC UNCERTAINTY OF THE ABSOLUTE RATE COEFFICIENT IS 20% AT 90% CONFIDENCE LEVEL.

$i$	1	2	3	4	5	6	7
$c_i$	4.395E-2	2.715E-2	1.140E-2	7.172E-3	3.070E-3	2.089E-7	1.844E-9
$E_i$	8.133E+5	4.360E+5	1.895E+5	5.758E+4	3.155E+4	1.193E+4	1.540E+2

TABLE 2. FIT PARAMETERS (CF. EQUATION 5) FOR THE DR PLASMA RATE COEFFICIENT OF  $\text{Si}^{3+}$  IONS. UNITS FOR  $c_i$  AND  $E_i$  ARE  $\text{cm}^3 \text{s}^{-1} \text{K}^{3/2}$  AND K, RESPECTIVELY. THE FIT IS VALID IN THE TEMPERATURE RANGE 120 K TO  $10^8$  K. IN THIS RANGE, THE SYSTEMATIC UNCERTAINTY OF THE ABSOLUTE RATE COEFFICIENT IS 25% AT 90% CONFIDENCE LEVEL. THE RATE COEFFICIENT COMPRISES ALL DR RESONANCES ASSOCIATED WITH THE FOLLOWING CORE EXCITATIONS:  $2s \rightarrow 3$ ,  $2s \rightarrow 4$ ,  $2p \rightarrow N'$ , AND  $3s \rightarrow N'$  WITH  $3 \leq N' < \infty$ .

$i$	1	2	3	4	5	6	7	8	9
$c_i$	2.31E-8	6.12E-8	1.10E-6	3.65E-6	1.45E-5	1.78E-5	3E-4	9.5E-3	1.9E-3
$E_i$	118	580	1.44E+3	2.83E+3	8.0E+3	1.77E+4	6.3E+4	1.02E+5	9.34E+5

TABLE 3. FIT PARAMETERS (CF. EQUATION 5) FOR THE PLASMA DR RATE COEFFICIENTS OF THE  $\text{Fe}^{q+}$ - $L$ -SHELL IONS WITH  $16 \leq q \leq 22$ . EACH FIT IS VALID IN THE SPECIFIED TEMPERATURE RANGE  $[T_{\min}, T_{\max}]$ . THE QUANTITY  $\Delta\alpha$  DENOTES THE SYSTEMATIC UNCERTAINTY OF THE ABSOLUTE RATE COEFFICIENT AT 90% CONFIDENCE LEVEL. THE ROW LABELED  $N \rightarrow N'$  SPECIFIES THE CORE EXCITATIONS THAT HAVE BEEN COVERED BY EACH EXPERIMENT. UNITS ARE  $\text{cm}^3 \text{s}^{-1} \text{K}^{3/2}$  FOR  $c_i$  AND K FOR  $E_i$ ,  $T_{\min}$ , and  $T_{\max}$ . EMPTY BOXES MEAN ZERO PARAMETERS  $c_i$  IN LINES  $i$ .

$q$	16	17	18	19	20	21	22
$c_1$	2.06E-1	4.79E-6	2.14E-5	1.24E-4	7.71E-5	1.46E-4	2.47E-6
$c_2$	1.24E+0	9.05E-5	1.05E-5	1.84E-4	6.08E-5	1.17E-3	1.21E-4
$c_3$		3.48E-5	4.34E-5	1.47E-4	3.93E-4	4.22E-3	2.18E-3
$c_4$		1.83E-4	6.62E-5	7.87E-4	1.14E-3	2.80E-3	1.50E-3
$c_5$		5.26E-4	3.86E-4	3.54E-3	7.63E-3	9.22E-3	1.47E-2
$c_6$		2.12E-3	1.24E-3	5.02E-3	1.37E-2	3.13E-2	3.14E-2
$c_7$		4.29E-3	5.56E-3	1.96E-2	2.08E-2	9.98E-2	7.98E-2
$c_8$		3.16E-2	4.07E-2	6.43E-2	7.86E-2		1.25E-1
$c_9$			2.92E-1				7.25E-1
$c_{10}$			1.46E+0				
$E_1$	4.38E+6	2.58E+3	1.01E+2	1.61E+1	6.75E+1	1.58E+3	1.04E+3
$E_2$	7.98E+6	6.08E+3	2.45E+2	7.90E+1	1.15E+2	2.43E+3	5.44E+3
$E_3$		1.35E+4	8.80E+2	7.73E+2	2.43E+3	4.85E+3	1.35E+4
$E_4$		2.92E+4	7.53E+3	3.86E+3	6.71E+3	1.09E+4	3.73E+4
$E_5$		7.62E+4	1.93E+4	1.66E+4	2.74E+4	7.13E+4	1.21E+5
$E_6$		2.21E+5	6.75E+4	6.08E+4	6.73E+4	2.72E+5	3.15E+5
$E_7$		6.57E+5	2.90E+5	2.33E+5	2.80E+5	9.92E+5	9.08E+5
$E_8$		1.40E+6	1.11E+6	9.74E+5	1.11E+6		4.64E+6
$E_9$			4.65E+6				1.15E+7
$E_{10}$			9.14E+6				
$T_{\min}$	12	580	120	12	12	230	12
$T_{\max}$	1.2E+9	1.2E+8	1.2E+8	1.2E+8	1.2E+8	1.2E+8	1.2E+8
$\Delta\alpha$	$\pm 22\%$ <sup>a</sup>	$\pm 20\%$	$\pm 20\%$ <sup>b</sup>	$\pm 20\%$	$\pm 20\%$ <sup>c</sup>	$\pm 20\%$	$\pm 20\%$
$N \rightarrow N'$	2 $\rightarrow$ 3	2 $\rightarrow$ 2	2 $\rightarrow$ 2, 2 $\rightarrow$ 3	2 $\rightarrow$ 2	2 $\rightarrow$ 2	2 $\rightarrow$ 2	2 $\rightarrow$ 2, 2 $\rightarrow$ 3

<sup>a</sup>fit parameters taken from theoretical work by Zatsarinny et al. [71]

<sup>b</sup>the uncertainty is larger at temperatures below 11600 K (Savin et al. [65])

<sup>c</sup>the uncertainty is larger at temperatures below 5800 K (Savin et al. [67])

TABLE 4. FIT PARAMETERS (CF. EQUATION 5) FOR THE PLASMA DR RATE COEFFICIENT OF THE  $\text{Fe}^{q+}$ - $M$ -SHELL IONS WITH  $7 \leq q \leq 10$  AND  $13 \leq q \leq 15$ . EACH FIT IS VALID IN THE SPECIFIED TEMPERATURE RANGE  $[T_{\min}, T_{\max}]$ . THE QUANTITY  $\Delta\alpha$  DENOTES THE SYSTEMATIC UNCERTAINTY OF THE ABSOLUTE RATE COEFFICIENT AT 90% CONFIDENCE LEVEL. THE ROW LABELED  $N \rightarrow N'$  SPECIFIES THE CORE EXCITATIONS THAT HAVE BEEN COVERED BY EACH EXPERIMENT. UNITS ARE  $\text{cm}^3 \text{s}^{-1} \text{K}^{3/2}$  FOR  $c_i$  AND K FOR  $E_i$ ,  $T_{\min}$ , AND  $T_{\max}$ . EMPTY BOXES MEAN ZERO PARAMETERS  $c_i$  IN LINES  $i$ .

$q$	7	8	9	10	13	14	15
$c_1$	5.978E-7	4.777E-7	6.485E-5	6.487E-5	3.55E-4	1.07E-4	3.875E-6
$c_2$	8.939E-7	1.231E-6	6.360E-5	8.793E-5	2.40E-3	8.26E-6	5.872E-2
$c_3$	1.640E-5	5.055E-5	3.720E-4	4.939E-4	7.83E-3	1.00E-6	2.173E-2
$c_4$	9.598E-5	3.413E-4	1.607E-3	3.787E-3	1.10E-2	1.46E-5	3.411E-3
$c_5$	1.105E-4	1.625E-3	3.516E-3	8.878E-3	3.30E-2	2.77E-6	9.398E-4
$c_6$	7.299E-4	3.873E-3	7.326E-3	5.325E-2	1.45E-1	1.51E-6	7.272E-5
$c_7$	3.858E-3	6.438E-3	2.560E-2	2.104E-1	8.50E-2	3.29E-6	
$c_8$	2.476E-2	6.970E-2	1.005E-1		2.59E-2	1.63E-4	
$c_9$	1.789E-1	2.925E-1	1.942E-1		8.93E-3	4.14E-4	
$c_{10}$					9.80E-3	2.17E-3	
$c_{11}$						6.40E-3	
$c_{12}$						4.93E-2	
$c_{13}$						1.51E-1	
$E_1$	8.385E+0	9.034E+0	3.994E+1	1.101E+2	2.54E+2	7.82E+1	2.006E+7
$E_2$	9.922E+1	1.128E+2	5.621E+2	5.654E+2	2.08E+3	1.14E+2	3.866E+5
$E_3$	5.234E+2	6.624E+2	1.992E+3	1.842E+3	8.74E+3	2.29E+2	2.144E+5
$E_4$	1.579E+3	1.143E+3	8.325E+3	7.134E+3	2.57E+4	2.95E+2	7.431E+4
$E_5$	4.489E+3	3.926E+3	2.757E+4	3.085E+4	1.11E+5	5.16E+2	3.194E+4
$E_6$	2.102E+4	1.300E+4	7.409E+4	1.878E+5	3.59E+5	7.08E+2	1.6504E4
$E_7$	9.778E+4	4.684E+4	1.552E+5	6.706E+5	7.39E+5	1.28E+3	
$E_8$	3.353E+5	2.670E+5	4.388E+5		2.54E+6	2.22E+3	
$E_9$	8.081E+5	7.358E+5	7.355E+5		1.74E+7	3.86E+3	
$E_{10}$					9.12E+7	1.12E+4	
$E_{11}$						2.87E+4	
$E_{12}$						1.25E+5	
$E_{13}$						4.45E+5	
$T_{\min}$	12	12	100	100	800	12	2300
$T_{\max}$	1.2E+9	1.2E+9	1E+7	1E+7	1E+8	1.2E+8	1E+14
$\Delta\alpha$	$\pm 25\%^a$	$\pm 29\%^b$	$\pm 25\%^c$	$\pm 25\%^d$	$\pm 29\%$	$\pm 29\%^e$	$\pm 20\%$
$N \rightarrow N'$	3 $\rightarrow$ 3	3 $\rightarrow$ 3	3 $\rightarrow$ 3	3 $\rightarrow$ 3	3 $\rightarrow$ 3, 3 $\rightarrow$ 4	3 $\rightarrow$ 3	3 $\rightarrow$ 3, 3 $\rightarrow$ 4

<sup>a</sup>the uncertainty is larger at temperatures below 5800 K (Schmidt et al. [59])

<sup>b</sup>the uncertainty is larger at temperatures below 11600 K (Schmidt et al. [59])

<sup>c</sup>the uncertainty is larger at temperatures below 10000 K (Lestinsky et al. [68])

<sup>d</sup>the uncertainty is larger at temperatures below 1000 K (Lestinsky et al. [68])

<sup>e</sup>the uncertainty is larger at temperatures below 11600 K (Lukić et al. [70])

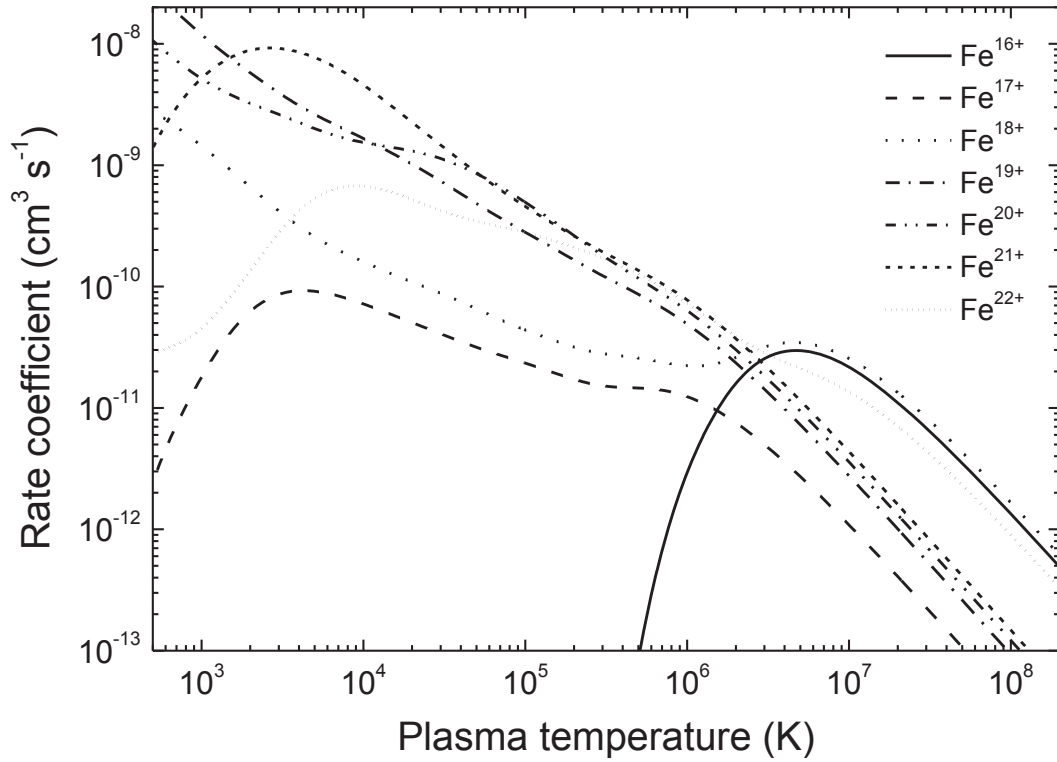


FIG. 8. Rate coefficients for DR of some Fe-L-shell ions in a plasma. The curves were obtained by using Eq. 5 with the tabulated parameters from Table 3.

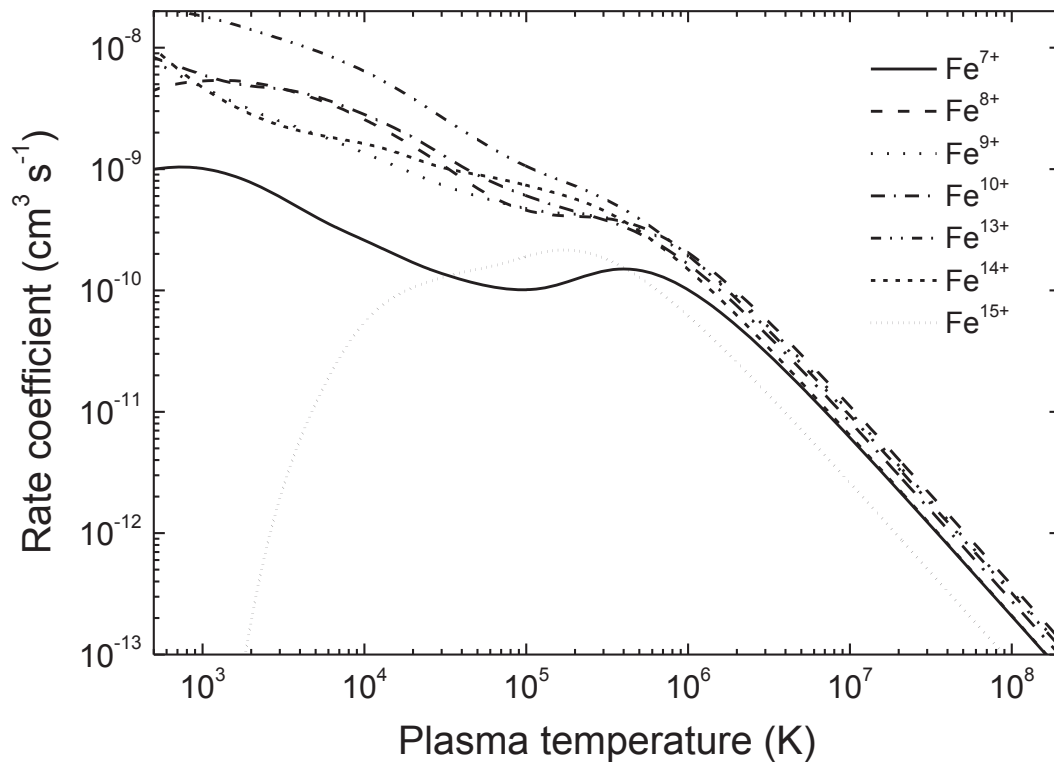


FIG. 9. Rate coefficients for DR of some Fe-M-shell ions in a plasma. The curves were obtained by using Eq. 5 with the tabulated parameters from Table 4.

## Note added in proof

During the editorial process several plasma-impurity related publications by our various collaborations have appeared which are directly related to the work described in this article and which provide details of the measurements and additional theoretical findings on electronic processes involving silicon, iron, nickel, and xenon ions. The new publications are listed at the end of the References Section [72-90].

## REFERENCES

- [1] LOCH, S.D., PINDZOLA, M.S., GRIFFIN, D.C., Electron-impact ionization of atomic ions in the Sn and Xe isonuclear sequences, *Int. J. Mass Spectrom.* **271** (2008) 68.
- [2] SCHNEIDER, D., DeWITT, D., CLARK, M.W., SCHUCH, R., COCKE, C.L., SCHMIEDER, R., REED, K.J., CHEN, M.H., MARRS, R.E., LEVINE, M., FORTNER, R., Ion-collision experiments with slow, very highly charged ions extracted from an electron-beam ion trap, *Phys. Rev. A* **42** (1990) 3889.
- [3] TENG, H., KNOPP, H., RICZ, S., SCHIPPERS, S., BERRINGTON, K.A., MÜLLER, A., Interference of direct and resonant channels in electron-impact ionization of  $C^{3+}$  ions: Unified  $R$ -matrix calculation and experiment, *Phys. Rev. A* **61** (2000) 060704.
- [4] VAN ZOEST, T., KNOPP, H., JACOBI, J., SCHIPPERS, S., PHANEUF, R.A., MÜLLER, A., Electron-impact ionization of  $Ti^{3+}$  ions, *J. Phys. B* **37** (2004) 4387.
- [5] BECKER, C., KNOPP, H., JACOBI, J., TENG, H., SCHIPPERS, S., MÜLLER, A., Electron-impact single and multiple ionization of  $Mg^+$  ions, *J. Phys. B* **37** (2004) 1503.
- [6] BOROVIK JR, A., MÜLLER, A., SCHIPPERS, S., BRAY, I., FURSA, D.V., Electron-impact ionization of ground-state and metastable  $Li^+$  ions, *J. Phys. B* **42** (2009) 025203.
- [7] JACOBI, J., KNOPP, H., SCHIPPERS, S., MÜLLER, A., LOCH, S.D., WITTHOEFT, M., PINDZOLA, M.S., BALLANCE, C.P., Strong contributions of indirect processes to the electron-impact ionization cross section of  $Sc^+$  ions, *Phys. Rev. A* **70** (2004) 042717.
- [8] JACOBI, J., KNOPP, H., SCHIPPERS, S., SHI, W., MÜLLER, A., Multiple ionization of  $Sc^+$ -ions by electron-impact, *J. Phys. B* **38** (2005) 2015.
- [9] BROETZ, F., TRASSL, R., McCULLOUGH, R.W., ARNOLD, W., SALZBORN, E., Design of compact all-permanent magnet electron cyclotron resonance (ECR) ion sources for atomic physics experiments, *Phys. Scr.* **T92** (2001) 278.
- [10] MÜLLER, A., TINSCHERT, K., ACHENBACH, C., SALZBORN, E., BECKER, R., A new technique for the measurement of ionization cross sections with crossed electron and ion beams, *Nucl. Instrum. Methods B* **10** (1985) 204  
and  
BECKER, R., MÜLLER, A., ACHENBACH, C., TINSCHERT, K., SALZBORN, E., A dense electron target for electron-ion collisions, *Nucl. Instr. and Meth. B* **9** (1985) 385
- [11] RINN, K., MÜLLER, A., EICHENAUER, H., SALZBORN, E., Development of single-particle detectors for keV ions, *Rev. Sci. Instrum.* **53** (1982) 829.
- [12] DEFRANCE, P., BROUILLARD, F., CLAEYS, W., WASENHOF, G.V., Crossed beam measurement of absolute cross sections: an alternative method and its application to the electron-impact ionisation of  $He^+$ , *J. Phys. B* **14** (1981) 103.
- [13] MÜLLER, A., HOFMANN, G., TINSCHERT, K., SAUER, R., SALZBORN, E., BECKER, R., Signal enhancement in electron-ion crossed-beams experiments, *Nucl. Instrum. Methods B* **24/25** (1987) 369.
- [14] MÜLLER, A., TINSCHERT, K., HOFMANN, G., SALZBORN, E., DUNN, G.H., Resonances in electron-impact single, double, and triple ionization of heavy metal ions, *Phys. Rev. Lett.* **61** (1988) 70.

- [15] KNOPP, H., BÖHME, C., JACOBI, J., RICZ, S., SCHIPPERS, S., MÜLLER, A., Electron-impact multiple ionization of  $Ba^{q+}$  ions ( $1 \leq q \leq 13$ ) via resonant 3d excitation, Nucl. Instrum. Methods B **205** (2003) 433.
- [16] MÜLLER, A., Electron-ion collisions: Fundamental processes in the focus of applied research, Adv. At. Mol. Phys. **55** (2008) 293.
- [17] MÜLLER, A., SALZBORN, E., FRODL, R., BECKER, R., KLEIN, H., WINTER, H., Absolute ionisation cross sections for electrons incident on  $O^+$ ,  $Ne^+$ ,  $Xe^+$  and  $Ar^{i+}$  ( $i=1, \dots, 5$ ) ions, J. Phys. B **13** (1980) 1877.
- [18] ACHENBACH, C., MÜLLER, A., SALZBORN, E., BECKER, R., Single ionisation of multiply charged xenon ions by electron-impact, J. Phys. B **17** (1984) 1405.
- [19] MAN, K.F., SMITH, A.C.H., HARRISON, M.F.A., A measurement of the cross section for electron-impact ionisation of  $Ne^+$ ,  $Ar^+$ ,  $Kr^+$  and  $Xe^+$ , J. Phys B **20** (1987) 5865.
- [20] BELL, E.W., DJURIĆ, N., DUNN, G.H., Electron-impact ionization of  $In^+$  and  $Xe^+$ , Phys. Rev. A **48** (1993) 4286.
- [21] ACHENBACH CH., MÜLLER A., SALZBORN E., BECKER R., Electron-impact double ionization of  $I^{1+}$  and  $Xe^{q+}$  ( $q=1, \dots, 4$ ) ions: role of 4d electrons like in photoionization, Phys. Rev. Lett., **50** (1983) 2070.
- [22] MÜLLER, A., ACHENBACH, C., SALZBORN, E., BECKER, R., Multiple ionisation of multiply charged xenon ions by electron-impact, J. Phys. B **17** (1984) 1427.
- [23] GRIFFIN, D.C., BOTTCHER, C., PINDZOLA, M.S., YOUNGER, S.M., GREGORY, D.C., CRANDALL, D.H., Electron-impact ionization in the xenon isonuclear sequence, Phys. Rev. A **29** (1984) 1729.
- [24] DANJO, A., MATSUMOTO, A., OHTANI, S., SUZUKI, H., TAWARA, H., WAKIYA, K., YOSHINO, M., Electron-impact single ionization of  $Ne^{2+}$ ,  $Ar^{2+}$ ,  $Kr^{2+}$  and  $Xe^{2+}$  ions, Journal of the Physical Society of Japan **53** (1984) 4091.
- [25] MATSUMOTO, A., DANJO, A., OHTANI, S., SUZUKI, H., TAWARA, H., TAKAYANAGI, T., WAKIYA, K., YAMADA, I., YOSHINO, M., HIRAYAMA, T., Measurements of absolute cross sections for electron-impact ionization of doubly charged rare gas ions:  $Ne^{2+}$ ,  $Ar^{2+}$ ,  $Kr^{2+}$ , and  $Xe^{2+}$ , Journal of the Physical Society of Japan **59** (1990) 902.
- [26] MAN, K.F., SMITH, A.C.H., HARRISON, M.F.A., A measurement of the cross section for electron-impact ionization of  $Ar^{2+}$ ,  $Kr^{2+}$  and  $Xe^{2+}$ , J. Phys. B **26** (1993) 1365.
- [27] RALCHENKO, YU., KRAMIDA, A.E., READER, J., NIST ASD TEAM, NIST Atomic Spectra Database (version 3.1.5), National Institute of Standards and Technology, Gaithersburg, MD, available: <http://physics.nist.gov/asd3>
- [28] GREGORY, D.C., DITTNER, P.F., CRANDALL, D.H., Absolute-cross-section measurements for electron-impact ionization of triply charged inert-gas ions:  $Ne^{3+}$ ,  $Ar^{3+}$ ,  $Kr^{3+}$ , and  $Xe^{3+}$ , Phys. Rev. A **27** (1983) 724.
- [29] EMMONS, E.D., AGUILAR, A., GHARAIBEH, M.F., SCULLY, S.W.J., PHANEUF, R.A., KILCOYNE, A.L.D., SCHLACHTER, A.S., ÁLVAREZ, I., CISNEROS, C., HINOJOSA, G., Photoionization and electron-impact ionization of  $Xe^{3+}$ , Phys. Rev. A **71** (2005) 042704.
- [30] PINDZOLA, M.S., GRIFFIN, D.C., BOTTCHER, C., CRANDALL, D.H., PHANEUF, R.A., GREGORY, D.C., Electron-impact double ionization of rare-gas ions, Phys. Rev. A **29** (1984) 1749.
- [31] GREGORY, D.C., CRANDALL, D.H., Measurement of the cross section for electron-impact ionization of  $Xe^{6+}$  ions, Phys. Rev. A **27** (1983) 2338.
- [32] HOWALD, A.M., GREGORY, D.C., PHANEUF, R.A., CRANDALL, D.H., PINDZOLA, M.S., Observation of multiple-electron processes in ionization of  $Xe^{6+}$  by electron-impact, Phys. Rev. Lett. **56** (1986) 1675.

- [33] BANNISTER, M.E., MUELLER, D.W., WANG, L.J., PINDZOLA, M.S., GRIFFIN, D.C., GREGORY, D.C., Cross sections for electron-impact single ionization of  $\text{Kr}^{8+}$  and  $\text{Xe}^{8+}$ , *Phys. Rev. A* **38** (1988) 38.
- [34] HOFMANN, G., NEUMANN, J., PRACHT, U., TINSCHERT, K., STENKE, M., VÖLPEL, R., MÜLLER, A., SALZBORN, E., AIP Conference Proceedings, Vol. **274**, RICHARD, P., STÖCKLI, M., COCKE, C.L., LIN, C.D., (Eds.), American Institute of Physics, New York, 1993, p. 485.
- [35] STENKE, M., AICHELE, K., HATHIRAMANI, D., HOFMANN, G., STEIDL, M., VÖLPEL, R., SALZBORN, E., A high-current electron gun for crossed-beams electron-ion collision studies at keV energies, *Nucl. Instr. and Meth. in Phys. Res. B* **98** (1995) 573.
- [36] MUELLER, D.W., WANG, L.J., GREGORY, D.C., Electron-impact double-ionization cross sections for  $\text{Xe}^{8+}$ , *Phys. Rev. A* **39** (1989) 2381.
- [37] BRANDAU, C., JACOBI, J., SCHIPPERS, S., MÜLLER, A., 2003, unpublished.
- [38] LOTZ, W., Electron-impact ionization cross sections and ionization rate coefficients for atoms and ions from scandium to zinc, *Z. Phys.* **220** (1969) 466.
- [39] MANDELBAUM, P., COHEN, M., SCHWOB, J.L., BAR-SHALOM, A., Excitation-autoionization cross sections and rate coefficients for Ge-like ions, *Eur. Phys. J. D* **33** (2005) 213.
- [40] MÜLLER, A., Plasma rate coefficients for highly charged ion–electron collisions: new experimental access via ion storage rings, *Int. J. Mass Spectrom.* **192** (1999) 9
- [41] SAVIN, D.W., BADNELL, N.R., BARTSCH, T., BEHAR, E., BRANDAU, C., CHEN, M.H., GRIESER, M., GORCZYCA, T.W., GWINNER, G., HOFFKNECHT, A., KAHN, S.M., MÜLLER, A., REPNOW, R., SAGHIRI, A.A., SCHIPPERS, S., SCHMITT, M., SCHWALM, D., WOLF, A., ZÁVODSZKY, P.A., AIP Conference Proceedings Vol. **547**, Atomic Processes in Plasmas, MANCINI, R.C., PHANEUF, R.A., (Eds.), American Institute of Physics, New York 2000, p. 267.
- [42] MÜLLER, A., SCHIPPERS, S., in ASP Conference Proceedings, Vol. **247**, Spectroscopic Challenges of Photoionized Plasmas, FERLAND, G., SAVIN, D.W., (Eds.), Astronomical Society of the Pacific, San Francisco, USA, 2001, p. 53
- [43] SAVIN, D.W., BARTSCH, T., CHEN, M.H., GRIESER, M., GORCZYCA, T.W., GWINNER, G., KAHN, S.M., LINKEMANN, J., MÜLLER, A., REPNOW, R., SAGHIRI, A., SCHIPPERS, S., SCHMITT, M., SCHWALM, D., WOLF, A., in ASP conference proceedings, Vol. **251**, New Century of X-Ray Astronomy, KUNIEDA, H., INOUE, H., (Eds.), Astronomical Society of the Pacific, Provo, Utah, 2001, p. 272.
- [44] SAVIN, D.W., AIP conference proceedings, Vol. **774**, X-ray diagnostics of astrophysical plasmas: Theory, Experiment, and Observation, SMITH, R.K., (Ed.), American Institute of Physics, Cambridge, Massachusetts, 2005, p. 297.
- [45] SCHIPPERS, S., in Highlights of Astronomy, Vol. 13, as presented at the XXVth General Assembly of the IAU, Sydney, Australia, August 13–26, 2003, Engvold O., (Ed.), Astronomical Society of the Pacific, San Francisco, 2005, p. 640, arXiv: astro-ph/0308544.
- [46] SAVIN, D.W., Can heavy ion storage rings contribute to our understanding of the charge state distributions in cosmic atomic plasmas?, *J. Phys. Conf. Ser* **88** (2007) 012071.
- [47] SCHWALM, D., Atomic and molecular astrophysics with heavy ion storage rings, *Progress in Particle and Nuclear Physics* **59** (2007) 156.
- [48] SCHIPPERS, S., Astrophysical relevance of storage-ring electron-ion recombination experiments, *J. Phys. Conf. Ser.* **163** (2009) 012001.
- [49] MÜLLER, A., WOLF, A., in Accelerator-based atomic physics techniques and applications, AUSTIN, J.C., SHAFROTH, S.M., (Eds.), AIP Press, Woodbury, New York, 1997, p. 147.
- [50] SCHMIDT, E.W., BERNHARDT, D., MÜLLER, A., SCHIPPERS, S., FRITZSCHE, S., HOFFMANN, J., JAROSHEVICH, A.S., KRANTZ, C., LESTINSKY, M., ORLOV, D.A., WOLF, A., LUKIĆ, D., SAVIN, D.W., Electron-ion recombination of

- Si IV forming Si III: Storage-ring measurement and multiconfiguration Dirac-Fock calculations, *Phys. Rev. A* **76** (2007) 032717.
- [51] SCHIPPERS, S., BARTSCH, T., BRANDAU, C., MÜLLER, A., GWINNER, G., WISSLER, G., BEUTELSPACHER, M., GRIESER, M., WOLF, A., PHANEUF, R.A., Dielectronic recombination of lithiumlike Ni<sup>25+</sup> ions: high-resolution rate coefficients and influence of external crossed electric and magnetic fields, *Phys. Rev. A* **62** (2000) 022708.
- [52] KILGUS, G., HABS, D., SCHWALM, D., WOLF, A., BADNELL, N.R., MÜLLER, A., High-resolution measurement of dielectronic recombination of lithiumlike Cu<sup>26+</sup>, *Phys. Rev. A* **46** (1992) 5730.
- [53] LAMPERT, A., WOLF, A., HABS, D., KENNTNER, J., KILGUS, G., SCHWALM, D., PINDZOLA, M.S., BADNELL, N.R., High-resolution measurement of the dielectronic recombination of fluorinelike selenium ions, *Phys. Rev. A* **53** (1996) 1413.
- [54] PASTUSZKA, S., SCHRAMM, U., GRIESER, M., BROUDE, C., GRIMM, R., HABS, D., KENNTNER, J., MIESNER, H.-J., SCHÜBLER, T., SCHWALM, D., WOLF, A., Electron cooling and recombination experiments with an adiabatically expanded electron beam, *Nucl. Instrum. Methods A* **369** (1996) 11.
- [55] SCHIPPERS, S., MÜLLER, A., GWINNER, G., LINKEMANN, J., SAGHIRI, A.A., WOLF, A., Storage ring measurement of the C IV recombination rate coefficient, *Astrophys. J.* **555** (2001) 1027.
- [56] SCHIPPERS, S., SCHNELL, M., BRANDAU, C., KIESLICH, S., MÜLLER, A., WOLF, A., Experimental Mg IX photorecombination rate coefficient, *Astron. Astrophys.* **421** (2004) 1185.
- [57] WOLF, A., BUHR, H., GRIESER, M., VON HAHN, R., LESTINSKY, M., LINDROTH, E., ORLOV, D.A., SCHIPPERS, S., SCHNEIDER, I.F., Progress in stored ion beam experiments on atomic and molecular processes, *Hyperfine Interact.* **172** (2006) 111.
- [58] LESTINSKY, M., LINDROTH, E., ORLOV, D.A., SCHMIDT, E.W., SCHIPPERS, S., BÖHM, S., BRANDAU, C., SPRENGER, F., TEREKHOV, A.S., MÜLLER, A., WOLF, A., Screened radiative corrections from hyperfine-split dielectronic resonances in lithiumlike scandium, *Phys. Rev. Lett.* **100** (2008) 033001.
- [59] SCHMIDT, E.W., SCHIPPERS, S., BERNHARDT, D., MÜLLER, A., HOFFMANN, J., LESTINSKY, M., ORLOV, D.A., WOLF, A., LUKIĆ, D.V., SAVIN, D.W., BADNELL, N.R., Electron-ion recombination for Fe VIII forming Fe VII and Fe IX forming Fe VIII: measurements and theory, *Astron. & Astrophys.* **492** (2008) 265.
- [60] SAVIN, D.W., GWINNER, G., GRIESER, M., REPNOW, R., SCHNELL, M., SCHWALM, D., WOLF, A., ZHOU, S.-G., KIESLICH, S., MÜLLER, A., SCHIPPERS, S., COLGAN, J., LOCH, S.D., BADNELL, N.R., CHEN, M.H., GU, M.F., Dielectronic recombination of Fe XXIII forming Fe XXII: laboratory measurements and theoretical calculations, *Astrophys. J.* **642** (2006) 1275.
- [61] GWINNER, G., HOFFKNECHT, A., BARTSCH, T., BEUTELSPACHER, M., EKLÖW, N., GLANS, P., GRIESER, M., KROHN, S., LINDROTH, E., MÜLLER, A., SAGHIRI, A.A., SCHIPPERS, S., SCHRAMM, U., SCHWALM, D., TOKMAN, M., WISSLER, G., WOLF, A., Influence of magnetic fields on electron-ion recombination at very low energies, *Phys. Rev. Lett.* **84** (2000) 4822.
- [62] BADNELL, N.R., Dielectronic recombination of Fe<sup>22+</sup> and Fe<sup>21+</sup>, *J. Phys. B* **19** (1986) 3827, <http://amdpp.phys.strath.ac.uk/autos/>.
- [63] SCHMIDT, E.W., BERNHARDT, D., HOFFMANN, J., LESTINSKY, M., LUKIĆ, D.V., MÜLLER, A., ORLOV, D.A., SAVIN, D.W., SCHIPPERS, S., WOLF, A., Experimental rate coefficient for dielectronic recombination of neonlike iron forming sodiumlike iron, *J. Phys. Conf. Ser.* **163** (2009) 012028.
- [64] SAVIN, D.W., KAHN, S.M., LINKEMANN, J., SAGHIRI, A.A., SCHMITT, M., GRIESER, M., REPNOW, R., SCHWALM, D., WOLF, A., BARTSCH, T., BRANDAU, C., HOFFKNECHT, A., MÜLLER, A., SCHIPPERS, S., CHEN, M.H.,

- BADNELL, N.R., Dielectronic recombination in photoionized gas. II. laboratory measurements for Fe XVIII and Fe XIX, *Astrophys. J. Suppl. Ser.* **123** (1999) 687.
- [65] SAVIN, D.W., KAHN, S.M., LINKEMANN, J., SAGHIRI, A.A., SCHMITT, M., GRIESER, M., REPNOW, R., SCHWALM, D., WOLF, A., BARTSCH, T., MÜLLER, A., SCHIPPERS, S., CHEN, M.H., BADNELL, N.R., GORCZYCA, T.W., ZATSARINNY, O., Dielectronic recombination of Fe XIX forming Fe XVIII: laboratory measurements and theoretical calculations, *Astrophys. J.* **576** (2002) 1098.
- [66] SAVIN, D.W., BEHAR, E., KAHN, S.M., GWINNER, G., SAGHIRI, A.A., SCHMITT, M., GRIESER, M., REPNOW, R., SCHWALM, D., WOLF, A., BARTSCH, T., MÜLLER, A., SCHIPPERS, S., BADNELL, N.R., CHEN, M.H., GORCZYCA, T.W., Dielectronic recombination (via  $N = 2 \rightarrow N' = 2$  core excitations) and radiative recombination of Fe XX: laboratory measurements and theoretical calculations, *Astrophys. J. Suppl. Ser.* **138** (2002) 337.
- [67] SAVIN, D.W., KAHN, S.M., GWINNER, G., GRIESER, M., REPNOW, R., SAATHOFF, G., SCHWALM, D., WOLF, A., MÜLLER, A., SCHIPPERS, S., Z'AVODSKY, P.A., CHEN, M.H., GORCZYCA, T.W., ZATSARINNY, O., GU, M.F., Dielectronic recombination of Fe XXI and Fe XXII via  $N = 2 \rightarrow N' = 2$  core excitations, *Astrophys. J. Suppl. Ser.* **147** (2003) 421.
- [68] LESTINSKY, M., BADNELL, N.R., BERNHARDT, D., GRIESER, M., HOFFMANN, J., LUKIĆ, D., MÜLLER, A., ORLOV, D.A., REPNOW, R., SAVIN, D.W., SCHMIDT, E.W., SCHIPPERS, S., WOLF, A., YU, D., Electron-ion recombination of Fe X forming Fe IX and of Fe XI forming Fe X: laboratory measurements and theoretical calculations, *Astrophys. J.* **698** (2009) 648.
- [69] SCHMIDT, E.W., SCHIPPERS, S., MÜLLER, A., LESTINSKY, M., SPRENGER, F., GRIESER, M., REPNOW, R., WOLF, A., BRANDAU, C., LUKIĆ, D., SCHNELL, M., SAVIN, D.W., Electron-ion recombination measurements motivated by AGN x-ray absorption features: Fe XIV forming Fe XIII, *Astrophys. J. (Lett.)* **641** (2006) L157.
- [70] LUKIĆ, D., SCHNELL, M., SAVIN, D.W., BRANDAU, C., SCHMIDT, E.W., BÖHM, S., MÜLLER, A., SCHIPPERS, S., LESTINSKY, M., SPRENGER, F., WOLF, A., ALTUN, Z., BADNELL, N.R., Dielectronic recombination of Fe XV forming Fe XIV: laboratory measurements and theoretical calculations, *Astrophys. J.* **664** (2007) 1244.
- [71] ZATSARINNY, O., GORCZYCA, T.W., KORISTA, K., BADNELL, N.R., SAVIN, D.W., Dielectronic recombination data for dynamic finite-density plasmas VII. The neon isoelectronic sequence, *Astron. Astrophys.* **426** (2004) 699.
- [72] SCHIPPERS, S., LESTINSKY, M., MÜLLER, A., SAVIN, D.W., SCHMIDT, E.W., WOLF, A., Dielectronic recombination data for astrophysical applications: Plasma rate-coefficients for Fe<sup>q+</sup> (q=7-10, 13-22) and Ni<sup>25+</sup> ions from storage-ring experiments *Int. Rev. At. Mol. Phys.* **1** (2010) 109.
- [73] BOROVNIK JR, A., BRANDAU, C., JACOBI, J., SCHIPPERS, S., MÜLLER, A., Electron-impact single ionization of Xe<sup>10+</sup> ions, *J. Phys. B* **44** (2011) 205205.
- [74] HAHN, M., GRIESER, M., KRANTZ, C., LESTINSKY, M., MÜLLER, A., NOVOTNÝ, O., REPNOW, R., SCHIPPERS, S., WOLF, A., SAVIN, D.W., Storage ring cross section measurements for electron impact ionization of Fe<sup>12+</sup> forming Fe<sup>13+</sup> and Fe<sup>14+</sup>, *Astrophys. J.* **735** (2011) 105.
- [75] HAHN, M., BERNHARDT, D., GRIESER, M., KRANTZ, C., LESTINSKY, M., MÜLLER, A., NOVOTNÝ, O., REPNOW, R., SCHIPPERS, S., WOLF, A., SAVIN, D.W., Storage ring cross section measurements for electron impact ionization of Fe<sup>11+</sup> forming Fe<sup>12+</sup> and Fe<sup>13+</sup>, *Astrophys. J.* **729** (2011) 76.
- [76] HAHN, M., GRIESER, M., KRANTZ, C., LESTINSKY, M., MÜLLER, A., NOVOTNÝ, O., REPNOW, R., SCHIPPERS, S., WOLF, A., SAVIN, D.W., Addendum: "Storage ring cross-section measurements for electron impact ionization of Fe<sup>12+</sup> forming Fe<sup>13+</sup> and Fe<sup>14+</sup>" (2011, ApJ, 735, 105), *Astrophys. J.* **761** (2012) 79.

- [77] HAHN, M., BERNHARDT, D., GRIESER, M., KRANTZ, C., LESTINSKY, M., MÜLLER, A., NOVOTNÝ, O., REPNOW, R., SCHIPPERS, S., WOLF, A., SAVIN, D.W., Addendum: "Storage ring cross section measurements for electron impact ionization of Fe<sup>11+</sup> forming Fe<sup>12+</sup> and Fe<sup>13+</sup>" (2011, ApJ, 729, 76), *Astrophys. J.* **761** (2012) 78
- [78] HAHN, M., BECKER, A., GRIESER, M., KRANTZ, C., LESTINSKY, M., MÜLLER, A., NOVOTNÝ, O., REPNOW, R., SCHIPPERS, S., SPRUCK, K., WOLF, A., SAVIN, D.W., Storage ring cross section measurements for electron impact single and double ionization of Fe<sup>9+</sup> and single ionization of Fe<sup>10+</sup>, *Astrophys. J.* **760** (2012) 80.
- [79] NOVOTNÝ, O., BADNELL, N.R., BERNHARDT, D., GRIESER, M., HAHN, M., KRANTZ, C., LESTINSKY, M., MÜLLER, A., REPNOW, R., SCHIPPERS, S., WOLF, A., SAVIN, D.W., Electron-ion recombination of Fe XII forming Fe XI: Laboratory measurements and theoretical calculations, *Astrophys. J.* **753** (2012) 57.
- [80] PINDZOLA, M.S., LOCH, S.D., BOROVNIK JR, A., GHARAIBEH, M.F., RUDOLPH, J.K., SCHIPPERS, S., MÜLLER, A., Electron-impact ionization of moderately charged xenon ions, *J. Phys. B* **46** (2013) 215202.
- [81] HAHN, M., BECKER, A., BERNHARDT, D., GRIESER, M., KRANTZ, C., LESTINSKY, M., MÜLLER, A., NOVOTNÝ, O., REPNOW, R., SCHIPPERS, S., SPRUCK, K., WOLF, A., SAVIN, D.W., Storage ring cross section measurements for electron impact single and double ionization of Fe<sup>13+</sup> and single ionization of Fe<sup>16+</sup> and Fe<sup>17+</sup>, *Astrophys. J.* **767** (2013) 47.
- [82] BERNHARDT, D., BECKER, A., GRIESER, M., HAHN, M., KRANTZ, C., LESTINSKY, M., NOVOTNÝ, O., REPNOW, R., SAVIN, D.W., SPRUCK, K., WOLF, A., MÜLLER, A., SCHIPPERS, S., Absolute rate coefficients for photo-recombination and electron-impact ionization of magnesium-like iron ions from measurements at a heavy-ion storage ring, *Phys. Rev. A* **90** (2014) 012702.
- [83] HAHN, M., BADNELL, N.R., GRIESER, M., KRANTZ, C., LESTINSKY, M., MÜLLER, A., NOVOTNÝ, O., REPNOW, R., SCHIPPERS, S., WOLF, A., SAVIN, D.W., Electron-ion recombination of Fe<sup>12+</sup> forming Fe<sup>11+</sup>: Laboratory measurements and theoretical calculations, *Astrophys. J.* **788** (2014) 46.
- [84] HAHN, M., BECKER, A., BERNHARDT, D., GRIESER, M., KRANTZ, C., LESTINSKY, M., MÜLLER, A., NOVOTNÝ, O., REPNOW, R., SCHIPPERS, S., SPRUCK, K., WOLF, A., SAVIN, D.W., Storage ring cross section measurements for electron impact ionization of Fe<sup>7+</sup>, *Astrophys. J.* **813** (2015) 16.
- [85] LIU, P., ZENG, J., BOROVNIK JR, A., SCHIPPERS, S., MÜLLER, A., Electron-impact ionization of Xe<sup>24+</sup> ions: theory versus experiment, *Phys. Rev. A* **92** (2015) 012701.
- [86] BERNHARDT, D., BRANDAU, C., HARMAN; Z., KOZHUHAROV, C., BÖHM, S., BOSCH, F., FRITZSCHE, S., JACOBI, J., KIESLICH, S., KNOPP, H., NOLDEN, F., SHI, W., STACHURA, Z., STECK, M., STÖHLKER, T., SCHIPPERS, S., MÜLLER, A., Spectroscopy of berylliumlike xenon ions using dielectronic recombination, *J. Phys. B* **48** (2015) 144008.
- [87] BERNHARDT, D., BRANDAU, C., HARMAN; Z., KOZHUHAROV, C., BÖHM, S., BOSCH, F., FRITZSCHE, S., JACOBI, J., KIESLICH, S., KNOPP, H., NOLDEN, F., SHI, W., STACHURA, Z., STECK, M., STÖHLKER, T., SCHIPPERS, S., MÜLLER, A., Electron-ion collision spectroscopy: Lithiumlike xenon ions, *Phys. Rev. A* **91** (2015) 012710.
- [88] BOROVNIK JR, A., GHARAIBEH, M.F., SCHIPPERS, S., MÜLLER, A., Plasma rate coefficients for electron-impact ionization of Xe<sup>9+</sup> ions (q = 8-17), *J. Phys. B* **48** (2015) 035203.
- [89] HAHN, M., BECKER, A., BERNHARDT, D., GRIESER, M., KRANTZ, C., LESTINSKY, M., MÜLLER, A., NOVOTNÝ, O., PINDZOLA, M.S., REPNOW, R., SCHIPPERS, S., SPRUCK, K., WOLF, A., SAVIN, D.W., Storage ring cross section measurements for electron impact ionization of Fe<sup>8+</sup>, *J. Phys. B* **49** (2016) 084006.
- [90] BERNHARDT, D., BECKER, A., BRANDAU, C., GRIESER, M., HAHN, M., KRANTZ, C., LESTINSKY, M., NOVOTNÝ, O., REPNOW, R., SAVIN, D.W.,

SPRUCK, K., WOLF, A., MÜLLER, A., SCHIPPERS, S., Absolute rate coefficients for photorecombination of berylliumlike and boronlike silicon ions, *J. Phys. B* **49** (2016) 074004

# THEORETICAL STUDIES ON CHARGE EXCHANGE AND ELECTRON EXCITATION IN COLLISIONS BETWEEN ALPHA PARTICLES, HELIUM ATOMS AND MULTIPLY CHARGED HEAVY ELEMENT IONS

V.K. NIKULIN, N.A. GUSCHINA

Division of Plasma Physics, Atomic Physics and Astrophysics of the Ioffe Institute,  
Russia

## Abstract

Theoretical charge exchange data for heavy-element impurities in plasmas obtained in accordance with the coordinated research project (CRP) are summarized. All calculations of the charge exchange and excitation cross-sections in ion-atom collisions were carried out in the framework of the close-coupling equation method involving a basis set of the many-electron quasimolecular states. New data on the partial and total cross-sections of single and double electron capture, transfer excitation and target excitation in collisions of impurity ions  $\text{Si}^{4+}$ ,  $\text{Ti}^{4+}$ ,  $\text{Cr}^{6+}$ ,  $\text{Fe}^{8+}$ ,  $\text{Ni}^{6+}$ ,  $\text{Cu}^{6+}$ ,  $\text{Mo}^{6+}$ , and  $\text{W}^{6+}$  with helium atoms in the ground state were obtained in the energy range of impurity ions 4 keV to 800 keV. The partial and total cross-sections of electron capture into the n-shells of  $\text{Ti}^{3+}$  ( $n=5-8$ ),  $\text{Cr}^{5+}$  ( $n=6-9$ ), and  $\text{Fe}^{7+}$  ( $n=8-11$ ) in collisions of the impurity ions with helium atoms in metastable states were calculated for the first time. New results are presented for the one electron transfer and the alpha particle neutralization through the quasi-resonant double electron capture into ground ( $1s^2$ ) and metastable ( $1snl$ ) states of the He atoms in their slow collisions with the  $\text{C}^{2+}$  and  $\text{Ti}^{2+}$  ions. Partial cross-sections for quasi-resonant double electron capture into the ground  $\text{He}(1s^2)$  and metastable  $\text{He}(1s2l)$  states in the  $\text{He}^{2+} + \text{He}$  collisions important for recently proposed active diagnostic of He “ash” are also reported.

## 1. INTRODUCTION

Energy loss due to photon emission from impurity ions excited through charge-exchange collisions with the hydrogen or helium atoms is a serious problem in fusion reactors. Destruction of ground and especially excited states of abundant neutral atomic and molecular hydrogen and the He atoms by Single Electron Capture (SEC) and Double Electron Capture (DEC) in their collisions with impurity ions are the most important processes in the edge plasma (see, e.g., review by Janev [1]).

In inverse reactions, slow alpha particles may be taken away at their neutralization through the quasi-resonant DEC collisions with impurities. This process could be important in cooling of plasmas containing alpha particles, since the DEC cross-sections may have even larger values than the corresponding SEC ones for some collision systems. This is shown in our study of the alpha particle neutralization reactions in collision with the  $\text{C}^{2+}$  ions. DEC transfer into the  $\text{He}(1s^2)$  ground state in this collision is the dominant process at alpha particle energies  $< 2 \text{ keV amu}^{-1}$ . Previously the key role of the alpha particle neutralization reactions in cooling the edge plasmas was discussed by Tawara [2]. The reactions were due to DEC into the metastable  $\text{He}(1s3l)$  states in collisions of alpha particles with  $\text{H}_2$  at low eV-energies.

The electron transfer and excitation processes in collisions between impurities and helium atoms in the ground and excited states of atomic beams used for edge and central plasma diagnostics could be important in the beam level population kinetics [1]. Recently new active spectroscopy diagnostic of He “ash” based on observation of line radiation (“helium holo”) emitted following resonant DEC collisions between the helium atoms of neutral beams and the plasma alpha particles has been proposed [3].

Within IAEA projects a serious effort was made by theorists to determine the relevant cross-sections involving heavy metallic impurities.

Total transfer cross-sections were determined by Katsonis et al. [4] within the classical-trajectory Monte Carlo method for collisions of  $\text{Ti}^{q+}$ ,  $\text{Cr}^{q+}$ ,  $\text{Fe}^{q+}$  and  $\text{Ni}^{q+}$  ( $4 \leq q \leq Z$ ,  $Z$  being the nuclear charge) with atomic hydrogen in the energy range from 10 to  $10^3$  keV amu $^{-1}$ .

Total and partial electron transfer cross-sections were determined by Fritsch [5] for collisions between atomic hydrogen and the most stable closed  $3p$ -shell ions of Ti, Cr, and Fe, since ions with unfilled shells are more difficult for study by theory and experiment and are less suitable for plasma diagnosis. The calculations were performed within the framework of the close-coupling equation method in the energy range from 0.5 to 100 keV amu $^{-1}$ .

Theoretical data on collision of heavy metallic ions with neutral helium atoms are very limited or even, such as data for elements Mo, W are lacking. To our knowledge, there are only two theoretical papers involving multiply charged metallic ions. McLaughlin et al. [6] carried out the multi-channel Landau-Zener calculations for  $\text{Fe}^{4+} + \text{He}$  collisions in low keV energy range which provide only a qualitative description of experimental data. Calculations of total and partial cross-sections for the  $\text{Ti}^{4+} + \text{He}$  collisions in the energy range 0.1–6 MeV were performed by Fritsch [7] within the framework of the close-coupling equation method and taking into consideration two active electrons, the important two-electron transfer excitation and DEC channels being omitted.

The purpose of our study was to obtain the theoretical data on the electron transfer and excitation processes in slow collisions of multiply charged impurity ions with the neutral helium atoms in ground and metastable states required for diagnostics and modeling of fusion plasmas. The specific objectives of the study were the following:

- (i) To calculate for above-mentioned collisions cross-sections for SEC and for electron transfer with excitation of the helium ion (transfer excitation – TE) as well as for DEC and true excitation of helium. The calculations were performed for metallic and some other impurity ions (C, Si, Ti, Cr, Fe, Ni, Cu, Mo, W).
- (ii) To obtain the SEC and true excitation cross-sections in slow collisions of impurity ions with the helium atoms in initially excited state  $\text{He}(1s2s) 2^1S$ .
- (iii) To reveal inverse reactions with neutralization of alpha particles through the quasi-resonant DEC in collisions with the helium atoms and impurity ions.

## 2. THEORETICAL METHOD

The study of charge transfer and excitation was performed by the use of the close-coupling equation method with the two- or many-electron quasi-molecular states as a basis. The Coulomb trajectories were used to integrate coupled equations with the program TANGO provided us by Piacentini and Salin [8].

A consistent method of construction of diabatic correlation diagrams for the quasimolecular description of many-electron ion-atom collisions was suggested previously in our paper [9]. Diabatic Screened Diatomic Molecular Orbitals (SDMO) were obtained by numerical solution of the two-center problem with an effective potential including screening of quasimolecule nuclei by electrons and allowing separation of variables in spheroidal coordinates. As a result, they have the same additional (hidden) symmetry as the well known diabatic Fano-Lichten One Electron Diatomic Molecular Orbitals (OEDMO).

SDMO and their energies are obtained by exact numerical solution of the one-electron Schrödinger equation

$$\left[ -\nabla_k^2 + V_{\text{eff}}^k(R, r_{1k}, r_{2k}) \right] \psi_k = 2\varepsilon_k(R) \psi_k \quad (1)$$

where  $r_{1k}$ ,  $r_{2k}$  are the distances from  $k$ -th electron to the nuclei with charges  $Z_1$  and  $Z_2$  respectively.  $R$  is the internuclear distance. The effective potential  $V_{\text{eff}}^k$  for the  $k$ -th electron which takes into account the screening of nuclei can be written in rectangular coordinates in the form [9]

$$V_{eff}^k = -\frac{2Z_1 - a_1^k - b_1^k}{r_{1k}} - \frac{2Z_2 - a_1^k + b_1^k}{r_{2k}} + \frac{\tilde{a}^k}{r_{1k}r_{2k}} + \frac{Ra_0^k}{r_{1k}r_{2k}} + \frac{b_2(r_{1k} - r_{2k})^2}{Rr_{1k}r_{2k}}. \quad (2)$$

It should be noted that similar effective potentials have been used in quantum chemistry for the computation of the hydrogen molecule in the ground state (see, e.g., review by Teller and Sahlin [10]). It is significant that the parameter  $\tilde{a}^k$  determining the subshell splitting at  $R=0$  has been taken into account for the first time in our paper [9]. In the limit  $R \rightarrow 0$ , the effective potential takes the form

$$V_{eff}^0 = -\frac{2}{r}(Z_1 + Z_2 - a_1^k) + \frac{\tilde{a}^k}{r^2}. \quad (3)$$

This is the well-known potential of the generalized hydrogen atom studied for the first time by Hans Hellmann [11]. The energy levels for this case may be written as

$$\varepsilon_k = -\frac{1}{2} \frac{(Z_1 + Z_2 - a_1^k)^2}{(n + \Delta_l)^2} \quad (4)$$

Where

$$\Delta_l = -\frac{(2l+1)}{2} + \left( \frac{(2l+1)^2}{4} + \tilde{a}^k \right)^{1/2}, \quad \Delta_l \text{ -quantum defect, } n = n_r + l + 1; \quad n_\lambda = n_r,$$

$n_\mu = l - m$ . Here  $n, n_r, l, m$  are the principal, radial, orbital and magnetic quantum numbers characterizing the energy level of the united atom and respectively SDMO ( $n_\lambda, n_\mu, m$  are the spheroidal quantum numbers).

The parameters of  $V_{eff}^k$  are fixed by requirement of coincidence at  $R=0$  of  $\varepsilon_k$  and  $\bar{V}_{eff}^0 = \langle \psi_k | V_{eff}^0 | \psi_k \rangle$  and at  $R \rightarrow \infty$  of asymptotic SDMO energies including Coulomb shifts with corresponding values from relativistic atomic calculation.

The two-electron wave function  $\phi_i$  for the orthonormal SDMO is taken in the form

$$\phi_i(r_k, r_\ell) = \frac{1}{\sqrt{2}} [\psi_k(r_k)\psi_\ell(r_\ell) \pm \psi_k(r_\ell)\psi_\ell(r_k)], \quad (5)$$

where the sign + (-) indicates a singlet (triplet) state. Two-electron total energy is given by [12]

$$E_i = \varepsilon_k + \varepsilon_l + J_{kl}^c \pm J_{kl}^{ex} - (\delta V_{kl}^k + \delta V_{kl}^l), \quad (6)$$

where  $J_{kl}^c, J_{kl}^{ex}$  are Coulomb and exchange integrals,

$$\delta V_{kl}^j = \langle \psi_l | V_{eff}^j + \frac{2Z_1}{r_{1j}} + \frac{2Z_2}{r_{2j}} | \psi_k \rangle, \quad j = l, k \quad (7)$$

The SDMO basis set was used for calculating of the many-electron wavefunctions, the total energies  $E_i$  and the matrix elements of dynamical (radial and rotational) and potential couplings.

In this study, an alternative approach proposed in Ref. [13] for single electron quasimolecules is used to take into account momentum transfer. A special coordinate system for electrons is used to calculate the matrix elements of the dynamic coupling of the states. It was shown [13] that, if the coordinate origin in a heteronuclear quasimolecule  $\text{He}^{2+} + \text{H}(1s)$  is set at the centroid of the charges on the internuclear axis, the transition probabilities calculated as a function of the impact parameter and the total cross-sections are close to those calculated after allowance for the translation factor (TF) in the form of a plane wave. This approach was discussed in our paper [14]. In the present paper comparison will be given between our results and those obtained with different TF.

### 3. STUDY OF ALPHA PARTICLE NEUTRALIZATION IN THEIR SLOW COLLISIONS WITH HELIUM ATOMS AND $C^{2+}$ AND $Ti^{2+}$ IONS THROUGH QUASI-RESONANT DOUBLE ELECTRON CAPTURE

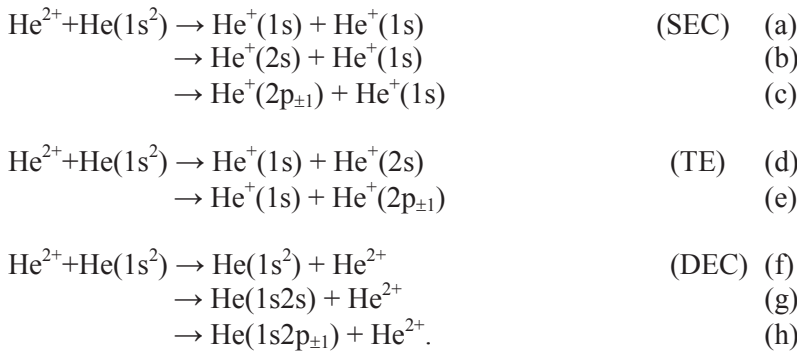
#### 3.1. $He^{2+} + He$ Collision

From the very beginning the two-electron  $He^{2+} + He(1s^2)$  collision system has been the touchstone for collision physics. Although a number of workers extensively studied this system, there are only few papers [15–17] wherein partial cross-sections for quasi-resonant DEC in the  $He^{2+} + He$  collisions have been considered. Studies [3] of the injection of neutral helium beams into tokamaks have rekindled our interest in these collisions. Helium neutral beams of  $29.5 \text{ keV amu}^{-1}$  have been injected into helium plasma on the JET tokamak. The main statement of this study was that thermal neutrals forms along the beam trajectory due to quasi-resonant double charge exchange of neutrals with alpha particles mainly in the ground state  $He(1s^2)$ . This statement is in contrast with theoretical results [15–17] on DEC into the ground  $He(1s^2)$  as well as into metastable  $He(1snl)$  states.

In our calculation [17], the contribution to the total DEC cross-section into metastable states is almost equal to that from resonant charge transfer into the ground state for alpha particle energy  $E_c \approx 30 \text{ keV amu}^{-1}$ . In calculations by Fritsch [15], this contribution is about 24%. The calculations [15] were performed with the close-coupling equation method, using travelling atomic orbitals and plane wave TF. The basis set consists of 102 two-electron one-centre and two-centre states, while very important double excited states of the united atom are omitted from the basis.

In pioneering calculations by Harel and Salin [16] using the quasimolecular approximation, two-electron states are expanded in terms of a linear combination of products of OEDMO. The electron-electron interaction is included in the theory at the calculation of energy and also coupling terms in the close-coupling equations. For the most part, our study is similar to that by Harel and Salin. However, the partial DEC cross-sections in their [16] as well as in our [17] studies were not presented explicitly.

In analyzing the processes of charge transfer and excitation, we restrict our calculation to the following reactions making the main contribution [17]:



Adiabatic two-electron wavefunctions were expanded in terms of linear combinations of products of OEDMO, the coefficients of combinations of one-configuration states being obtained from the configuration interaction calculations. Seven gerade and five ungerade combinations from a singlet manifold were included for the processes (a–h). Coulomb trajectories (as distinct from the straight-line one's in [15]) were used for the motion of nuclei.

Results of our DEC total and partial cross-section calculation along with theoretical results by Fritsch and the experimental data of Afrosimov et al. [18] and Zastrov et al. [3] are shown in Fig. 1. It is clearly seen that below  $15 \text{ keV amu}^{-1}$ , the two-electron resonant charge exchange into the ground state is dominant, while the contribution of channels of (g) and (h)

is almost equal to that from resonant charge transfer into the ground state close to 30 keV  $\text{amu}^{-1}$ . This correlates with results by Fritsch [15].

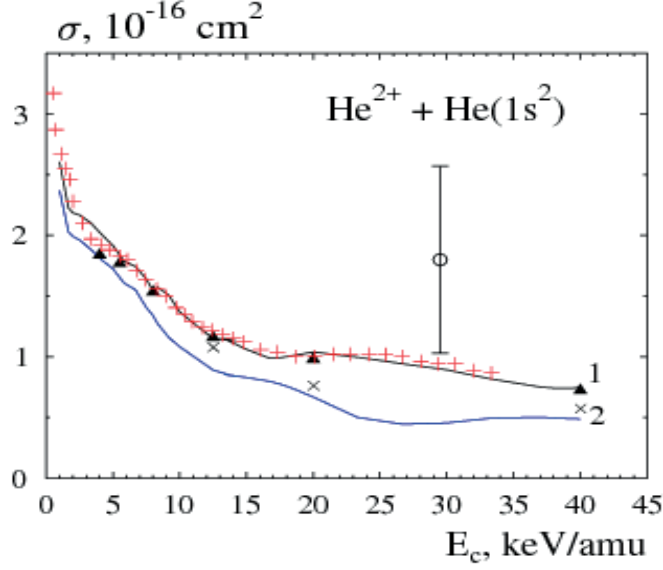
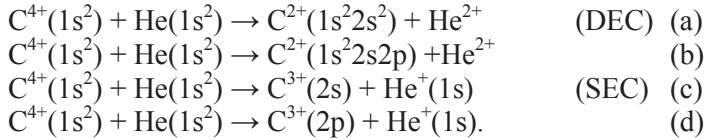


FIG. 1. Cross-sections for DEC in the  $\text{He}^{2+} + \text{He}$  collision. Theoretical data: the total DEC cross-section (present results - curve 1;  $\blacktriangle$ , results by Fritsch [15]). The cross-section for DEC into the ground state of the He (curve 2, present results;  $\times$ , results by Fritsch). Experimental data for the total DEC:  $+$  - by Afrosimov et al. [18],  $O$  - by Zastrov et al. [3].

### 3.2. $\text{He}^{2+} + \text{C}^{2+}(1s^2 2s^2)$ Collision

In slow ion-atom collisions, SEC reactions are generally dominant with the only one exception – the collision system  $\text{C}^{4+} + \text{He}$ . The DEC reaction dominates over SEC at energies below 20 keV [19] for collisions:



It is believed that DEC would dominate over SEC for the inverse ion-ion reaction  $\text{He}^{2+} + \text{C}^{2+}(1s^2 2s^2)$ . Calculations for this reaction were carried out in our study using the basis set of seven quasimolecular four active-electron states. At first glance, it would seem that the collision system  $\text{C}^{4+}(1s^2) + \text{He}(1s^2)$  may be considered as a system with only two active electrons, as long as primary action of the other, presumably inactive core electrons of  $\text{C}^{4+}(1s^2)$  ion can be considered restricted to some screening of  $\text{C}^{6+}$  nuclear charge. In such treatment of multi-electron system  $(\text{C}^{4+} + \text{He}^{2+})e^2$ , adiabatic electronic energies were calculated in papers [20, 21], the active electron interaction with core being described with some semi-empirical model potential. During our preliminary study, it was doubtful that two-electron model would work due to drastic relaxation of core electrons in the case of correlated transitions of two electrons from the entrance channel into the final states  $\text{C}^{2+}(1s^2 2s^2, 1s^2 2p^2)$ . In Fig. 2 diabatic correlation diagram of the four active-electron  $(\text{CHe})^{4+}$  quasimolecule, calculated on the basis set of diabatic SDMO is given.

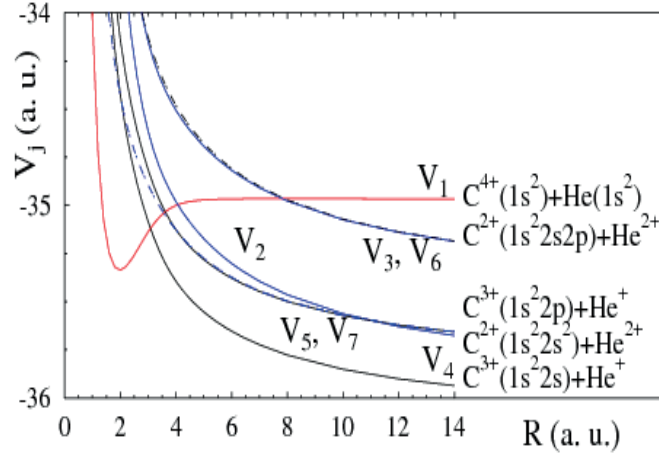


FIG. 2. Diabatic potential curves  $V_i=E_i+12/R$  of the four active-electron  $(CHe)^{4+}$  quasimolecule, as functions of the internuclear distance  $R$ . Full curves,  $\Sigma$ -symmetry potentials; dotted curves,  $\Pi$ -symmetry potentials.

Results of our calculations exchange cross-sections for direct (a–d) and for inverse (a'–d') reactions are shown in Fig. 3, respectively.

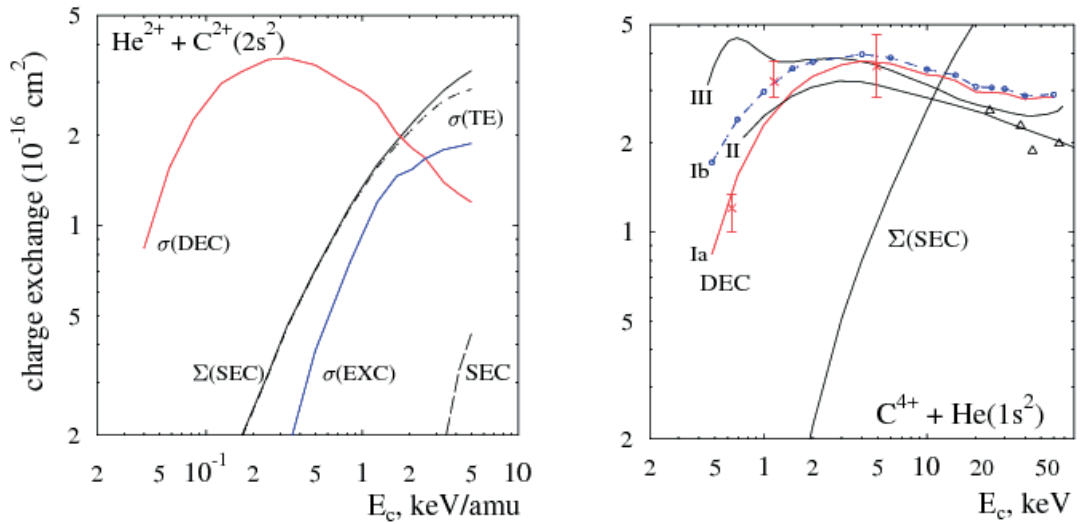
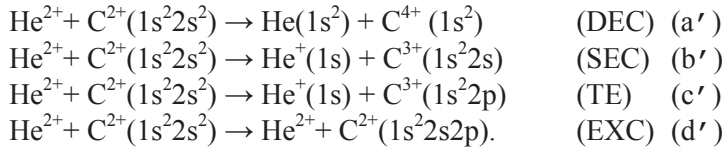


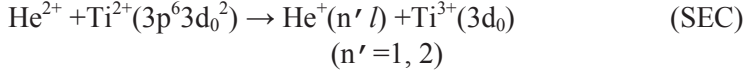
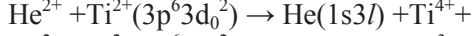
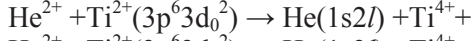
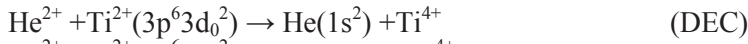
FIG. 3. Left panel: Cross-sections for electron capture and excitation in the  $\text{He}^{2+} + \text{C}^{2+}$  collisions versus the  $\text{He}^{2+}$  ion energy:  $\sigma(\text{DEC})$ , reaction – a';  $\Sigma(\text{SEC})$ , the total SEC cross-section, reactions – (b' + c');  $\sigma(\text{EXC})$ , reaction – d'; SEC, reaction – b'. Right panel: Cross-sections for electron capture in the  $\text{C}^{4+} + \text{He}(1s^2)$  collisions as a function of the  $\text{C}^{4+}$  ion energy.  $\Sigma(\text{SEC})$ , reaction – (c+d), our results; DEC: Ia, Ib – reactions (a+b), our results for the Coulomb and straight line trajectories of nucleus motion; II, DEC – results by Kimura and Olson [20]; III, DEC – results by Errea et al. [21]. Experimental data for DEC: x, by Phaneuf and Crandall [22];  $\Delta$ , by Crandall [19].

For direct reactions (Fig. 3, right panel), our results are shown for the Coulomb and straight line trajectories of nucleus motion. It is clearly seen that at low energies, our calculations (curve Ia) using Coulomb trajectories are in the better agreement with the experiment than calculations in papers [20, 21] with straight line interatomic trajectories. Kimura and Olson [20] have performed the two active-electron configuration-interaction calculation of  $C^{4+}+He$  electron states. Two-electron TF were included in scattering calculation.

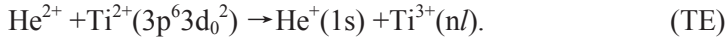
Two active-electron molecular calculations with “common” TF were performed by Errea et al. [21].

### 3.3 $He^{2+} + Ti^{2+}(3d_0^2)$ Collision

The partial and total cross-sections of DEC and SEC were calculated using the basis set of seventeen two-electron states [23] for reactions



$$(n'=1, 2)$$



$$(n=3-5)$$

The energies of these states for the  $He^{2+} + Ti^{2+}$  and  $Ti^{4+} + He(1s^2)$  quasimolecules are shown in Fig. 4.

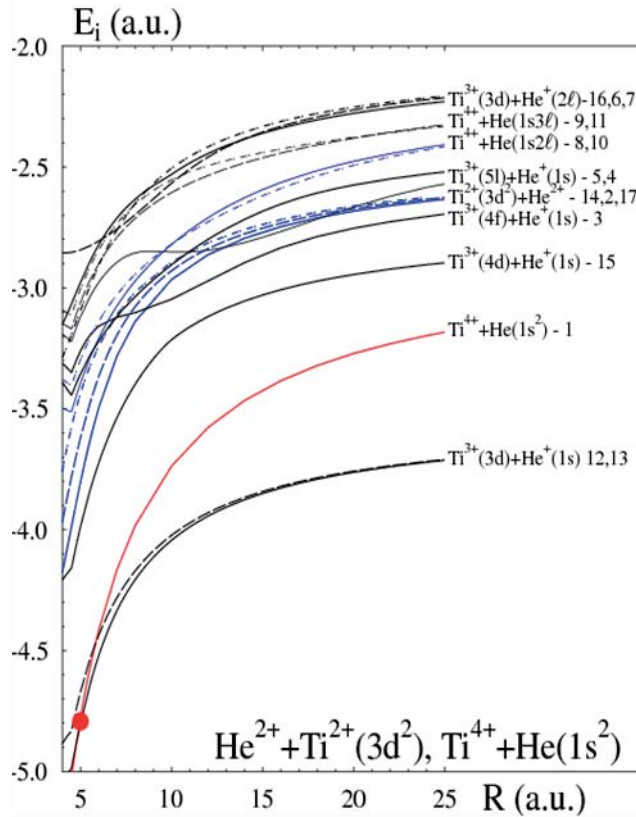


FIG. 4. The energies  $E_i(R)$  of the two-electron states  $\phi_i(\psi_j, \psi_{j'})$  of the  $(He^{2+} + Ti^{2+})$  and  $(Ti^{4+} + He)$  quasimolecules.

$He^{2+} + Ti^{2+}(3d_0^2)$  collision:

- a) the entrance channel (blue curve) –  $\phi_{14}(4f\sigma', 4f\sigma')$ ;
- b) channels of the DEC into the  $1s^2$ ,  $1s2s$ ,  $1s2p_{\pm 1}$ ,  $1s3p_0$ , and  $1s3p_{\pm 1}$  states of the He atoms –  
 $\phi_1(3d\sigma', 3d\sigma')$ ;  $\phi_8(3d\sigma, 5f\sigma')$ ,  $\phi_{10}(3d\sigma, 5g\pi')$ ,  $\phi_9(3d\sigma, 8i\sigma')$ ,  $\phi_{11}(3d\sigma, 7h\pi')$ ;
- c) channels of SEC into the  $nl$  states of the  $He^+$  ions –  
 $\phi_{12}(3d\sigma, 4f\sigma)$  ( $n/l=1s$ ),  $\phi_{16}(4f\sigma, 5f\sigma)$  ( $n/l=2s$ ),  $\phi_6(4f\sigma, 5g\sigma)$  ( $n/l=2p_0$ ),  $\phi_7(4f\sigma, 4f\pi)$  ( $n/l=2p_{\pm 1}$ );
- d) TE channels (SEC into the  $1s$ ,  $2p$  states of the  $He^+$  with the simultaneous  $3d_0 \rightarrow nl$  excitation of  $Ti^{3+}$ ):  
 $\phi_{13}(3d\sigma, 3d\pi)$  ( $n/l=3d_{\pm 1}$ ),  $\phi_3(3d\sigma, 6h\sigma)$  ( $n/l=4f_0$ ),  $\phi_4(3d\sigma, 6g\sigma)$  ( $n/l=5f_0$ ),  $\phi_5(3d\sigma, 7i\sigma)$  ( $n/l=5g_0$ ),  $\phi_{15}(3d\sigma, 4d\sigma)$  ( $n/l=4d_0$ ).

Results of our calculations DEC cross-sections into the ground  $\sigma(1s^2)$  and excited  $\sigma(1s2s)+\sigma(1s2p_{\pm 1})$  states of the He atom are shown in Fig. 5. At low velocities, the capture into excited states dominates over the capture into the ground state. The ground state (the channel  $\phi_1$ ) is populated mainly by potential coupling with the SEC channel  $\phi_{12}$  (red point in Fig 4).

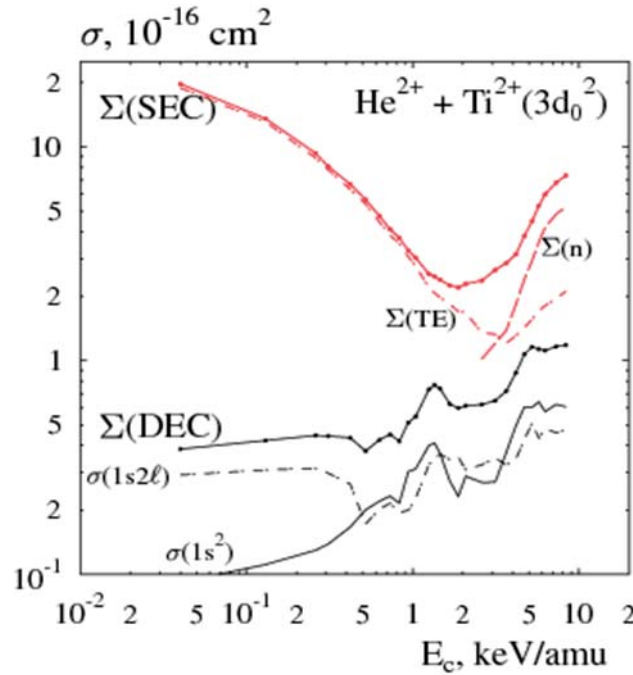


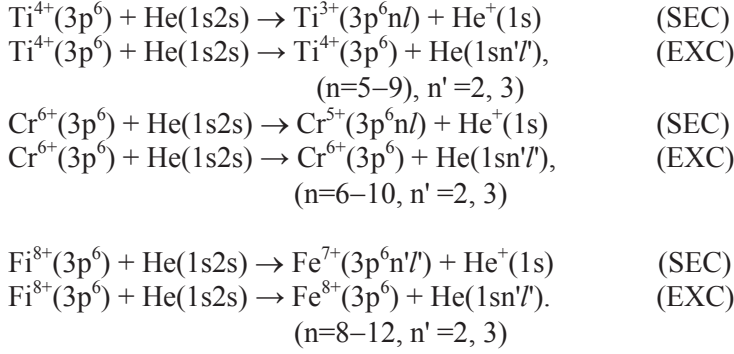
FIG. 5. Cross-sections for the  $He^{2+} + Ti^{2+}(3d_0^2)$  collision versus the alpha particle energy:  $\Sigma(SEC)$  – the total SEC cross-section ( $\Sigma(n) + \Sigma(TE)$ ),  $\Sigma(n)$  – the total cross-section for one electron transfer into the  $1s$ ,  $2p$  states of the  $He^+$  ions,  $\Sigma(TE)$  – the cross-section for one electron transfer into the  $1s$ ,  $2p$  states of the  $He^+$  ions with the  $3d_0 \rightarrow 3d_{\pm 1}, 4d_0, 4f_0, 5f_0, 5g_0$  excitations of ions  $Ti^{3+}$ ;  $\Sigma(DEC)$  and  $\sigma(1s^2)$ ,  $\sigma(1s2l)$  – the total and partial DEC cross-sections.

#### 4. THEORETICAL STUDY OF THE SINGLE ELECTRON TRANSFER AND EXCIATION PROCESSES IN COLLISIONS OF $Ti^{4+}$ , $Cr^{6+}$ AND $Fe^{8+}$ WITH HELIUM ATOMS IN THE METASTABLE STATE

Atomic and ion species in metastable excited states have significant effect on the kinetics of partially ionized edge and divertor plasmas. The most important of the collision processes involving metastables and plasma impurity ions are those leading to the excitation or to the electron capture.

The charge transfer cross-sections in the collisions of impurity ions with metastable helium atoms are of the order of magnitude larger than the corresponding cross-sections for the ground-state helium. A small admixture of metastable helium in a neutral beam can change spectra of charge-exchange spectroscopy considerably. The state selective and total cross-sections for electron capture, excitation and ionization processes in slow collisions of metastables  $H(2s)$  and  $He^+(2s)$  with light bare ions ( $Z=1-5$ ) were calculated by Janev et al. [24] using the hidden crossing method. Electron transfer and excitation cross-sections were calculated by Fritsch and Tawara [25] for the  $Be^{4+}-He(1s2s)$  collision using the close-coupling equation method with a one-electron AO expansion. The classical trajectory Monte Carlo (CTMC) calculations of the state selective SEC and excitation cross-sections for collisions between excited helium and bare light ions ( $Z=3-6, 8$ ) were performed in paper [26].

We carried out [27, 28] calculations of the state selective SEC and excitation cross-sections for slow collisions:



Cross-sections of the processes were calculated with the basis of seventeen one-electron states for the  $Ti^{4+}+He(1s2s)$  collision and ten states for the  $Cr^{6+}$ ,  $Fe^{8+}+He(1s2s)$  collisions.

The one-electron SDMO correlation diagrams for quasimolecules  $(Ti^{4+}+He^+(1s))e$ ,  $(Cr^{6+}+He^+(1s))e$ , and  $(Fe^{8+}+He^+(1s))e$  are shown in Figs. 6-8.

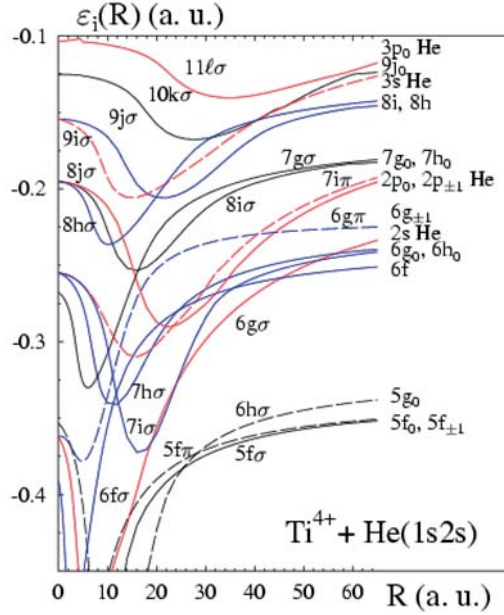


FIG. 6. Energies  $\varepsilon_i(R)$  of SDMO  $\psi_i(r; R)$  of the  $(Ti^{4+} + He^+(1s))e$  quasimolecule and their atomic limits at  $R \rightarrow \infty$ :

- the entrance channel – He(2s) state ( $\psi_1=6g\sigma$ );
- channels of SEC into the  $nl$  states of ions  $Ti^{3+}$ :  
 $n=5$  –  $5f_0, 5f_{\pm 1}, 5g_0$  states ( $\psi_1=5f\sigma, \psi_2=5f\pi, \psi_3=6h\sigma$ );  $n=6$  –  $6f_0, 6g_0, 6g_{\pm 1}, 6h_0$  states ( $\psi_4=6f\sigma, \psi_5=7h\sigma, \psi_{16}=6g\pi, \psi_6=7i\sigma$ );  $n=7$  –  $7g_0, 7h_0$  states ( $\psi_7=7g\sigma, \psi_8=8i\sigma$ );  $n=8$  –  $8h_0, 8i_0$  states ( $\psi_9=8h\sigma, \psi_{10}=9j\sigma$ );  $n=9$  –  $9j_0$  state ( $\psi_{11}=10k\sigma$ );
- channels of the electron  $2s \rightarrow nl$  excitation of the He(1s2s) atoms:  $nl=2p_0, 2p_{\pm 1}$  ( $\psi_{13}=8j\sigma, \psi_{17}=7i\pi$ ),  $nl=3s, 3p_0$  ( $\psi_{14}=9i\sigma, \psi_{15}=11l\sigma$ ).

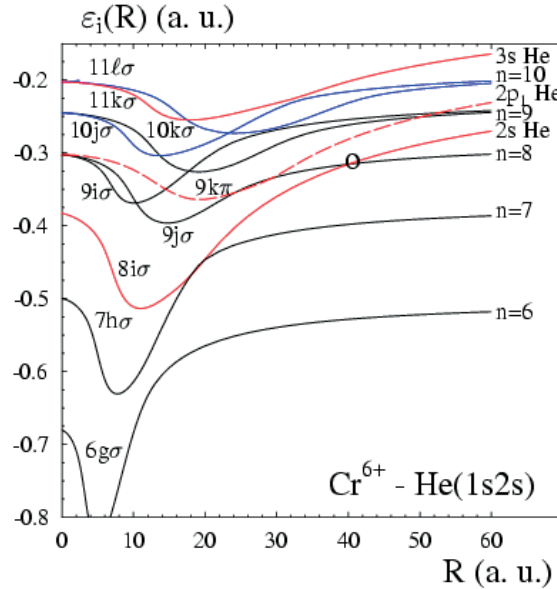


FIG. 7. Energies  $\varepsilon_i(R)$  of SDMO  $\psi_i(r; R)$  of the  $(Cr^{6+} + He^+(1s))e$  quasimolecule and their atomic limits at  $R \rightarrow \infty$ :

- the entrance channel – He(2s) state ( $\psi_1=8i\sigma$ );
- channels of SEC into the  $nl$  states of ions  $Cr^{5+}$ :  
 $n=6$  –  $6g_0$  state ( $\psi_2=6g\sigma$ );  $n=7$  –  $7h_0$  state ( $\psi_3=7h\sigma$ );  $n=8$  –  $8i_0$  state ( $\psi_4=9j\sigma$ );  $n=9$  –  $9i_0, 9j_0$  states ( $\psi_5=9i\sigma, \psi_6=10k\sigma$ );  $n=10$  –  $10j_0, 10k_0$  states ( $\psi_7=10j\sigma, \psi_8=11l\sigma$ );
- channels of the electron  $2s \rightarrow nl$  excitation of the He(1s2s) atoms:  $nl=2p_{\pm 1}$  ( $\psi_9=9k\pi$ ),  $nl=3s$  ( $\psi_{10}=11k\sigma$ ).

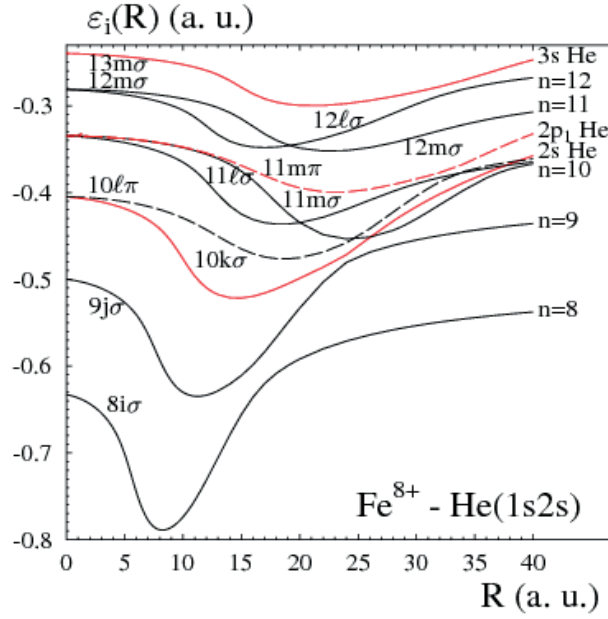


FIG. 8. Energies  $\varepsilon_i(R)$  of SDMO  $\psi_i(r; R)$  of the  $(Fe^{8+} + He^+(1s))e$  quasimolecule and their atomic limits at  $R \rightarrow \infty$ :

- a) the entrance channel – He(2s) state ( $\psi_1=10k\sigma$ );
- b) channels of SEC into the  $nl$  states of the  $Fe^{7+}$  ions:  
 $n=8$  –  $8i_0$  state ( $\psi_2=8i\sigma$ );  $n=9$  –  $9j_0$  state ( $\psi_3=9j\sigma$ );  $n=10$  –  $10k_0, 10l_0, 10l_{\pm 1}$  states ( $\psi_4=11l\sigma, \psi_7=11m\sigma, \psi_8=10l\pi$ );  $n=11$  –  $11l_0$  state ( $\psi_5=12m\sigma$ );  $n=12$  –  $12l_0$  state ( $\psi_{10}=12l\sigma$ );
- c) channels of the electron  $2s \rightarrow nl$  excitation of the He(1s2s) atoms:  $nl=2p_{\pm 1}$ , ( $\psi_9=11m\pi$ ),  $nl=3s$ , ( $\psi_6=13m\sigma$ ).

The cross-sections of SEC into the  $nl$  states of  $Ti^{3+}$  ( $n=5-8$ ),  $Cr^{5+}$  ( $n=6-9$ ),  $Fe^{8+}$  ( $n=8-11$ ) and of the electron He( $2s \rightarrow nl$ ) excitation in collisions of the excited helium atoms He(1s2s) and the impurity ions were obtained in the energy range 5 – 400 keV. The data are shown in graphical form in Figs. 9–12. The following maximum values the total electron transfer and excitation cross-sections were obtained:

- i)  $Ti^{4+} + He$  [27]:  $\Sigma(\text{SEC}) = 2.05 \times 10^{-14} \text{ cm}^2$  and  $\Sigma(\text{EXC}) = 7.7 \times 10^{-16} \text{ cm}^2$  at  $E_c=300 \text{ keV}$ ;
- ii)  $Cr^{6+} + He$  [28]:  $\Sigma(\text{SEC}) = 2.32 \times 10^{-14} \text{ cm}^2$  and  $\Sigma(\text{EXC}) = 2.00 \times 10^{-15} \text{ cm}^2$  at  $E_c=400 \text{ keV}$ ;
- iii)  $Fe^{8+} + He$  [28]:  $\Sigma(\text{SEC}) = 3.40 \times 10^{-14} \text{ cm}^2$  and  $\Sigma(\text{EXC}) = 9.54 \times 10^{-15} \text{ cm}^2$  at  $E_c=400 \text{ keV}$ .

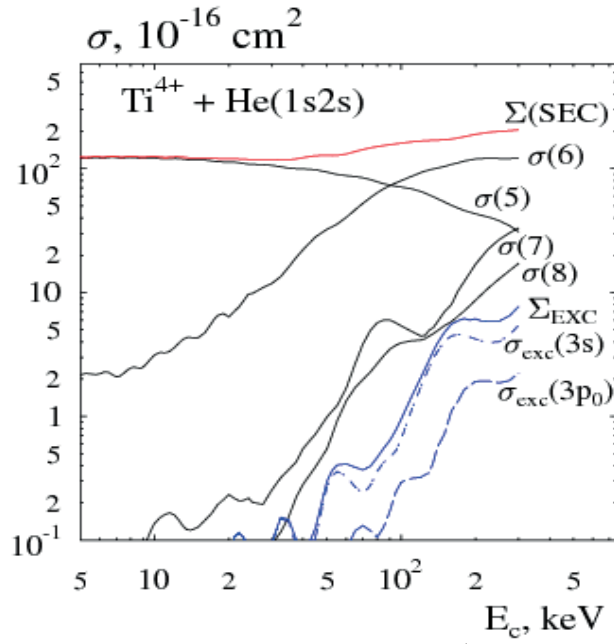


FIG. 9. Cross-sections for SEC and excitation in the  $Ti^{4+} + He(1s2s)$  collision versus the impurity ion energy  $E_c$ :  $\Sigma(SEC)$  – the total SEC cross-section,  $\sigma(n)$  – SEC cross-sections into the  $n$  shells with  $n=6-8$  of the  $Ti^{3+}$  ions;  $\Sigma_{EXC}$ ,  $\sigma(3l)$  – the total and partial cross-sections for the  $2s \rightarrow 3l$  excitation in the He atoms.

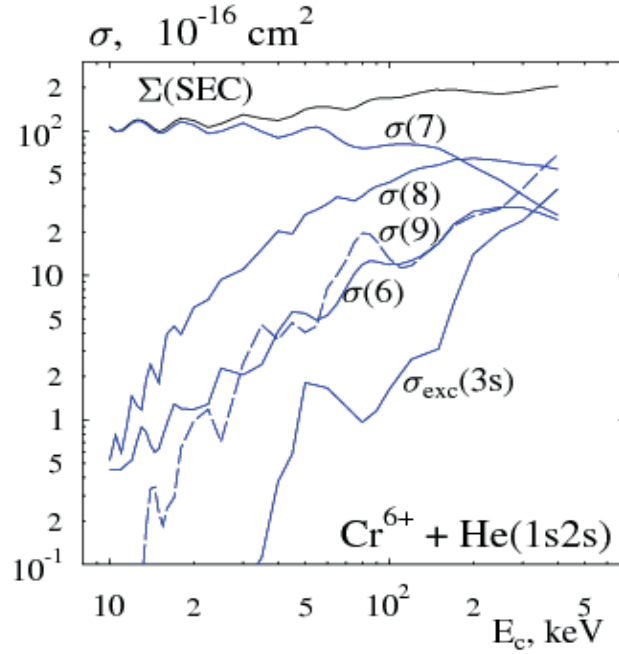


FIG. 10. Cross-sections versus the impurity ion energy  $E_c$  for the  $Cr^{6+} + He(1s2s)$  collisions:  $\Sigma(SEC)$  – the total SEC cross-section;  $\sigma(n)$  – SEC cross-sections into the  $n$  shells with  $n=6-9$  of the  $Cr^{5+}$  ions;  $\sigma_{exc}(3s)$  – the cross-section of the  $2s \rightarrow 3s$  excitation in the He atoms.

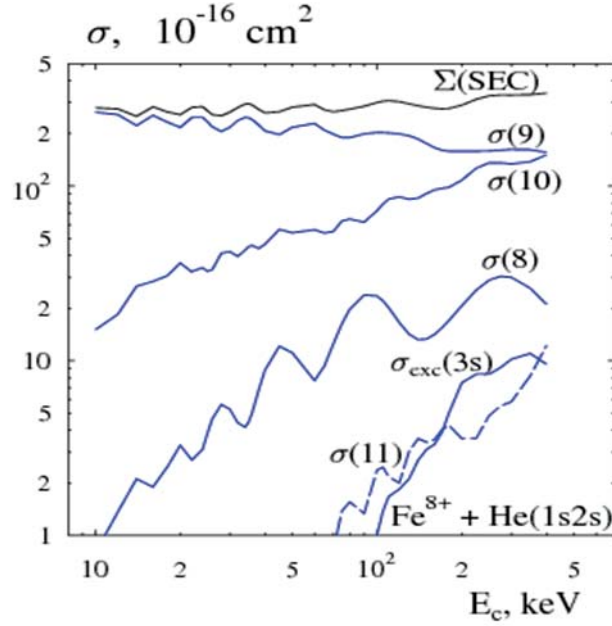


FIG. 11. Cross-sections versus the impurity ion energy  $E_c$  for the  $Fe^{8+} + He(1s2s)$  collision:  $\Sigma(SEC)$  – the total SEC cross-section;  $\sigma(n)$  – SEC cross-sections into the  $n$  shells with  $n=8-11$  of the  $Fe^{7+}$  ions;  $\sigma_{exc}(3s)$  – the cross-section of the  $He(2s \rightarrow 3s)$  excitation.

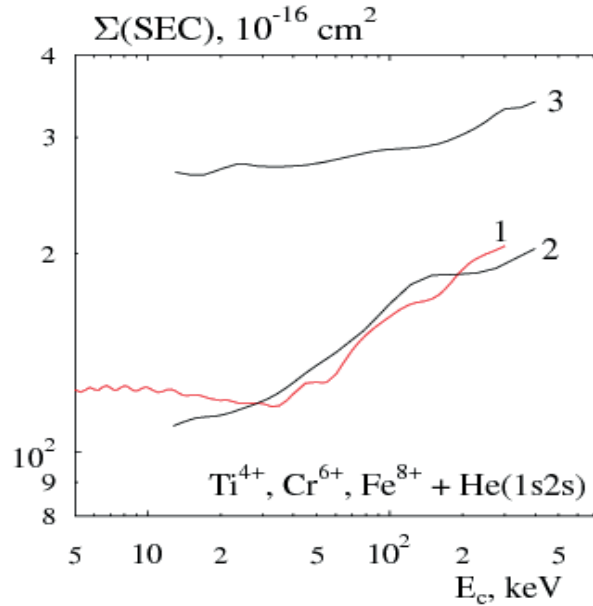


FIG. 12. Total cross-sections of the single electron transfer versus the impurity ion energy  $E_c$  for collisions: 1 –  $Ti^{4+} + He(1s2s)$ , 2 –  $Cr^{6+} + He(1s2s)$ , 3 –  $Fe^{8+} + He(1s2s)$ .

Partial and total cross-sections for  $Cr^{6+}$ ,  $Fe^{8+} + He(1s2s)$  collisions (Figs. 10–11) exhibit small oscillatory structures due to interference effects as an artifact of close-coupling calculation. They would vanish in calculation with a much larger basis set (compare the results with seventeen states for  $Ti^{4+} + He(1s2s)$  (Fig. 9) and with ten states for  $Cr^{6+}$ ,  $Fe^{8+} + He(1s2s)$ ). In Fig. 12, we present the results for the latter cases with smoothed off oscillatory structure.

The calculated  $n$ -distribution of the electron transfer cross-section for the  $\text{Ti}^{4+}$ ,  $\text{Cr}^{6+}$ ,  $\text{Fe}^{8+} + \text{He}(1s2s)$  collisions is shown in Figs. 13–15.

In Fig. 13, we compare the calculated  $n$ -distribution in the  $\text{Ti}^{4+} + \text{He}(1s2s)$  collision at 240 keV ( $5 \text{ keV amu}^{-1}$ ) with results by Fritsch and Tawara [25] for the  $\text{Be}^{4+} + \text{He}(1s2s)$  collisions. The agreement is only qualitative because we considered the  $\text{Ti}^{4+}$  ion with the Ar-like core but not the bare ion.

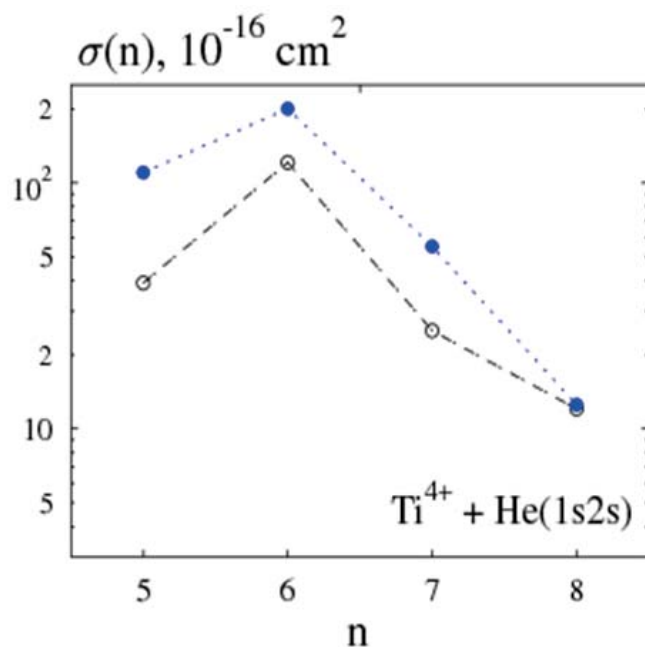


FIG. 13. The  $n$ -distribution of the electron transfer cross-section in the  $\text{Ti}^{4+} + \text{He}(1s2s)$  collision (o, our results) and in the  $\text{Be}^{4+} + \text{He}(1s2s)$  collision (•, results by Fritsch and Tawara [25]) at  $E_c = 5 \text{ keV amu}^{-1}$ .

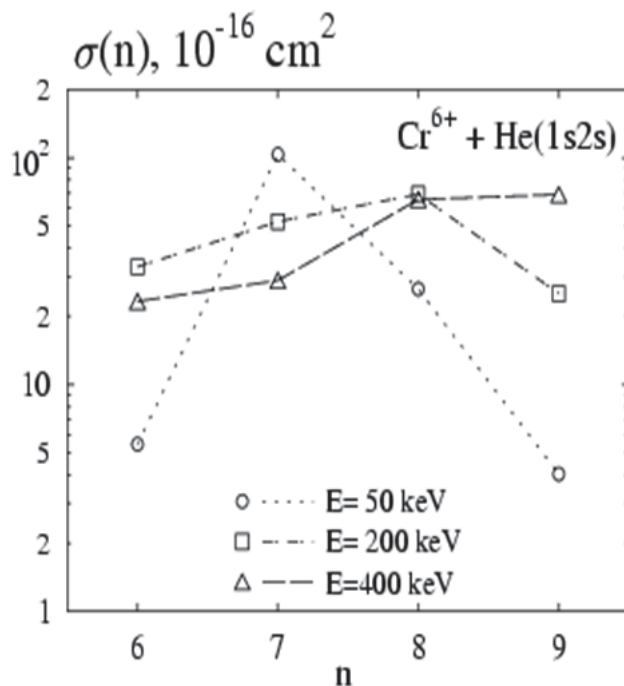


FIG. 14. The  $n$ -distribution of the electron transfer cross-section in the  $\text{Cr}^{6+} + \text{He}(1s2s)$  collision.

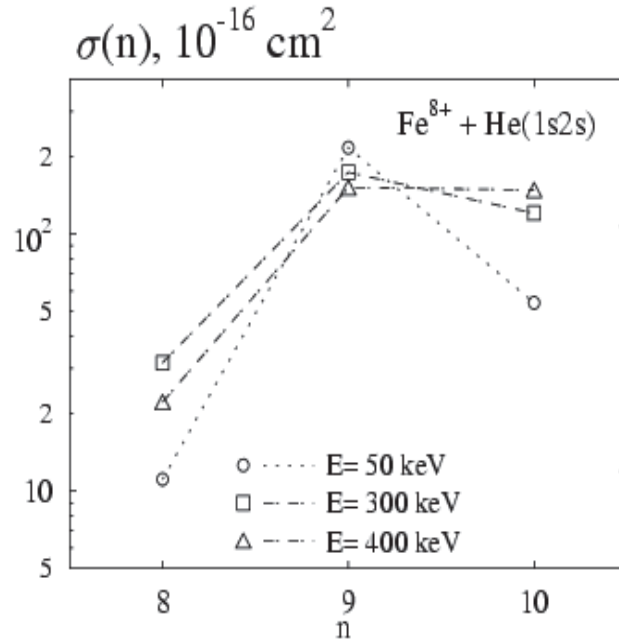


FIG. 15. The  $n$ -distribution of the electron transfer cross-section in the  $Fe^{8+} + He(1s2s)$  collision.

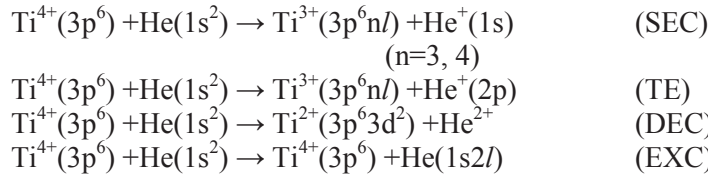
## 5. CALCULATION OF CHARGE EXCHANGE, TRANSFER EXCITATION AND EXCITATION CROSS-SECTIONS IN COLLISIONS OF $Ti^{4+}$ , $Si^{4+}$ , $Cr^{6+}$ , $Fe^{8+}$ , $Mo^{6+}$ , AND $W^{6+}$ WITH HELIUM ATOMS IN THE GROUND STATE

SEC and DEC, transfer excitation (TE), and excitation of helium (EXC) were calculated at relative keV-collision energies important for modeling and diagnostics of the plasma edge.

Calculations for the  $Ti^{4+} + He$  collisions in the energy range 0.1–6 MeV were performed by Fritsch [7] within the framework of the close-coupling method using plane-wave TF and with regard to two active electrons, but the important two-electron transfer excitation and DEC channels being omitted.

### 5.1. $Ti^{4+} + He$ Collision

Detailed calculations of the cross-sections were performed [23] for following reactions:



The basis set for this system consists of 17 two-electron quasimolecular states (see Fig. 4) involving:

- the entrance channel (red curve 1);
- channels of SEC into the 3d, 4d, 4f, and 5f, 5g states of ions  $Ti^{3+}$ ;
- channels of DEC into the 3d states of ions  $Ti^{2+}$ ;
- TE channels (SEC into the 3d states of the  $Ti^{3+}$  ion with the  $1s \rightarrow 2s$ ,  $2p_0$ ,  $2p_{\pm 1}$  excitation of the He atom);
- channels of the  $1s \rightarrow 2s$ ,  $2p_{\pm 1}$ ,  $3p_0$ , and  $3p_{\pm 1}$  excitation of the He atoms.

The calculated cross-sections as a function of the  $\text{Ti}^{4+}$  ion energy are shown in Fig. 16 together with the theoretical results by Fritsch [7]. It is clearly seen that our data for SEC agree with the results by Fritsch at energy  $\sim 100$  keV.

The electron transfer process in the  $\text{Ti}^{4+} + \text{He}$  collisions populates predominantly the 3d level of projectile. Maximum values of the total cross-section for excitation of helium to its  $^12\text{S}+^12\text{P}$  states and for DEC were obtained to be equal  $\sim 2.6 \times 10^{-16} \text{ cm}^2$  at  $E_c=400$  and  $\sim 1.3 \times 10^{-16} \text{ cm}^2$  at  $E_c=250$  keV.

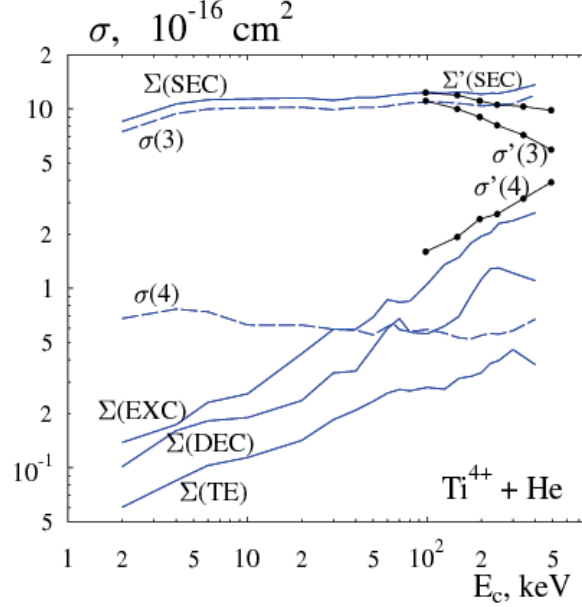
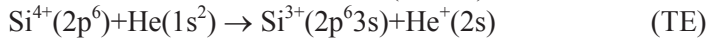
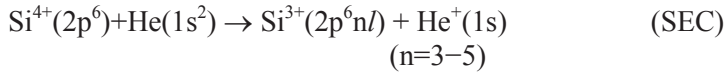


FIG. 16. Cross-sections versus the energy  $E_c$  for the  $\text{Ti}^{4+} + \text{He}(1s^2)$  collision:  $\Sigma(\text{SEC})$  – the total SEC cross-section ( $\Sigma_n \sigma(n) + \Sigma(\text{TE})$ ),  $\sigma(n)$  – SEC cross-sections into the  $n$  shells of the  $\text{Ti}^{3+}$  ions with  $n=3-5$ ,  $\Sigma(\text{TE})$  – the cross-section for SEC into the 3s state of the  $\text{Ti}^{3+}$  ion with the  $1s \rightarrow 2s, 2p$  excitation of the He atoms;  $\Sigma(\text{DEC})$  – DEC cross-section. •  $\Sigma'(\text{SEC})$ ,  $\sigma'(3)$ ,  $\sigma'(4)$  – results by Fritsch [7].

## 5.2. $\text{Si}^{4+} + \text{He}$ Collision

The partial and total cross-sections for SEC and TE were calculated [29] for reactions



using the basis set of nine two-electron quasimolecular states involving:

- the entrance channel;
- channels of SEC into the 3s, 3p, 3d, 4p, 4d, and 5d states of the  $\text{Si}^{3+}$  ions;
- the TE channel (SEC into the 3s state of the  $\text{Si}^{3+}$  ions with the  $1s \rightarrow 2s$  excitation of the He atom).

Calculated cross-sections as functions of the energy from 2 keV to 300 keV are shown in Fig. 17 together with the SEC cross-section obtained by Fritsch [7]. Our data on total SEC agree with the results by Fritsch at the energy  $\sim 300$  keV. SEC into the  $3l$  states of  $\text{Si}^{3+}$  dominates in the overall range of collision energies. The transfer excitation cross-section was obtained less than  $10^{-21} \text{ cm}^2$ .

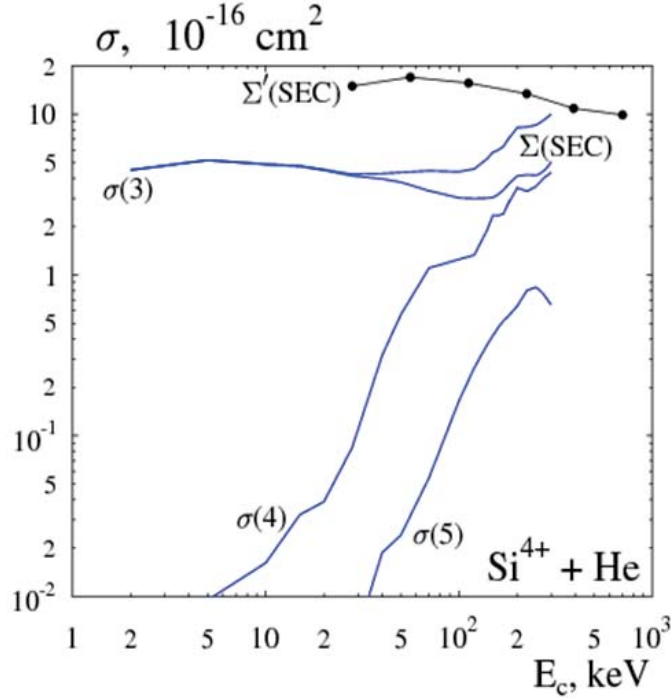
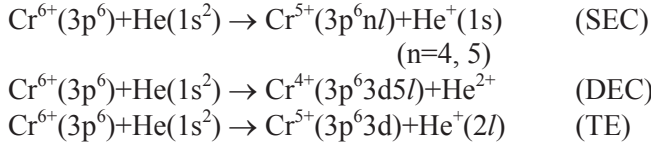


FIG. 17. Cross-sections versus the energy  $E_c$  for the  $\text{Si}^{4+} + \text{He}$  collision:  $\sigma(n)$  – SEC cross-sections into the  $n$  shells of the  $\text{Si}^{3+}$  ions with  $n=3-5$ ,  $\Sigma(\text{SEC})$  – the total SEC cross-section.  $\Sigma'(\text{SEC})$  – results by Fritsch [7] (•, black curve).

### 5.3 $\text{Cr}^{6+} + \text{He}$ Collision

Cross-sections for SEC, DEC and TE channels were calculated [30] for reactions



using the basis set of eleven two-electron quasimolecular states involving:

- the entrance channel;
- channels of SEC into the 4s, 4p, 4d, 4f<sub>0</sub>, 4f<sub>±1</sub>, and 5f, 5g states of the  $\text{Cr}^{5+}$  ions;
- the channel of DEC into the 3d5g state of the  $\text{Cr}^{6+}$  ions;
- TE channels (SEC into the 3d state of ion  $\text{Cr}^{5+}$  with the  $1s \rightarrow 2l$  excitation of the He atom).

Calculated cross-sections for the  $\text{Cr}^{6+} + \text{He}(1s^2)$  collision in the energy range from 2 to 400 keV are shown in Fig. 18. The maximum value of the total SEC and DEC cross-sections obtained is equal to  $4.72 \times 10^{-15} \text{ cm}^2$  (at  $E_c \sim 400 \text{ keV}$ ) and  $1.9 \times 10^{-16} \text{ cm}^2$  (at  $E_c \sim 250 \text{ keV}$ ).

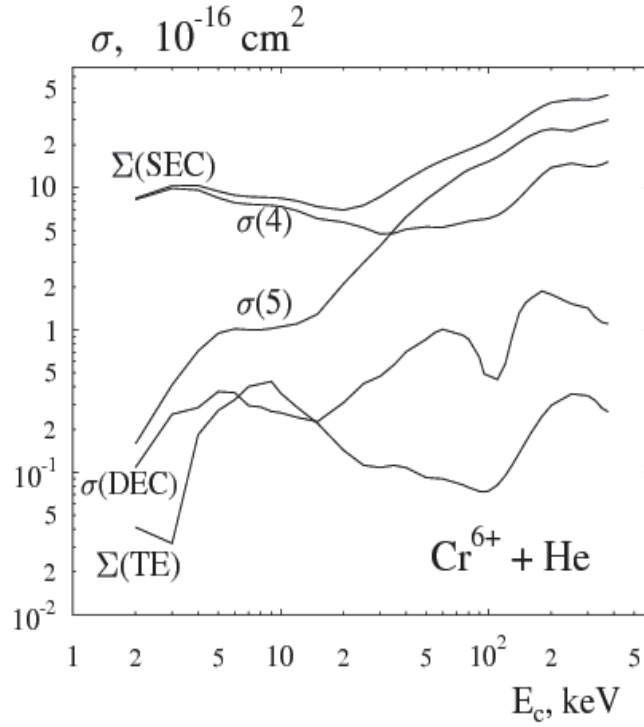
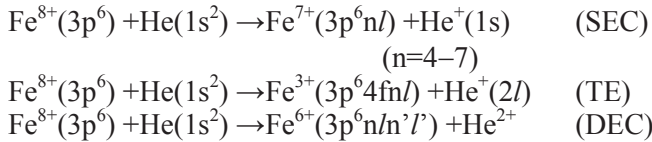


FIG. 18. Cross-sections versus the energy  $E_c$  for the  $\text{Cr}^{6+} + \text{He}$  collision:  $\Sigma(\text{SEC})$  – the total cross-section of SEC + TE;  $\sigma(n)$  – the cross-sections of SEC into  $n$  shells of the  $\text{Cr}^{5+}$  ions with  $n=4, 5$ ,  $\Sigma(\text{TE})$  – cross-section for one electron transfer into the  $3d$  state of  $\text{Cr}^{5+}$  with the  $1s \rightarrow 2s, 2p$  excitation of the He atom,  $\Sigma(\text{DEC})$  – DEC cross-section.

#### 5.4 $\text{Fe}^{8+} + \text{He}$ Collision

Cross-sections for SEC, DEC and TE channels were calculated [31] for reactions



using the basis set of eight two-electron quasimolecular states involving:

- the entrance channel;
- channels of SEC into the  $4f, 5g, 6h, 7i$  states of the  $\text{Fe}^{7+}(nl)$  ions;
- channels of DEC into the  $4f^2$  and  $4f5g$  states of the  $\text{Fe}^{6+}$  ions;
- the channel of TE (SEC into the  $4f$  state of ion  $\text{Fe}^{7+}$  with the  $s \rightarrow 2p_0$  excitation of the He atom.

Calculated cross-sections for the  $\text{Fe}^{8+} + \text{He}(1s^2)$  collision in the energy range from 2 to 400 keV are shown in Fig. 19. The maximum value of the total SEC cross-section obtained for the  $\text{Fe}^{8+} + \text{He}$  collision is equal to  $1.3 \times 10^{-14} \text{ cm}^2$  at  $E_c \cong 400 \text{ keV}$ ; the value of DEC cross-section is less than  $1.3 \times 10^{-17} \text{ cm}^2$ .

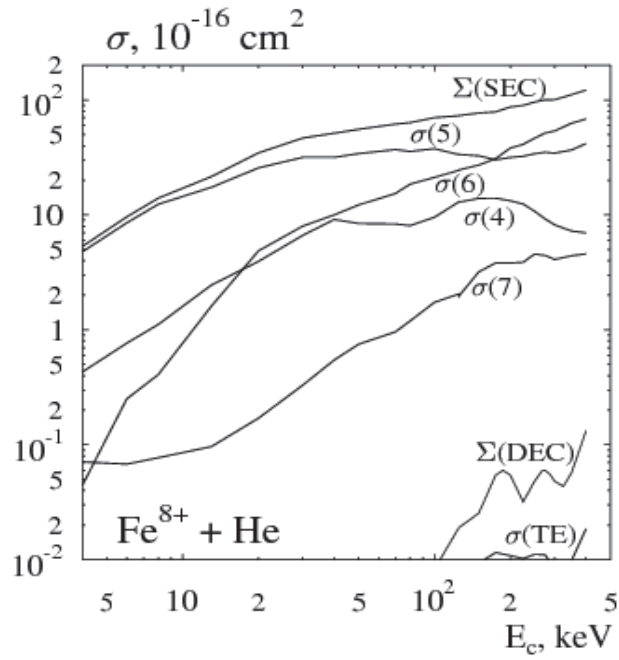
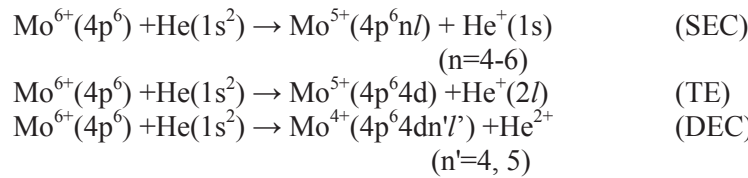


FIG. 19. Cross-sections versus the energy  $E_c$  for the  $Fe^{8+} + He$  collision:  $\Sigma(SEC)$  – the total cross-section of SEC + TE;  $\sigma(n)$  – cross-sections of SEC into the  $n$  shells of the  $Fe^{7+}$  ions with  $n=4-7$ ,  $\Sigma(TE)$  – TE cross-section;  $\Sigma(DEC)$  – DEC cross-section.

### 5.5 $Mo^{6+} + He$ Collision

Cross-sections for SEC, DEC and TE channels were calculated [32] for reactions



by the use of fourteen two-electron quasimolecular states involving:

- the entrance channel;
- channels of SEC into the 4f, 5d, 5f, 5g, 6f, 6g, and 6h states of the  $Mo^{5+}$  ions;
- channels of DEC into the 4d4f, 4d5d, 4f5f and 4f5g states of the  $Mo^{4+}$  ions;
- channels of TE (SEC into the 4d state of the  $Mo^{5+}$  ion with the  $1s \rightarrow 2l$  excitation of the He atom).

The SEC and DEC cross-sections in collisions between the  $Mo^{6+}$  ions with energies of 5 – 400 keV and the helium atoms are presented in Fig. 20.

SEC into the 5g state of the  $Mo^{5+}$  ion dominates at all energies. The maximum value of the total SEC cross-section was obtained to be equal  $1.1 \times 10^{-14} \text{ cm}^2$  at the collision energy  $\sim 175 \text{ keV}$ ; DEC cross-section was obtained to be less than  $1.6 \times 10^{-17} \text{ cm}^2$ .

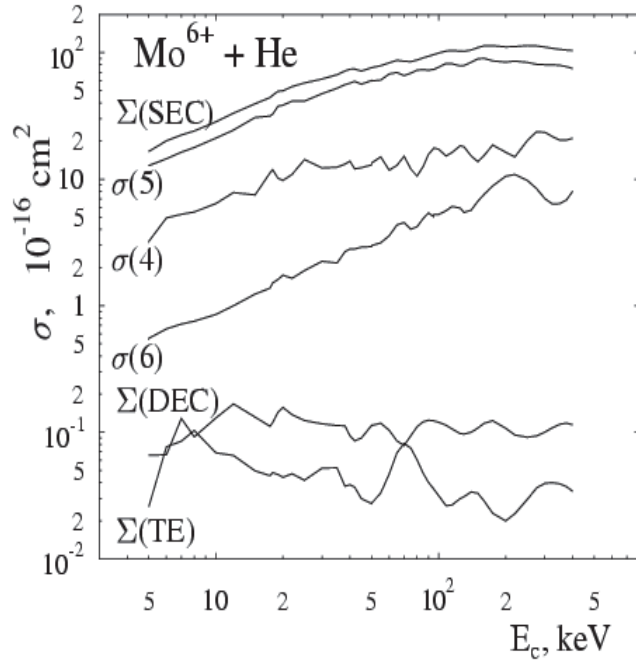
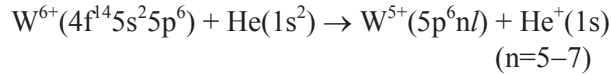


FIG. 20. Cross-sections versus the energy  $E_c$  for the  $\text{Mo}^{6+} + \text{He}$  collision:  $\Sigma(\text{SEC})$  ( $\sigma(4) + \sigma(5) + \sigma(6) + \sigma(\text{TE})$ ) – the total SEC + TE cross-section,  $\sigma(n)$  – SEC cross-sections into the  $n$  shells of the  $\text{Mo}^{5+}$  ions with  $n=4-6$ ,  $\Sigma(\text{TE})$  – TE cross-section;  $\Sigma(\text{DEC})$  – DEC cross-section.

### 5.6 $\text{W}^{6+} + \text{He}$ Collision

Cross-sections for SEC channels were calculated [33] for the reactions



with the basis set of nine two-electron quasimolecular states involving:

- a) the entrance channel;
- b) channels of SEC into the 5d, 5f, 5g, 6f, 6g, 6h, 7g, and 7h states of ions  $\text{W}^{5+}$ .

The calculated total and partial SEC cross-sections for collision of the  $\text{W}^{6+}$  ions with energies of 20 ~ 800 keV with helium atoms are shown in Fig. 21.

The channels of the electron capture into the 5g and 6h states of the  $\text{W}^{5+}$  ions make the main contribution at the collision energy of 500 keV. The maximum value of the total SEC cross-section at this energy was obtained to be equal  $5.8 \times 10^{-15} \text{ cm}^2$ .

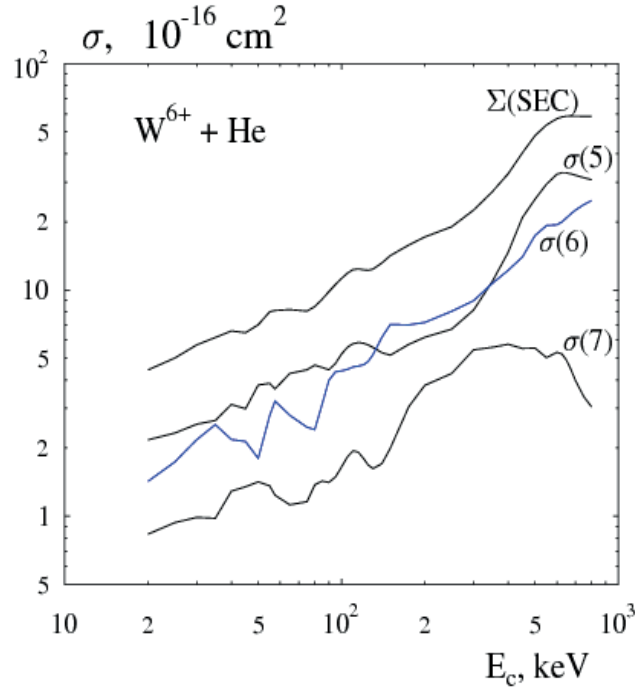


FIG. 21. Cross-sections versus the energy  $E_c$  for the  $W^{6+} + He$  collision:  $\Sigma(\text{SEC})$  – the total SEC cross-section,  $\sigma(n)$  – SEC cross-sections into the  $n$  shells of ions  $W^{5+}$  with  $n=5-7$ .

Calculated total SEC cross-sections versus energy of the impurity ions  $A^{q+}$  for collisions  $A^{q+} + He(1s^2)$  are shown in Fig. 22. The  $nl$  states of the  $A^{(q-1)+}$  ions which are populated in the collision much stronger than others in the overall energy range are indicated.

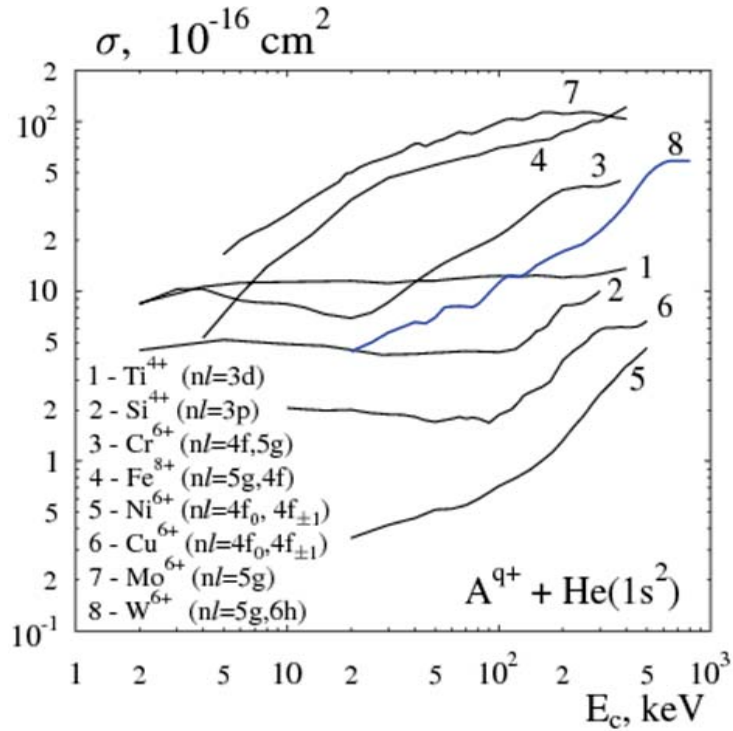


FIG. 22. SEC cross-sections for collisions  $A^{q+} + He(1s^2)$  versus the impurity ion energy  $E_c$ .

Results for collision systems  $\text{Ni}^{6+}$ ,  $\text{Cu}^{6+} + \text{He}$  are described more fully in the reports [34, 35].

Data on the partial and total cross-sections for electron transfer, transfer excitation, and excitation in collisions of the multiply charged heavy element impurity ions with the helium atoms in the ground state were obtained for the first time in the energy range of 2 keV to 800 keV.

## 6. CONCLUSIONS

New data for 15 collision systems which are of great importance for charge exchange recombination spectroscopy have been produced and included in the IAEA A+M databases under the name: State-Selective and Total Electron Capture, Excitation and Neutralization Cross-Sections in Collisions between Heavy-Element Impurity Ions, Helium Atoms and Alpha Particles.

The collisions systems  $\text{He}^{2+} + \text{O}^{4+}$ ,  $\text{Bi}^{4+} + \text{Bi}^{4+}$  studied within this CRP were considered at length in [36–38] so the results were not included in the present paper. Data on the partial and total cross-sections for SEC and target excitation in collisions of alpha particles with the Be-like oxygen ions were obtained [36] in the high energy range 0.2 – 2 MeV using four active-electron quasimolecular states.

Pioneering theoretical data were obtained [37, 38] for charge exchange and excitations in collisions due to betatron oscillations in the ion beams between the  $\text{Bi}^{4+}$  ions in the ground (6s) and metastable (6p) states. The fraction of metastable ions in the beams was estimated by comparison of our theoretical data with the Giessen experimental results [39] for the total charge exchange cross-section. Gaining insight into charge transfer between identical low-charged heavy ions at their collisions due to betatron oscillations is vital to designing accelerators and storage rings with the aim to generate intense ion beams [40]. Such beams can also find application in heavy-ion-driven inertial fusion.

## ACKNOWLEDGEMENTS

This study has been performed within an IAEA CRP on “Atomic Data for Heavy Element Impurities in Fusion Reactors” (2005 – 2009). The authors are indebted to R.E.H. Clark and the other participants for the open exchange of results and ideas at the CRP meetings.

This work was funded through IAEA Research Contract No 13348/RBF.

## REFERENCES

- [1] JANEV, R.K., *Comm. At. Mol. Phys.* **26** (1991) 83.
- [2] TAWARA, H., “Roles of atomic and molecular processes in fusion plasma researches”. NIFS-DATA-25 (1995).
- [3] ZASTROW, K.-D., O’ MULLANE, M., BRIX, M., GIROUD, C., MEIGS, A.G., PROSCHEK, M., SUMMERS, H.P., Double charge exchange from helium neutral beams in a tokamak plasma, *Plasma Phys. Control. Fusion* **45** (2003) 1747.
- [4] KATSONIS, K., MAYNARD, G., and JANEV, R.K., Charge transfer and ionization cross-sections for collisions of  $\text{Ti}^q$ ,  $\text{Cr}^{q+}$ ,  $\text{Fe}^{q+}$  and  $\text{Ni}^{q+}$  ions with atomic hydrogen, *Physica Scripta* **T37** (1991) 80.
- [5] FRITSCH, W., Theoretical investigation of electron transfer in collisions between atomic hydrogen and the closed-3p-shell ions of Ti, Cr, and Fe, *Physica Scripta* **T37** (1991) 75.
- [6] McLAUGHLIN, T.K., HODGKINSON, J.M., TAWARA, H., McCULLOUGH, R.W., GILBODY, H.B, State-selective electron capture in collisions of slow  $\text{Fe}^{3+}$  and  $\text{Fe}^{4+}$  ions with H and He atoms, *J Phys. B: At. Mol. Opt. Phys.* **26** (1993) 3587.

- [7] FRITSCH, W., Theoretical studies of slow collisions between medium-Z metallic ions and neutral H, H<sub>2</sub>, or He, *Atomic and Plasma-Material Interaction Data for Fusion* **6** (1995) 131.
- [8] PIACENTINI, R.D., SALIN, A., Multistate molecular treatment of atomic collisions in the impact parameter approximation. III - integration of coupled equations and calculation of transition amplitudes for coulomb trajectories, *Computer Phys. Comm.* **12** (1976) 199.
- [9] NIKULIN, V.K., GUSCHINA, N.A., Diabatic correlation diagrams for the quasi-molecular description of ion-atom collisions, *J. Phys. B: Atom and Molec. Phys.* **11** (1978) 3553.
- [10] TELLER, E., SAHLIN, H.L., *Physical Chemistry: An Advanced Treatise*, New York: Academic Press, (1970) vol. 5.
- [11] HELLMAN, HANS, *Einführung in der Quantenchemie*, Deuticke, Leipzig, (1937).
- [12] NIKULIN, V.K., SAMOYLOV, A.V., Quasimolecular states for He<sup>2+</sup> + He collisions, *Phys. Lett. A* **89** (1982) 225.
- [13] HATTON, G.J., LANE, N.F., WINTER, T.G., Charge transfer for He<sup>2+</sup> on H using molecular bases with plane-wave translational factors, *J. Phys. B: Atom. Molec. Phys.* **12** (1979) L571.
- [14] NIKULIN, V.K., GUSCHINA, N.A., Cross-Sections for Electron Capture and Excitation Processes in Collisions Between the Hydrogen-Like He+(1s) and B4+(1s), C5+(1s), N6+(1s), O7+(1s) Ions, *Atomic and Plasma-Material Interaction Data for Fusion* **13** (2007) 122.
- [15] FRITSCH, W., Theoretical study of electron processes in slow He<sup>2+</sup>-He collisions, *J. Phys. B: At. Mol. Opt. Phys.* **27** (1994) 3461.
- [16] HAREL, C., SALIN, A., Application of OEDM orbitals to many-electron systems: He<sup>2+</sup>-He collisions, *J. Phys. B: At. Mol. Phys.* **13** (1980) 785.
- [17] NIKULIN, V.K., GUSHCHINA, N.A., Charge transfer and charge transfer with excitation of a target ion in slow collisions of alpha particles with helium atoms, *Optics and Spectroscopy* **80** (1996) 333.
- [18] AFROSIMOV, V.V., BASALAEV, A.A., LEIKO, G.A., PANOV, M.N., Formation of He<sup>+</sup> ions in various electronic states in He<sup>2+</sup> + He collisions, *Sov. Phys. – JETP* **47** (1978) 837.
- [19] CRANDALL, D.H., Electron transfer between He-like ions and He, *Phys. Rev. A* **16** (1977) 958.
- [20] KIMURA, M., OLSON, R.E., Electron capture to (nl) states in collisions of C<sup>4+</sup> and C<sup>6+</sup> with He, *J. Phys. B: At. Mol. Phys.* **17** (1984) L713.
- [21] ERREA, L.F., HERRERO, B., MÉNDEZ, L., RIERA, A., Molecular calculation of total and differential charge transfer cross-sections in C<sup>4+</sup>+He collisions, *J. Phys. B: At. Mol. Phys.* **28** (1995) 693.
- [22] PHANEUF, R.A., CRANDALL, D.H., from ref. [20] (1981).
- [23] NIKULIN, V.K., GUSCHINA, N.A., “Alpha particle neutralization at their slow collisions with Ti<sup>2+</sup> ions through quasi-resonant double electron capture”. Report of Ioffe Physico-Technical Institute N 1799, St. Petersburg, 2008.
- [24] SOLOV’EV, E.A., STEPHENS, J.A., JANEV, R.K., State-selective and total electron capture, excitation and ionization cross-sections for slow collisions of H(2s) and He+(2s) with H<sup>+</sup>, He<sup>2+</sup>, Li<sup>3+</sup>, Be<sup>4+</sup>, and B<sup>5+</sup>, *Atomic and Plasma-Material Interaction Data for Fusion* **9** (2001) 179.
- [25] FRITSCH, W., TAWARA, H., “Present Status on Atomic and Molecular DATA Relevant to Fusion Plasma and Modeling”. NIFS–DATA–39 (1997).
- [26] SALASNICH, L., SATTIN, F., Charge-exchange processes between excited helium and fully stripped ions, *Phys. Rev. A* **51** (1995) 4281.
- [27] NIKULIN, V.K., GUSCHINA, N.A., “State-selective and total electron transfer and excitation cross-sections in slow collisions of excited He(1s2s) atoms and Ti<sup>4+</sup>, Cr<sup>6+</sup>, Fe<sup>8+</sup> ions. I. Ti<sup>4+</sup> – He(1s2s) collision”. Report of Ioffe Physico-Technical Institute N 1793, St. Petersburg, 2007.

- [28] NIKULIN, V.K., GUSCHINA, N.A., “State-selective and total electron transfer and excitation cross-sections in slow collisions of excited He(1s2s) atoms and  $Ti^{4+}$ ,  $Cr^{6+}$ ,  $Fe^{8+}$  ions. II.  $Cr^{6+}$ ,  $Fe^{8+}$ – He(1s2s) collisions”. Report of Ioffe Physico-Technical Institute N 1794, St. Petersburg, 2007.
- [29] NIKULIN, V.K., GUSCHINA, N.A., “Charge exchange and excitation processes in collisions  $Si^{4+}$ ,  $Si^{2+}$  ions with helium atoms and alpha particles”. Report of Ioffe Physico-Technical Institute N 1801, St. Petersburg, 2009.
- [30] NIKULIN, V.K., GUSCHINA, N.A., “Electron transfer and excitation in collisions between  $Ti^{4+}$ ,  $Cr^{6+}$  ions and helium atoms”. Report of Ioffe Physico-Technical Institute N1791, St. Petersburg, 2006.
- [31] NIKULIN, V.K., GUSCHINA, N.A. “Electron transfer and excitation in collisions between  $Fe^{8+}$  ions and helium atoms”. Report of Ioffe Physico-Technical Institute N 1792, St. Petersburg, 2007.
- [32] NIKULIN, V.K., GUSCHINA, N.A., “State-selective and total electron transfer cross-sections in collisions between heavy metal element ions and helium atoms. II.  $Mo^{6+}$ + He”. Report of Ioffe Physico-Technical Institute N 1797, St. Petersburg, 2008.
- [33] NIKULIN, V.K., GUSCHINA, N.A., “State-selective and total electron transfer cross-sections in collisions between heavy metal element ions and helium atoms. I.  $W^{6+}$ + He”. Report of Ioffe Physico-Technical Institute N 1796, St. Petersburg, 2008.
- [34] NIKULIN, V.K., GUCSHINA, N.A., “State-selective and total electron transfer cross-sections in collisions between heavy metal element ions and helium atoms. III.  $Ni^{6+}$ + He”. Report of Ioffe Physico-Technical Institute N 1798, St. Petersburg, 2008.
- [35] NIKULIN, V.K., GUSCHINA, N.A., “State-selective and total electron transfer cross-sections in collisions between heavy metal element ions and helium atoms. IV.  $Cu^{6+}$ + He”. Report of Ioffe Physico-Technical Institute N 1800, St. Petersburg, 2008.
- [36] NIKULIN, V.K., GUSCHINA, N.A., Charge exchange and excitation cross-sections at collisions of alpha particles with Be-like impurity oxygen ions in a plasma, *Technical Physics* **51** (2006) 1276.
- [37] NIKULIN, V.K., GUSCHINA, N.A., Single-electron charge transfer and excitations at collisions between  $Bi^{4+}$  ions in the kiloelectronvolt energy range, *Technical Physics* **52** (2007) 148.
- [38] NIKULIN, V.K., GUSCHINA, N.A., ‘Theoretical study of charge transfer and excitation in slow collisions between  $Bi^{4+}$  ions in the ground and metastable states”, Abstracts of contributed papers to XXV ICPEAC (Freiburg, Germany 2007) p. Mo082.
- [39] DIEHL, A., BRÄUNING, H., TRASSL, R., HATHIRAMANI, D, TREISS, A., KERN, H., SALZBORN, E., HOFMANN, I., Charge transfer and ionization in collisions between multiply charged noble gas ions, *J. Phys. B* **34** (2001) 4073.
- [40] HOFMANN, I., Heavy ion inertial fusion in Europe, *Nucl. Instrum. Methods A* **464** (2001) 24.

# SPECTRAL PROPERTIES OF HEAVY ELEMENTS OF FUSION INTEREST

W.L. WIESE, M.A. ALI, I.N. DRAGANIC, J.R. FUHR, J.D. GILLASPY,  
R. IBACACHE, D.E. KELLEHER, A. KRAMIDA, L.I. PODOBEDOVA,  
YU. RALCHENKO, J. READER, E.B. SALOMAN, P.M. STONE

National Institute of Standards and Technology, USA

## Abstract

The spectroscopic research program of the NIST Atomic Spectroscopy Group during the last 5 years has been focused on heavy elements of fusion interest and has achieved some significant advances. With an electron beam ion trap (EBIT), the spectra of numerous highly charged ions of tungsten were observed in the EUV and soft x-ray spectral regions, where the principal emission occurs. The spectra were analyzed utilizing isoelectronic ions from neighboring elements and by applying the NOMAD and FAC modeling codes. Numerous new E1, M1, and E2 lines were identified. Also, comprehensive critical compilations of the spectra of tungsten and several other heavy elements of interest to fusion energy science (Al, Si, S, Ar, Cl, Fe, Kr and Xe) were completed, and calculations of ionization and excitation cross sections for tungsten and molybdenum were carried out with the BEB method.

## 1. INTRODUCTION

The spectral properties of heavy elements, which are important for magnetic fusion energy science are a principal current research area of the Atomic Spectroscopy Group at the U.S. National Institute of Standards and Technology (NIST). During the five-year period 2005 – 2009, the NIST work focused on three broad topics:

(A) Detailed observations, accurate measurements and analyses of the spectra of numerous ions of tungsten, from low to extremely high charge states, since tungsten is a likely candidate for a divertor material.

(B) Calculations of ionization and excitation cross sections of selected ions of tungsten and neighboring elements, and molybdenum.

(C) Critical compilations of spectral data for a number of heavy elements of fusion interest, which are comprehensive new tabulations of reference data, usually for many or all stages of ionization of a specific element.

In the following, detailed discussions of our work in these research areas will be presented, including our main results.

## 2. OBSERVATIONS AND ANALYSES OF THE SPECTRA OF HIGHLY IONIZED TUNGSTEN

The Electron Beam Ion Trap (EBIT), a low-density table-top laboratory device, is ideally suited to generate and observe spectra of highly charged ions. We thus used the NIST EBIT [1], shown schematically in Fig.1, to investigate a variety of heavy metal and gas ions in very high charge states. Here, we limit our discussion to the part of this work involving the spectroscopy of tungsten (and select metals of similar mass) in the extreme ultraviolet (EUV) and x-ray spectral regions [2– 5], with emphasis on possible fusion modeling and diagnostics applications. At the end of this section, we also refer to our work on other heavy ions of potential interest.

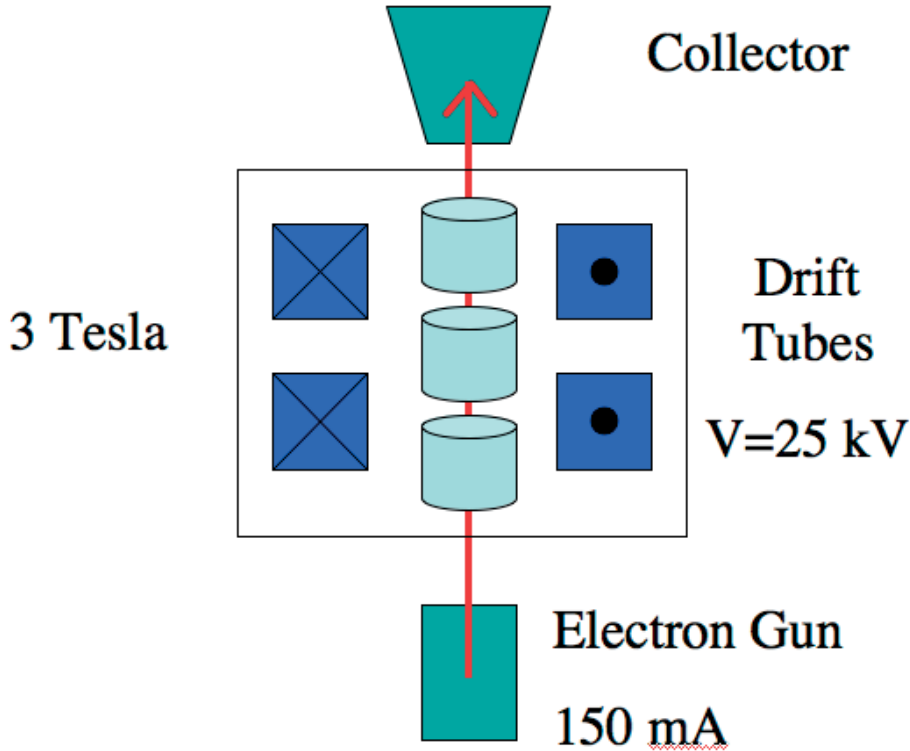


FIG. 1. Schematic of an Electron Beam Ion Trap, showing a beam from an electron gun accelerating through drift tubes held at 25 kV in a 3 Tesla magnetic field. Ions are trapped in the central drift tube by a combination of forces from (1) the radial electric field of the electron beam, (2) the axial magnetic field, and (3) the mirror fields formed by biasing the upper and lower drift tubes a few hundred volts above the central drift tube. Photons escape horizontally through slits (not shown) in the central drift tube. The components surrounded by the square box in the center of the figure are cooled to 4.2 K by liquid helium.

In 2005, we completed the buildup of advanced instrumentation to carry out this work in conjunction with the EBIT, specifically a special EUV spectrometer [6], an x-ray microcalorimeter [7], and a multi-cathode metal ion injector [8].

Throughout our investigations, we used modeling to help interpret the spectra and to accurately predict the observed line intensities. For most of our work, we used a collisional-radiative model based on the NOMAD code [9], with all fundamental atomic and collision input data generated by the FAC code [10] for up to 6600 levels. There was essentially only one fit parameter required (related to the unknown neutral background gas density, which contributes to the charge exchange). The model includes the effects of electron-impact ionization, autoionization, radiative recombination, charge exchange, electron-impact excitation, and spontaneous decay. Neglected are three-body recombination and collisional de-excitation, appropriate to the case of EBIT in which the electron density is relatively low ( $< 10^{13} \text{ cm}^{-3}$ ). The ion number density is even lower than the electron density; the ratio of the two includes a factor containing the effective charge of the trapped ion cloud, the beam neutralization factor, and the square of the ion cloud to electron cloud diameters [11].

Our first observations of W in the x-ray regime were made using a micro calorimeter with a typical quantum efficiency of  $>90\%$  in the 2 Angstrom to 8 Angstrom range, and  $>10\%$  in the 0.6 Angstrom to 50 Angstrom range. The electron-ion collision energy was approximately 4 keV and most of the photons were detected between 3 Angstroms and 10 Angstroms, as shown in Fig. 2 (the lines marked with letters in this figure are identified in Table I of our original manuscript [2]). Our collisional radiative modeling shown in the lower half of this figure shows excellent agreement with the observations. A wide range of phenomena beyond the usual E1 transitions of the most loosely bound electrons is evident in

this figure, including core transitions (lines E and H, 3p-4d and 3p-4s with a closed 3d<sup>10</sup> shell, respectively), transitions between excited states (line N, 4p-6d), two-electron transitions (line O, 3d<sup>10</sup>4p-3d<sup>9</sup>4s<sup>2</sup>), and large effects due to a magnetic octupole transition (line M, 3d<sup>10</sup>-3d<sup>9</sup>4s, in part with  $\Delta J = 3$ ). This line was previously identified as an electric quadrupole line, but is according to our analysis a blend of a magnetic octupole and electric quadrupole line at nearly the same wavelength and intensity. The relatively weak lines L (3d-4s, E2 transition), N (as discussed above), and O (as discussed above) were never observed before, although this region of the spectrum was previously studied in a Tokamak [12].

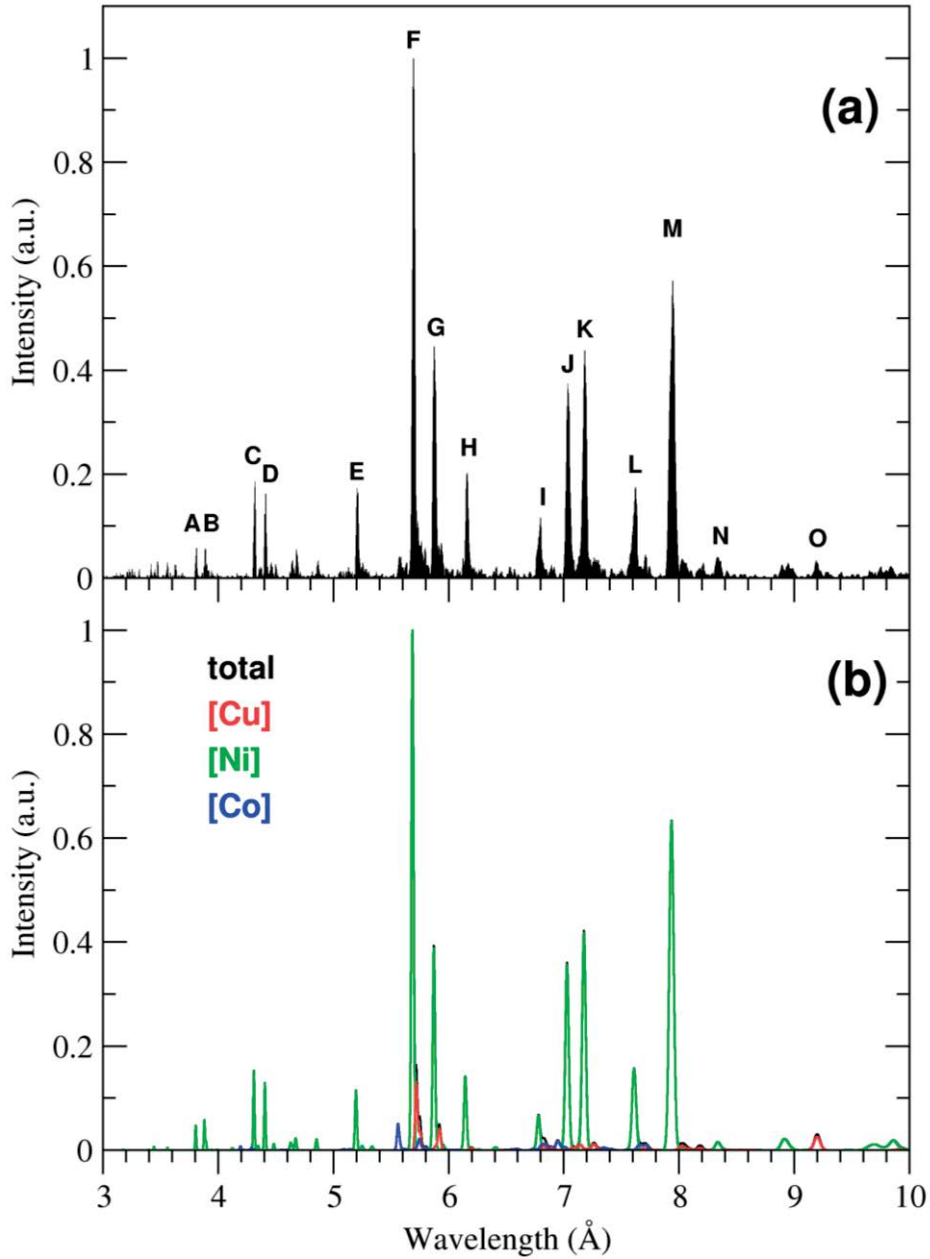


FIG. 2. X-ray spectra of W measured with a microcalorimeter (2a) and calculated (2b), at a nominal electron-ion collision energy of 4.08 keV. Contributions from the dominant charge states are color coded in 2b. The vertical axis is proportional to the number of detected photons. This figure originally appeared in reference [2].

TABLE 1. EUV LINES IDENTIFIED FOR THE TUNGSTEN IONS  $W^{54+}$  TO  $W^{63+}$ . THIS TABLE ORIGINALLY APPEARED IN REFERENCE [4]

Ion	Isoelectronic Sequence	Lower level	Upper level	Type	$\lambda_{\text{exp}}$ (nm)	$\lambda_{\text{th}}$ (nm)	$A$ ( $s^{-1}$ )
$W^{54+}$	Ca	$3d^2\ ^3F_2$	$3d^2\ ^3F_3$	M1	17.078(3)	17.1498	$3.86 \times 10^6$
		$3d^2\ ^3F_2$	$3d^2\ ^3P_2$	M1	14.961(3)	14.980	$1.81 \times 10^6$
$W^{55+}$	K	$3p^6 3d\ ^2D_{3/2}$	$3p^6 3d\ ^2D_{5/2}$	M1	15.961(3)	16.007	$2.60 \times 10^6$
		$3p^6 3d\ ^2D_{5/2}$	$3p^5 3d^2\ ^2G_{7/2}$	E1	6.622(3)	6.5873	$5.65 \times 10^6$
$W^{56+}$	Ar	$3p^5 3d\ ^3F_3$	$3p^5 3d\ ^3F_4$	M1	17.372(3)	17.453	$2.09 \times 10^6$
		$3p^5 3d\ ^3D_2$	$3p^5 3d\ ^1D_2$	M1	17.137(3)	17.189	$8.71 \times 10^5$
		$3p^5 3d\ ^3P_1$	$3p^5 3d\ ^1D_2$	M1	15.359(3)	15.358	$1.85 \times 10^6$
		$3p^5 3d\ ^3D_2$	$3p^5 3d\ ^3D_3$	M1	14.785(3)	14.787	$2.54 \times 10^6$
		$3p^5 3d\ ^3F_3$	$3p^5 3d\ ^3D_3$	M1	14.098(3)	14.087	$7.79 \times 10^5$
		$3p^6\ ^1S_0$	$3p^5 3d\ ^3P_1$	E1	4.931(2)	4.9279	$6.14 \times 10^9$
$W^{57+}$	Cl	$3p^4 3d\ ^2F_{7/2}$	$3p^4 3d\ ^4D_{7/2}$	M1	17.428(3)	17.530	$6.07 \times 10^5$
		$3p^4 3d\ ^2F_{7/2}$	$3p^4 3d\ ^4F_{9/2}$	M1	16.911(3)	16.996	$2.27 \times 10^6$
		$3p^4 3d\ ^4D_{5/2}$	$3p^4 3d\ ^4D_{7/2}$	M1	16.613(3)	16.669	$1.84 \times 10^6$
		$3p^5\ ^2P_{3/2}$	$3p^4 3d\ ^4D_{3/2}$	E1	5.254(2)	5.2558	$2.60 \times 10^9$
$W^{58+}$	S	$3p^5\ ^2P_{3/2}$	$3p^4 3d\ ^4D_{5/2}$	E1	5.121(2)	5.1209	$4.20 \times 10^9$
		$3p^3 3d\ ^3F_3$	$3p^3 3d\ ^3F_4$	M1	16.444(3)	16.466	$2.59 \times 10^6$
		$3p^4\ ^3P_2$	$3p^3 3d\ ^3D_2$	E1	5.280(2)	5.2841	$8.73 \times 10^9$
$W^{59+}$	P	$3p^4\ ^3P_2$	$3p^3 3d\ ^3F_3$	E1	5.086(2)	5.0912	$1.53 \times 10^9$
		$3s^2 3p^2 3d\ ^4F_{3/2}$	$3s^2 3p^3\ ^2D_{5/2}$	E1	10.042(3)	10.016	$6.24 \times 10^7$
		$3s^2 3p^3\ ^2D_{5/2}$	$3s 3p^4\ ^4P_{5/2}$	E1	7.607(3)	7.6260	$9.81 \times 10^9$
$W^{60+}$	Si	$3s^2 3p^3\ ^2P_{3/2}$	$3s^2 3p^2 3d\ ^4F_{3/2}$	E1	5.396(2)	5.4037	$1.24 \times 10^{10}$
		$3s^2 3p^2\ ^1D_2$	$3s 3p^3\ ^3P_2$	E1	7.648(3)	7.6660	$1.23 \times 10^{10}$
		$3s^2 3p^2\ ^3P_1$	$3s 3p^3\ ^3P_2$	E1	7.189(3)	7.2436	$1.54 \times 10^{10}$
$W^{61+}$	Al	$3s^2 3p^2\ ^2P_{1/2}$	$3s 3p^2\ ^4P_{1/2}$	E1	7.404(2)	7.3953	$3.88 \times 10^{10}$
		$3s 3p^2\ ^4P_{1/2}$	$3s^2 3p^2\ ^2P_{3/2}$	E1	6.318(3)	6.3246	$3.05 \times 10^8$
$W^{62+}$	Mg	$3s^2\ ^1S_0$	$3s 3p\ ^3P_1$	E1	7.991(2)	7.9904	$1.82 \times 10^{10}$
$W^{63+}$	Na	$3s\ ^2S_{1/2}$	$3p\ ^2P_{1/2}$	E1	7.769(2)	7.7617	$4.37 \times 10^{10}$

An example of the unusual atomic physics one encounters at the very high temperatures associated with fusion energy devices is provided by the discovered importance of forbidden radiative transitions between excited states for an accurate description of line intensities. These transitions are extremely weak in low-charge ions and therefore cannot

compete with collisional processes in practically any laboratory plasma. As the transition probabilities  $A$  for the forbidden lines are known to strongly depend on the ion charge  $Z$  ( $A \sim Z^6 - Z^{10}$ ), for high-charge states as those in Ni-like W, such transitions between the excited states become comparable with collision rates and can therefore alter the x-ray line ratios. For example, if the M1 transition rate between the  $J = 1$  and the lower  $J = 2$  level shown in Fig. 3 were zero, the M/L x-ray line ratio in figure 2 would be reduced by a factor of 2, due to both an increase in L and a decrease in M.

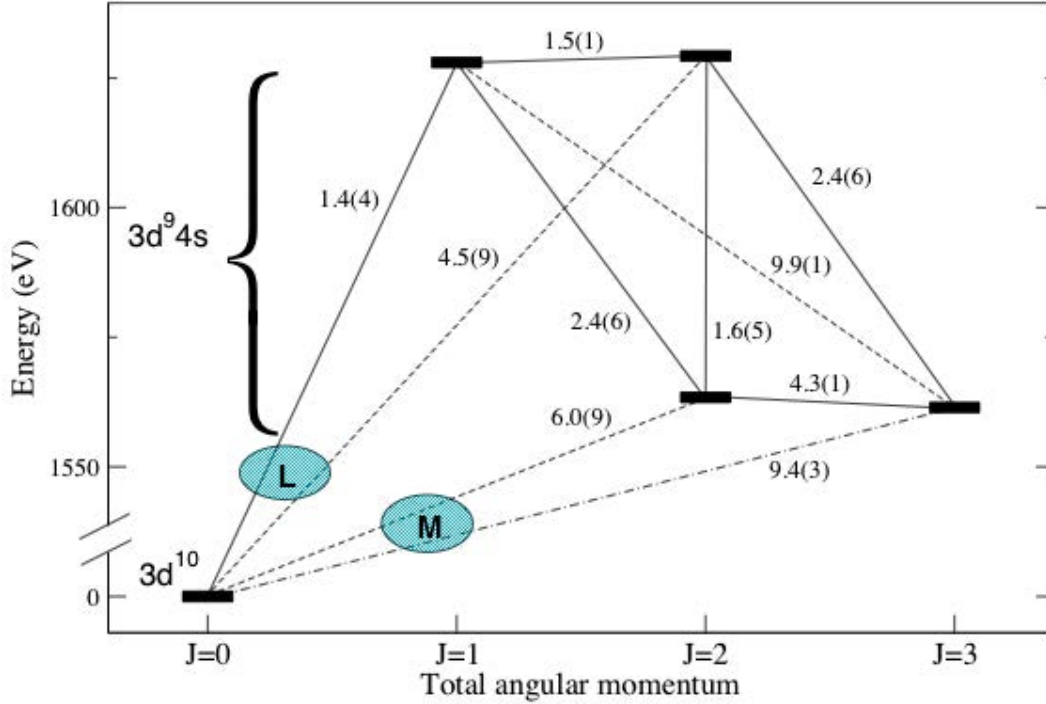


FIG. 3. Ground and first excited configurations of states in Ni-like W. Connecting lines indicate M1 (solid), E2 (dashed) and M3 (dot-dashed) transitions. There are no E1 transitions to the ground state from the first excited configuration. Transition probabilities (in  $s^{-1}$ ) are given next to the corresponding lines, using the notation  $a(b)$  for  $a \times 10^b$ . The labels L and M correspond to the unresolved pairs of lines labeled in Fig. 2. This figure is a modified version of the one that originally appeared in Ref. [2].

In 2007, we extended our observations of W into the EUV spectral range from 4 to 20 nm as shown in Fig. 4. The initial observations were done with a Zr filter in place to block light above 250 nm and to isolate the vacuum of the EBIT from that of the spectrometer. The filter also contributed significantly to the reduction in sensitivity of the spectrometer below 7 nm (red curve in Fig. 4). Over the course of two experimental runs, spectra were recorded at 12 additional electron beam energies, which extended up to 4228 eV. Plots of all these spectra are shown in Ref. [3]. We concentrated our analysis in the long wavelength half of the spectrum, as the (4–8.5) nm range was well covered previously by the LLNL EBIT group [13] and the Berlin EBIT and Garching ASDEX Upgrade groups [14]. Tokamak data are available for comparison in Ref. [12]. Our paper [3] contains eight new identifications of E1 and M1 lines in the (12–20) nm range, and shows predicted spectra in comparison to our measurements at 2169 eV, 2429 eV, 2885 eV, and 4228 eV. In these series of measurements, the charge states observed were 39+ to 47+.

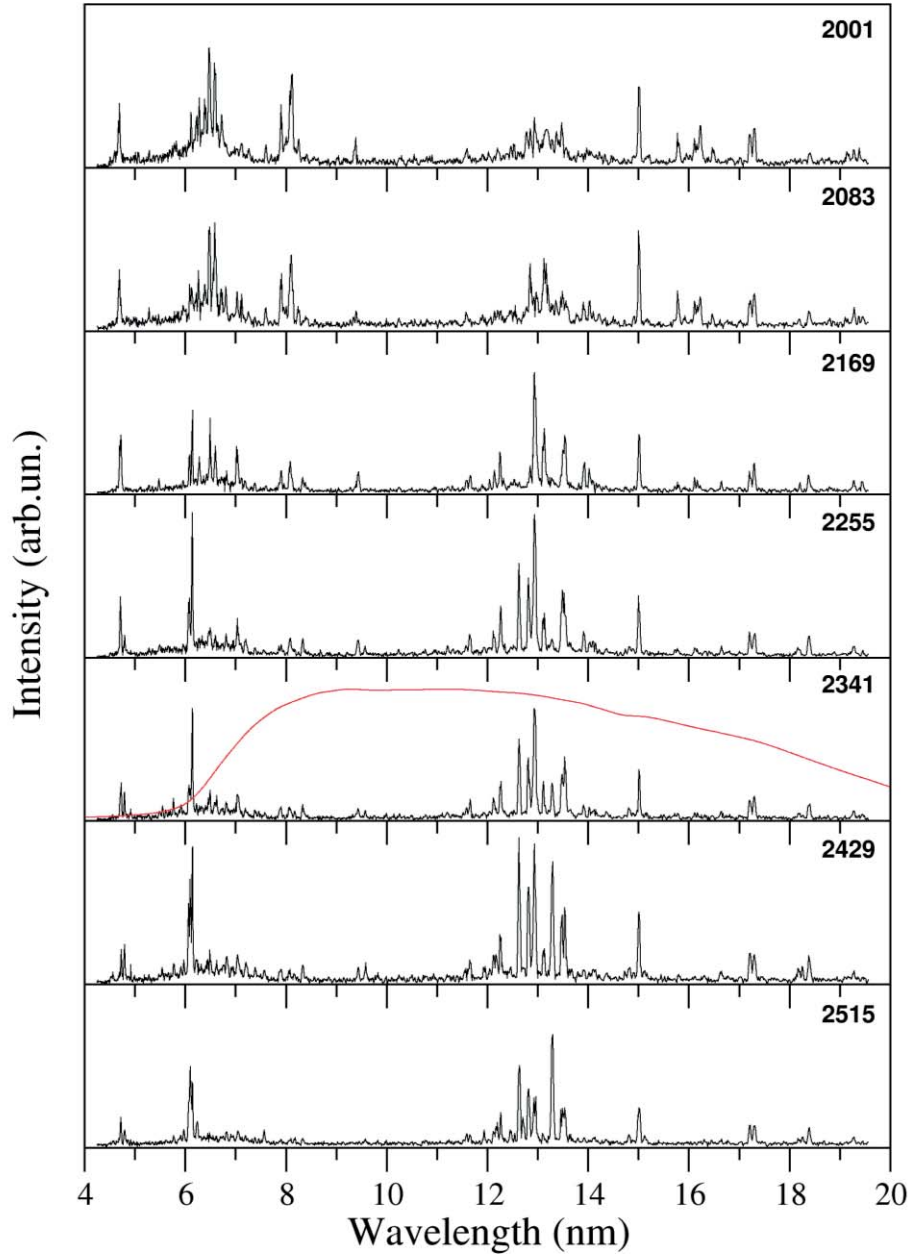


FIG. 4. EUV spectra of W, observed through a Zr filter, as a function of the electron beam energy (eV) indicated in upper right. The red curve is a calculation of the efficiency of the spectrometer, detector, and filter transmission. The vertical axis is proportional to the energy detected per unit bandwidth. This figure originally appeared in Ref. [3].

In subsequent experiments, the Zr filter was removed and observations were made directly into the EBIT. This increased the signal strength of the lines observed at both ends of the initial (4–20) nm spectral range, and opened the possibility of later extending the spectral range to even shorter wavelengths, as described below. Additionally, we increased the electron beam energy to study charge states up to 63+. A series of such measurements, spanning beam energies from 8.8 keV to 25 keV ( $E/k = 100$ –290 million K collision temperature), is shown in Fig. 5. The ion temperature is  $<15$  keV ( $E/k = 180$  million K) due to the finite trap depth and the action of evaporative cooling. Spectra were also recorded for several elements above and below W in the isoelectronic sequence to aid in the analysis. Shifts in the prominent Na-like (number of electrons  $N = 11$ ), Mg-like ( $N = 12$ ), and Al-like ( $N = 13$ ) lines in Hf (nuclear charge  $Z = 72$ ), Ta ( $Z = 73$ ), W ( $Z = 74$ ), and Au ( $Z = 79$ ) are

seen in the spectra shown in Fig. 6, and the isoelectronic dependence of the wave-numbers on core charge is plotted in Fig. 7. The associated scaling coefficients presented in our publication [4] can be used to predict the wavelengths of these strong lines in other elements. Detailed comparisons of the full (4–20) nm W spectrum to model predictions at a beam energy of 8.8 keV are also given in that paper [4]. The principal lines of the Na-like, Mg-like, and Al-like ions are sufficiently widely spaced that they should be easily resolved in fusion reactors, yet sufficiently close that their ratios will be relatively insensitive to spectrometer efficiency variations; hence they may be particularly well-suited for use as a temperature diagnostic.

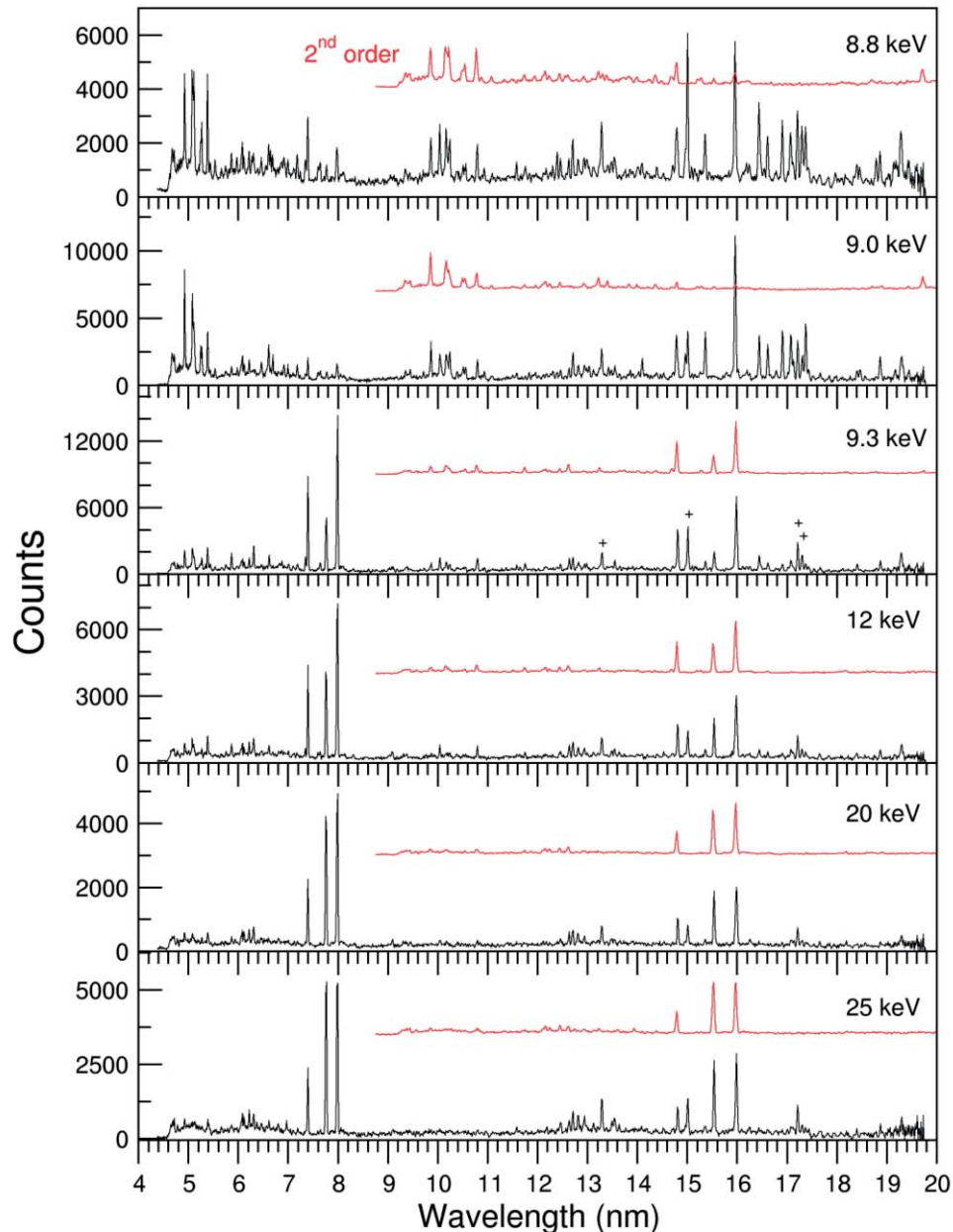


FIG. 5. Tungsten spectra, observed with Zr filter removed, and beam energy increased. The counts on the vertical axis are proportional to the energy observed per unit bandwidth. This figure originally appeared in Ref. [4].

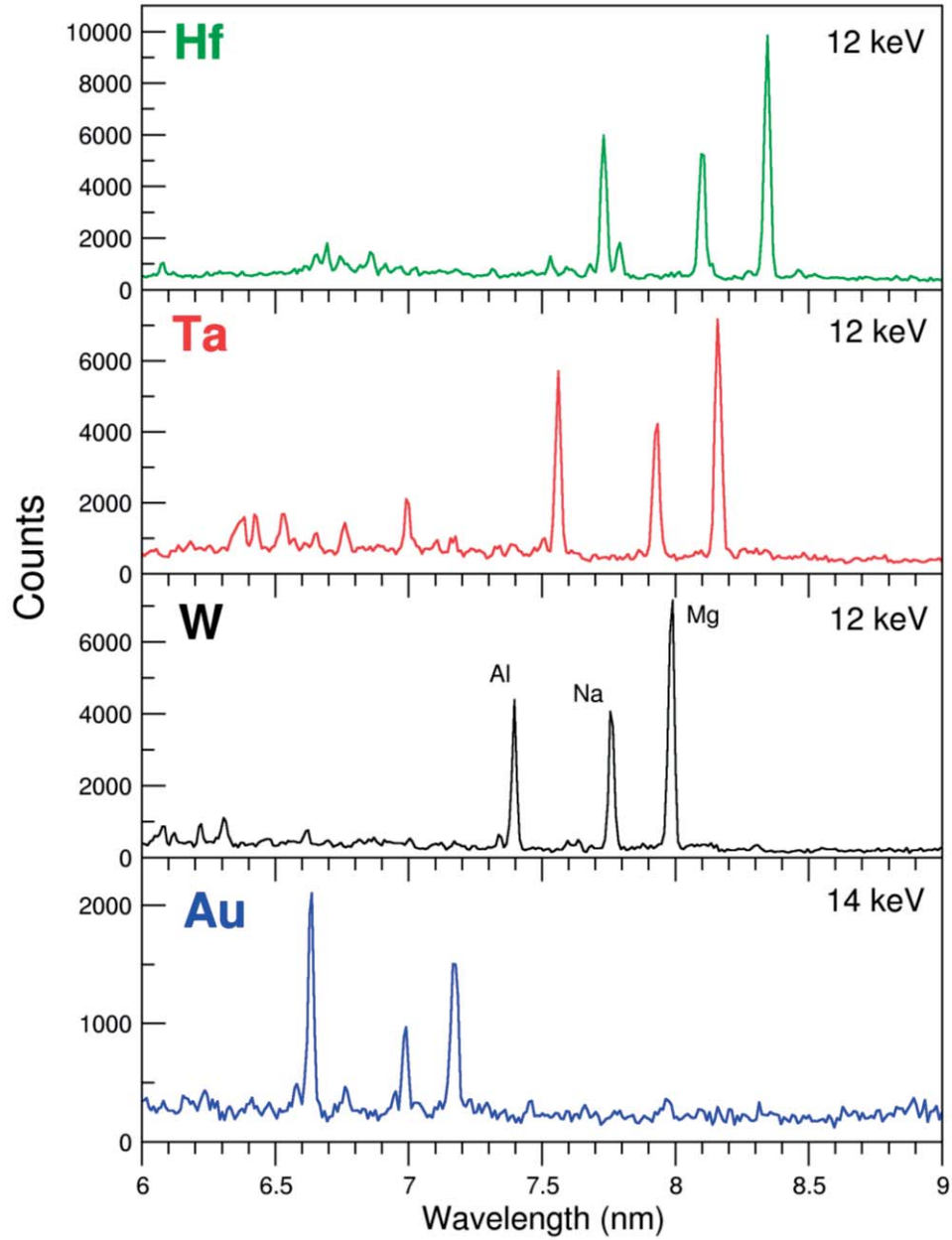


FIG. 6. Spectra of Hf, Ta, W and Au in the 6nm to 9nm wavelength range, for electron-impact energies of approximately  $2.2Z^2$  eV. The isoelectronic trend to shorter wavelengths with increasing  $Z$  is seen in the prominent  $3s_{1/2}$ - $3p_{1/2}$  transitions in Al-like, Na-like and Mg-like ions indicated (see also Fig. 7). The counts on the vertical axis are proportional to the energy observed per unit bandwidth. This figure originally appeared in Ref. [4].

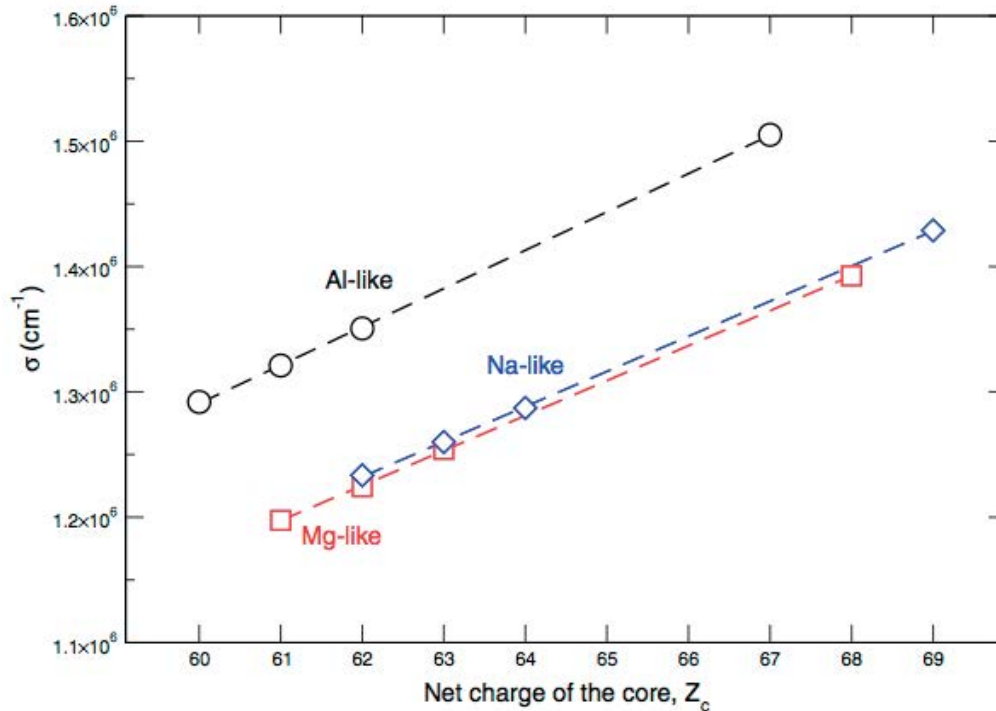


FIG. 7. Isoelectronic variation of the three strong lines in Fig. 6. This figure originally appeared in Ref. [4].

In the Na-like spectra discussed above and shown in Fig. 6, the very strong  $3s_{1/2} - 3p_{1/2}$  component of the principal doublet is visible but the  $3s_{1/2} - 3p_{3/2}$  component is shifted to a wavelength too short for us to observe in the initial experiment. In neutral sodium, the splitting of these two lines is only one part in a thousand and the intensity ratio is 2:1 (with the shorter wavelength line being the stronger of the two), while in Na-like W, the relative splitting is predicted to be larger than unity, and the intensity ratio is predicted to increase to 5:1 (largely due to the fact that intensity is defined as energy radiated per unit time and each of the shorter wavelength photons carries much more energy than the longer wavelength photons). The physical origin of the huge splitting is that the effective nuclear charge in Na-like W is so large that the outer electron is orbiting the nucleus at an appreciable fraction of the speed of light. Relativistic fine structure effects are thus very large. This is another illustration of how unusual atomic spectra can be at high charge states, compared to those of their neutral atom counterparts. We were eventually able to observe both components of the doublet in one spectrum, as described in the next paragraph.

In 2008, we shifted the spectral range of our grazing incidence spectrometer by translating the detector in the focal plane. This enabled us to observe spectra at wavelengths more than a factor of two shorter than previously possible with this instrument. We recorded data analogous to that shown in Fig. 6, but extending down to and including the other half of the Na-like doublet for each of the 4 species, including  $\text{Au}^{68+}$  at 1.8 nm. The Au data were initially recorded at 14 keV as in Fig. 6, but analysis of the region of the spectrum near the short wavelength component of the doublet revealed a strong line blend with other charge states, so the Au data were retaken at a much higher beam energy (24 keV) to purify the spectrum and allow a reliable extraction of the wavelengths. The enhancement of the Na-like charge state in the Au spectra was clearly evident in the long wavelength component of the doublet, which is fully resolved from the Mg-like and other nearby charge states. Because the Na-like charge states are quasi-hydrogenic (one electron in the  $n = 3$  shell, with closed  $n = 1$  and  $n = 2$  shells screening the nucleus), predictions of the low-lying transitions have been the subject of several very extensive *ab initio* calculations [15,16]. Our results [5] are in excellent agreement with those of Blundell [16]. These results were first presented at the 16th APiP Conference and the 2009 APS April Meeting.

An example of one of our EUV spectral data tables, published in 2008, is given in Table I. A table listing a similar number of lines in lower charge states was published by us in 2007 [3]. A table with an additional 15 lines in the x-ray regime was published in 2006 [2]. Earlier results of our work presented at the conferences noted above, as well as at the 2008 APS DAMOP conference and the 2008 International Conference on Highly Charged Ions, and presently being prepared for independent publication, include more than 100 new EUV line identifications in W, Hf, Ta, and Au.

Detailed in several publications are other results reported by us during the 2005-2009 period on Ni x-ray spectra [17], Xe EUV spectra [18,19], Xe visible spectra [20], Kr, Ar, and Ne charge exchange x-ray spectra [21,22], and Xe photoionization cross sections [23]. Also discussed elsewhere is our concurrent work on the damage that highly charged ions cause to materials [24, 25], which is of interest to fusion research, too.

### 3. CALCULATIONS OF ELECTRON-IMPACT IONIZATION AND EXCITATION CROSS SECTIONS

#### 3.1. Introduction

Earlier work on excitation and ionization cross sections by Y.-K. Kim and colleagues [26, 27] included calculations for He, Li, Be, C, N, O, Na, Mg, Al, K, Ca, Ga, Rb, Sr, In, Cs, Ba, Hg, Pb, and Tl. These calculations used the Binary-Encounter-Bethe (BEB) approximation [26] of Kim and Rudd for ionization and the scaled Plane Wave Born (PWB) approximation of Kim for excitation. This work was continued by us with similar calculations for other heavy atoms and ions, including work summarized here for Cl, Br, I, Si, Ge, Sn, Pb, Ar, Mo, Mo<sup>+</sup>, W, and W<sup>+</sup>.

#### 3.2. Ionization

The BEB approximation for ionization requires only the binding energies and kinetic energies of the target atomic orbital. For the lowest binding energies, experimental vertical ionization potentials are used to make the ionization threshold energy agree with the experimentally determined values. The approximation does not use any parameters that are adjusted or selected to fit measurements and does not use any description of the continuum wavefunctions. Therefore, once the atomic orbitals are determined, the cross sections can be calculated rapidly and the result is not arbitrary. This makes the approximation useful for computer modeling of gases and plasmas where many cross sections are needed for many levels.

The ionization cross-section formula is

$$\sigma_{BEB} = \frac{S}{t + (u + 1)/m} \left[ \frac{\ln t}{2} \left( 1 - \frac{1}{t^2} \right) + 1 - \frac{1}{t} - \frac{\ln t}{t + 1} \right] \quad (1)$$

where  $t = T/B$ ,  $u = U/B$ ,  $S = 4\pi a_0^2 N R^2 / B^2$ ,  $a_0$  is the Bohr radius,  $R$  is the Rydberg energy,  $B$ ,  $U$ , and  $N$  are the binding energy, the kinetic energy, and the occupation number respectively for the atomic orbital. The constant  $m$  is the principal quantum number  $n$  for orbitals when  $n > 2$ , and  $m = 1$  for orbitals  $n = 1$  and  $2$ . The formula is calculated for each orbital of the target atom and the total cross-section is the sum of the values over all the orbitals.

#### Cl, Br, and I

We published results for chlorine [27] in 2005. Our BEB results agree well with experimental measurements [28]. Calculations for Br [29] gave results in agreement within the measurement uncertainty estimates of  $\pm 11\%$  and good agreement for I [29] at the

threshold energy up to and including the peak of the cross-section. Beyond the peak, the calculated cross sections are somewhat lower than measurements.

### Si, Ge, Sn and Pb

We completed calculations of cross sections for these carbon-like elements of the IV A column of the periodic table in 2007 [30]. It is clear that autoionization is important in these elements and must be included to obtain accurate total ionization cross sections. In these calculations, we included excitation to the autoionizing levels by the scaled PWB approximation. The calculated ionization cross sections are in good agreement with experimental measurements. An example of the results is shown in Fig. 8.

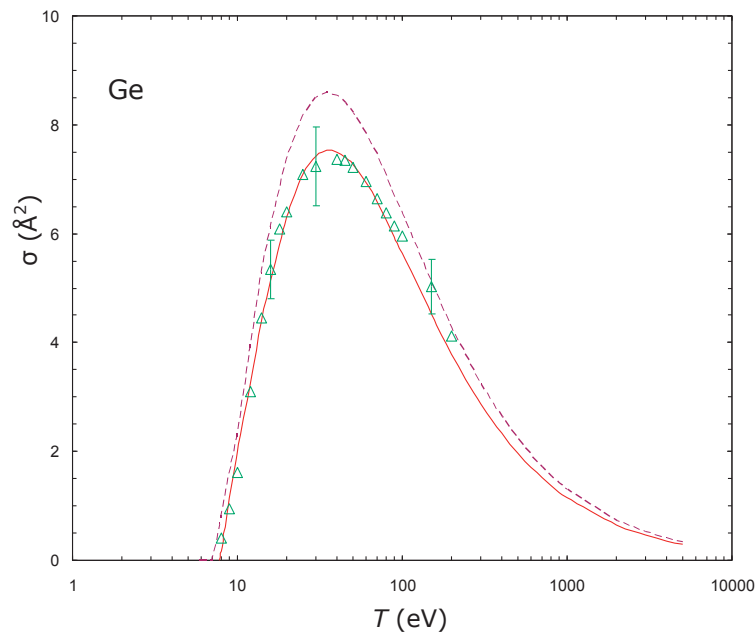


FIG. 8. Ionization cross-section for the  $^3P_2$  level (solid line) of the ground term and the  $^1D_2$  level (dotted line) of germanium. The measurements of Freund et al. [31] are shown (triangles) for comparison. The calculated values include autoionization. The  $^3P_2$  calculated values agree well with the measurements. The  $^3P_0$  and  $^3P_1$  ground terms cross sections differ noticeably from the  $^3P_2$  and do not agree as well with the measurements, especially in the peak and high energy regions.

The rather good agreement with experimental measurements for these elements emphasizes that 1) autoionization must be included and 2) that the measurements of Freund et al. [31] were done with most of the target atoms in the  $^3P_2$  level of the ground term. The agreement with experiment is not as good for Pb as shown here for Ge although the results are within the rather large uncertainty limits of the measurements.

### Mo, Mo<sup>+</sup>, W and W<sup>+</sup>

We calculated cross sections for Mo and Mo<sup>+</sup> ionization in 2005 [32]. These targets have many metastable levels near the ground level and numerous upper levels that are excited and autoionize in the electron-impact collision. Excitation to the autoionizing levels has been calculated in the scaled PWB approximation. Calculation of hundreds of autoionizing levels were done by a multiconfiguration Dirac-Fock computer code and only those levels that have excitation oscillator strengths calculated to be larger than 0.05 were included in the autoionization process. For the ground state Mo, the indirect autoionization processes

contribute only about 5%, while for metastable Mo indirect processes contribute about 30%. For  $\text{Mo}^+$  indirect processes contribute less than 15%. There are no measurements for Mo with which to compare. The total cross-section for  $\text{Mo}^+$  is in good agreement with two sets of measurements available in the literature.

Cross sections for W and  $\text{W}^+$  were calculated next [33]. The calculations were done in the same way as described for Mo and  $\text{Mo}^+$ . Single ionization cross sections for  $\text{W}^+$  are increased by about 10% by autoionization of 5p electron levels, while autoionization is very small for the first metastable term of W ( $^7\text{S}_3$ ) but can be as large as 25% for the second metastable term ( $^3\text{P}$ ).

The situation is complicated because of the many levels involved and reference to the publications is necessary to understand the results. There are many figures showing the calculated values. Comparison with measurements is shown here in Fig.9 for  $\text{W}^+$  as an example.

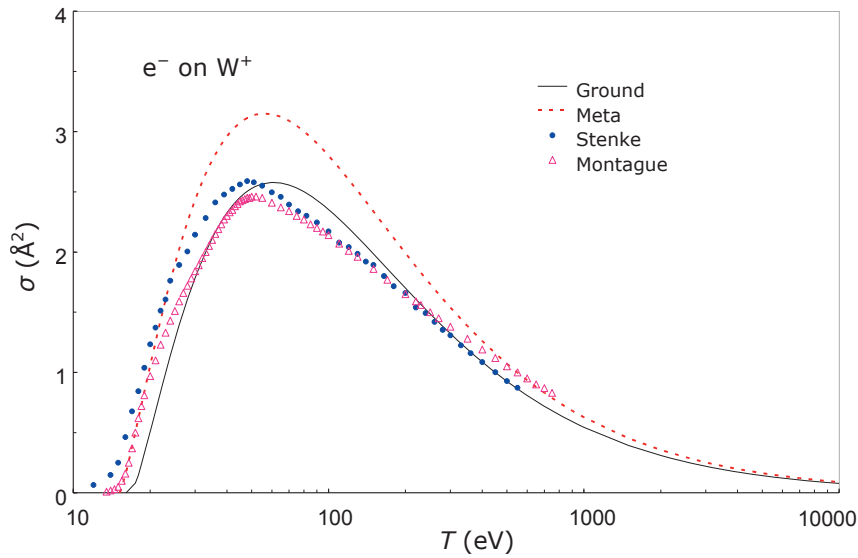


FIG. 9. Direct single ionization cross sections of  $\text{W}^+$ . Ionization of the ground level  $^6\text{D}_{1/2}$  (solid curve) and the metastable level  $^6\text{S}_{5/2}$  (dotted curve). The measurements of Montague and Harrison [34] (open triangles) and Stenke et al. [35] (solid circles) are shown for comparison.

### 3.3. Excitation

Current work includes calculation of excitation cross sections for neutral argon from the two  $3\text{p}^54\text{s}$  metastable levels ( $1\text{s}_3$  and  $1\text{s}_5$  in Paschen notation) to the  $3\text{p}^55\text{p}$  levels ( $3\text{p}_1$ – $3\text{p}_{10}$  in Paschen notation). The scaled PWB approximation for excitation modifies the PWB cross-section as follows:

$$\sigma_{\text{Excitation}} = \sigma_{\text{PWB}} \left( \frac{T}{T + B + E} \right) \quad (2)$$

where  $B$  is the binding energy for the target orbital,  $E$  is the excitation energy and  $T$  is the incident electron energy.

Measurements have been reported recently [36] of these excitation cross sections. We used  $jj$  coupling in a single configuration Dirac-Fock calculation to describe the target wavefunctions. The work has been completed and published in 2010 (see Note Added in Proofs). Preliminary results were presented at the Gaseous Electronics Conference in October, 2007.

When the value of  $j$  for the core remains unchanged in the excitation ( $1s_3-3p_2$  and  $3p_4$ ,  $1s_5-3p_6$ ,  $3p_7$ ,  $3p_8$ ,  $3p_9$  and  $3p_{10}$ ), our cross sections agree well with the measurements. When the core  $j$ -value changes ( $1s_3-3p_7$  and  $1s_3-3p_{10}$ ) our cross sections do not agree as well with the measurements. This same behavior has been seen in recent relativistic distorted wave calculations [37]. An example of the results is shown in Fig. 10.

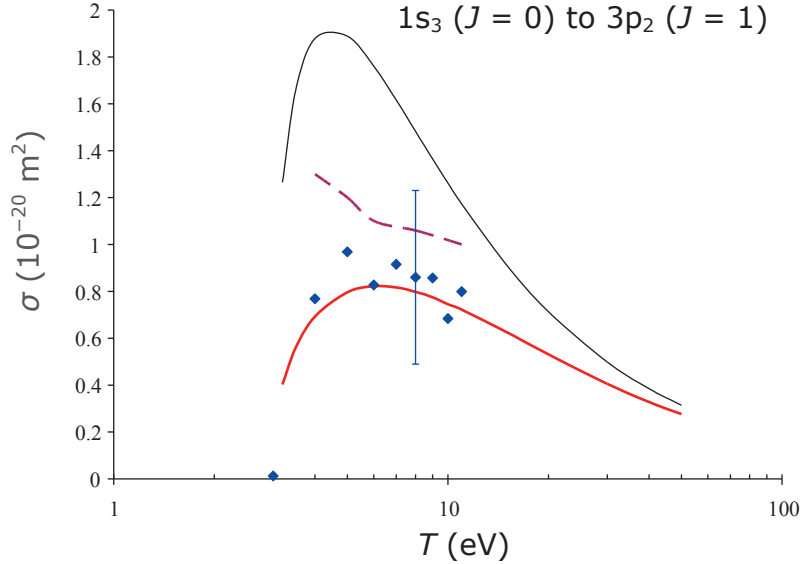


FIG. 10. Argon excitation cross-section from the  $1s_3$  metastable level to the  $3p_2$  excited level. The thick solid line is the scaled PWB calculation, the narrow line is the PWB approximation, and the dashed line is the relativistic distorted wave calculation of Sharma et al. [37]. Solid diamonds are the measurements of Jung et al. [36]. The measurement uncertainty at 8 eV includes both the statistical uncertainty and the  $\pm 40\%$  systematic uncertainty quoted by the authors.

Ongoing work includes calculations of ionization cross sections for Au, Cu and Ag, and excitation cross sections of Kr, Xe and Au.

## 4. CRITICAL COMPILATIONS

### 4.1. Transition Probabilities

We have critically evaluated and compiled atomic transition probabilities of aluminum (nuclear charge  $Z = 13$ ) [38] and silicon ( $Z = 14$ ) [39] for spectral lines of all stages of ionization. In total, these comprehensive compilations contain data for about 5000 lines in the various spectra of aluminum and 5800 lines of silicon. The cited values and their estimated uncertainties are based on the evaluation of all available theoretical and experimental literature sources. The data are presented in separate tables for the two neutral atoms and all ions. Furthermore, the allowed (i.e., electric dipole) and forbidden (magnetic dipole, and electric and magnetic quadrupole) transitions are listed in separate tables. For each spectrum, the lines are grouped into multiplets, which are arranged in order of ascending lower and upper energy levels. For each transition, the transition probability for spontaneous emission, the line strength and the absorption oscillator strength are given, and its spectroscopic designation, wavelength, statistical weights and energy levels of the lower and upper atomic states are listed. Also, the literature sources are cited. Only spectral lines with sufficiently accurate transition probabilities have been included, since these tables are considered as tables of reference data.

Analogous comprehensive tables of transition probabilities are published for sulfur [40], and a significant progress has been made in the work on argon [41] and chlorine [42]. For some ions of chlorine, the existing material on atomic energy levels was found to be widely scattered in the literature and had to be critically evaluated and compiled, too.

A new, expanded tabulation of the transition probabilities for allowed and forbidden lines of Fe I and Fe II was carried out [43] after recent experimental and theoretical results changed and improved the data situation drastically for these two spectra. For more than 1000 transitions of Fe I, the uncertainties are now estimated to be smaller than 10%, up from about 200 lines in the earlier 1988 NIST compilation [44]. For Fe II, the body of data could be increased by 42%.

We also compiled the transition probabilities for dipole-allowed lines of neutral and singly ionized tungsten [45]. In this compilation, the  $A$ -values are given for 522 transitions of W I and 211 transitions of W II. About half of the  $A$ -values for W I and all  $A$ -values for W II have uncertainties estimated to be below 10%. In a recent compilation on the higher ionization stages of tungsten by the same authors [46], experimental  $A$ -values are given for 37 transitions of W III.

## **4.2. Energy Levels and Wavelengths**

### **4.2.1. Tungsten**

Tungsten is a principal candidate as the material for the plasma-facing components of the divertor region of the ITER device. Therefore, the properties of this element are of intense interest for magnetic fusion devices, and this has prompted an urgent need for atomic spectroscopic data on atomic and ionized tungsten. The NIST Atomic Spectroscopy Group responded to this need with a series of extensive research projects devoted to critical compilation of the relevant atomic data. The first result of those projects was a critical compilation of wavelengths, energy levels, and transition probabilities for W I and W II [45]. In this work, energy level values are given for 509 levels of W I and 264 levels of W II, and wavelengths and energy level assignments are given for 7049 lines of W I and 2838 lines of W II. As noted in the previous section, a significant number of those lines are supplemented with transition probability values. The subsequent work on the higher ionization stages of tungsten by the same authors [46] provides a comprehensive account of all known energy levels and spectral lines for W III through W LXXIV. A separate investigation [47] was devoted to ionization energies of tungsten in all stages of ionization. In this work, an accurate semi-empirical method was used to obtain the ionization energies using, as reference points, known values for a few ionization stages of tungsten and several neighboring chemical elements. The graph below i.e., Fig.11 illustrates the amount of spectroscopic data available for various stages of ionization of tungsten.

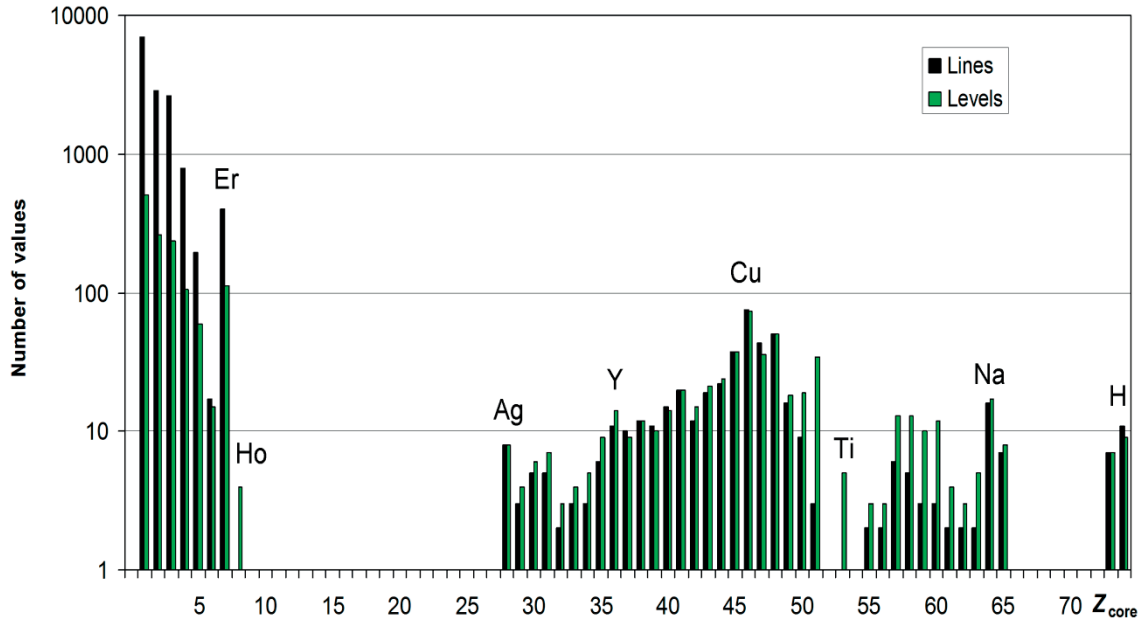


FIG. 11. The number of known spectral lines and energy levels per ionization stage of tungsten, included in compilation [46]. The element symbols on the graph represent the isoelectronic sequences.

It is seen from this graph that there remain large intervals of ionization stages, such as IX through XXVI (Dy-like through Cd-like) and LXVI through LXXII (F-like through Li-like), for which nothing is known except for the ionization energies. For several ionization stages, such as W VIII, IX, XII, XIII (Ho-like, Dy-like, Eu-like, Sm-like), even the ground state assignment (and hence, the ionization energy) is uncertain, because different electronic shells compete for the lowest energy, making calculations difficult. However, the ionization stages that are most important for the diagnostics of tokamak plasmas are studied fairly well. In particular, neutral and moderately-ionized tungsten, important for the diagnostics of the plasma edge regions of tokamaks, have been investigated in great detail. For these spectra, several thousands of spectral lines and several hundreds of energy levels are identified and well-measured. The highly charged ions W XVIII through W LXV (Ag-like through Ne-like), having ionization energies 0.9–16 keV, are important for the diagnostics of the high-temperature core plasma regions of tokamaks, and their spectra are also studied fairly well. For these stages of ionization, a significant amount of spectroscopic data included in our compilation [46] was obtained at NIST with the Electron Beam Ion Trap (EBIT) [3, 4], where the spectra W XL through W XLVIII (Br-like through Co-like) and W LV through W LXIV (Ca-like through Na-like) were studied and analyzed. The successful identification of the EBIT spectra was accomplished with new plasma-kinetics modeling techniques developed at NIST [2, 48, 49].

#### 4.2.2. Heavy Noble Gases

The energy levels and observed spectral lines of xenon, in all stages of ionization for which experimental data were available through December 2002, have been compiled and published [50]. Sufficient data were found to generate level and line tables for Xe I through Xe XI, Xe XIX, Xe XXV through Xe XXIX, Xe XLIII through Xe XLV, and Xe LI through Xe LIV. For Xe LIII and Xe LIV theoretical values are compiled for the energy levels. In 15 of the other stages a few lines are reported. Experimental  $g$ -factors are included for Xe I, Xe II, and Xe III. A numerical value, either experimental, semi-empirical, or theoretical, is included for the ionization energy of each ion. Table 2 lists the number of line classifications for each stage of ionization for xenon. It is seen that for many intermediate stages of ionization, the data are either very sparse or not available at all.

TABLE 2. XENON CLASSIFICATIONS

Ionization Stage	Number of line Classifications	Ionization Stage	Number of line Classifications
Xe I	1134	Xe XXVIII	3
Xe II	1117	Xe XXIX	17
Xe III	852	Xe XXX	0
Xe IV	445	Xe XXXI	0
Xe V	273	Xe XXXII	0
Xe VI	126	Xe XXXIII	0
Xe VII	132	Xe XXXIV	0
Xe VIII	135	Xe XXXV	0
Xe IX	144	Xe XXXVI	0
Xe X	83	Xe XXXVII	0
Xe XI	208	Xe XXXVIII	0
Xe XII	0	Xe XXXIX	0
Xe XIII	0	Xe XL	0
Xe XIV	0	Xe XLI	0
Xe XV	0	Xe XLII	0
Xe XVI	0	Xe XLIII	3
Xe XVII	0	Xe XLIV	4
Xe XVIII	3	Xe XLV	25
Xe XIX	2	Xe XLVI	0
Xe XX	0	Xe XLVII	0
Xe XXI	0	Xe XLVIII	0
Xe XXII	0	Xe XLIX	0
Xe XXIII	0	Xe L	0
Xe XXIV	0	Xe LI	11
Xe XXV	12	Xe LII	8
Xe XXVI	18	Xe LIII	5
Xe XXVII	11	Xe LIV	2

The energy levels and observed spectral lines of krypton, in all stages of ionization for which experimental data were available through December 2003, have been compiled and published [51]. Sufficient data were found to generate level and line tables for Kr I through Kr X and Kr XVIII through Kr XXXVI. For Kr XXXV and Kr XXXVI and most of Kr XXXIV theoretical values are compiled for the energy levels. In all of the other stages a few lines, some of which may be only tentative classifications, are reported. Table 3 lists the number of line classifications for each stage of ionization for krypton.

TABLE 3. KRYPTON CLASSIFICATIONS

Ionization Stage	Number of line Classifications	Ionization Stage	Number of line Classifications
Kr I	860	Kr XIX	2
Kr II	1178	Kr XX	4
Kr III	877	Kr XXI	6
Kr IV	485	Kr XXII	7
Kr V	174	Kr XXIII	24
Kr VI	142	Kr XXIV	14
Kr VII	73	Kr XXV	50
Kr VIII	177	Kr XXVI	71
Kr IX	26	Kr XXVII	62
Kr X	43	Kr XXVIII	69
Kr XI	0	Kr XXIX	16
Kr XII	0	Kr XXX	10
Kr XIII	0	Kr XXXI	11
Kr XIV	0	Kr XXXII	10
Kr XV	0	Kr XXXIII	12
Kr XVI	0	Kr XXXIV	60
Kr XVII	0	Kr XXXV	110
Kr XVIII	12	Kr XXXVI	21

Note that due to limited resolution, an observed line may be due to more than one possible transition. Atomic model calculations are used to remove very weak transitions but in many cases more than one possibility remains and is included in the tables.

A compilation of the energy levels and observed spectral lines of all the ionized stages of argon was published (see note Added in Proofs).

## 5. SUMMARY

Research on the spectra and structure of heavy elements by the Atomic Spectroscopy Group of NIST has produced considerable advances during the last 5 years. With an EBIT, we have observed the spectra of highly charged ions of tungsten in the range from  $W^{54+}$  to  $W^{63+}$ , and we analyzed their structure and identified the principal transitions with modeling codes utilizing isoelectronic trends. Also, we carried out comprehensive critical compilations of spectral data – energy levels, wavelengths and transition probabilities – for all spectra of tungsten as well as several other heavy elements of fusion interest, specifically Al, Si, S, Ar, Cl, Fe, Kr and Xe. Calculations of ionization and excitation cross sections were carried out for some W, Mo and noble gas ions with the BEB method, and good agreement with experiments was obtained.

Note Added in Proofs

This work was presented at an IAEA meeting in 2009 and prepared for publication shortly thereafter. Since that time, much more work has been done in the areas discussed, and several studies referred to as "underway" or "to be published" have been completed and published. In particular, the work on collisional excitation of Ar described in section 3.3 was published in 2010; see Ali, M.A., Stone, P. M., *Int. J. Mass Spectrom.*, **294** (2010) 59. A critical compilation of argon spectral data mentioned in the end of section 4.2.2 was also published; see Saloman, E.B., *J. Phys. Chem. Ref. Data* **39** (2010) 033101. The ongoing work on critical compilation of transition probabilities in argon [41] and chlorine [42] spectra, mentioned in

section 4.1, is going to be continued by other authors, since D.E. Kelleher has died in March 2017, and L.I. Podobedova is no longer associated with the Atomic Spectroscopy Group at NIST.

## ACKNOWLEDGEMENTS

This work was partially supported by the Office of Fusion Energy Sciences, U.S. Department of Energy.

## REFERENCES

- [1] GILLASPY, J.D., EBIT spectra of highly stripped ions from the visible to the x-ray, *Phys. Scr.* **T65** (1996) 168.
- [2] RALCHENKO, YU., TAN, J.N., GILLASPY, J.D., POMEROY, J.M., SILVER, E., Accurate modeling of benchmark x-ray spectra from highly charged ions of tungsten, *Phys. Rev. A* **74** (2006) 042514.
- [3] RALCHENKO, YU., READER, J., POMEROY, J.M., TAN, J. N., GILLASPY, J.D., Spectra of  $W^{39+}$ – $W^{47+}$  in the 12–20 nm region observed with an EBIT light source, *J. Phys. B* **40** (2007) 3861.
- [4] RALCHENKO, YU., DRAGANIC, I.N., TAN, J.N., GILLASPY, J.D., POMEROY, J.M., READER, J., FELDMAN, U., HOLLAND, G.E., EUV spectra of highly-charged ions  $W^{54+}$ – $W^{63+}$  relevant to ITER diagnostics, *J. Phys. B* **41** (2008) 021003.
- [5] GILLASPY, J.D., DRAGANIĆ, I.N., RALCHENKO, YU., READER, J., TAN, J.N., POMEROY, J.M., BREWER, S.M., Measurement of the *D*-line doublet in high-*Z* highly charged sodiumlike ions, *Phys. Rev. A* **80** (2009) 010501(R).
- [6] BLAGOJEVIĆ, B., LE BIGOT, E.-O., FAHY, K., AGUILAR, A., MAKONYI, K., TAKÁCS, E., TAN, J.N., POMEROY, J.M., BURNETT, J.H., GILLASPY, J.D., ROBERTS, J.R., A high efficiency ultrahigh vacuum compatible flat field spectrometer for extreme ultraviolet wavelengths, *Rev. Sci. Instrum.* **76** (2005) 083102.
- [7] TAN, J.N., SILVER, E., POMEROY, J., LAMING, J.M., GILLASPY, J., An electron beam ion trap (EBIT) plus a microcalorimeter: a good combination for laboratory astrophysics, *Phys. Scr.* **T119** (2005) 30.
- [8] HOLLAND, G.E., BOYER, C.N., SEELY, J.F., TAN, J.N., POMEROY, J.M., GILLASPY, J.D., Low jitter metal vapor vacuum arc ion source for electron beam ion trap injections, *Rev. Sci. Instrum.* **76** (2005) 073304.
- [9] RALCHENKO, YU., MARON, Y., Accelerated recombination due to resonant deexcitation of metastable states, *J. Quant. Spectrosc. Radiat. Transfer* **71** (2001) 609.
- [10] GU, M.F., The flexible atomic code, *Can. J. Phys.* **86** (2008) 675.
- [11] PORTO, J.V., KINK, I., GILLASPY, J.D., Direct imaging of highly charged ions in an electron beam ion trap, *Rev. Sci. Instrum.* **71** (2000) 3050.
- [12] NEU, R., FOURNIER, K.B., SCHLÖGL, D., RICE, J., Observations of x-ray spectra from highly charged tungsten ions in tokamak plasmas, *J. Phys. B* **30** (1997) 5057.
- [13] UTTER, S.B., BEIERSDORFER, P., TRÄBERT, E., Electron-beam ion-trap spectra of tungsten in the EUV, *Can. J. Phys.* **80** (2002) 1503.
- [14] PÜTTERICH, T., NEU, R., BIEDERMANN, C., RADTKE, R., ASDEX UPGRADE TEAM, Disentangling the emissions of highly ionized tungsten in the range 4–14 nm, *J. Phys. B* **38** (2005) 3071.
- [15] KIM, Y.-K., BAIK, D.H., INDELICATO, P., DESCLAUX, J.P., Resonance transition energies of Li-, Na-, and Cu-like ions, *Phys. Rev. A* **44** (1991) 148.
- [16] BLUNDELL, S.A., Calculations of the screened self-energy and vacuum polarization in Li-like, Na-like, and Cu-like ions, *Phys. Rev. A* **47** (1993) 1790.

- [17] CHEN, G.X., KIRBY, K., SILVER, E., BRICKHOUSE, N.S., GILLASPY, J.D., TAN, J.N., POMEROY, J.M., LAMING, J.M., The  $3C/3D$  line ratio in Ni XIX: new *ab initio* theory and experimental results, *Phys. Rev. Lett.* **97** (2006) 143201.
- [18] FAHY, K., SOKELL, E., O'SULLIVAN, G., AGUILAR, A., POMEROY, J.M., TAN, J.N., GILLASPY, J.D., Extreme-ultraviolet spectroscopy of highly charged xenon ions created using an electron-beam ion trap, *Phys. Rev. A* **75** (2007) 032520.
- [19] FAHY, K., SOKELL, E., O'SULLIVAN, G., CUMMINGS, A., AGUILAR, A., GILLASPY, J.D., POMEROY, J.M., TAN, J.N., *Optical Sensing and Spectroscopy*, Proc. SPIE 5826, 351-362 (ed. by Byrne, H.J., et al., SPIE, Bellingham, WA, 2005).
- [20] TAKÁCS, E., BLAGOJEVIC, B., MAKÓNYI, K., LE BIGOT, E.-O., SZABÓ, C.I., KIM, Y.-K., GILLASPY, J.D., Direct observation of the  ${}^2D_{3/2}$ - ${}^2D_{5/2}$  ground-state splitting in  $\text{Xe}^{9+}$ , *Phys. Rev. A* **73** (2006) 052505.
- [21] TAWARA, H., TAKÁCS, E., SUTA, T., MAKÓNYI, K., RATLIFF, L.P., GILLASPY, J.D.,  $K$  x-rays produced in collisions of bare ions with atoms: contribution of multiple-electron transfer in  $\text{Kr}^{36+}$ ,  $\text{Ar}^{18+}$ , and  $\text{Ne}^{10+}+\text{Ar}$  collisions, *Phys. Rev. A* **73** (2006) 012704.
- [22] TAKÁCS, E., TÖKÉSI, K., TAWARA, H., VERZANI, C.J., HOHL, T., GILLASPY, J.D., PÁLINKÁS, J., Target dependence of charge exchange x-rays, *Rad. Phys. Chem.* **76** (2007) 617.
- [23] AGUILAR, A., GILLASPY, J.D., GRIBAKIN, G.F., PHANEUF, R.A., GHARAIBEH, M.F., KOZLOV, M.G., BOZEK, J.D., KILCOYNE, A.L.D., Absolute photoionization cross sections for  $\text{Xe}^{4+}$ ,  $\text{Xe}^{5+}$ , and  $\text{Xe}^{6+}$  near 13.5 nm: experiment and theory, *Phys. Rev. A* **73** (2006) 032717.
- [24] POMEROY, J.M., RATLIFF, L.P., GILLASPY, J.D., BAJT, S., *EUV Sources for Lithography*, Ch. 38, 1033-1044 (ed. by Bakshi, V., SPIE Press, 2006).
- [25] POMEROY, J.M., PERRELLA, A.C., GRUBE, H., GILLASPY, J.D., Gold nanostructures created by highly charged ions, *Phys. Rev. B* **75** (2007) 241409(R).
- [26] KIM, Y.-K., RUDD, M.E., Binary-encounter-dipole model for electron-impact ionization, *Phys. Rev. A* **50** (1994) 3954.
- [27] ALI M.A., KIM, Y.-K., Total ionization cross sections of Cl and  $\text{Cl}_2$  by electron-impact, *Surf. Interface Anal.* **37** (2005) 969.
- [28] HAYES, T.R., WETZEL, R.C., FREUND, R.S., Absolute electron-impact-ionization cross-section measurements of the halogen atoms, *Phys. Rev. A* **35** (1987) 578.
- [29] ALI M.A., KIM, Y.-K., Ionization cross sections by electron-impact on halogen atoms, diatomic halogen and hydrogen halide molecules, *J. Phys. B* **41** (2008) 145202.
- [30] KIM, Y.-K., STONE, P.M., Ionization of silicon, germanium, tin and lead by electron-impact, *J. Phys. B* **40** (2007) 1597.
- [31] FREUND, R.S., WETZEL, R.C., SHUL, R.J., HAYES, T.R., Cross-section measurements for electron-impact ionization of atoms, *Phys. Rev. A* **41** (1990) 3575.
- [32] KWON, D.-H., RHEE, Y.-J., KIM, Y.-K., Cross sections for ionization of Mo and  $\text{Mo}^+$  by electron-impact, *Int. J. Mass Spectrom.* **245** (2005) 26.
- [33] KWON, D.-H., RHEE, Y.-J., KIM, Y.-K., Ionization of W and  $\text{W}^+$  by electron-impact, *Int. J. Mass Spectrom.* **252** (2006) 213.
- [34] MONTAGUE, R.G., HARRISON, M.F.A., A measurement of the cross-section for electron-impact ionisation of singly charged tungsten ions, *J. Phys. B* **17** (1984) 2707.
- [35] STENKE, M., AICHELE, K., HARTHIRAMANI, D., HOFMANN, G., STEIDL, M., VÖLPEL, R., SALZBORN, E., Electron-impact single-ionization of singly and multiply charged tungsten ions, *J. Phys. B* **28** (1995) 2711.
- [36] JUNG, R.O., BOFFARD, J.B., ANDERSON, L.W., LIN, C.C., Excitation into  $3p^5 5p$  levels from the metastable levels of Ar, *Phys. Rev. A* **75** (2007) 052707.
- [37] SHARMA, L., SRIVASTAVA, R., STAUFFER, A.D., Excitation of the  $3p^5 5p$  levels of argon from the  $3p^5 4s$  metastable states, *Phys. Rev. A* **76** (2007) 024701.
- [38] KELLEHER, D.E., PODOBEDOVA, L.I., Atomic transition probabilities of aluminum. a critical compilation, *J. Phys. Chem. Ref. Data* **37** (2008) 709.

- [39] KELLEHER, D.E., PODOBEDOVA, L.I., Atomic transition probabilities of silicon. a critical compilation, *J. Phys. Chem. Ref. Data* **37** (2008) 1285.
- [40] KELLEHER, D.E., PODOBEDOVA, L.I., WIESE, W.L. *J. Phys. Chem. Ref. Data* **38** (2009) 171.
- [41] KELLEHER, D.E., PODOBEDOVA, L.I. unfinished work.
- [42] KELLEHER, D.E., PODOBEDOVA, L.I. unfinished work.
- [43] FUHR, J.R., WIESE, W.L., A critical compilation of atomic transition probabilities for neutral and singly ionized iron, *J. Phys. Chem. Ref. Data* **35** (2006) 1669.
- [44] FUHR, J.R., MARTIN, G.A., WIESE, W.L., "Atomic transition probabilities. Iron through Nickel." *Journal of Physical and Chemical Reference Data* **17** (1988) 4.
- [45] KRAMIDA, A.E., SHIRAI, T., Compilation of wavelengths, energy levels, and transition probabilities for W I and W II, *J. Phys. Chem. Ref. Data* **35** (2006) 423.
- [46] KRAMIDA, A.E., SHIRAI, T., Energy levels and spectral lines of tungsten, W III through W LXXIV, *At. Data Nucl. Data Tables* **95** (2009) 305.
- [47] KRAMIDA, A.E., READER, J., Ionization energies of tungsten ions: W<sup>2+</sup> through W<sup>71+</sup>, *At. Data Nucl. Data Tables* **92** (2006) 457.
- [48] RALCHENKO, YU., Density dependence of the forbidden lines in Ni-like tungsten, *J. Phys. B* **40** (2007) F175.
- [49] FELDMAN, U., SEELY, J.F., LANDI, E., RALCHENKO, YU., Bright EUV lines emitted by highly ionized tungsten ions as diagnostic indicators of the tungsten transport in ITER core plasmas ( $T_e > 7$  keV), *Nucl. Fusion* **48** (2008) 045004.
- [50] SALOMAN, E.B., Energy levels and observed spectral lines of xenon, XeI through XeLIV, *J. Phys. Chem. Ref. Data* **33** (2004) 765.
- [51] SALOMAN, E.B., Energy levels and observed spectral lines of krypton, Kr I through Kr XXXVI, *J. Phys. Chem. Ref. Data* **36** (2007) 215.

# ELECTRON-IMPACT INNER SHELL IONIZATION CROSS-SECTION MEASUREMENTS FOR HEAVY ELEMENT IMPURITIES IN FUSION REACTORS

J. J. ZHU, Y. WU, Z. AN

Key Laboratory of Radiation Physics and Technology of Ministry of Education,  
Institute of Nuclear Science and Technology,  
Sichuan University,  
Chengdu 610064, PR China

## Abstract

The measurements of electron-impact inner shell ionization cross-sections and x-ray production cross-sections of some heavy elements which are useful in fusion research are reported in this paper. The thin-target with thick substrate method and the thick-target method have been used for these measurements. The effects of backscattering electrons from substrates and multiple scattering of incident electrons have been corrected by using Monte Carlo method. The results of *K*-shell ionization cross-sections and *L*-shell x-ray production cross-sections for these elements were presented and compared with some theoretical values and the values of empirical formulae.

## 1. INTRODUCTION

In the fusion research, the knowledge about the impurity elements in plasma is very important, because the radiation energy loss of the impurity elements in fusion plasma will affect the fusion efficiency, and a large number of impurity elements in plasma will affect the stability of the fusion reactors. Therefore, we need to know the density of impurity elements in fusion plasma precisely. The atomic inner-shell ionization cross-sections or x-ray production cross-sections by electron-impact are needed in the diagnosis of impurity elements. However, the experimental data of electron-impact inner-shell ionization cross-section are still limited at present, especially for the energy region from threshold to several ten keV, although the study on electron-impact inner-shell ionization cross-section has been carried out in experiment for many years.

Generally, the self-supporting thin target was utilized in previous experimental measurements of inner-shell ionization cross-section. The difficulty of this method is that a very thin self-supporting target film needs to be prepared, and the very thin film is also very fragile. To avoid these problems, we developed a new method to measure the electron-impact inner-shell ionization cross-section, i.e., the thin-target with thick substrate method. The target element has been evaporated on a thick substrate by vacuum coating technique. The effect of backscattered electrons from the substrate has been corrected by using Monte Carlo method. Furthermore, we also developed a thick-target method, in which the fabrication of thin-target films and the film thickness determination can be avoided.

## 2. EXPERIMENTAL METHODS

In our measurements, we used an electron gun to provide the mono-energetic electron beams with the energies from near-threshold to several ten keV, and the intensity of the electron beam was adjustable. The incident electron beam was collected by a deep Faraday cup and then led to an ORTEC digital current integrator with accuracy of less than 1%. The target was placed inside a deep Faraday cup, and the characteristic x-rays from the target impacted by incident electrons were recorded by a Si(Li) detector. The direction of the detector was vertical to the direction of incident electron beam, and the angles of the target to the incident electron beam and detector were 45°. The Monte Carlo simulation code PENELOPE [1] has been used to estimate the escape rate of incident electrons and secondary

electrons from the deep Faraday cup, and we found that it was less than 2% at the energy range of interest here, i.e., from near-threshold to several ten keV. The full-width at half-maximum (FWHM) of the detector is 190 eV at  $^{55}\text{Mn}$  5.9 keV  $K\alpha$  x-rays.

The  $^{241}\text{Am}$  standard radioactive source and bremsstrahlung spectrum of carbon thick target by electron-impact [2–5] have been used for detection efficiency calibration of the Si(Li) detector. The 19 keV electron beams were used to generate the bremsstrahlung from thick carbon target. The measured bremsstrahlung spectrum was compared to the theoretical bremsstrahlung spectra calculated by Monte Carlo simulation code PENELOPE. The ratio of the two bremsstrahlung spectra was the shape of the efficiency calibration curve. Then we used  $^{241}\text{Am}$  standard radioactive source to determine the absolute values of the efficiency calibration. The reliability and validity of the Monte Carlo PENELOPE code have been demonstrated in [6–8]. The uncertainty of the detection efficiency calibration by this method was mainly from the standard radioactive sources and was estimated to be ~5% [2,4,5].

The thin targets with thick carbon substrates were made at China Institute of Atomic Energy by evaporating the target elements on to highly pure thick carbon substrates. The mass thickness values of the thin target films were determined by weighing, and we used 2 MeV  $^4\text{He}^+$  Rutherford Backscattering Spectrometry (RBS) method to check them. The details of RBS can be seen in Ref. [9].

### 3. MEASUREMENTS WITH THE THIN-TARGET METHOD

By using the thin-target with thick substrate method, the following effects should not be ignored: the effect of multiple scattering of incident electrons in the thin films, the effect of backscattering of incident electrons from the thick substrates, and the effect of bremsstrahlung photons produced by incident electrons in both thin films and thick substrates. These effects were corrected by Monte Carlo method. Here we give a brief description and the details can be found in Ref.[2].

Usually, the x-ray production cross-sections can be expressed as

$$\sigma(E_e) = \frac{4\pi A}{N_A t N_e \varepsilon(E_{ph}) \Omega} N(E_e), \quad (1)$$

where  $\sigma$  is the x-ray production cross-section,  $E_e$  is the incident electron energy,  $N$  is the net count of the characteristic x-ray peaks,  $A$  is the atomic weight,  $E_{ph}$  is the characteristic x-ray photon energy,  $N_A$  is the Avogadro constant,  $t$  is the thin film mass thickness,  $N_e$  is the number of incident electrons,  $\varepsilon(E_{ph})$  is the intrinsic detection efficiency of the detector, and  $\Omega$  is the solid angle subtended by the detector system. For  $K$ -shell ionization, the ionization cross-section can be easily deduced from the x-ray production cross-section by using the  $K$ -shell fluorescence yield  $\omega_k$ .

In our experiment, the Eq. 1 should be corrected because of the effects mentioned above. We assume the count of the characteristic x-ray peaks contributed by these effects as  $\Delta N$ , and define a  $K$  factor as the ratio of  $\Delta N$  to  $N$ , then the x-ray production cross-section can be denoted as

$$\sigma(E_e) = \frac{4\pi A(1 - K(E_e))}{N_A t N_e \varepsilon(E_{ph}) \Omega} N(E_e), \quad (2)$$

here the definitions of symbols are the same as in Eq. 1.

We can use the Monte Carlo simulations to obtain the  $K$  factors. For example, the atomic  $L_{\alpha}$  x-ray production cross-sections by electron-impact can be expressed as Eq. 3

$$\sigma_{L_{\alpha},MC} = \frac{2A}{N_e N_A t} N_{L_{\alpha},MC}, \quad (3)$$

where  $A$ ,  $N_e$ ,  $N_A$  and  $t$  are same as in Eq.1,  $N_{L_{\alpha},MC}$  is the corresponding characteristic x-ray counts from the backscattered x-ray spectra generated by the Monte Carlo PENELOPE code. The inner-shell ionization cross-sections of the optical-data model [10] and the other atomic parameters (e.g., fluorescence yields, Coster-Kronig transition probabilities, and x-ray emission rates) used in the Monte Carlo simulations can be obtained from the databases of the PENELOPE code, and they can be converted into the  $L_{\alpha}$ ,  $L_{\beta}$  and  $K$ -shell x-ray production cross-sections according to Eqs. 4–6 [11,12]

$$\sigma_{L_{\alpha},th} = \frac{\Gamma_{L_3-M_{4,5}}}{\Gamma_3} \omega_3 [\sigma_{L_3} + \sigma_{L_2} f_{23} + \sigma_{L_1} (f_{13} + f_{12} f_{23})] \quad (4)$$

$$\sigma_{L_{\beta},th} = \frac{\Gamma_{L_3-N_{1,4,5}} + \Gamma_{L_3-O_{1,4,5}} + \Gamma_{L_3-P_1}}{\Gamma_3} \omega_3 [\sigma_{L_3} + \sigma_{L_2} f_{23} + \sigma_{L_1} (f_{13} + f_{12} f_{23})] \quad (5)$$

$$+ \frac{\Gamma_{L_2-M_4}}{\Gamma_2} \omega_2 (\sigma_{L_1} f_{12} + \sigma_{L_2}) + \frac{\Gamma_{L_1-M_{2,3}}}{\Gamma_1} \omega_1 \sigma_{L_1},$$

$$\sigma_{K,th} = \omega_K \sigma_K, \quad (6)$$

where  $\sigma_{L_1}$ ,  $\sigma_{L_2}$ ,  $\sigma_{L_3}$ , and  $\sigma_K$  are the  $L$ -subshell and  $K$ -shell ionization cross-sections by electron-impact;  $\omega_1, \omega_2, \omega_3$  and  $\omega_K$  are the  $L$ -subshell and  $K$ -shell fluorescence yields;  $f_{12}, f_{13}, f_{23}$  are the Coster-Kronig transition probabilities;  $\Gamma_{ij}, \Gamma_i$  are the fractional and total x-ray emission rates for  $L$ -shell ionization, respectively. When the incident electron energy is larger than the  $K$ -shell ionization threshold energy, the vacancy transfers from the  $K$  shell to  $L$  subshells should be taken into account. Finally, we can obtain the K factors according to the Eq. 7

$$K = \frac{\sigma_{MC} - \sigma_{th}}{\sigma_{MC}}. \quad (7)$$

The sensitivity of K factors to the  $K$ ,  $L$ -shell ionization cross-sections used in the database of PENELOPE code has also been studied. The inner-shell ionization cross-sections of the PWBA-C-Ex theory [13,14] and of the Mayol and Salvat's model [10] have been used to calculate the K factors. We found that the K factors are not sensitive to the inner-shell ionization cross-sections. The differences of the (1-K) factors calculated from the two sets of inner-shell ionization cross-sections are less than 3% although they are very different both in shape and in magnitude. The  $K$ - and  $L$ -shell x-ray production cross-sections can be obtained according to Eq. 2 with the calculated K factors.

By using the method of thin-target with thick substrate, we have measured the electron-impact inner-shell x-ray production cross-sections near the threshold energy for the following elements and shells: S-K, Cl-K, Ca-K, Zn-K, W- $L_{\alpha}$ ,  $L_{\beta}$ , Bi- $L_{\alpha}$ ,  $L_{\beta}$ , Ba- $L_{\alpha}$  and Gd- $L_{\alpha}$ . We used the  $K$ -shell fluorescence yields to convert the  $K$ -shell x-ray production cross-sections to the  $K$ -shell ionization cross-sections [15]. The experimental results are summarized in Tables 1-8, and the comparisons with the results of some theoretical models and empirical formulae are shown in Figs. 1-8. The experimental uncertainties come from several factors: values of the net peak counts (~5-9%), detection efficiency (~5%), target thickness (~5%), number of incident electrons (~1%), (1-K) factors (~3%) and inhomogeneity of the target (~4%). The uncertainties of  $K$ -shell fluorescence yields should be considered for

*K*- shell ionization cross-sections [15]. Therefore, the total uncertainties by quadratic addition are estimated to be ~10-15%.

TABLE 1. MEASURED *K*-SHELL IONIZATION CROSS-SECTIONS FOR S ELEMENTS  
(E: keV;  $\sigma_K$  AND ERROR: cm<sup>2</sup>)

E	$\sigma_K$	Error	E	$\sigma_K$	Error
4	5.19E-22	6.1E-23	18	3.532E-21	4.27E-22
5	1.547E-21	1.52E-22	19	3.388E-21	4.09E-22
6	2.857E-21	3.33E-22	20	3.384E-21	4.10E-22
7	3.506E-21	4.22E-22	21	3.353E-21	4.05E-22
8	3.665E-21	4.42E-22	22	3.283E-21	3.97E-22
9	3.942E-21	4.77E-22	23	3.206E-21	3.88E-22
10	4.056E-21	4.89E-22	24	3.071E-21	3.73E-22
11	4.038E-21	4.86E-22	25	3.004E-21	3.64E-22
12	4.035E-21	4.86E-22	26	2.951E-21	3.58E-22
13	4.008E-21	4.83E-22	27	2.847E-21	3.47E-22
14	3.863E-21	4.66E-22	28	2.829E-21	3.47E-22
15	3.707E-21	4.48E-22	29	2.692E-21	3.57E-22
16	3.637E-21	4.39E-22	30	2.681E-21	3.45E-22
17	3.549E-21	4.27E-22			

TABLE 2. MEASURED *K*-SHELL IONIZATION CROSS-SECTIONS FOR Cl ELEMENT  
(E: keV;  $\sigma_K$  AND ERROR: cm<sup>2</sup>)

E	$\sigma_K$	Error	E	$\sigma_K$	Error
6	1.863E-21	1.81E-22	19	2.755E-21	2.68E-22
7	2.259E-21	2.19E-22	21	2.650E-21	2.57E-22
8	2.760E-21	2.68E-22	22	2.633E-21	2.56E-22
10	3.029E-21	2.94E-22	23	2.588E-21	2.51E-22
12	3.167E-21	3.08E-22	24	2.490E-21	2.42E-22
14	3.044E-21	2.96E-22	27	2.342E-21	2.27E-22
16	2.950E-21	2.86E-22	28	2.344E-21	2.17E-22
18	2.796E-21	2.72E-22	30	2.110E-21	1.90E-22

TABLE 3. MEASURED *K*-SHELL IONIZATION CROSS-SECTIONS FOR Ca ELEMENT  
(E: keV;  $\sigma_K$  AND ERROR: cm<sup>2</sup>)

E	$\sigma_K$	Error	E	$\sigma_K$	Error
5	2.19E-22	2.5E-23	14	1.592E-21	1.97E-22
6	6.63E-22	7.7E-23	16	1.617E-21	2.00E-22
7	8.67E-22	1.07E-22	18	1.654E-21	2.05E-22
8	1.122E-21	1.39E-22	20	1.656E-21	2.05E-22
9	1.237E-21	1.53E-22	22	1.632E-21	2.02E-22
10	1.361E-21	1.69E-22	24	1.573E-21	1.95E-22
11	1.471E-21	1.82E-22	26	1.517E-21	1.88E-22
12	1.518E-21	1.88E-22	28	1.489E-21	1.85E-22
13	1.596E-21	1.98E-22	30	1.414E-21	1.75E-22

TABLE 4. MEASURED *K*-SHELL IONIZATION CROSS-SECTIONS FOR Zn ELEMENT  
(E: keV;  $\sigma_K$  AND ERROR: cm<sup>2</sup>)

E	$\sigma_K$	Error	E	$\sigma_K$	Error
11	9.10E-23	1.1E-23	21	3.45E-22	4.0E-23
12	1.49E-22	1.7E-23	22	3.51E-22	4.1E-23
13	1.97E-22	2.3E-23	23	3.46E-22	4.0E-23
14	2.31E-22	2.7E-23	24	3.58E-22	4.2E-23
15	2.49E-22	3.9E-23	25	3.48E-22	4.1E-23
16	2.77E-22	3.2E-23	26	3.47E-22	4.0E-23
17	3.01E-22	3.5E-23	27	3.57E-22	4.2E-23
18	3.23E-22	3.8E-23	28	3.52E-22	4.1E-23
19	3.28E-22	3.8E-23	29	3.57E-22	4.2E-23
20	3.31E-22	3.9E-23	30	3.49E-22	4.1E-23

TABLE 5. MEASURED *L*-SHELL X-RAY PRODUCTION CROSS-SECTIONS FOR W ELEMENT  
(E: keV;  $\sigma_{L_\alpha}$ ,  $\sigma_{L_\beta}$  AND ERROR: cm<sup>2</sup>)

E	$\sigma_{L_\alpha}$	Error	$\sigma_{L_\beta}$	Error
13	7.3E-23	9E-24	3.8E-23	5E-24
14	9.7E-23	1.3E-23	5.3E-23	9E-24
15	1.16E-22	1.5E-23	7.2E-23	1.1E-23
16	1.35E-22	1.8E-23	8.1E-23	1.2E-23
17	1.47E-22	2.0E-23	9.5E-23	1.3E-23
18	1.51E-22	2.0E-23	1.02E-22	1.4E-23
19	1.60E-22	2.1E-23	1.09E-22	1.5E-23
20	1.68E-22	1.2E-23	1.16E-22	1.6E-23
21	1.71E-22	2.2E-23	1.22E-22	1.7E-23
22	1.76E-22	2.2E-23	1.25E-22	1.8E-23
24	1.82E-22	2.4E-23	1.32E-22	2.0E-23
26	1.85E-22	2.6E-23	1.38E-22	2.0E-23
28	1.88E-22	2.7E-23	1.37E-22	2.1E-23
30	1.89E-22	2.7E-23	1.42E-22	2.1E-23
32	1.90E-22	2.6E-23	1.46E-22	2.2E-23
34	1.86E-22	2.6E-23	1.45E-22	1.6E-23
36	1.86E-22	2.6E-23	1.46E-22	1.1E-23
38	1.84E-22	2.8E-23	1.40E-22	2.2E-23
40	1.80E-22	3.0E-23	1.42E-22	2.3E-23

TABLE 6. MEASURED *L*-SHELL X-RAY PRODUCTION CROSS-SECTIONS FOR Bi ELEMENT  
(E: keV;  $\sigma_{L_\alpha}$ ,  $\sigma_{L_\beta}$  AND ERROR: cm<sup>2</sup>)

E	$\sigma_{L_\alpha}$	Error	$\sigma_{L_\beta}$	Error
17	6.8E-23	9E-24	2.1E-23	3E-24
18	7.1E-23	9E-24	3.0E-23	5E-24
19	9.3E-23	1.2E-23	4.9E-23	8E-24
20	1.01E-22	1.3E-23	6.2E-23	1.0E-23
21	1.09E-22	1.4E-23	6.5E-23	1.0E-23
22	1.15E-22	1.4E-23	7.2E-23	1.1E-23
24	1.28E-22	1.7E-23	8.1E-23	1.2E-23
26	1.39E-22	1.8E-23	8.6E-23	1.3E-23
28	1.42E-22	1.8E-23	8.9E-23	1.3E-23

30	1.45E-22	1.9E-23	9.0E-23	1.4E-23
32	1.53E-22	1.9E-23	9.4E-23	1.6E-23
34	1.57E-22	1.9E-23	9.5E-23	1.4E-23
36	1.54E-22	1.9E-23	9.7E-23	1.5E-23
38	1.59E-22	2.0E-23	9.3E-23	1.4E-23
40	1.59E-22	2.2E-23	9.5E-23	1.4E-23

TABLE 7. MEASURED  $L$ -SHELL X-RAY PRODUCTION CROSS-SECTIONS FOR Ba ELEMENT

(E: keV;  $\sigma_{L\alpha}$  AND ERROR: cm<sup>2</sup>)

E	$\sigma_{L\alpha}$	Error
7	6.4E-23	9E-24
8	1.39E-22	1.7E-23
10	2.04E-22	2.3E-23
12	2.27E-22	2.6E-23
14	2.59E-22	3.0E-23
16	2.57E-22	2.9E-23
18	2.45E-22	2.8E-23
19	2.41E-22	2.8E-23
21	2.47E-22	2.8E-23
22	2.39E-22	2.7E-23
23	2.35E-22	2.7E-23
24	2.33E-22	2.7E-23
27	2.24E-22	2.6E-23
28	2.21E-22	2.5E-23
30	1.93E-22	2.2E-23

TABLE 8. MEASURED  $L$ -SHELL X-RAY PRODUCTION CROSS-SECTIONS FOR Gd ELEMENT

(E: keV;  $\sigma_{L\alpha}$  AND ERROR: cm<sup>2</sup>)

E	$\sigma_{L\alpha}$	Error
9	5.2E-23	7E-24
10	1.08E-22	1.4E-23
11	1.36E-22	1.7E-23
12	1.63E-22	2.0E-23
13	1.68E-22	2.1E-23
14	1.86E-22	2.3E-23
15	1.78E-22	2.2E-23
16	1.96E-22	2.5E-23
18	2.09E-22	2.6E-23
20	2.04E-22	2.6E-23
22	2.03E-22	2.5E-23
24	2.07E-22	2.6E-23
26	1.97E-22	2.5E-23
28	2.11E-22	2.6E-23
30	2.06E-22	2.6E-23
32	1.95E-22	2.4E-23
33	1.94E-22	2.4E-23
36	1.99E-22	2.5E-23

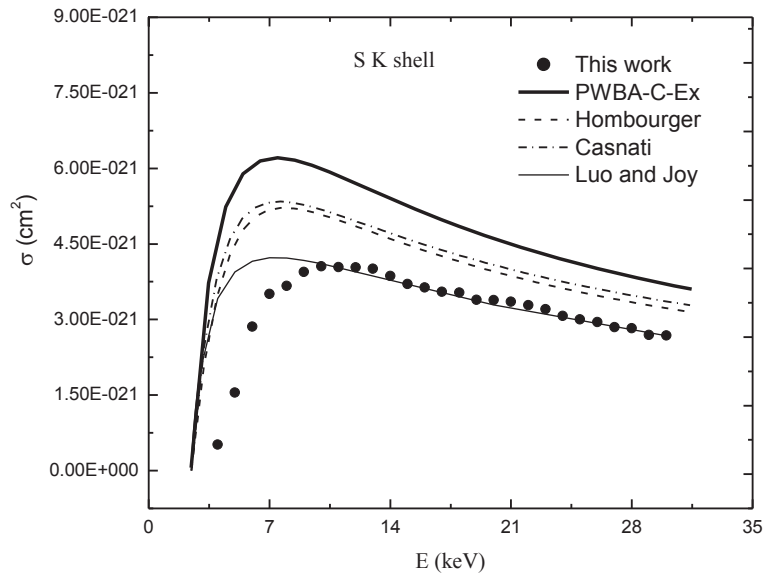


FIG. 1. The present experimental data of K-shell ionization cross-sections by electron-impact for S element are compared with the results from the PWBA-C-Ex theory [13,14] and the Luo and Joy's theory [16,17] as well as the results from the empirical formulae of Casnati and co-workers [18] and of Hombourger [19].

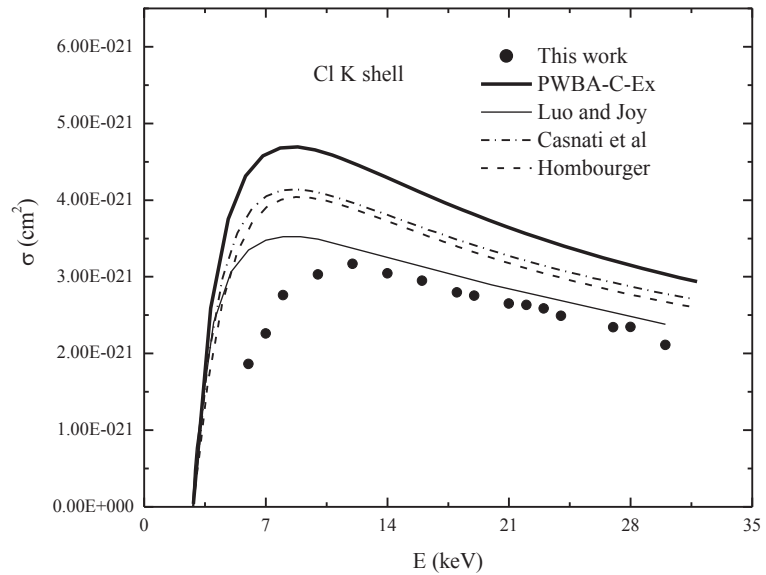


FIG. 2. The present experimental data of K-shell ionization cross-sections by electron-impact for Cl element are compared with the results from the PWBA-C-Ex theory [13,14] and the Luo and Joy's theory [16,17] as well as the results from the empirical formulae of Casnati and co-workers [18] and of Hombourger [19].

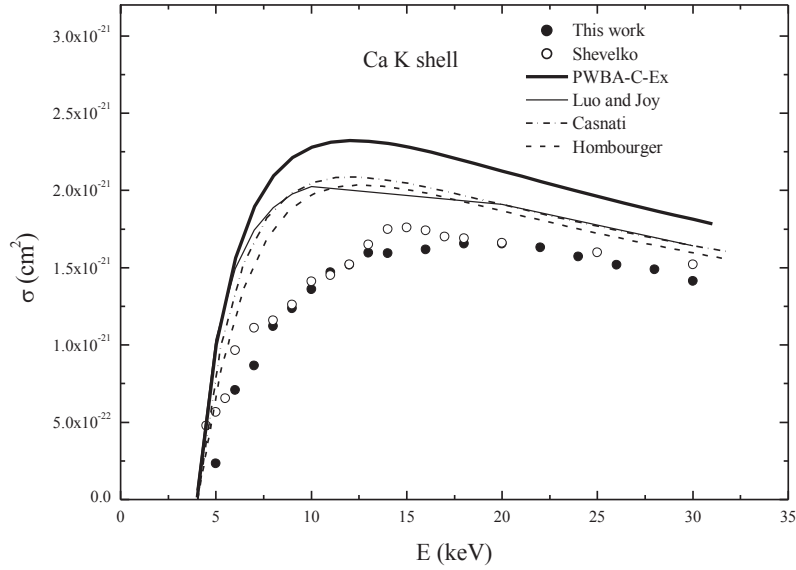


FIG. 3. The present experimental data of K-shell ionization cross-sections by electron-impact for Ca element are compared with the results from the PWBA-C-Ex theory [13,14] and the Luo and Joy's theory [16,17] as well as the results from the empirical formulae of Casnati and co-workers [18] and of Hombourger [19]. The experimental data of Shevelko and co-workers [20] for Ca element are also plotted for comparison.

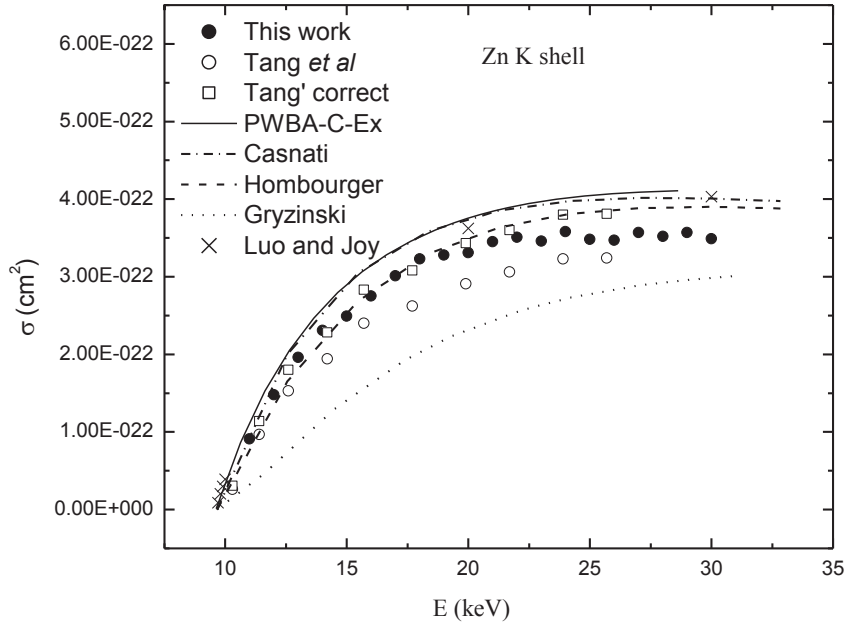


FIG. 4. The present experimental data of K-shell ionization cross-sections by electron-impact for Zn element are compared with the results from the PWBA-C-Ex theory [13,14] and the Luo and Joy's theory [16,17] as well as the results from the empirical formulae of Casnati and co-workers [18] and of Hombourger [19] and of Gryzinski [21]. The experimental data of Tang and co-workers [22,23] for Zn element are also plotted for comparison.

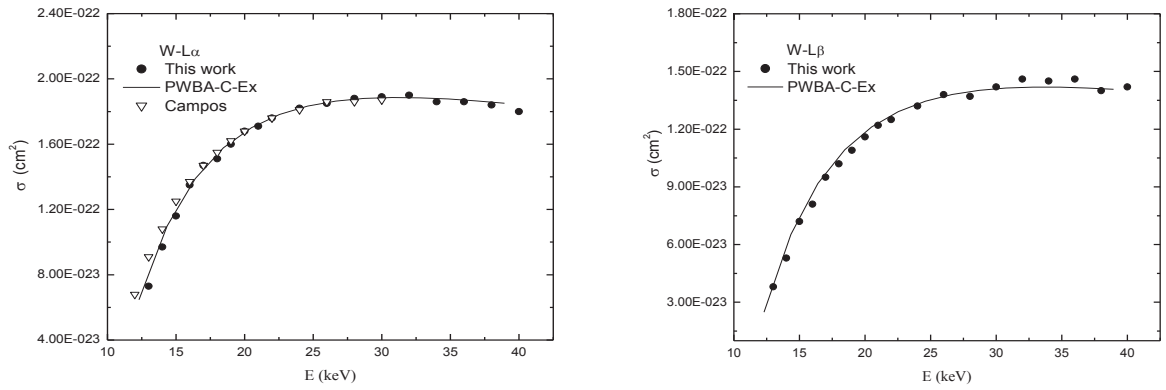


FIG. 5. The present experimental data of  $L_{\alpha}$ ,  $L_{\beta}$  x-ray production cross-sections by electron-impact for W element are compared with the PWBA-C-Ex theory [13,14] and the experimental data of Campos et al. [24].

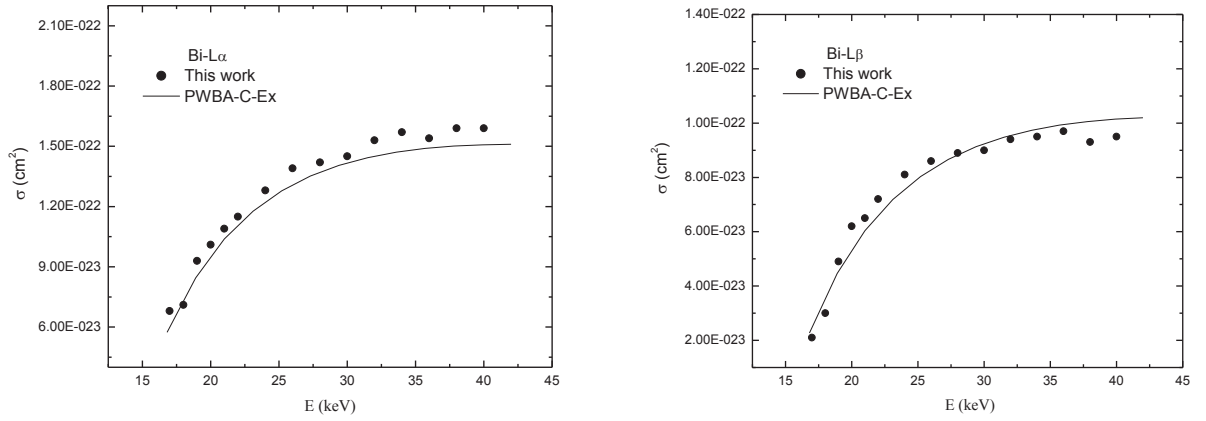


FIG. 6. The present experimental data of  $L_{\alpha}$ ,  $L_{\beta}$  x-ray production cross-sections by electron-impact for Bi element are compared with the PWBA-C-Ex theory [13,14].

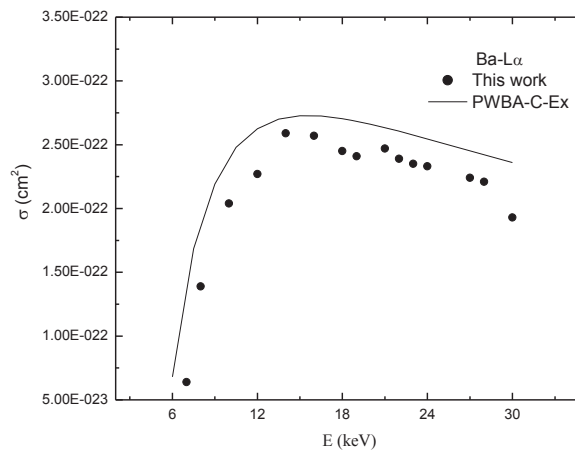


FIG. 7. The present experimental data of  $L_{\alpha}$  x-ray production cross-sections by electron-impact for Ba element are compared with the PWBA-C-Ex theory [13,14].

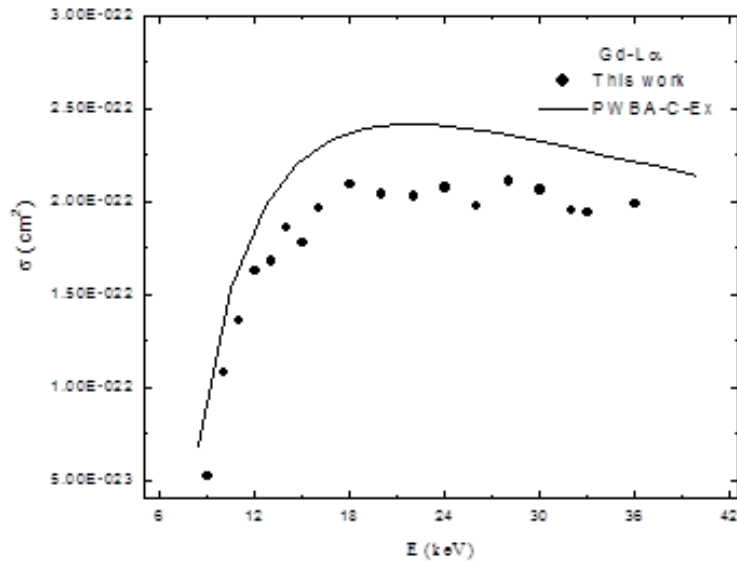


FIG. 8. The present experimental data of  $L_{\alpha}$  x-ray production cross-sections by electron-impact for Gd element are compared with the PWBA-C-Ex theory [13,14].

#### 4. MEASUREMENTS WITH THE THICK-TARGET METHOD

In the thick-target method, the atomic inner-shell ionization cross-sections were obtained previously by employing the derivatives of polynomials which were fitted to the experimental data of characteristic x-ray yields. However, the relation between the characteristic x-ray yields and the atomic inner-shell ionization cross-sections is expressed by a Fredholm integral equation of first kind, for which the solution is an ill-posed inverse problem [25]. Therefore, it is hard to appropriately obtain the atomic inner-shell ionization cross-sections by simply employing the derivatives of polynomials which are fitted to the experimental characteristic x-ray yields. Based on our previous work [26], we use two methods to extract the inner-shell ionization cross-sections in the thick-target method. The first method is the well-known Tikhonov regularization method, which can deal with a wide range of ill-posed inverse problems. Another method is the classical molecular dynamics (CMD), which has been successfully used to handle some inverse problems in recent years by our group. We found that these two methods can solve the inverse problem involved in the thick-target method successfully [25]. The total estimated error is about 10%, which is the same order as that in thin-target with thick substrate method [25]. Therefore, the thick-target method can be reliably used in the measurement of inner-shell ionization cross-sections by electron-impact near the threshold energy region, and the difficulty of thin-target film fabrication and the film thickness determination can be avoided. By using Tikhonov regularization method, we have measured the K-shell ionization cross-sections of Si and Ni elements by electron-impact with the thick-target method [25,27]. The experimental results for Si and Ni elements with the thick-target method are summarized in Tables 9–10, and comparisons with some theoretical results and the other available experimental data for Si and Ni elements are also shown in Figs. 9–10.

TABLE 9. MEASURED *K*-SHELL IONIZATION CROSS-SECTIONS FOR Si ELEMENT  
(E: keV;  $\sigma_K$  AND ERROR: cm<sup>2</sup>)

E	$\sigma_K$	Error
3.35	7.612E-21	1.033E-21
4.85	8.777E-21	1.191E-21
6.36	9.043E-21	1.228E-21
7.87	8.858E-21	1.205E-21
9.37	9.007E-21	1.227E-21
10.88	8.915E-21	1.216E-21
12.39	8.468E-21	1.158E-21
13.89	8.067E-21	1.106E-21
15.40	7.853E-21	1.077E-21
16.91	7.489E-21	1.030E-21
18.41	7.138E-21	0.984E-21
19.92	7.072E-21	0.978E-21
21.43	7.246E-21	1.002E-21
22.93	7.019E-21	0.974E-21
24.44	6.880E-21	0.956E-21

TABLE10. MEASURED *K*-SHELL IONIZATION CROSS-SECTIONS FOR Ni ELEMENT  
(E: keV;  $\sigma_K$  AND ERROR: cm<sup>2</sup>)

E	$\sigma_K$	Error
9.44	2.51E-22	2.5E-23
10.6	2.68E-22	2.7E-23
11.7	3.50E-22	3.5E-23
12.8	3.61E-22	3.6E-23
13.9	3.83E-22	3.8E-23
15.0	4.33E-22	4.3E-23
16.2	4.40E-22	4.4E-23
17.3	4.58E-22	4.6E-23
18.4	4.60E-22	4.6E-23
19.5	4.95E-22	5.0E-23
20.6	4.96E-22	5.0E-23
21.8	5.10E-22	5.1E-23
22.9	5.24E-22	5.2E-23
24	5.17E-22	5.2E-23

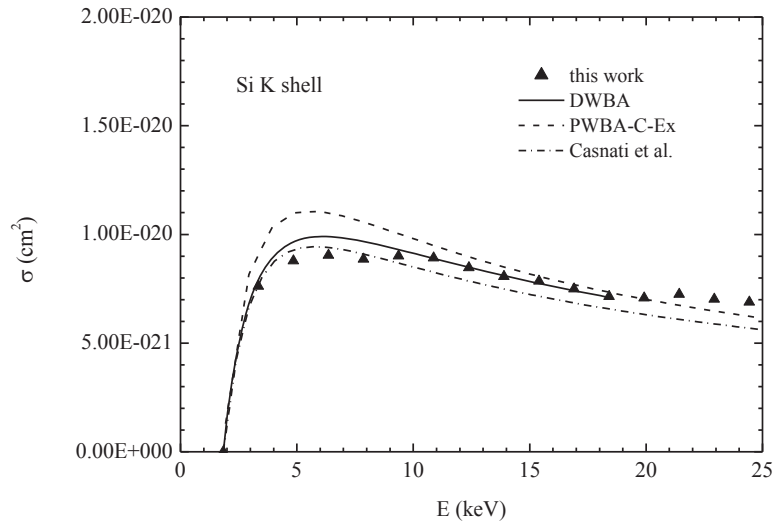


FIG. 9. The measured  $K$ -shell ionization cross-sections for Si element by the thick-target method. The predictions of DWBA [28] and PWBA-C-Ex [13,14] theories and the values of Casnati empirical formula [18] are also shown for comparison.

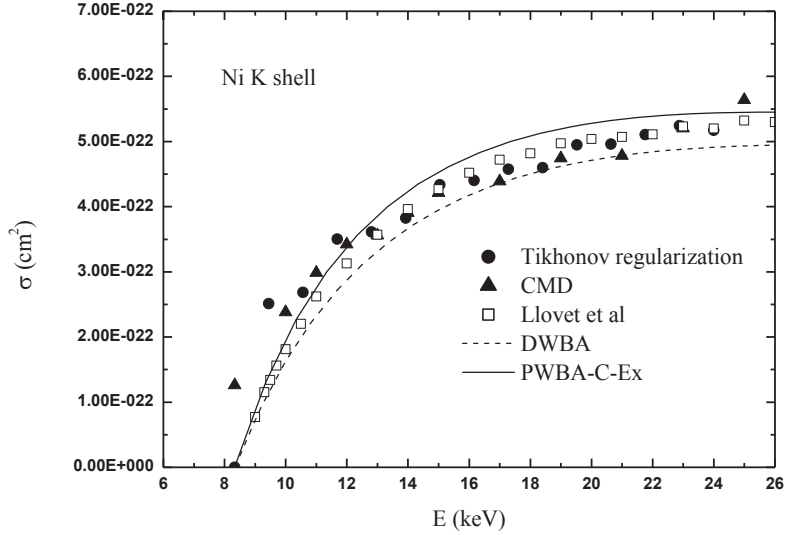


FIG. 10. The  $K$ -shell ionization cross-sections for Ni element determined by the Tikhonov regularization method and the classical molecular dynamics (CMD) method. The experimental data of Llovet et al. [29] and the predictions of DWBA [28] and PWBA-C-Ex [13,14] theories are also shown for comparison.

The effect of surface roughness has also been studied by using Monte Carlo simulations when measuring the electron-impact inner-shell ionization cross-section with the thick-target method [30]. The definition of surface roughness structures was a series of hemispheres produced randomly on the smooth surface of a thick Ni target. We used Monte Carlo simulations to obtain the characteristic x-ray yields of Ni  $K$ -shell ionization by electron-impact for the target with smooth surface and the targets with various surface roughness. Then we used Tikhonov regularization method to deal with the inverse problem and obtained the  $K$ -shell ionization cross-sections. The Ni  $K$ -shell ionization cross-sections obtained with smooth surface and various surface roughness have been compared. The result shows that the influence of surface roughness increases as the roughness increases, and the surface roughness of the target should be less than 100 nm if the experimental error originated from surface roughness would be kept less than 2%.

## 5. SUMMARY

In this paper, the  $K$ -shell ionization cross-sections for S, Cl, Ca, Zn elements and the  $L$ -shell x-ray production cross-sections for W- $L_{\alpha}$ ,  $L_{\beta}$ , Bi- $L_{\alpha}$ ,  $L_{\beta}$ , Ba- $L_{\alpha}$  and Gd- $L_{\alpha}$  have been measured from the threshold energy to several ten keV by using the thin-target with thick substrate method. The effect of multiple scattering of incident electrons in the thin films, the effect of backscattering of incident electrons from the thick substrates, and the effect of bremsstrahlung photons produced by incident electrons in both thin films and thick substrates have been corrected by using Monte Carlo method. Moreover, the  $K$ -shell ionization cross-sections for Si and Ni elements have also been measured by using the thick-target method, in which the ill-posed inverse problem has been dealt with successfully by the Tikhonov regularization method and the classical molecular dynamics. The experimental results

reported in this paper have been compared with some theoretical values and the values of empirical formulae.

## ACKNOWLEDGEMENT

This work is supported by the National Natural Science Foundation of China under Grant Nos. 10774106 and 10674097 and the IAEA Research Contract No. RC-13491/R2.

## REFERENCES:

- [1] SALVAT, F., FERNANDEZ-VAREA, J.M., ACOSTA, E., SEMPAU, J. PENELOPE, A Code System for Monte Carlo Simulation of Electron and Photon Transport, OECD/NEA Data Bank, Issy-les-Moulineaux, France, 2003.
- [2] Wu, Y., AN, Z., LIU, M.T., DUAN, Y.M., TANG, C.H., LUO, Z.M., Measurements of *L*-shell x-ray production cross-sections of Au and Ag by low energy electron-impact, *J. Phys. B* **37** (2004) 4527.
- [3] MERLET, C., LLOVET, X., SALVAT, F., Measurements of absolute *K* -shell ionization cross-sections and *L* -shell x-ray production cross-sections of Ge by electron-impact, *Phys. Rev. A* **69**(2004) 032708.
- [4] AN, Z., LIU, M.T., On the efficiency calibration of Si(Li) detector in the low-energy region using thick-target bremsstrahlung, *Nucl. Instrum.Methods Phys. Res. B* **194** (2002) 513.
- [5] AN, Z., LIU, M.T., WU, Y., DUAN, Y.M., Efficiency calibration of Si(Li) detector in low-energy region, *Atomic Energy Science and Technology* **40** (2006) 83 (in Chinese).
- [6] ACOSTA, E., LLOVET, X., SALVAT, F., Monte Carlo simulation of bremsstrahlung emission by electrons, *Appl. Phys. Lett.* **80** (2002) 3228.
- [7] LLOVET, X., SORBIER, L., CAMPOS, C.S., ACOSTA, E., SALVAT, F., Monte Carlo simulation of x-ray spectra generated by kilo-electron-volt electrons, *J. Appl. Phys.* **93** (2003) 3844.
- [8] SEMPAU, J., FERNÁNDEZ-VAREA, J.M., ACOSTA, E., SALVAT, F., Experimental benchmarks of the Monte Carlo code PENELOPE, *Nucl. Instrum. Methods Phys. Res. B* **207** (2003) 107.
- [9] AN, Z., LIU, M.T., FU, Y.C., LUO, Z.M., TANG, C.H., LI, C.M., ZHANG, B.H., TANG, Y.J., Some recent progress on the measurement of *K*-shell ionization cross-sections of atoms by electron-impact: application to Ti and Cr elements, *Nucl. Instrum. Methods Phys. Res. B* **207** (2003) 268.
- [10] MAYOL, R., SALVAT, F., Cross-sections for *K*-shell ionisation by electron-impact, *J. Phys. B* **23** (1990) 2117.
- [11] TIRAŞOĞLU, E., ÇEVİK, U., ERTUĞRAL, B., ATALAY, Y., KOPYA, A.İ., Measurements of  $L_{\alpha}$ ,  $L_{\beta}$  and  $L_{\gamma}$  x-ray fluorescence cross-sections in  $70 \leq Z \leq 92$  elements excited by 59.543 keV photons, *Radiat. Phys. Chem.* **60** (2001) 11.
- [12] PURI, S., CHAND, B., MEHTA, D., GARG, M.L., SINGH, N., TREHAN, P.N., K and L shell x-ray fluorescence cross-sections, *At. Data Nucl. Data Tables* **61** (1995) 289.
- [13] HIPPLER, R., Plane wave born calculations of *K*-shell ionization at low velocities, *Phys. Lett. A* **144** (1990) 81.
- [14] KHARE, S.P., WADEHRA, J.M., *K*-, *L*-, and *M*-shell ionization of atoms by electron and positron impact, *Can. J. Phys.* **74** (1996) 376.
- [15] HUBBELL, J.H., TREHAN, P.N., SINGH, N., CHAND, B., MEHTA, D., GARG, M.L., GARG, R.R., SINGH, S., PURI, S., A review, bibliography, and tabulation of K, L, and higher atomic shell x-ray fluorescence yields, *J. Phys. Chem. Ref. Data* **23** (1994) 339.
- [16] LUO, S., Ph.D. thesis, The University of Tennessee, Knoxville, 1994 (unpublished).

- [17] LUO, S., JOY, D.C., in *Microbeam Analysis-1991*, edited by D. G. Howitt (San Francisco Press, San Francisco, 1991), p 67.
- [18] CASNATI, E., TARTARI, A., BARALDI, C., An empirical approach to *K*-shell ionisation cross-section by electrons, *J. Phys. B* **15** (1982)155 (Corrigenda: *J.Phys.B* 16 (1983) 505).
- [19] HOMBOURGER, C., An empirical expression for *K*-shell ionization cross-section by electron-impact, *J. Phys. B* **31** (1998) 3693.
- [20] SHEVELKO, V.P., SOLOMON, A.M., VUKSTICH, V.S., *K*-shell ionization of free metal atoms K, Ca, Rb and Sr by electron-impact, *Phys. Scripta* **43** (1991) 158.
- [21] GRZYŃSKI, M., Classical theory of atomic collisions. I. theory of inelastic collisions, *Phys. Rev. A* **138** (1965) 336.
- [22] TANG, C., AN, Z., LI, T., LUO, Z., Measurement of zinc and manganese *K*-shell ionization cross-sections by electron-impact, *Nucl. Instrum. Methods Phys. Res. B* **155** (1999) 1.
- [23] DUAN, Y.M., WU, Y., TANG, C.H., et al., *Journal of Sichuan University (Science Edition)* **41** (2004) 1221.
- [24] CAMPOS, C.S., VASCONCELLOS, M.A.Z., LLOVET, X., SALVAT, F., Measurements of *L*-shell x-ray production cross-sections of W, Pt, and Au by 10–30-keV electrons, *Phys. Rev. A* **66** (2002) 012719.
- [25] AN, Z., HOU, Q., Inverse problem in the thick-target method of measurements of inner-shell ionization cross-sections by electron or positron impact, *Phys. Rev. A* **77**(2008) 042702.
- [26] AN, Z., WU, Y., LIU, M.T., DUAN, Y.M., TANG, C.H., Thick-target method in the measurement of inner-shell ionization cross-sections by low-energy electron-impact, *Nucl. Instrum. Methods Phys. Res. B* **246** (2006) 281.
- [27] ZHU, J.J., AN, Z., LIU, M.T., TIAN, L.X., Measurements of the *K* -shell ionization cross-sections of Si by 3–25 keV electron-impact using the thick-target method, *Phys. Rev. A* **79** (2009) 052710.
- [28] CAMPOS, C.S., VASCONCELLOS, M.A.Z., TRINCAVELLI, J.C., SEGUI, S., Analytical expression for *K*- and *L*-shell cross-sections of neutral atoms near ionization threshold by electron-impact, *J. Phys. B* **40** (2007) 3835.
- [29] LLOVET, X., MERLET, C., SALVAT, F., Measurements of *K*-shell ionization cross-sections of Cr, Ni and Cu by impact of 6.5-40 keV electrons, *J. Phys. B* **33** (2000) 3761.
- [30] TIAN, L.X., AN, Z., Effect of surface roughness on the measurement of electron-impact inner-shell ionization cross-sections using thick-target method, *Nucl. Instrum. Methods Phys. Res.B* **266** (2008) 5037.

# COLLISIONAL DATA FOR THE Si, Cl AND Ar ISONUCLEAR SEQUENCES USING THE LOS ALAMOS ATOMIC COLLISION CODES

J. COLGAN<sup>1</sup>, H.L. ZHANG<sup>2</sup>, C.J. FONTES<sup>2</sup>

<sup>1</sup>Theoretical Division  
Los Alamos National Laboratory  
Los Alamos, NM 87545, USA

<sup>2</sup>Applied Physics Division  
Los Alamos National Laboratory  
Los Alamos, NM 87545, USA

## Abstract

The Los Alamos suite of atomic physics codes has been used to generate electron-impact excitation and ionization data for all ions in the Si, Cl and Ar isonuclear sequences. For excitation processes, level-resolved cross-sections are presented which were calculated using first-order many-body perturbation theory. For ionization, we present level-resolved cross-sections using distorted-wave theory. Our data are generated in support of an IAEA Coordinated Research Project on atomic data for heavy element impurities in fusion reactors. The data described in this report have been archived in the IAEA ALADDIN database, and should prove useful for modeling the effects of impurities in fusion reactors.

## 1. INTRODUCTION

The use of atomic data in fusion modeling is of continued importance to understanding the complex physical processes that take place in fusion devices. As ITER draws closer to realization, the demand for large quantities of accurate atomic data remains strong. Some recent, focused efforts have allowed a large quantity of useful atomic data to be generated [1–5], which should have direct relevance to fusion modeling efforts.

As part of this effort, we have used the Los Alamos Atomic Physics Codes to generate electron-impact collisional data for a variety of systems [6,7]. In this report, we briefly describe our method and give an overview of the calculations that have been completed. The bulk of our calculations have been made for all ion stages of Si, Cl and Ar. Ar is a candidate for the mitigation of tokamak disruptions [8]. Cl is commonly used to clean tokamaks and its spectral lines are thus often seen in experimental spectra from fusion devices. All of our data have been archived in the IAEA's ALADDIN database [9], which allows for easy access by plasma modellers.

In the following, we give a brief overview of the methods employed in the Los Alamos Atomic Physics Codes and then present some highlights of the excitation and ionization results that have been obtained.

## 2. METHOD

The calculations presented in this report were performed with the Los Alamos suite of atomic physics codes. These codes have been continuously used and improved over the last 20 or more years, and subjected to thorough testing and comparisons with other methods and with experiment, for both fundamental cross-sections, and in spectra arising from kinetics modeling. Although the primary focus is on producing atomic data for use in higher-density plasma modeling, the Los Alamos codes are also quite suitable for providing atomic data (and kinetics modeling) for a range of lower-density plasmas. We note that these codes can also be

run through our web interface [10], where cross-sections for a variety of atomic processes can be easily obtained.

The first step in our calculations is to run the semirelativistic structure code CATS [11], which is based on Cowan's codes [12]. Most of the calculations presented here were made within the fine-structure approximation, which include the spin-orbit interaction when diagonalizing the appropriate Hamiltonian. Excitation cross-sections were computed using the ACE code [13], in which we used the first-order many-body theory option [14,15] to compute the cross-sections of interest. For electron-impact ionization, the multipurpose ionization code GIPPER [16] was used, with which cross-sections were computed within the distorted-wave approximation.

### 3. RESULTS

Many of the results presented here were discussed in detail previously [6,7]. Here we give a selection of results from these calculations.

#### 3.1. Electron-Impact Excitation

In Fig. 1 we present excitation collision strengths for the  $2s^22p\ ^2P_{1/2} \rightarrow 2s2p^2\ ^2S_{3/2}$  transition in B-like Si, Cl and Ar. We compare with previous relativistic distorted-wave calculations made by the Sampson group [17]. Good agreement is generally found, although some differences are found at higher electron energies. A further test calculation, which included mixing only between states that arise from the three  $n=2$  configurations,  $2s^22p$ ,  $2s2p^2$  and  $2p^3$  (as was done in Ref. [17]), was made to assess the accuracy of the current calculations. The closer agreement between the test calculation and the calculations of [17] indicate that the differences are due to configuration-interaction effects. We regard our current calculations as more accurate, since they include more detailed configuration-interaction. Relativistic effects appear to play a minor role for these mid- $Z$  elements.

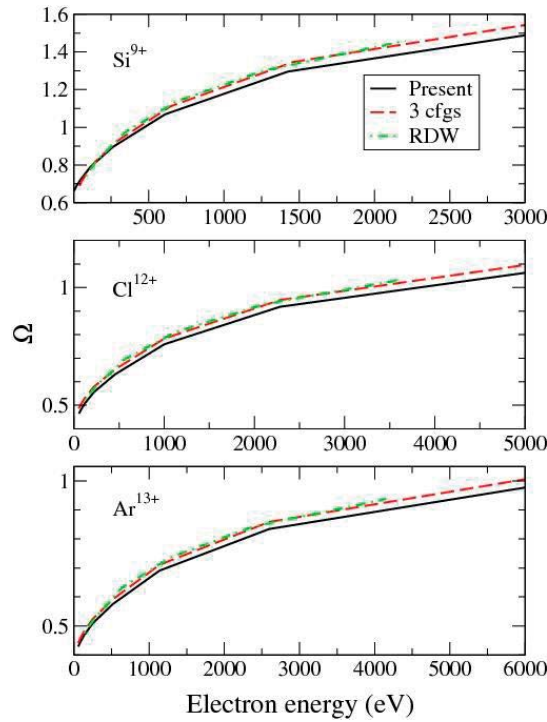


FIG. 1. Collision strengths ( $\Omega$ ) for the  $2s^22p\ ^2P_{1/2} \rightarrow 2s2p^2\ ^2S_{3/2}$  transition in B-like Si, Cl and Ar. We compare the current calculations with the results of [17] and a test, three-configuration calculation.

### 3.2. Electron-impact Ionization

Since our previous study [6] largely focused on electron-impact ionization of Si ions, we present here several examples of electron-impact ionization of Cl and Ar ions. Previously, we showed how distorted-wave approaches appear quite accurate for ionization from ions that are twice or more ionized [6].

In Figs. 2 and 3 we present electron-impact ionization cross-sections from the ground level of Mg-like Cl and Ar. For  $\text{Cl}^{5+}$  we compare with measurements of [18], which have previously been shown to be in good agreement with earlier distorted-wave calculations [19]. We present level-resolved calculations from the ground  $3s^2\ ^1S_0$  level, and also configuration-average calculations from the  $3s^2$  ground configuration. The close agreement between these calculations indicates that configuration-interaction effects play a relatively minor role in the ionization cross-sections. We find that our current calculations are in good agreement with the measurements for the direct portion of the ionization cross-section, from threshold to 200 eV. Beyond this energy, excitation-autoionization processes strongly contribute to the total ionization cross-section. In this case the contributions are largely due to autoionization from the excited  $2p^5 3s^2 n/$  configurations. Although it is straightforward to compute the excitation-autoionization contribution, we choose not to show it here. The set of data computed using the Los Alamos codes and archived in the ALADDIN database includes direct excitation to autoionizing states, as well as direct ionization from these states. In the Los Alamos approach to kinetics modeling [20], autoionizing states are treated explicitly, and direct excitation and ionization processes between all possible levels are included. Thus, our plasma modeling efforts automatically include the excitation-autoionization contributions.

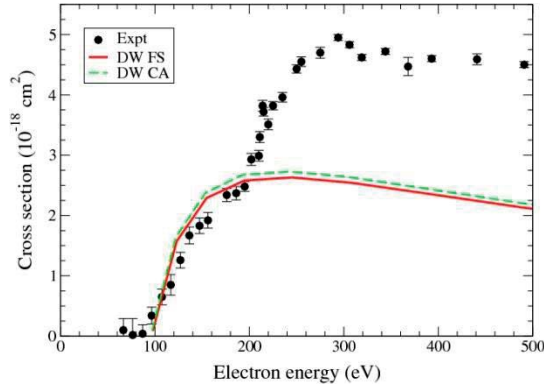


FIG. 2. Electron-impact ionization cross-sections for Mg-like Cl. We compare our current calculations with the measurements of [18].

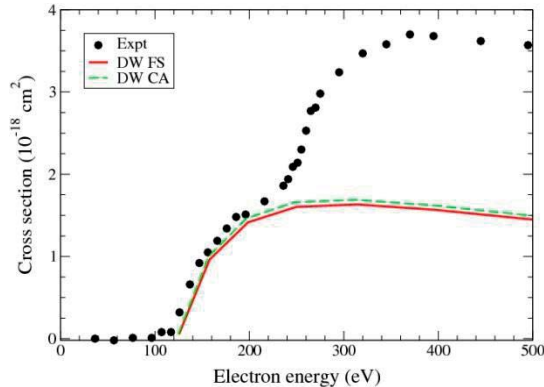


FIG. 3. Electron-impact ionization cross-sections for Mg-like Ar. We compare our current calculations with the measurements of [18].

Fig. 3 shows ionization cross-sections from Mg-like Ar. A similar trend is found to that observed for  $\text{Cl}^{5+}$ ; before the onset of excitation-autoionization, the measurements are in good agreement with the distorted-wave calculations. We note that previous distorted-wave calculations of ionization from Ar ions [4,19] are also in good agreement with the current calculations.

### 3.3. Inner-shell Ionization

We also present calculations of inner-shell ionization of neutral Fe [7], which are compared to ionization measurements made from thin targets [21]. Although these calculations are not as directly relevant to fusion modeling efforts, we present them to highlight the capability of the Los Alamos Atomic Physics Codes to perform fully relativistic structure and collisional calculations. Such approaches may prove useful in modeling ionization and excitation from heavy, highly charged ions such as W, which is expected to play a crucial role in ITER.

Fig. 4 shows the  $K$ -shell ionization of neutral Fe. Fully relativistic distorted-wave calculations [7] are compared to measurements [21]. The fully relativistic capability in the Los Alamos suite of codes has been under development over the past 15 or so years [22]. The calculations begin with the RATS structure code, which is based on the Dirac-Fock-Slater approach of Sampson et al. [23]. Fully relativistic calculations of excitation and ionization are performed using appropriate options within the ACE and GIPPER codes, respectively, which are based on the distorted-wave approach of Zhang et al. [24, 25]. The calculations are in excellent agreement with the measurements. A further semirelativistic calculation (shown as the dashed line) is lower than the measurements, indicating the need for a fully relativistic approach when considering ionization at high energies from heavy targets.

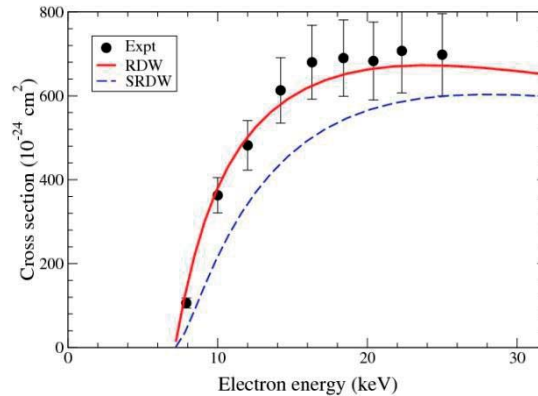


FIG. 4.  $K$ -shell electron-impact ionization of neutral Fe. We compare our current calculations with the measurements of [21].

## 4. CONCLUSIONS

We have presented a brief overview of recent efforts made using the Los Alamos suite of atomic physics codes to compute collisional data of interest to fusion modeling. For ions that are twice or more ionized, the perturbative approaches used in the Los Alamos codes are expected to be accurate. In the future, it is expected that the atomic data needs for fusion modeling will be primarily focused on tungsten, due to its importance in the divertor region of ITER. The strength of the Los Alamos codes is the ability to compute large quantities of accurate atomic data in an efficient manner. In particular, it is straightforward to compute collisional data for excitation between, and ionization from, large numbers of configurations and/or levels, for a large number of ion stages of a given element. Thus the Los Alamos

Atomic Physics Codes are capable of generating many of the data needs for future fusion modeling.

## ACKNOWLEDGMENTS

The Los Alamos National Laboratory is operated by Los Alamos National Security, LLC for the National Nuclear Security Administration of the U.S. Department of Energy under Contract No. DE-AC5206NA25396.

## REFERENCES

- [1] LOCH, S.D., COLGAN, J., WITTHOEFT, M.C., PINDZOLA, M.S., BALLANCE, C.P., MITNIK, D.M., GRIFFIN, D.C., O'MULLANE, M.G., BADNELL, N.R., SUMMERS, H.P., Generalised collisional-radiative model for light elements. A: Data for the Li isonuclear sequence, *At. Data Nucl. Data Tables* **92** (2006) 813.
- [2] LOCH, S.D., PINDZOLA, M.S., BALLANCE, C.P., GRIFFIN, D.C., COLGAN, J., BADNELL, N.R., O'MULLANE, M.G., SUMMERS, H.P., Generalized collisional radiative model for light elements. Part B: Data for the Be isonuclear sequence, *At. Data Nucl. Data Tables* **94** (2008) 257.
- [3] LOCH, S.D., LUDLOW, J.A., PINDZOLA, M.S., WHITEFORD, A.D., GRIFFIN, D.C., Electron-impact ionization of atomic ions in the W isonuclear sequence, *Phys. Rev. A* **72** (2005) 052716.
- [4] LOCH, S.D., ABDEL-NABY, SH.A., BALLANCE, C.P., PINDZOLA, M.S., Electron-impact ionization and recombination of M -shell atomic ions in the argon isonuclear sequence, *Phys. Rev. A* **76** (2007) 022706.
- [5] WITTHOEFT, M.C., WHITEFORD, A.D., BADNELL, N.R., *R*-matrix electron-impact excitation calculations along the F-like iso-electronic sequence, *J. Phys. B* **40** (2007) 2969.
- [6] COLGAN, J., ZHANG, H.L., FONTES, C.J., Electron-impact excitation and ionization cross-sections for the Si, Cl, and Ar isonuclear sequences, *Phys. Rev. A* **77** (2008) 062704.
- [7] COLGAN, J., FONTES, C.J., ZHANG, H.L., Inner-shell electron-impact ionization of neutral atoms, *Phys. Rev. A* **73** (2006) 062711.
- [8] WHYTE, D.G., JERNIGAN, T.C., HUMPHREYS, D.A., HYATT, A.W., LASNIER, C.J., PARKS, P.B., EVANS, T.E., ROSENBLUTH, M.N., TAYLOR, P.L., KELLMAN, A.G., GRAY, D.S., HOLLMANN, E.M., COMBS, S.K., Mitigation of tokamak disruptions using high-pressure gas injection, *Phys. Rev. Lett.* **89** (2002) 055001.
- [9] <http://www-amdis.iaea.org/ALADDIN>
- [10] <http://aphysics2.lanl.gov/tempweb>
- [11] ABDALLAH, J., CLARK, R.E.H., COWAN, R.D., Los Alamos National Laboratory, Los Alamos Manual No. LA 11436-M-I (1988).
- [12] COWAN, R.D., *The Theory of Atomic Structure and Spectra* (1981) (University of California Press, Berkeley).
- [13] CLARK, R.E.H., et al., Los Alamos National Laboratory, Los Alamos Manual No. LA 11436-M-II (1988).
- [14] CSANAK, G., TAYLOR, H.S., YARIS, R., Green's function technique in atomic and molecular physics, *Adv. At. Mol. Phys.* **7** (1971) 287.
- [15] CSANAK, G., TAYLOR, H.S., YARIS, R., Many-body methods applied to electron scattering from atoms and molecules. II. inelastic processes, *Phys. Rev. A* **3** (1971) 1322.
- [16] CLARK, R.E.H., ABDALLAH, J., MANN, J.B., Integral and differential cross-section for electron-impact ionization, *Astrophys. J.* **381** (1991) 597; ARCHER, B.J., CLARK, R.E.H., FONTES, C.J., ZHANG, H.L., (2002) Los Alamos Memorandum No. LA-UR-02-1526.

- [17] ZHANG, H.L., SAMPSON, D.H., Relativistic distorted-wave collision strengths and oscillator strengths for the 105  $\Delta n = 0$  transitions with  $n = 2$  in the 85 B-like ions with  $8 \leq Z \leq 92$ , *At. Data Nucl. Data Tables* **56** (1994) 41.
- [18] HOWALD, A.M., Gregory, D.C., Meyer, F.W., PHANEUF, R.A., MÜLLER, A., DJURIC, N., DUNN, G.H., Electron-impact ionization of Mg-like ions:  $S^{4+}$ ,  $Cl^{5+}$ , and  $Ar^{6+}$ , *Phys. Rev. A* **33** (1986) 3779.
- [19] PINDZOLA, M.S., GRIFFIN, D.C., BOTTCHEER, C., Electron-impact ionization in the magnesium-isoelectronic sequence, *Phys. Rev. A* **33** (1986) 3787.
- [20] HAKEL, P., SHERRILL, M.E., MAZEVET, S., ABDALLAH JR., J., COLGAN, J., KILCREASE, D.P., MAGEE, N.H., FONTES, C.J., ZHANG, H.L., The new Los Alamos opacity code ATOMIC, *J. Quant. Spectrosc. Radiat. Transfer* **99** (2006) 265.
- [21] LUO, Z., AN, Z., HE, F., LI, T., LONG, X., PENG, X., Correction of the influence of the substrate upon the measurement of *K*-shell ionization cross-sections, *J. Phys. B* **29** (1996) 4001.
- [22] FONTES, C.J., ZHANG, H.L., ABDALLAH, JR., J., in *Atomic Processes in Plasmas* (2004), AIP Conf. Proc. No. 730, (AIP, NY, 2004), p. 41.
- [23] SAMPSON, D.H., ZHANG, H.L., MOHANTY, A.K., CLARK, R.E.H., A Dirac-Fock-Slater approach to atomic structure for highly charged ions, *Phys. Rev. A* **40** (1989) 604.
- [24] ZHANG, H.L., SAMPSON, D.H., MOHANTY, A.K., Fully relativistic and quasirelativistic distorted-wave methods for calculating collision strengths for highly charged ions, *Phys. Rev. A* **40** (1989) 616.
- [25] ZHANG, H. L., SAMPSON D.H., Rapid relativistic distorted-wave approach for calculating cross-sections for ionization of highly charged ions, *Phys. Rev. A* **42** (1990) 5378.

# RADIATIVE RECOMBINATION AND PHOTOIONIZATION OF HEAVY ELEMENT IMPURITIES IN PLASMAS

M.B. TRZHASKOVSKAYA<sup>1</sup>, V.K. NIKULIN<sup>2</sup>, R.E.H. CLARK<sup>3</sup>

<sup>1</sup> National Research Center “Kurchatov Institute”  
Petersburg Nuclear Physics Institute, Gatchina, Russia

<sup>2</sup> Division of Plasma Physics, Atomic Physics and Astrophysics of the Ioffe Institute,  
Russia

<sup>3</sup> Nuclear Data Section  
International Atomic Energy Agency  
Vienna, Austria

## Abstract

We present a new unified database of atomic data for heavy element impurities in plasmas. The database contains the radiative recombination and photoionization cross-sections for 67 ions of Si, Cl, Ar, Ti, Cr, Fe, Ni, Cu, Kr, Mo, Xe, and W in the electron energy range closely above the ionization threshold to 50 keV as well as radiative rates for 9 tungsten ions in the temperature range from  $10^3\text{K}$  to  $10^{10}\text{K}$ . The total radiative recombination cross-sections included in the database have been obtained with regard to contributions of the ground and all excited electron states up to the principal quantum number  $n=20$ . Subshell photoionization cross-sections for states with  $n\leq 12$  and the orbital momenta  $\ell\leq 6$  were fitted by a simple analytical expression with five fit parameters. The fit parameters are given in the database. Calculations have been performed in the framework of the fully relativistic Dirac-Fock treatment of photoionization and radiative recombination processes taking into account all significant multipoles of the radiative field. The influence of relativistic and non-dipole effects is discussed. It is shown that the relativistic Maxwell-Jüttner distribution of continuum electrons should be used in the radiative rate calculations at a high temperature. This changes the results significantly compared to the commonly used Maxwell-Boltzmann distribution.

## 1. INTRODUCTION

The radiative recombination process is one of the important mechanism influencing the ionization equilibria and the thermal balance of fusion and astrophysical plasmas. The rate equations governing the ion-atom distributions involve data for radiative recombination and for the inverse photoionization process. Of special interest are the data for heavy element ions which are major impurities in fusion reactors. Accurate values of the photoionization cross-sections (PCS) and the radiative recombination cross-sections (RRCS) as well as the radiative recombination rate coefficients (RR rates) for impurity ions are required for a comprehensive diagnostics of temperature, density, and ionization state of plasmas.

A number of extensive relevant calculations are available. The configuration-averaged PCS were computed by Clark et al. [1] within the Hartree-Fock method including relativistic corrections, for ground and excited electron states  $1s \leq n\ell \leq 5g$  in the He-like through Al-like iso-electronic sequences of elements with atomic numbers  $6 \leq Z \leq 100$ . The PCS were fitted by analytical expressions involving 15 fit parameters in the photon energy range between the ionization threshold  $E_{\text{th}}$  and  $10E_{\text{th}}$ . The non-relativistic Hartree-Fock and close-coupling calculations of PCS for the ground and low excited states of atoms and ions were made under the Opacity Project led by Seaton [2]. Data for a great deal of atoms and ions were obtained, primarily for astrophysical applications (see e.g. [3], TOPbase, version 0.7).

Verner and Ferland [4] calculated RR rates for ions of all elements from H through Zn using PCS from [5, 6] obtained within the Dirac-Slater (DS) method for ground states and

PCS from [1] for excited states. Calculations of RRCS by Gu [7] for iso-electronic sequences from H-like to F-like of elements with  $Z \leq 28$  were performed within the DS method using the dipole approximation for energies  $\leq 10E_{\text{th}}$ . At higher energies, the PCS values were found using the fitting formulas obtained by Verner et al. [5, 6].

Calculations of both radiative and dielectronic recombination were carried out by Nahar and Pradhan [8–10] in the framework of the  $R$ -matrix method with allowance made for relativistic effects in the Breit-Pauli approximation. The dipole approximation was used. To date, PCS and RR rates were obtained for above 50 ions, primarily for elements of astrophysical interest.

Exact relativistic benchmark calculations of RRCS with regard to all multipoles of the radiative field were performed by Ichihara and Eichler [11] for radiative recombination of an electron with bare nuclei ( $1 \leq Z \leq 112$ ) with a capture of the electron into the K, L, and M shells. Tabulations are presented in the energy range from the ionization threshold to the relativistic regime.

In the paper by Badnell [12], RR rates for iso-electronic sequences, from the H-like to Na-like, for elements  $Z \leq 30$ ,  $Z = 36, 42$ , and  $54$  are presented. Calculations were carried out taking into account the multiconfiguration interaction and semi-relativistic corrections. The highest electron energy under consideration is equal to  $1.36 \cdot Z^2$  keV. The dipole approximation was used.

Our aim is to develop a new unified database of RRCS, PCS and RR rates for the heavy element impurity ions of elements from Si to W which are of importance for modeling and diagnostics of plasmas [13]. Particular attention is given to tungsten ions because tungsten impurities are deeply involved in fusion studies. Moreover, the data on highly-charged tungsten ions are important in the performance of future fusion devices which are under development, for example, in the framework of the tungsten programme [14]. However, there exist only a few calculations of PCS and RRCS for excited states of tungsten ions [1, 11]. As to RR rates, data for three tungsten ions obtained using an approximate method were presented in [15].

Our calculations are based on the fully relativistic treatment of the photoionization and radiative recombination processes. We use the Dirac-Fock (DF) method where the exchange electron interaction was taken into account exactly, as distinct from the commonly used DS method where the exchange is included approximately.

In the present paper, we, first, consider the method of calculations. Second, we study the influence of the non-dipole and some specific relativistic effects on RRCS and RR rates. These effects are shown to play an essential role in calculations of PCS, RRCS and RR rates, altering the results considerably at enough high electron energies. An important finding is that the relativistic Maxwell-Jüttner distribution of continuum electrons should be used in calculations of RR rates at a high temperature instead of the usual Maxwell-Boltzmann distribution. Preliminary results concerning the impact of the relativistic and non-dipole effects in the radiative recombination process in hot plasmas, were presented in [16].

Third, we deal with the proper asymptotic behavior of the relativistic PCS with regard to all multipoles as well as a role of the exact consideration of the electron exchange. Fourth, our results are compared with other calculations.

Finally, we discuss the results of calculations included in the database [17]: (i) Partial PCS and RRCS for 67 ions of twelve elements which are important in plasma investigation [18, 19]. Calculations were performed for ground and all excited electron states up to states with the principal quantum number  $n = 20$ . To minimize a great bulk of data, PCS for states with  $n \leq 12$  and the orbital quantum number  $\ell \leq 6$  obtained in the calculations were fitted by an analytical expression involving five fit parameters. The database contains fit parameters for  $\sim 7500$  electron states. (ii) Total RRCS for more than 40 values of electron kinetic energy  $E_k$  from closely above the ionization threshold to  $E_k \approx 50$  keV [18, 19]. Total RRCS were found as a result of summation over all states with  $n \leq 20$ . (iii) Partial and total RR rates for nine highly-charged ions of tungsten from the Pd-like ion  $W^{28+}$  to the bare nucleus  $W^{74+}$  in the wide temperature range  $10^3 \text{ K} \leq T \leq 10^{10} \text{ K}$  [20].

Calculations were carried out by the use of our computer code package RAINE [21]. Numerical methods applied in the codes, as well as problems of an accuracy of the calculations, were discussed at length in [22, 23]. Note that PCS and RRCS are calculated with a numerical accuracy of  $\sim 0.1\%$ .

## 2. METHOD OF CALCULATION

Relativistic treatment of the photoionization process leads to the following expression for the cross-section per one electron of the  $i$ -th atomic subshell [24]:

$$\sigma_{ph}^{(i)} = \frac{4\pi^2\alpha}{k(2j_i+1)} \sum_L \sum_{\kappa} \left[ (2L+1)Q_{LL}^2(\kappa) + LQ_{L+1L}^2(\kappa) \right. \\ \left. + (L+1)Q_{L-1L}^2(\kappa) - 2\sqrt{L(L+1)}Q_{L-1L}(\kappa)Q_{L+1L}(\kappa) \right]$$

Here  $k$  is the photon energy,  $L$  is the multipolarity of the radiative field,  $\kappa = (\ell - j)(2j + 1)$  is the relativistic quantum number,  $j$  and  $\ell$  are the total and orbital momentum of the electron, and  $\alpha$  is the fine structure constant. Relativistic units ( $\hbar = m_0 = c = 1$ ) are used in Eqs. (1) - (3).

The reduced matrix element  $Q_{\Lambda L}(\kappa)$  is determined by the expression

$$Q_{\Lambda L}(\kappa) = ([\bar{\ell}][\ell_i]/[\Lambda])^{1/2} C_{\bar{\ell}0\ell_i,0}^{\Lambda 0} A \begin{pmatrix} \bar{\ell} & 1/2 & j \\ \ell_i & 1/2 & j_i \\ \Lambda & 1 & L \end{pmatrix} R_{1\Lambda} \\ + ([\ell][\bar{\ell}_i]/[\Lambda])^{1/2} C_{\ell 0\bar{\ell}_i,0}^{\Lambda 0} A \begin{pmatrix} \ell & 1/2 & j \\ \bar{\ell}_i & 1/2 & j_i \\ \Lambda & 1 & L \end{pmatrix} R_{2\Lambda}, \quad (2)$$

Where  $\bar{\ell} = 2j - \ell$ ,  $C_{\bar{\ell}_1 0 \ell_2 0}^{\Lambda 0}$  is the Clebsch-Gordan coefficient,  $A \begin{pmatrix} \ell_1 & 1/2 & j_1 \\ \ell_2 & 1/2 & j_2 \\ \Lambda & 1 & L \end{pmatrix}$  is the

recoupling coefficient for the four angular momenta,  $[a]$  denotes the expression  $(2a+1)$ ,  $R_{1\Lambda}$  and  $R_{2\Lambda}$  are the radial integrals in the form

$$R_{1\Lambda} = \int_0^{\infty} G_i(r) F(r) j_{\Lambda}(kr) dr, \\ R_{2\Lambda} = \int_0^{\infty} G(r) F_i(r) j_{\Lambda}(kr) dr. \quad (3)$$

Here  $G(r)$  and  $F(r)$  are the large and small components of the Dirac electron wavefunction multiplied by  $r$ ,  $j_{\Lambda}(kr)$  is the spherical Bessel function of the  $\Lambda$ -th order. The subscript  $i \equiv n_i \kappa_i$  is related to the bound electron state while designations with no subscript are related to the continuum state. Electron wavefunctions are calculated in the framework of the DF method where the exchange electron interaction is included exactly both between bound electrons and between bound and free electrons [22, 23]. The bound and continuum wavefunctions are calculated in the self-consistent field of the corresponding ions with  $N+1$  and  $N$  electrons, respectively.

The partial RRCS for the recombining  $N$ -electron ion when an electron is captured into the  $i$ -th subshell, can be expressed in terms of the corresponding PCS for the recombined  $(N+1)$ -electron ion as follows

$$\sigma_{rr}^{(i)} = q^{(i)} A \sigma_{ph}^{(i)}, \quad (4)$$

where  $q^{(i)}$  is the number of vacancies in the  $i$ -th subshell prior to recombination and  $A$  is the transformation coefficient which can be derived from the principle of the detailed balance. The exact relativistic expression for the transformation coefficient is written as follows [11, 22]

$$A_{rel} = \frac{k^2}{2m_0c^2E_k + E_k^2}, \quad (5)$$

while the non-relativistic approximation yields

$$A = \frac{k^2}{2m_0c^2E_k}. \quad (6)$$

The difference between RRCS obtained with coefficients  $A_{rel}$  and  $A$  is discussed in Section 3.

The relativistic RR rates  $\alpha_{rel}^{(i)}(T)$  can be found using the thermal average over fully relativistic RRCS provided the continuum electron velocity is described by the relativistic so-called Maxwell-Jüttner distribution when the distribution function  $f(E)$  normalized to unity is written as follows [25]

$$f(E)dE = \frac{E(E^2 - 1)^{1/2}}{\theta e^{1/\theta} K_2(1/\theta)} \times e^{-(E-1)/\theta} dE. \quad (7)$$

Here  $E$  is the total electron energy in units of  $m_0c^2$  including the rest energy,  $\theta = k_\beta T / m_0c^2$  is the characteristic dimensionless temperature,  $k_\beta$  is the Boltzmann constant,  $T$  is the temperature, and  $K_2$  denotes the modified Bessel function of the second order.

With allowance made for the relativistic distribution (Eq. (7)) along with the relativistic transformation coefficient  $A_{rel}$  (Eq. (5)), the expression for the relativistic RR rates takes the factorized form

$$\alpha_{rel}^{(i)}(T) = \langle \nu \sigma_{rr}^{(i)} \rangle = F_{rel}(\theta) \cdot \alpha^{(i)}(T) \quad (8)$$

Here  $\nu = (p/E)c$  is the electron velocity with the momentum  $p = \sqrt{E^2 - 1}$ . The factor  $\alpha^{(i)}(T)$  has the form of the usual RR rate with the non-relativistic distribution [26]

$$\alpha^{(i)}(T) = \left(\frac{2}{\pi}\right)^{1/2} c^{-2} (m_0 k_\beta T)^{-3/2} q^{(i)} \int_{E_{ih}}^{\infty} k^2 \sigma_{ph}^{(i)}(k) e^{(E_{ih}-k)/(k_\beta T)} dk. \quad (9)$$

According to Eq. (8), to obtain the relativistic RR rates,  $\alpha^{(i)}(T)$  involving relativistic values of  $\sigma_{ph}^{(i)}(k)$ , should be multiplied by the relativistic factor  $F_{rel}(\theta)$  which has the form

$$F_{rel}(\theta) = \sqrt{\frac{\pi}{2}} \theta / K_2(1/\theta) e^{1/\theta}. \quad (10)$$

This is just the factor which comes from the relativistic distribution together with the relativistic transformation coefficient. It should be emphasized that the factor was disregarded in all previous calculations and databases.

One may easily obtain an approximate expression for the relativistic factor  $F_{rel}(\theta)$  using the asymptotic expansion of the Bessel function  $K_2(1/\theta)$  at large  $1/\theta$  [27], that is, at low temperature. The approximate relativistic factor may be written as

$$\tilde{F}_{rel}(\theta) = 1/(1 + 1.875\theta + 0.8203\theta^2 + \dots) \quad (11)$$

As will be shown in Section 3,  $\tilde{F}_{rel}(\theta)$  provides an excellent approximation for  $F_{rel}(\theta)$  with the terms through order  $\theta^2$  at  $\theta \leq 1$ .

The integral in Eq. (9) was calculated with the five-point Newton-Coates quadrature formula at temperature  $T \leq 10^8$  K. At higher temperature for a rapid convergence of the integral, we calculated the integral written in the form proposed by Nahar et al. [28]

$$\alpha^{(i)}(T) = \left(\frac{2}{\pi}\right)^{1/2} c^{-2} m_0^{-3/2} (k_\beta T)^{-3/2} q^{(i)} \int_0^1 (E_{th} - k_\beta T \ln x)^2 \sigma_{ph}^{(i)}(k) dx. \quad (12)$$

The integral in Eq. (12) was estimated using the Gauss and refined quadrature nodes [29]. The integration was terminated if the difference between the integral values obtained with the Gauss and refined quadratures, was less than a prescribed accuracy. If the integral was calculated with an insufficient accuracy, the integration interval was reduced and the integral was recalculated. Then the rest of the interval was estimated. This method turns out to be efficient and provides the accuracy required in calculations.

### 3. INFLUENCE OF RELATIVISTIC, NON-DIPOLE, AND EXCHANGE EFFECTS ON RADIATIVE RECOMBINATION AND PHOTOIONIZATION CROSS-SECTIONS AND RADIATIVE RATES

As is well known, the relativistic and non-dipole (multipole) effects are of great importance in consideration of photoionization and radiative recombination at high electron energies, especially for heavy and highly-charged ions [11, 22, 30]. For example, the relativistic RRCS calculations [11] taking account of all multipoles were compared for a few representative cases with those performed within the widely used non-relativistic dipole (ND) approximation in order to assess the accuracy of the latter. Discrepancies between the two calculations for bare nuclei were demonstrated to reach 10% for  $Z=30$  and electron kinetic energy  $E_k \leq 10$  keV and may exceed 10% for  $Z = 50$  and  $E_k \leq 10$  keV. The discrepancy amounts to more than 10% for  $Z = 92$  even at the lowest electron energy  $E_k = 1$  eV. At the high energy  $E_k = 1000$  keV, the exact relativistic RRCS values exceed the ND values by a factor of  $\sim 10$  for  $Z=10$  and by a factor of  $\sim 30$  and more for  $Z=30, 50$  and  $92$ .

Nevertheless, the multipole and relativistic effects are usually neglected in plasma calculations. For example, the dipole approximation is used in [8–10] while energies to 100 keV were considered. The dipole approximation is also adopted in [12] although the highest electron energy equals  $\sim 4000$  keV for  $Z=54$ . As to relativistic effects, the majority of calculations [1, 8–10, 12] were carried out using semi-relativistic corrections. The widely-used tables of hydrogenic RR rates by Burgess [31] were calculated within the ND approximation for temperatures up to  $T = \infty$ .

Here we will consider the influence of the relativistic transformation coefficient on RRCS as well as of the relativistic factor  $F_{rel}(\theta)$  on RR rates. Although the relativistic transformation coefficient between PCS and RRCS has the form of Eq. (5), the majority of calculations [4, 9, 10, 12] make use of the non-relativistic form of Eq. (6). The difference between RRCS obtained with Eq. (5) and Eq. (6), can be written as

$$\frac{\sigma_{rr}^{(i)}(A) - \sigma_{rr}^{(i)}(A_{rel})}{\sigma_{rr}^{(i)}(A_{rel})} = \frac{E_k}{2m_0 c^2}. \quad (13)$$

As is evident, the difference depends on the electron energy  $E_k$  only and does not exceed  $\sim 10\%$  at  $E_k \leq 100$  keV. However the difference becomes considerable at higher energies and reaches  $\sim 100\%$  at 1000 keV.

The relativistic factor  $F_{rel}(\theta)$ , as it follows from Eq. (10), depends on a temperature only. The  $T$ -dependence of the factor is demonstrated in Fig. 1. As is seen, the factor  $F_{rel}(\theta)$  differs from unit noticeably beginning with several tens of keV. Adopting the relativistic distribution of continuum electrons instead of the non-relativistic distribution results in a decrease of the RR rate value by a factor of 1.2 at plasma temperature  $k_\beta T = 50$  keV and up to a factor of 7 at  $k_\beta T = 1000$  keV. It should be noted that the hydrogenic RR rates [31] tabulated for temperatures up to  $T = \infty$  were calculated for the non-relativistic Maxwell-Boltzmann distribution.

In Fig. 1, one can also compare the exact relativistic factor  $F_{rel}(\theta)$  (Eq. (10)) and the approximate factor  $\tilde{F}_{rel}(\theta)$  (Eq. (11)). As can be seen, there is a little difference between them. The approximate and exact values of the factor differ by  $\sim 4\%$  at 500 keV and  $\sim 25\%$  at 1000 keV.

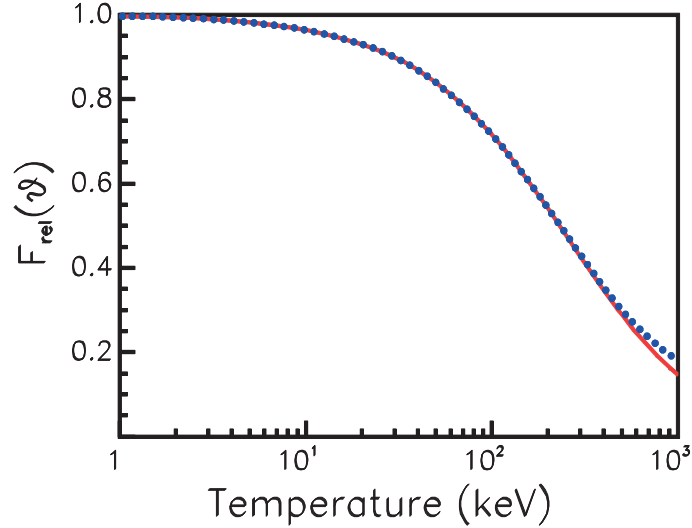


FIG. 1. The relativistic factor for RR rates. Red solid, the exact factor  $F_{rel}(\theta)$ ; blue dotted, the approximate factor  $\tilde{F}_{rel}(\theta)$ . This figure was changed from Fig. 1 of Ref. [16].

To gain a better illustration, we display in Fig. 2 RR rates obtained with and without regard to the relativistic factor  $F_{rel}(\theta)$  for recombination of the He-like ion of Xe with a capture of an electron into the  $2s$  state. One can see that the inclusion of the relativistic factor changes  $\alpha^{(2s)}(T)$  considerably at high temperatures.

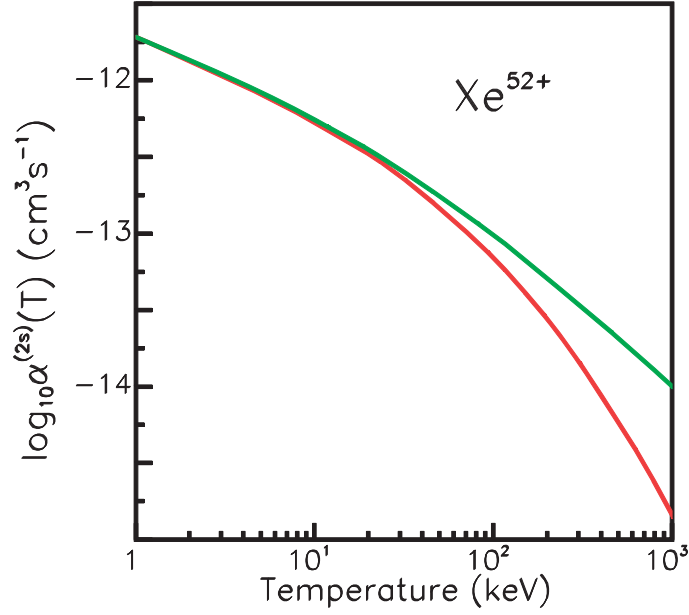


FIG. 2. The RR rates  $\alpha^{(2s)}(T)$  for recombination of  $Xe^{52+}$  with a capture of an electron into the 2s state. Red, calculation with regard to the relativistic factor  $F_{rel}(\theta)$ ; green, without regard to the factor.

To assess the impact of non-dipole effects, that is terms with  $L > 1$  in Eq. (1), we compare in Fig. 3 RRCS obtained by the DF method within the electric dipole approximation  $\sigma_{rr}^{(i)}(dip)$  (blue curves) with the DF calculations including all necessary multipoles  $\sigma_{rr}^{(i)}(L)$  (red curves) for ions of Fe and W in the energy range  $1 \text{ keV} \leq E_k \leq 1000 \text{ keV}$ . As is shown, red and blue curves diverge noticeably even at several keV. At  $E_k = 10 \text{ keV}$ , the difference  $\Delta_{dip} = [\sigma_{rr}^{(i)}(L) - \sigma_{rr}^{(i)}(dip)] / \sigma_{rr}^{(i)}(L)$  between exact and dipole values of RRCS is from 8% to 18% in dependence on the orbital quantum number. At the highest energy 1000 keV in the case of  $W^{74+}$ ,  $\sigma_{rr}^{(i)}(dip)$  is smaller than the exact value  $\sigma_{rr}^{(i)}(L)$  by factors of 5.4, 14.5, 22 and 43 for the 1s, 2p<sub>1/2</sub>, 3d<sub>3/2</sub>, and 4f<sub>5/2</sub> subshells, respectively.

As is demonstrated in Fig. 3, the difference  $\Delta_{dip}$  is scarcely affected by the atomic number, ion charge, and principal quantum number of the shell. There is practically the same difference, for example, for recombination of the bare nucleus  $W^{74+}$  with an electron into the 1s state and for recombination of the many-electron ion  $W^{6+}$  with an electron into the 6s state as well as for recombination of the bare nucleus  $Fe^{26+}$  with an electron into the 1s, 2p<sub>1/2</sub>, and 3d<sub>3/2</sub> states and for recombination of the ion  $Fe^{8+}$  into 4s, 4p<sub>1/2</sub> and 3d<sub>3/2</sub> states, respectively. However, as is seen, there is a noticeable dependence of  $\Delta_{dip}$  on the orbital quantum number  $\ell_i$ , the difference being larger for larger  $\ell_i$ .

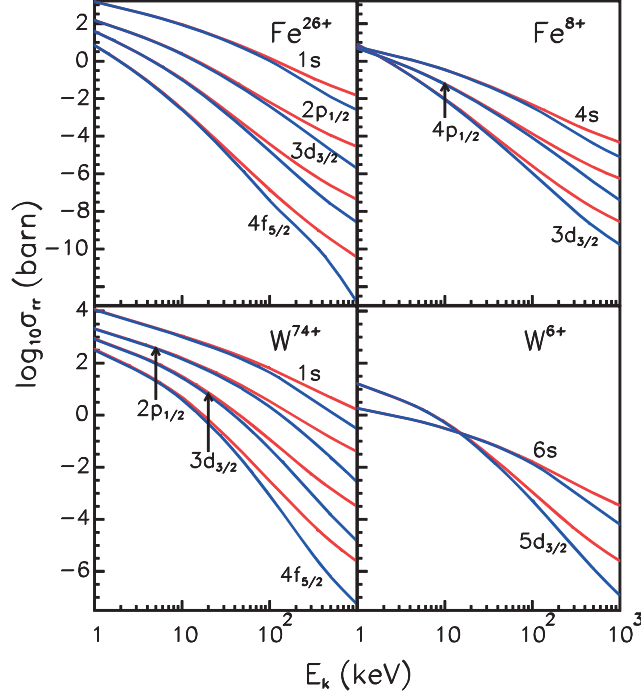


FIG. 3. Subshell RRCS calculated by the DF method taking into account all multipoles  $L$  (red) and within the electric dipole approximation (blue). This figure was taken from Fig. 2 of Ref. [20].

These results show that relativistic RRCS obtained within the dipole approximation are inaccurate at high energies. Table 1 demonstrates how many multipoles  $L$  must be taken into consideration for various shells of the recombined ion  $W^{73+}$  at various electron energies to achieve a numerical accuracy  $\sim 0.1\%$  prescribed in our PCS calculations.

TABLE 1. A NUMBER OF MULTIPOLES  $L$  TAKEN INTO ACCOUNT IN THE PCS CALCULATIONS FOR THE  $W^{73+}$  ION

$E_k$ , keV	1s	$2p_{1/2}$	$3d_{3/2}$	$4f_{5/2}$
10	5	6	8	10
50	6	7	10	12
100	7	8	11	14
500	13	16	21	26
1000	19	24	31	37

As is seen, a number of multipoles is vastly larger than  $L=1$  as is assumed in the dipole approximation.

From the aforesaid, it may be inferred that the dipole approximation is also inadequate in calculations of RR rates at high temperature. In Fig. 4, we present the percentage difference between the exact  $\alpha_{rel}^{(i)}(L)$  and dipole  $\alpha_{rel}^{(i)}(dip)$  values of RR rates which may be written as

$$\Delta_{\alpha} = \left[ \frac{\alpha_{rel}^{(i)}(L) - \alpha_{rel}^{(i)}(dip)}{\alpha_{rel}^{(i)}(L)} \right] \cdot 100\% \quad (14)$$

The difference is given for recombination of the He-like ions  $\text{Fe}^{24+}$ ,  $\text{Xe}^{52+}$ , and  $\text{W}^{72+}$  with electrons captured into the  $2s$ ,  $2p_{1/2}$ ,  $3s$ ,  $3p_{1/2}$  and  $3d_{3/2}$  shells. These shells (along with appropriate fine structure components) are the lowest states making a significant contribution to total RR rates. As is evident from Fig. 4, the difference  $\Delta_\alpha$  is larger for heavy elements. The inclusion of higher multipoles may change partial RR rates for  $\text{W}^{72+}$  by  $\sim 7\%$  at temperature  $T = 10^8$  K, by  $\sim 20\%$  at  $T = 10^9$  K, and by  $\sim 50\%$  at  $T = 10^{10}$  K. Consequently, total RR rates obtained within the dipole approximation have to be considerably smaller than accurate values obtained using all multipoles at a high temperature.

Another problem in the RR rate calculations is concerned with the necessity to involve PCS or RRCS at high electron energies. Because the proper PCS calculation at a high energy is a difficult task, asymptotic tails are frequently matched [4, 12]. For example, it was noted in [4] that the analytical expression for PCS presented in [1] did not ensure a correct asymptotic behavior above  $10E_{\text{th}}$ . PCS for excited states decrease too slowly with increasing energy to give the unnaturally high RR rates. To avoid this situation, the appropriate high energy tails were matched. It should be noted that high-energy tails given in TOP base [3] are also inaccurate.

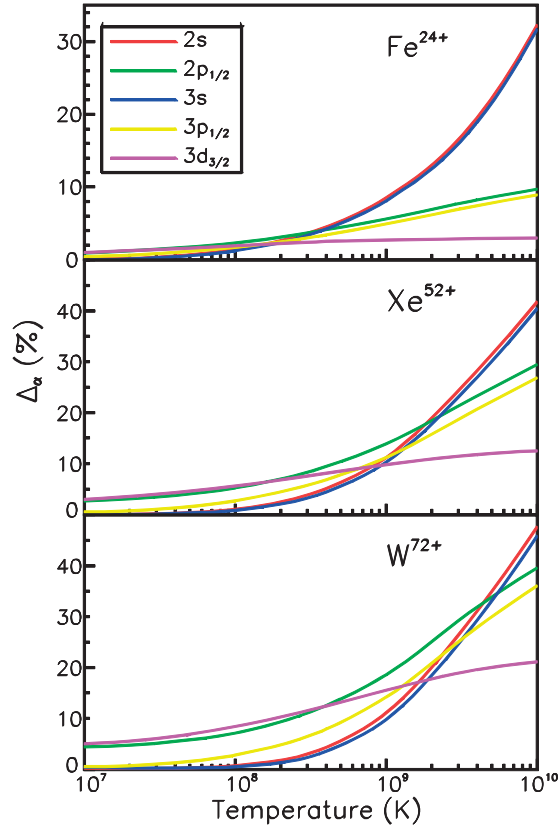


FIG. 4. Difference  $\Delta_\alpha$  between RR rates calculated with regard to all multipoles and in the electric dipole approximation for recombination of the He-like ions with an electron captured into the  $2s$ ,  $2p_{1/2}$ ,  $3s$ ,  $3p_{1/2}$ , and  $3d_{3/2}$  shells. This figure was taken from Fig. 3 of Ref. [20].

Usually, the well-known asymptotic expression is involved which has been derived in the framework of the ND approximation and has the form [32, 33]

$$\sigma_{ph}^{(i)}(k) \propto k^{-(3.5+\ell_i)} \quad (15)$$

However, this  $k$ -dependence of PCS breaks down for the asymptotic behavior of the relativistic PCS with regard to all multipoles. In Fig. 5, we present the product  $\sigma_{ph}^{(ns)} \times k^m$  for

the  $ns$  electrons of the Li-like ion  $\text{Fe}^{23+}$  and Na-like ion  $\text{W}^{63+}$ . The DF calculations of  $\sigma_{ph}^{(ns)}$  were carried out with allowance made for all  $L$  (blue and red solid curves) and within the electric dipole approximation (green dashed curves). If the PCS asymptotic behavior (Eq. (15)) holds, the product  $\sigma_{ph}^{(ns)} \times k^{3.5}$  should be a constant at enough high photon energies  $k$ . As is seen, blue curves increase in the whole photon energy range  $1 \text{ keV} \leq k \leq 1100 \text{ keV}$  at  $m=3.5$  (Figs. 5(a) and 5(b)). Green curves behave like an approximate constant at the photon energy  $k \approx 100\text{--}400\text{keV}$ . However, at higher energies they also increase.

We found that the PCS asymptotic  $k$ -dependence for the  $s$  electrons in the relativistic multipole case has the following form

$$\sigma_{ph}^{(ns)}(k) \propto k^{-2.2}. \quad (16)$$

In Figs. 5(c) and 5(d), the product  $\sigma_{ph}^{(ns)} \times k^{2.2}$  is shown (red curves). The value  $m=2.2$  was obtained through fitting the  $\sigma_{ph}^{(ns)}$  values at lower energies. In this case, red curves associated with relativistic calculations including all multipoles, reach a rather good asymptote at high energies  $k \approx 500\text{--}600\text{keV}$ . As is shown, this asymptotic behavior holds for the  $s$  shells with various  $n$  ( $2 \leq n \leq 12$ ). We checked also that Eq. (16) holds for various elements and various ion charges.

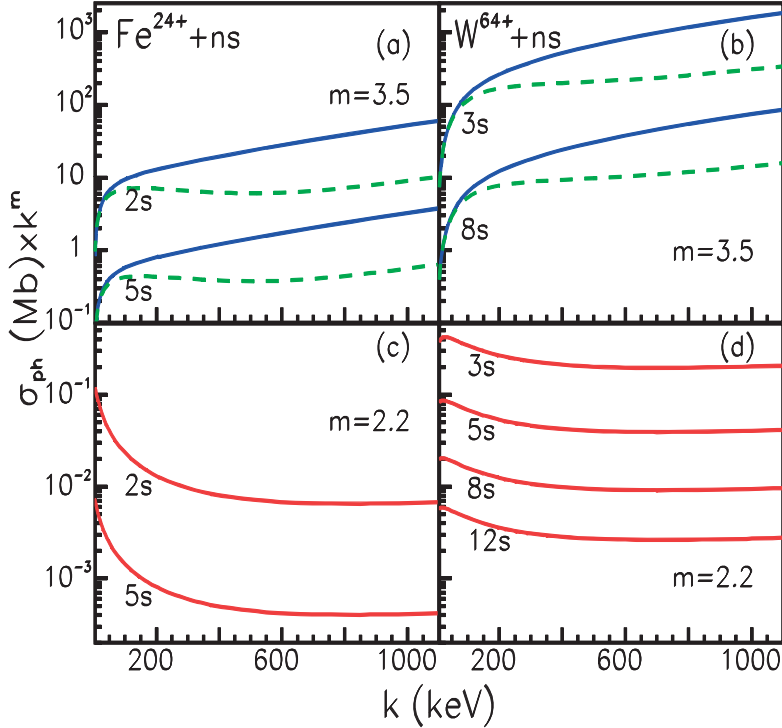


FIG. 5. PCS  $\sigma_{ph}^{(ns)}(k)$  multiplied by  $k^m$  where  $m=3.5$  ((a) and (b)) and  $m=2.2$  ((c) and (d)) for the  $ns$  shells of the Fe and W ions. Blue and red solid, DF calculation with regard to all multipoles; green dashed DF calculation within the electric dipole approximation. This figure was taken from Fig. 4 of Ref. [20].

It should be noted that the asymptotic behavior (Eq. (16)) obtained in the present work for the  $s$  electrons, correlates well with the energy-dependence  $\sigma_{ph}(k)$  for the  $1s$  shell of the hydrogen-like high- $Z$  ions presented by Bethe and Salpeter [33]. They stated that in the

relativistic case,  $\sigma_{ph}^{(1s)} \propto k^{-m}$  where  $m$  varies almost monotonously from  $m \approx 2.7$  to  $m=1$  at the ultra-relativistic limit, never taking the value  $m=3.5$

However, in a general case, the PCS asymptotic behavior is unknown. So in computing RR rates, we found values of  $\sigma_{ph}^{(i)}$  with no any analytical asymptote by the direct DF calculation. The calculations were carried out up to the energy  $E_k \approx 7000$  keV for the  $s$ ,  $p$ , and  $d$  states and to several hundred keV for states with larger orbital momenta.

A proper consideration of the electron exchange may be also of importance in the PCS and RRCS calculations. In Fig. 6, values of RRCS obtained by the DF method (red curves) for low-charged ions  $Ti^{4+}$ ,  $Xe^{8+}$ , and  $W^{6+}$  are compared with calculations performed by the DS method where the exchange is taken into account approximately (blue curves). The electron states presented are the lowest ones making a major contribution to total RRCS. As is seen, there is a significant difference between the DF and DS calculations especially at low electron energies and in the vicinity of the Cooper minimum.

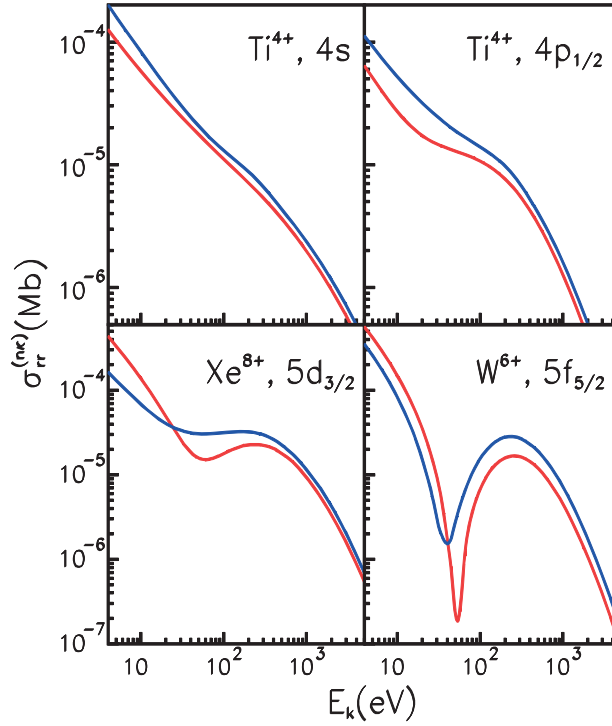


FIG. 6. Subshell RRCS versus the electron energy  $E_k$ . Red, DF calculation; blue, DS calculation

Exact values of the difference between the DF and DS results

$$\Delta_{DS} = \left[ \frac{\sigma_{rr}(DS) - \sigma_{rr}(DF)}{\sigma_{rr}(DF)} \right] \cdot 100\% \quad (17)$$

are listed in Table 2 for several energies from the range under consideration.

TABLE 2. DIFFERENCE  $\Delta_{DS}$  (IN %) BETWEEN THE SUBSHELL RRCS CALCULATED BY THE USE OF THE DF AND DS MODELS

$E_k, \text{eV}$	$\text{Ti}^{4+}$		$\text{Xe}^{8+}$	$\text{W}^{6+}$
	$4s$	$4p_{1/2}$	$5d_{3/2}$	$5f_{5/2}$
10	44	92	-50	-45
109	18	30	71	116
1153	20	27	24	61
9646	22	33	29	69
31392	24	37	31	71
50327	24	37	31	71

As is seen, the difference  $\Delta_{DS}$  is considerable not only at low electron energies but at higher energies as well. For example,  $\Delta_{DS}$  is also large at  $E_k > 30$  keV where it changes from 24% to 71% and kept constant. Due to such essential difference in the RRCS and PCS values, the more accurate DF model should be preferred.

For highly-charged ions at reasonably high energies, the difference  $\Delta_{DS}$  is not so important. For example, our DF calculation of RRCS for recombination of the He-like nickel with an electron into the  $2s$ ,  $2p_{1/2}$  and  $2p_{3/2}$  shells agree with the DS results by Scofield [34] within 3% in the energy range  $4 \text{ keV} \leq E_k \leq 50 \text{ keV}$ .

Note that at the very low photoelectron energy, both the one-electron approximations may be not quite accurate due to possible influence of electron correlations. However, the correlation effect is not expected to be substantial for photoionization of ions with the only electron above a closed core or the He-like ions considered here (see Table 5 below). In Fig. 7, our DF values of  $\sigma_{ph}(E_k)$  are compared with the background non-resonant PSC obtained by Nahar et al. [8, 10] using the Breit-Pauli  $R$ -matrix method where the electron correlations are taken into account. The comparison is given for the available Li-like ions, namely, for the  $2s$  shell of  $\text{Ne}^{7+}$  (7(a)) and of the highly-charged  $\text{Fe}^{23+}$  (7(b)). As is clearly seen, our results are in a good agreement with the  $R$ -matrix calculations in the energy range under consideration. Average deviations between the two calculations are 3.7% for  $\text{Ne}^{7+}$  and 1.6% for  $\text{Fe}^{23+}$ .

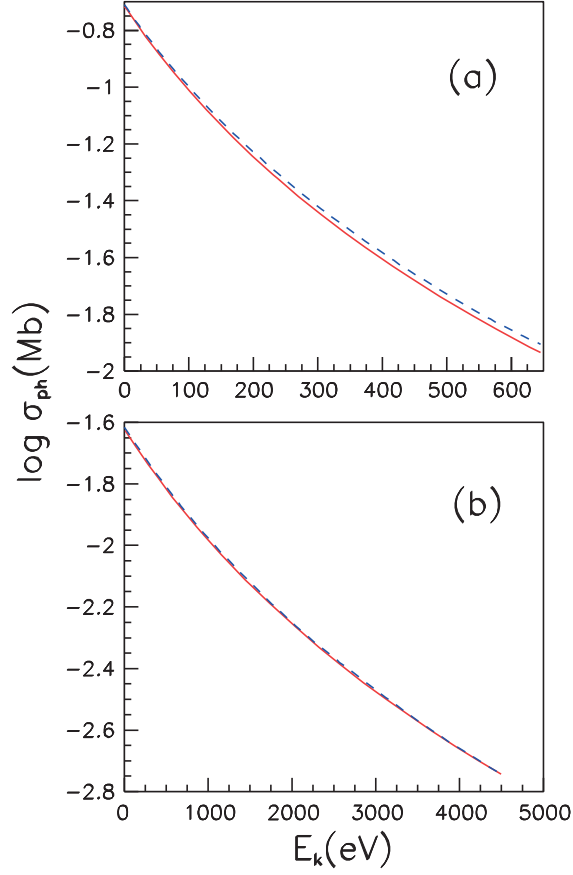


Fig. 7. PCS calculated within the DF method (red solid) and the Breit-Pauli R-matrix method [8, 10] (blue dashed) for the 2s shell of the Li-like ions  $Ne^{7+}$  (a) and  $Fe^{23+}$  (b). This figure was taken from Fig. 2 of Ref. [18].

In Table 3, our PCS calculations are compared with results by Ichihara et al. [11] and by Badnell [12] for the 1s shell of the H-like ion  $Xe^{53+}$ . The case of a one-electron ion is particularly convenient for study of the influence of non-dipole effects and the method of calculation in general because the ion is free from any inter-electron interactions. Besides for a one-electron ion, values of PCS obtained in the velocity and length gauge coincide.

As is evident from Table 3, our calculation is in excellent agreement in the wide range of electron energy  $1eV \leq E_k \leq 6000$  keV with values from relativistic calculations [11] where all multipoles were included. Values of  $\sigma_{ph}^{(1s)}$  coincide with an accuracy of three significant digits given in [11]. The only difference  $\sim 1\%$  between the two calculations is at the highest energy  $E_k = 6000$  keV. The comparison of PCS for all  $K$ ,  $L$ , and  $M$  shells from [11] with our calculations for ions  $Xe^{53+}$  and  $W^{73+}$  revealed also the excellent agreement which is not more than 1% at highest energies.

By contrast, PCS obtained by Badnell exceed our values by  $\sim 16\%$  in the energy range  $E_k < 4$  keV and become smaller at higher energies, decreasing by a factor of 7.6 at  $E_k \approx 1800$  keV and by a factor of 30 at  $E_k \approx 4000$  keV. The comparison of our calculation of  $\sigma_{ph}^{(2s)}$  for the comparatively light ion  $Fe^{23+}$  with the corresponding results by Badnell, reveals the similar tendency, but smaller in magnitude at low energies. It is possible that the difference at low energies arises due to a failing of the method of calculations used in [12].

TABLE 3. COMPARISON OF OUR PCS CALCULATIONS WITH RESULTS BY ICHIHARA et al. [11] AND BY BADNELL [12] FOR THE  $1s$  SHELL OF  $\text{Xe}^{53+}$

$E_k$ , keV	$\sigma_{ph}^{(1s)}$ , Mb		$E_k$ , keV	$\sigma_{ph}^{(1s)}$ , Mb		Difference
	Ichihara et al.	Present		Badnell	Present	
0.001	1.94(-3)	1.94(-3)	0.00083	2.246(-3)	1.937(-3)	-16%
0.04	1.94(-3)	1.94(-3)	0.03967	2.240(-3)	1.935(-3)	-16%
0.4	1.89(-3)	1.89(-3)	0.3967	2.186(-3)	1.892(-3)	-16%
2.	1.71(-3)	1.71(-3)	1.824	1.938(-3)	1.732(-3)	-15%
4.	1.52(-3)	1.52(-3)	3.967	1.734(-3)	1.523(-3)	-14%
40.	3.08(-4)	3.08(-4)	39.67	3.256(-4)	3.114(-4)	-4.5%
80.	9.94(-5)	9.94(-5)	83.31	9.095(-5)	9.206(-5)	1.2%
200.	1.40(-5)	1.41(-5)	182.4	1.539(-5)	1.740(-5)	12%
400.	2.75(-6)	2.75(-6)	396.7	1.894(-6)	2.802(-6)	factor 1.5
800.	5.97(-7)	5.97(-7)	833.1	2.071(-7)	5.495(-7)	factor 2.6
2000.	1.13(-7)	1.13(-7)	1824.	1.730(-8)	1.318(-7)	factor 7.6
4000.	4.07(-8)	4.07(-8)	3967.	1.350(-9)	4.117(-8)	factor 30
6000.	2.39(-8)	2.36(-8)				

However, the difference at higher energies is due to a combination of ignoring the higher multipoles and using the semi-relativistic approximation in [12].

Our total RR rates for tungsten ions  $\text{W}^{74+}$ ,  $\text{W}^{64+}$ , and  $\text{W}^{56+}$  were compared with the relativistic calculations by Kim and Pratt [15] performed using a number of approximations, in particular, only few RRCS values were calculated by the DS method and thereafter all other necessary cross-sections for each a state  $n\kappa$  were obtained by interpolation using the quantum defect method. Total RR rates are given for four values of temperature in the range  $1 \text{ keV} \leq k_\beta T \leq 30 \text{ keV}$ . Although the approximate approach was used in [15], the comparison revealed a reasonable agreement between the two calculations. For example, the difference ranged from 3% to 11% depending on the temperature for bare nucleus and from 15% to 30 % for the many-electron ion  $\text{W}^{56+}$ .

#### 4. RESULTS PRESENTED IN UNIFIED DATABASE

The ionic states of the heavy element impurities which are of the most importance in fusion studies, are the fully stripped and H-like ions, the most stable He-, Ne-, Ar-, Kr-, and Pd-like ions with closed shells, besides the Ni-like ions and the Er-like ion for tungsten [13]. The Ni-like and Er-like ions with open electron shells are shown in our calculations to be metastable. Ground states of such ions have closed shells. Total energies  $E_{\text{tot}}$  calculated within the DF method for the Ni-like and Er-like ions together with total energies for the ions in ground states are presented in Table 4 for elements under consideration. As is seen, total energies for ions with closed shells lie always lower than for ions with the same configurations as in the relevant neutral atoms. Because of this, we adopted the configuration  $[\text{Ar}]3d_{3/2}^4 3d_{5/2}^6$  as the ‘‘Ni-like’’ one and the configuration  $[\text{Xe}]4f_{5/2}^6 4f_{7/2}^8$  as the ‘‘Er-like’’ one. Now the database contains the total RRCS for 67 ions listed in Table 5 and partial PCS for ground and excited states of the associated recombined ions.

TABLE 4. TOTAL ENERGY OBTAINED IN THE DF CALCULATION FOR THE Ni-LIKE ( $[Ar] 3d_{3/2}^4 3d_{5/2}^4 4s^2$ ) AND Er-LIKE ( $[Xe] 4f_{5/2}^6 4f_{7/2}^6 6s^2$ ) IONS AS COMPARED WITH THE CORRESPONDING IONS HAVING THE CLOSED SHELL CONFIGURATIONS

Ion	$-E_{\text{tot}}$ , eV			Difference, eV
	Closed shell ions	Ni-like ions	Er-like ion	
Kr <sup>8+</sup>	75396.0	75214.5		181.5
Mo <sup>14+</sup>	108295.3	107859.6		435.7
Xe <sup>26+</sup>	193702.8	192497.4		1205.0
W <sup>46+</sup>	399294.0	396132.0		3162.0
W <sup>6+</sup>	439443.0		439325.1	117.9

TABLE 5. CHARGES OF RECOMBINING IONS

Element Configuration	Si	Cl	Ar	Ti	Cr	Fe	Ni	Cu	Kr	Mo	Xe	W
Bare nucleus	14	17	18	22	24	26	28	29	36	42	54	74
H-like	13	16	17	21	23	25	27	28	35	41	53	73
He-like	12	15	16	20	22	24	26	27	34	40	52	72
Ne-like	4	7	8	12	14	16	18	19	26	32	44	64
Ar-like				4	6	8	10	11	18	24	36	56
“Ni-like”									8	14	26	46
Kr-like										6	18	38
Pd-like											8	28
“Er-like”												6

For these ions, RRCS and PCS were calculated for more than 40 values of the electron energy  $E_k$  in the range from the energy closely above the ionization threshold to  $E_k \approx 50$  keV. We computed total RRCS for the capture of an electron into all states beginning from the first open shell up to subshells with  $n = 20$  as follows

$$\sigma_{rr}^{\text{tot}} = \sum_{n=n_{\text{min}}}^{\infty} \sum_{\kappa=\mp 1, \mp 2, \dots, -n} \sigma_{rr}^{(n\kappa)}, \quad (18)$$

where  $n_{\text{min}}$  combined with the appropriate value of  $\kappa$  refers to the ground state. The sum over  $\kappa$  in Eq. (18) has a finite number of terms which decrease rather rapidly as  $\kappa$  increases. Higher the energy  $E_k$ , the more rapidly the terms decrease. So for a specific value of  $n$ , all possible  $2n-1$  values of the quantum number  $\kappa$  were taken into account, provided the corresponding  $\sigma_{rr}^{(n\kappa)}$  contribute to  $\sigma_{rr}^{\text{tot}}$  more than 0.01%.

A different situation exists in summation of the infinite series over  $n$  in Eq. (18). Relative contributions of states with various  $n$  to the total RRCS

$$B_n = \left[ \sum_{\kappa} \sigma_{rr}^{(n\kappa)} / \sigma_{rr}^{\text{tot}} \right] \cdot 100\%, \quad (19)$$

are displayed in Fig. 8 for the Ne-like ions Cu<sup>19+</sup>, Mo<sup>32+</sup>, and W<sup>64+</sup> and for four values of the energy  $E_k$ . We see that  $B_n$  decreases rapidly at  $n \leq 6$  but there is no rapid convergence at higher  $n$ . Although the contributions  $B_n$  for the largest value  $n = 20$  do not exceed several percent, the tails of all curves in Fig. 8 decrease very slow – the lower  $E_k$ , the slower the

decrease. So in a general case, the remainder of the infinite series over  $n$  should be taken into consideration.

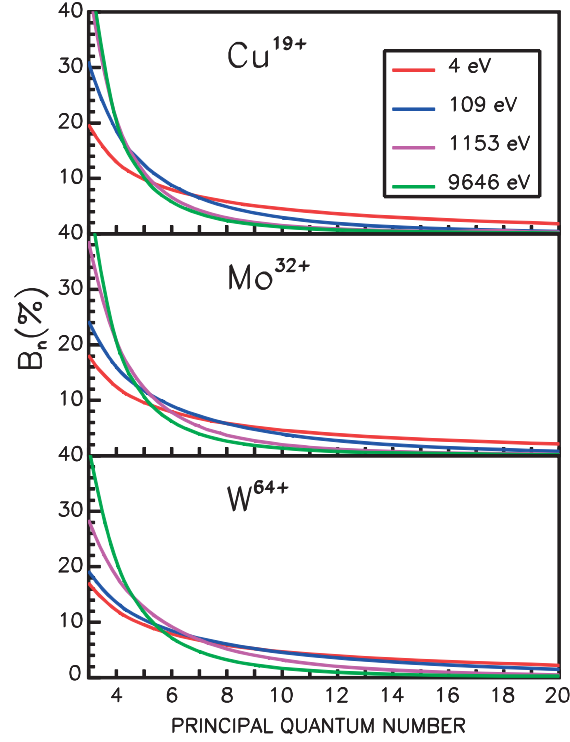


FIG. 8. Convergence of the infinite series over  $n$  (Eq. (18)) in the form of contributions  $B_n$  to the total RRCS for four values of the electron energy  $E_k$ . This figure was taken from Fig. 4 of Ref. [18].

In a real plasma, however, there is a cutoff of bound levels from density effects, above which recombination is not meaningful. For fusion plasmas with electron density in the range of  $10^{14} / \text{cm}^3$ , the upper limit on the principal quantum number is  $n \leq 20$ . Therefore, the correction associated with the remainder of the infinite series in Eq. (18) is not needed in fusion plasmas. In our calculations, the series over  $n$  was found as a result of summation up to  $n = 20$ . Nevertheless, the correction should be taken into account for ideal plasmas, for example, the low-density astrophysical plasma. If necessary, this may be arranged by a number of ways [16, 35].

Total RRCS are presented in the database for 41 values of the electron energy from the range  $4 \text{ eV} \leq E_k \leq 50 \text{ keV}$ . Energy points are logarithmic over the range. Besides, we included six equidistant values of the energy near the threshold  $1 \text{ eV} \leq E_k \leq 3.5 \text{ eV}$  for ions of Si, Cl, Ar, Ti, and Cr which are of interest for astrophysical plasmas as well.

The  $E_k$ -dependence of total RRCS for all ions included in the database [17] is shown in Fig. 9. As is seen, the energy dependence  $\sigma_{rr}^{tot}(E_k)$  for the lowest-charged ions is a non-monotone function in the range  $E_k < 1 \text{ keV}$ . This is associated with non-monotone behavior of partial cross-sections  $\sigma_{rr}^{(nk)}(E_k)$  for the lowest states (see Fig. 6). For the higher-charged ions, the  $E_k$ -dependence shows up as smooth monotone curves.

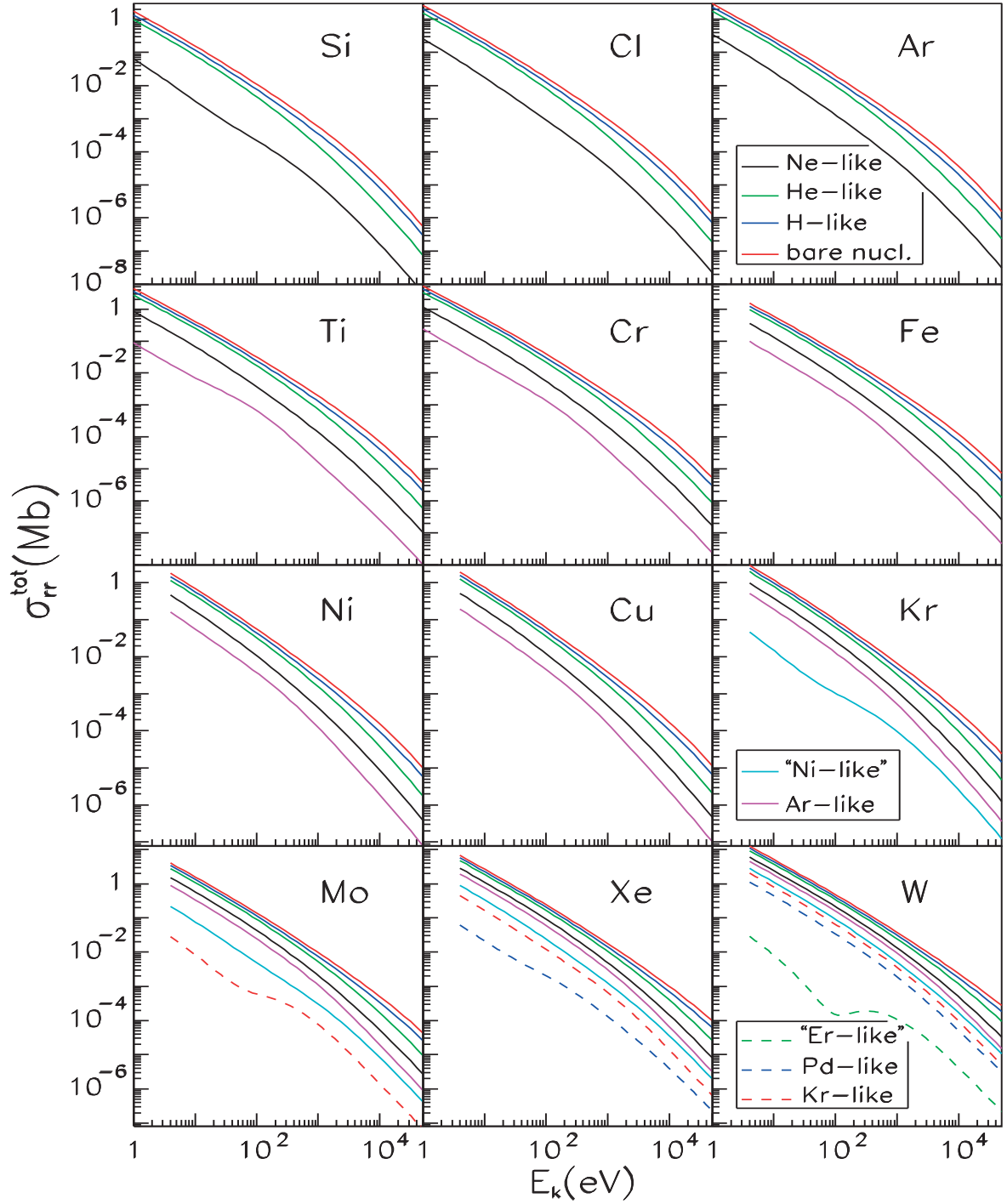


FIG. 9. Total RRCS for ions under consideration.

To decrease a wealth of data, subshell PCS for electron states with  $n \leq 12$  and  $\ell \leq 6$  were fitted by the following analytical expressions obtained in [6]

$$\sigma_{ph}^{(n\ell)}(k) = \sigma_0 F(y), \quad y = k / k_0. \quad (20)$$

Here  $\sigma_0$  and  $k_0$  are fit parameters and the function  $F(y)$  has the form

$$F(y) = \left[ (y-1)^2 + y_w^2 \right] y^{-Q} \left( 1 + \sqrt{y/y_a} \right)^p, \quad (21)$$

where  $y_w$ ,  $y_a$  and  $p$  are three additional fit parameters, and  $Q = 5.5 + \ell - 0.5p$ . With Eqs. (20) and (21), the fit parameters were found by minimizing the mean-square deviation from calculated values. We used the simplex search method described in [36].

The fitting procedure was carried out in the photon energy range from  $k_{\min} = E_{th} + 1\text{eV}$  for  $Z \leq 24$  and  $k_{\min} = E_{th} + 4\text{eV}$  for  $Z \geq 26$  to the energy  $k_{\max}$  where  $\sigma_{ph}^{(nk)}(k_{\max})$  falls by five orders of magnitude as compared with its maximum value, the energy  $E_k = k_{\max} - E_{th}$  being less than 50 keV. Usually,  $k_{\max}$  is of the order of  $100E_{th}$  for the  $s$ ,  $p$ ,  $d$  and  $f$  shells and of the order of  $10E_{th}$  for the  $g$ ,  $h$  and  $i$  shells.

To assess the accuracy of the fitting procedure, we found the relative root-mean-square error  $\delta_{av}$  as follows:

$$\delta_{av} = \sqrt{\frac{1}{M} \sum_{i=1}^M \left[ \frac{\sigma_{calc}^{(nk)}(k_i) - \sigma_{fit}^{(nk)}(k_i)}{\sigma_{calc}^{(nk)}(k_i)} \right]^2} \cdot 100\%, \quad (22)$$

where  $M$  is the number of points involved in the fitting,  $\sigma_{calc}^{(nk)}(k_i)$  and  $\sigma_{fit}^{(nk)}(k_i)$  are values of PCS calculated and obtained in the fitting, respectively. As a rule, the fit accuracy was good with  $\delta_{av} \leq 2\%$ . However, there exist some worst-fitting cases where the error may be greater and reaches  $\sim 10\%$ . Fig. 10 shows that even non-monotone curves  $\sigma_{ph}^{(nk)}(k)$  having a deep Cooper minima may be fitted quite good. Note that the high  $nf$  shells of the low-charged  $W^{5+}$  ion refer to the worst-fitting cases.

Using the fit parameters and Eqs. (20) and (21), one can obtain PCS  $\sigma_{ph}^{(nk)}(k)$  per one electron at any photon energy in the range from  $k_{\min}$  to  $k_{\max}$ . The associated value of RRCS  $\sigma_{rr}^{(nk)}(k)$  may be also obtained with Eqs. (4) and (5).

Presented in the database [17] are the fit parameters for  $\sim 7500$  electron states of 67 recombined ions (see Table 5 for associated recombining ions) along with values of the ionization threshold energy  $E_{th}$  obtained in the DF calculations, the maximum energy  $k_{\max}$  and the error  $\delta_{av}$ .

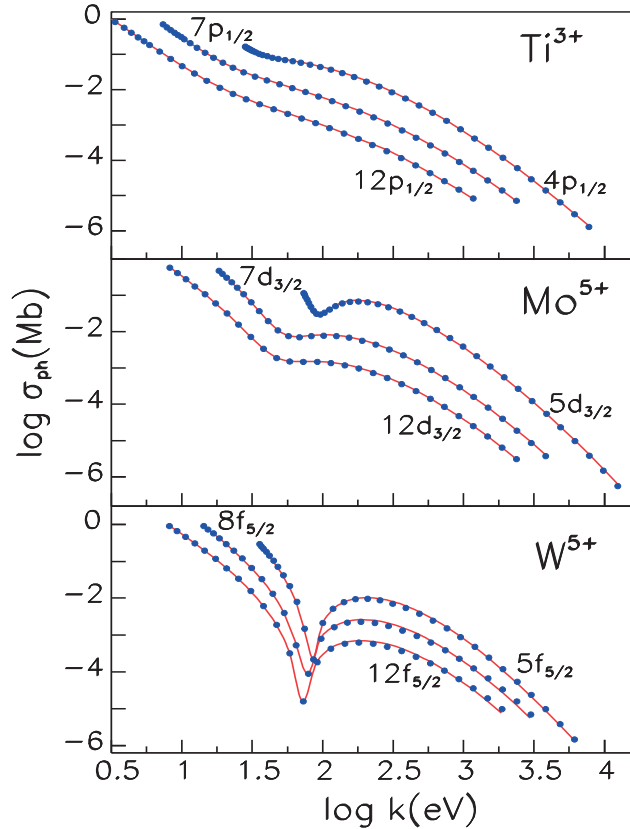


FIG. 10. Fitting non-monotone curves  $\sigma_{ph}^{(nk)}(k)$ . Red curves, calculated PCS; blue circles, fitted PCS.

As was mentioned above, the majority of previous calculations refer to ions of elements with atomic numbers  $Z \leq 54$  [2–4,6–10,12] while there are a few calculations for ions as heavy as tungsten [1,11,15]. Because tungsten impurities are of importance in fusion studies and accurate atomic data on ionization-recombination coefficients are currently unavailable [14], we present in [17] RR rates for the following highly-charged ions of tungsten: the bare nucleus  $W^{74+}$ , the H-like ion  $W^{73+}$ , the He-like ion  $W^{72+}$ , the Be-like ion  $W^{70+}$ , the Ne-like ion  $W^{64+}$ , the Ar-like ion  $W^{56+}$ , the "Ni-like" ion  $W^{46+}$ , the Kr-like ion  $W^{38+}$  and the Pd-like ion  $W^{28+}$ . Values of RR rates are given for fifteen values of temperature from the range  $10^3 \text{ K} \leq T \leq 10^{10} \text{ K}$ . Relativistic DF calculations were performed using expressions and methods described above.

The database contains partial RR rates  $\alpha_{rel}^{(n\kappa)}$  for electron states with  $n \leq 12$  and  $\ell \leq 6$  as well as total RR rates which are written as

$$\alpha_{tot} = \sum_{n\kappa} \alpha_{rel}^{(n\kappa)} \quad (23)$$

The summation in Eq. (23) was extended over all electron states with  $n \leq 20$ .

We present partial RR rates for high electron shells because their magnitudes are sometimes larger or comparable to those for lower shells. In Fig. 11, partial RR rates  $\alpha_{rel}^{(n\kappa)}$  are shown versus the principal quantum number  $n$  for shells with various orbital momenta  $0 \leq \ell \leq 6$ . The data are given for recombination of the ion  $W^{72+}$  with an electron at the temperature  $T=10^7$  K. It is seen that  $\alpha_{rel}^{(n\kappa)}$  for shells with large  $\ell$  are at times comparable with values for shells with smaller  $\ell$  at the specific  $n$  and at other times exceed them. Though RR rates usually fall with increasing  $n$ ,  $\alpha_{rel}^{(n\kappa)}$  for shells with large  $\ell$  first increases with  $n$  (see the  $n$ -dependence of the  $g$ ,  $h$ , and  $i$  shells). So that a number of shells with large  $n$  and  $\ell$  contribute considerably to  $\alpha_{tot}$ , especially at low temperature.

A dependence of partial RR rates on temperature is displayed in Fig. 12. One can see that at  $T \leq 10^8$  K,  $\alpha_{rel}^{(3p_{3/2})}$  and  $\alpha_{rel}^{(3d_{5/2})}$  are very close to each other and exceed  $\alpha_{rel}^{(3s)}$  for the more inner  $3s$  shell. At  $T \leq 10^5$  K,  $\alpha_{rel}^{(4f_{7/2})}$  and  $\alpha_{rel}^{(3s)}$  have approximately the same magnitude. In the case of  $W^{64+}$  and  $T = 10^3$  K, the maximum contribution to  $\alpha_{tot}$  from the low  $3d_{5/2}$  state is  $1.02 \times 10^{-10} \text{ cm}^3/\text{s}$  while the contribution of the highest state presented,  $12i_{13/2}$ , is  $1.83 \times 10^{-11} \text{ cm}^3/\text{s}$ , i.e., 18% of the maximum contribution. Shells presented in the database contribute from 70% to 99% into total RR rates. Total RR rates  $\alpha_{tot}$  for nine tungsten ions under consideration are presented in Fig. 13.

## RESULTS PRESENTED IN UNIFIED DATABASE

In succeeding years the database was supplemented with the data for 53 tungsten ions from the range  $W^{14+} - W^{71+}$  [37].

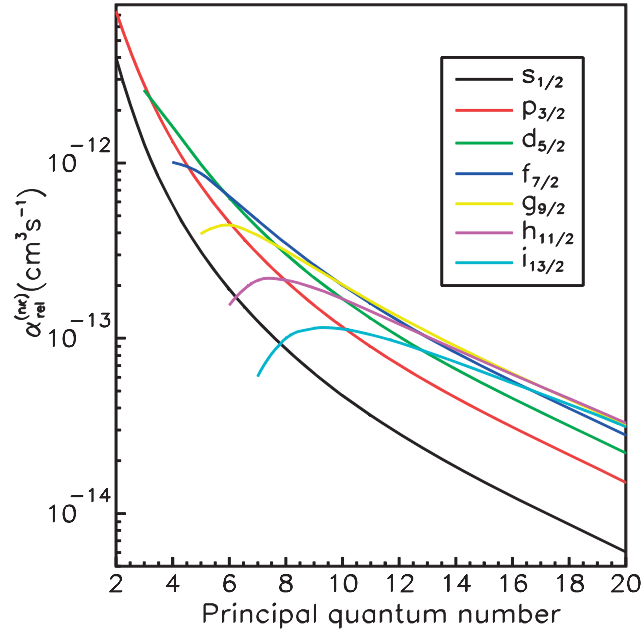


FIG. 11. Partial RR rates  $\alpha_{rel}^{nk}$  versus the principal quantum number  $n$  for recombination of  $W^{72+}$  with an electron into various states at  $T=10^7$ K. This figure was taken from Fig. 5 of Ref. [20].

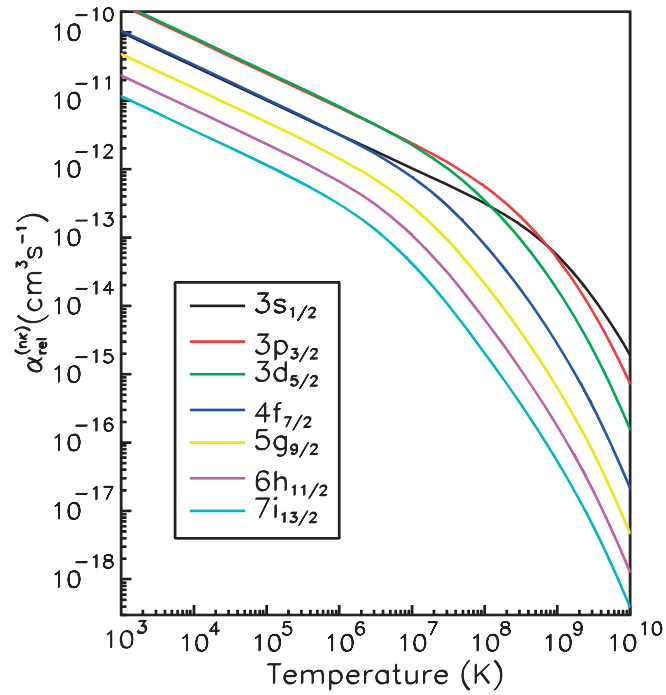


FIG. 12. Partial RR rates  $\alpha_{rel}^{nk}$  versus temperature  $T$  for recombination of  $W^{64+}$  with an electron into various states. This figure was taken from Fig. 6 of Ref. [20].

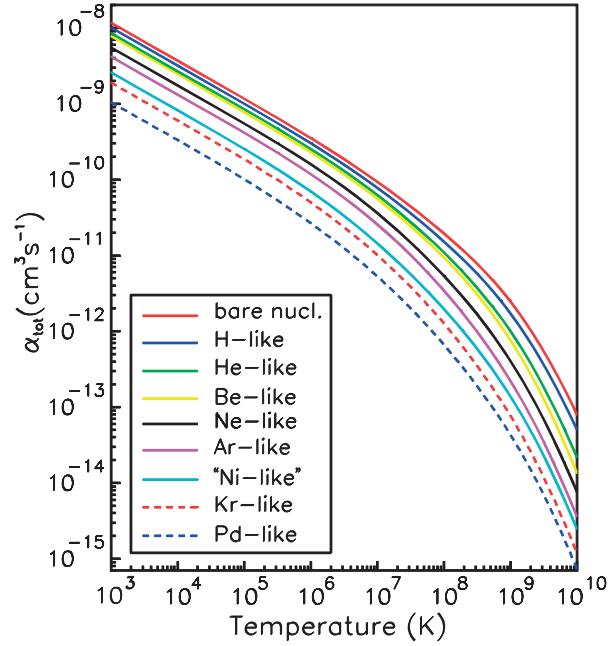


FIG. 13. Total RR rates  $\alpha_{\text{tot}}$  for tungsten ions.

## 5. CONCLUSIONS

A new unified database of atomic data for heavy element impurities in plasmas has been developed. Partial PCS and RRCS as well as total RRCS have been included in the database. Relativistic DF calculations have been performed in the electron energy range closely above ionization thresholds to 50 keV for 67 ions of 12 elements which are of importance in fusion study. Partial PCS have been fitted by a simple analytical expression.

The database contains also the relativistic partial and total RR rates calculated using the DF method in the wide temperature range  $10^3 \text{ K} \leq T \leq 10^{10} \text{ K}$  for nine tungsten ions which are of great current interest and for which the data are not available.

New fully relativistic formula for RR rates has been derived using the relativistic Maxwell-Jüttner distribution of continuum electrons. The formula is factorized giving rise to the temperature-dependent relativistic correction factor for which the usual expression should be multiplied. The factor changes RR rates considerably at a high energy.

A contribution of non-dipole effects in the RR rates calculation has been shown to be significant at electron energies of the order of several keV and higher.

## ACKNOWLEDGMENTS

This work was funded through International Atomic Energy Agency Contract No.13349/RBF and partially by Russian Foundation for Basic Research (project No. 09-02-00352) which are gratefully acknowledged.

## REFERENCES

- [1] CLARK, R.E.H., COWAN, R.D., BOBROWICZ, F.W., Isoelectronic sequence fits to configuration-averaged photoionization cross-sections and ionization energies, *At. Data Nucl. Data Tables* **34** (1986) 415.
- [2] SEATON, M.J., Atomic data for opacity calculations. I. General description, *J. Phys. B* **20** (1987) 6363.
- [3] CUNTO, W., MENDOZA, C., OCHSENBEIN, F., ZEIPEN, C.J., TOPbase at thr CDS, *Astron. Astrophys.* **275** (1993) L5.
- [4] VERNER, D.A., FERLAND, G.J., Atomic data for astrophysics. I. Radiative recombination rates for H-like, He-like, Li-like and Na-like ions over a broad range of temperature, *Ap. J. Suppl.* **103** (1996) 467.

- [5] BAND, I.M., TRZHASKOVSKAYA, M.B., VERNER, D.A., YAKOVLEV, D.G., K-shell photoionization cross sections: calculations and simple fitting formulae, *Astron. Astrophys.* **237** (1990) 267.
- [6] VERNER, D.A., YAKOVLEV, D.G., BAND, I.M., TRZHASKOVSKAYA, M.B., Subshell photoionization cross-sections and ionization energies of atoms and ions from He to Zn, *At. Data Nucl. Data Tables* **55** (1993) 233.
- [7] GU, M.F., Radiative recombination rate coefficients for bare through F-like isosequences of Mg, Si, S, Ar, Ca, Fe, and Ni, *Astrophys. J.* **589** (2003) 1085.
- [8] NAHAR, S.N., PRADHAN, A.K., ZHANG, H.L., Electron-ion recombination rate coefficients and photoionization cross-sections for astrophysically abundant elements. V. relativistic calculations for Fe XXIV and Fe XXV for x-ray modeling, *Astrophys. J. Suppl. Series*, **133** (2001) 255.
- [9] NAHAR, S.N., PRADHAN, A.K., Self-consistent R-matrix approach to photoionization and unified electron-ion recombination, *Radiation Phys. Chem.* **70** (2004) 323.
- [10] NAHAR, S.N., PRADHAN, A.K., Electron-ion recombination rate coefficients and photoionization cross-sections for astrophysically abundant elements. X. Ne VIII and Ne IX for ultraviolet and x-ray modeling, *Astrophys. J. Suppl. Series* **162** (2006) 417.
- [11] ICHIHARA, A., EICHLER, J., Cross-sections for radiative recombination and the photoelectric effect in the K, L, and M shells of one-electron systems with  $1 \leq Z \leq 112$  calculated within an exact relativistic description, *At. Data Nucl. Data Tables* **74** (2000) 1.
- [12] BADNELL, N.R., Radiative recombination data for modeling dynamic finite-density plasmas, *Astrophys. J. Suppl. Series* **167** (2006) 334.
- [13] O'MULLANE, M., BADNELL, N.R., SUM-MERS, H.P., WHITEFORD, A.D., WITTHOEFT, M., "Atomic Data and Modelling for Analysis of Heavy Impurity Behavior in Fusion Plasmas". 1-st IAEA RCM "Atomic Data for Heavy Element Impurities in Fusion Reactors", November 2005, IAEA, Vienna, Austria; Available from: <[www.admdis.iaea.org/CRP/Heavy\\_elements/Presentations/](http://www.admdis.iaea.org/CRP/Heavy_elements/Presentations/)>.
- [14] NEU, R., et al., Tungsten: an option for divertor and main chamber plasma facing components in future fusion devices, *Nucl. Fusion* **45** (2005) 209.
- [15] KIM, Y.S., PRATT, R.H., Direct radiative recombination of electrons with atomic ions: cross-sections and rate coefficients, *Phys. Rev. A* **27** (1983) 2913.
- [16] TRZHASKOVSKAYA, M.B., NIKULIN, V.K., CLARK, R.E.H., Multipole and relativistic effects in radiative recombination process in hot plasmas, *Phys. Rev. E* **78** (2008) 035401(R).
- [17] TRZHASKOVSKAYA, M.B., NIKULIN, V.K., CLARK, R.E.H., Radiative Recombination and Photoionization Cross Sections for Heavy Element Impurities in Plasmas", CRP "Atomic Data for Heavy Element Impurities in Fusion Reactors"; Available from: <<http://www-amdis.iaea.org/ALADDIN>> (accessed 2009).
- [18] TRZHASKOVSKAYA, M.B., NIKULIN, V.K., CLARK, R.E.H., Radiative recombination and photoionization cross-sections for heavy element impurities in plasmas, *At. Data Nucl. Data Tables* **94** (2008) 71.
- [19] TRZHASKOVSKAYA, M.B., NIKULIN, V.K., CLARK, R.E.H., Radiative recombination and photoionization cross-sections for heavy element impurities in plasmas: II. Ions of Si, Cl, Ar, Ti, Cr, Kr, and Xe, *At. Data Nucl. Data Tables* **95** (2009) 987.
- [20] TRZHASKOVSKAYA, M.B., NIKULIN, V.K., CLARK, R.E.H., Radiative recombination rate coefficients for highly-charged tungsten ions, *At. Data Nucl. Data Tables* **96** (2010) 1.
- [21] BAND, I.M., LISTENGARTEN, M.A., TRZHASKOVSKAYA, M.B., FOMICHEV, V.I., "Computer Program Complex RAINE", Pts. I-VI, LNPI Reports LNPI-289 (1976); LNPI-298; LNPI-299; LNPI-300 (1977); LNPI-498 (1979); LNPI-1479 (1989).
- [22] TRZHASKOVSKAYA, M.B., NIKULIN, V.K., Radiative recombination of an electron with multiply charged uranium ions, *Optics and Spectroscopy* **95** (2003) 537.

- [23] BAND, I.M., TRZHASKOVSKAYA, M.B., NESTOR, JR, C.W., TIKKANEN, P.O., RAMAN, S., Dirac–Fock internal conversion coefficients, *At. Data Nucl. Data Tables* **81** (2002) 1.
- [24] RACAVY, G., RON, A., “Spectroscopic and Group Theoretical Methods in Physics” (North-Holland, Amsterdam, 1968) p. 175.
- [25] ALEXANIAN, M., Photon bremsstrahlung from an extreme-relativistic electron gas, *Phys. Rev.* **165** (1968) 253.
- [26] BARFIELD, W.D., Photoionisation cross-sections and radiative recombination rate coefficients for molybdenum ions, *J. Phys. B: At. Mol. Opt. Phys.* **13** (1980) 931.
- [27] “Handbook of Mathematical Functions”, ed. by M. ABRAMOWITZ, M. and STEGUN, I.A. (National Bureau of Standards, Appl. Math. Series **5**, 1964).
- [28] NAHAR, S.N., PRADHAN, A.K., Unified treatment of electron-ion recombination in the close-coupling approximation, *Phys. Rev. A* **49** (1994) 1816.
- [29] KRONROD, A.S., “Nodes and Weights of Quadrature Formulas” (Consultants Bureau, New York, 1965).
- [30] TRZHASKOVSKAYA, M.B., NIKULIN, V.K., NEFEDOV, V.I., YARZHEMSKY, V.G., Relativistic photoelectron angular distribution parameters in the quadrupole approximation, *J. Phys. B: At. Mol. Opt. Phys.* **34** (2001) 3221.
- [31] BURGESS, A., Tables of hydrogenic photoionization cross-sections and recombination coefficients, *Memoirs of the Royal Astronomical Society* **69** (1965) 1.
- [32] FANO, U., COOPER, J.W., Spectral distribution of atomic oscillator strengths, *Rev. Mod. Phys.* **40** (1968) 441.
- [33] BETHE, H.A., SALPETER, E.E., “Quantum Mechanics of One- and Two-Electron Atoms” (Springer-Verlag, Berlin, 1957) Chapter IV.
- [34] SCOFIELD, J.H., Angular and polarization correlations in photoionization and radiative recombination, *Phys. Rev. A* **40** (1989) 3054.
- [35] ANDERSEN, L.H., BOLKO, J., Radiative recombination between fully stripped ions and free electrons, *J., Phys. Rev. A* **42** (1990) 1184.
- [36] HIMMELBLAU, D.M., “Applied nonlinear programming” (McGraw-Hill, 1972) p. 163.
- [37] TRZHASKOVSKAYA, M.B., NIKULIN, V.K., Radiative recombination and photoionization data for tungsten ions. Electron structure of ions in plasmas, *Atoms* **3** (2015) 86



# PLASMA DIAGNOSTICS BY THE INTENSITY RATIOS OF EMISSION LINES OF Fe IONS AND RECOMMENDED EXCITATION RATE COEFFICIENTS

I. MURAKAMI<sup>1,2</sup>, N. YAMAMOTO<sup>3</sup>, H.A. SAKAUE<sup>1</sup>, S. MORITA<sup>1,2</sup>, D. KATO<sup>1,2</sup>, T. KATO<sup>1</sup>

<sup>1</sup>National Institute for Fusion Science, National Institutes of Natural Sciences, Toki, Gifu, 509-5292, Japan

<sup>2</sup>SOKENDAI (The Graduate University for Advanced Studies), Hayama, Kanagawa 240-0193, Japan

<sup>3</sup>Chubu University, Kasugai, Aichi, 487-8501, Japan

## Abstract

Density diagnostics using the density sensitive intensity ratios of Fe XIII, Fe XXI, and Fe XXII lines are studied with the EUV spectra measured from plasmas of Large Helical Device. We calculated the spectral line intensities by our collisional radiative models for Fe ions. The calculated results are compared with measurements. The effective collision strengths for Fe ions are evaluated and the recommended data are given in a table and graphs.

## 1. INTRODUCTION

Iron is a common impurity in fusion laboratory plasmas because of its presence in the plasma vessel material. Therefore, iron spectral lines are important for plasma diagnostics and plasma modeling. The spectra of Fe ions are also important in astrophysics and the Sun. Many kinds of EUV spectral lines of Fe ions have been measured from solar and stellar plasmas (e.g., [1]) as well as from laboratory fusion plasmas [2, 3]. The EUV spectra from Fe ions are also measured in the Electron Beam Ion Trap (EBIT) (e.g., [4]).

We measured EUV Fe ion spectra from Large Helical Device (LHD) at the National Institute for Fusion Science (NIFS) and studied density diagnostics using the intensity ratios of Fe XIII, Fe XXI and Fe XXII lines. When we use the line intensity ratios from different ions, we must be sure that these lines are emitted at the same place. It is useful to use the intensity ratios of spectral lines from the same ion for plasma diagnostics because we can avoid an ambiguity of the plasma parameters as well as the ion densities. The intensity ratios of Fe ions lines were studied with the measured spectra from a Tokamak plasma [3] and from LHD [5, 6]. This method has been applied extensively in the observed solar spectra to determine the electron density in the Sun [7, 8]. In order to diagnose electron density from the intensity ratios, we made collisional radiative models of Fe ions [5]. We need much atomic data for collisional radiative models, i.e. energy levels, wavelengths, radiative transition probabilities, ionization rate coefficients, recombination rate coefficients, and excitation rate coefficients.

Among the many kinds of atomic data, the intensities depend especially on the excitation rate coefficients. In 1992 an assessment meeting was held for reviewing available theoretical data for the electron excitation of atoms and ions [9]. At that time not many calculations had been conducted for Fe ions using the *R*-matrix method, which gives better results than a distorted wave approximation method at low temperature region. Pradhan & Zhang [10] reviewed available atomic data of electron-impact excitation published up to 1999. During the decade since the review of Pradhan & Zhang, many new data have been calculated using various *R*-matrix methods. We evaluate excitation data for all Fe ions and the neutral atom, and show the results for effective collision strengths in this paper.

## 2. MEASUREMENTS

In the EUV regions of 10 – 30 nm, many lines of Fe ions from Fe VIII to Fe XXIV have been measured from laboratory plasma as well as from the Sun. From *M*-shell ions at lower temperature, the emission lines for the transitions  $n = 3$  to  $n = 3$  lines are dominant. From *L*-shell ions at higher temperature,  $n = 2$  to  $n = 2$  transitions are dominant where  $n$  is a principal quantum number. In this paper we discuss the spectral lines from *M*-shell ions Fe XIII and from *L*-shell ions Fe XXI and Fe XXII for density diagnostics.

### 2.1. Fe XIII Lines

The spectral data were recorded at the LHD stellarator at NIFS. The magnetic field used for plasma confinement in this machine is generated with a superconducting electromagnet, which makes steady state operation possible. The helical coils produce a magnetic field up to 3 Tesla. We analysed the spectra observed in shot #66810, where an iron pellet was injected into LHD [5]. The discharge in this shot lasted about 4.5 s and attained a line-averaged density of about  $2.5 \times 10^{13} \text{ cm}^{-3}$ . The temperature reached 2 - 3 keV during the main part of the discharge. This temperature is, however, greatly reduced during the plasma decay phase after the end of the heating by neutral beam injection. The line-averaged electron density also drops after neutral beam heating and may be as low as  $10^{13} \text{ cm}^{-3}$ .

By recording spectra throughout the discharge every 0.1 sec, spectra with different ionization balances are obtained. For example, the emission from Fe XXIV dominates the spectral region near 20 nm during the main part of the discharge. In fact, essentially no other lines of iron are seen during these times. After the end of the plasma heating the temperature is sufficiently low to see emission from Fe VIII through Fe XIII.

The present measurements were made with the SOXMOS EUV grazing-incidence spectrometer [11] covering the wavelength range from 15.8 to 21.4 nm. The instrument utilized a 600 lines/mm grating.

Because iron is not, or is only weakly, seen in LHD plasmas, the iron concentration was increased by pellet injection. Iron thus dominates the emission in the region of interest, and essentially no lines from other elements are seen, with the possible exception of C V lines near 22.7 nm and above.

Fig. 1 shows the iron spectrum in the range from 19 to 21 nm measured on LHD. The spectrum represents the sum of the data recorded between 4.3 and 4.4 s. The spectral emission is dominated by Fe XIII, which produces the strongest feature in the spectrum at 20.38 nm. Lines from Fe XII are also visible, and lines from other charge states as low as Fe VIII can be identified. Essentially all lines in the spectrum have been identified, as indicated in Fig. 1.

### 2.2. Fe XXI and Fe XXII Lines

We analysed the EUV spectra measured for the LHD plasma, shot number #64921, in which Fe pellets were injected. The measured spectrum is shown in Fig. 2. For these measurements, an EUV spectrometer with a flat-field grazing incidence was used [12]. In the spectra, many spectral lines of Fe *M*-shell and *L*-shell ions are found. In this paper, we chose 4 lines for density diagnostics: 11.4412nm, 11.7144nm, 12.1201nm and 12.8755nm. The observed line intensities are obtained from the spectra by fitting with a Gaussian profile. As for the electron density, we use an averaged electron density through space as a rough guide to compare with the calculated intensity ratios by the CR-models, since the electron density has a time-dependent profile after pellet injection for the LHD plasma and it is difficult to estimate the location where Fe XXII and Fe XXI lines are emitted.

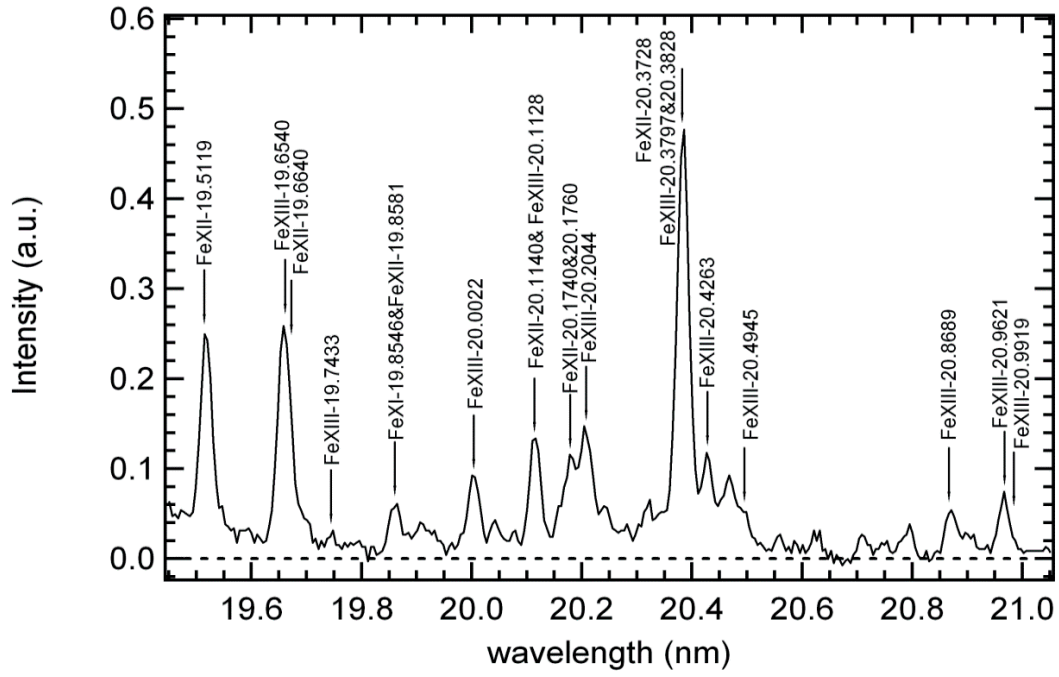


FIG. 1. Iron spectrum from 19.4 – 21.05 nm measured at LHD. Wavelengths given are from the CHIANTI and the NIST database. Reproduced from ref. [5] by permissions of the AAS.

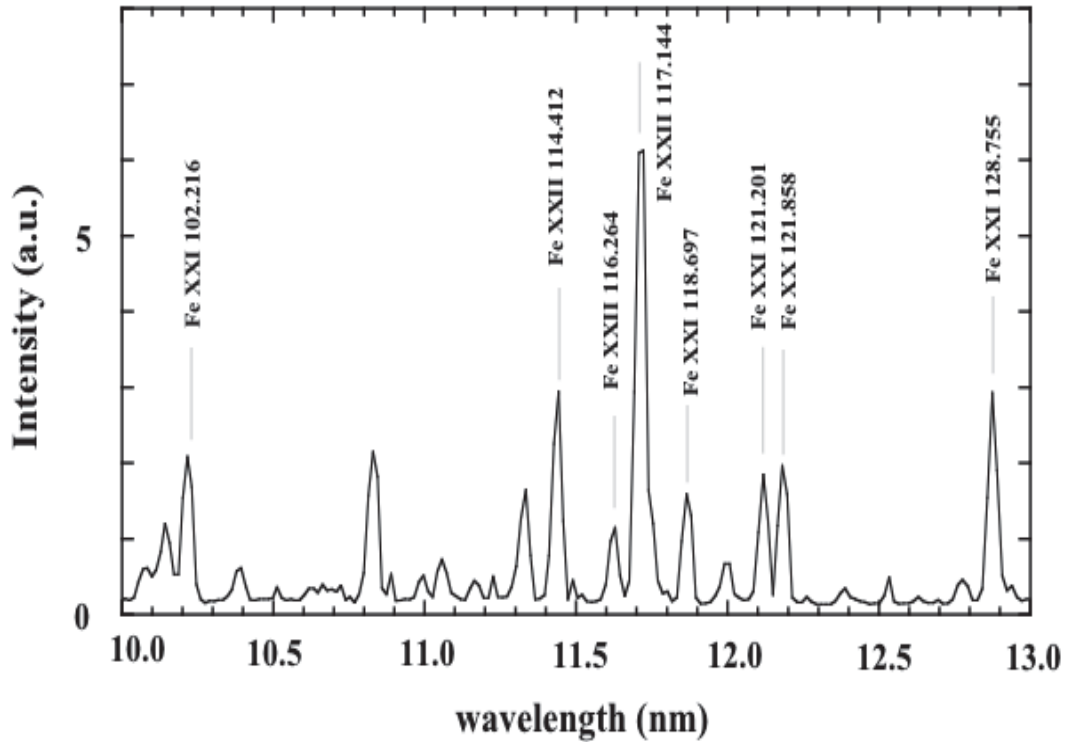


FIG. 2. Iron spectrum from 10 – 13 nm EUV spectra measured from LHD.

### 3. COLLISIONAL RADIATIVE MODEL

#### 3.1. Density Sensitive Line Ratios

The ground state of the *M*-shell and *L*-shell ions consists of several levels called fine structure levels. In the density ranges of our interest,  $10^{10} - 10^{14} \text{ cm}^{-3}$ , the population of each fine structure level of the ground state configuration depends on the densities. In fusion laboratory plasmas such as LHD, EUV spectral lines of Fe ions are emitted mainly by excitation from the ground state. Therefore, the intensities emitted from the excited states depend on the population densities of the fine structure levels of the ground state from which the excitation to the excited states of the different configuration occurs. The fine structure population densities of the ground state are excited by electron-impact as well as proton-impact. The intensities depend on the electron densities as well as the proton densities. The excitation by proton-impact becomes important at higher temperature. In order to diagnose the densities of plasma by the intensity ratios, we need a model that includes the fine structure levels to calculate the line intensities.

#### 3.2. Fe XIII

We constructed an original collisional-radiative (CR) model of Fe ions including the fine structure levels up to  $n = 5$  [5]. This model includes processes of excitation and de-excitation by electron-impact, radiative decay, radiative recombination, ionization, three-body recombination, and autoionization, as well as dielectronic capture and dielectronic recombination. Transition probabilities and cross-sections of these processes were calculated with the HULLAC code [13]. The data obtained with an *R*-matrix code by Aggarwal & Keenan (2005) [14] were used to calculate the electron-impact excitation rate coefficients for the transitions between the  $3s^23p^2$ ,  $3s3p^3$ , and  $3s^23p3d$  states. They were evaluated by Skobelev et al. [15] and fitted by analytical functions. The excitation rate coefficients for proton-impact evaluated by Skobelev et al. [16, 17] are also included for the transitions between fine structure levels of the ground state configuration. For radiative transition probabilities between fine structure levels of the ground state, we used the data in CHIANTI [18, 19]. CHIANTI is a spectral modeling code including atomic data often used for solar physics. The population densities needed to calculate line intensities are obtained by solving the coupled rate equations for each energy level. In this paper the population densities during the ionizing phase are applied to the analysis of the measured spectra.

We applied three radiation models to analyze the measured spectra. Two of the three models are our own models using different atomic data sets, i.e., from Aggarwal & Keenan [14] and from HULLAC [13]. The third model is CHIANTI [18, 19].

#### 3.3. Fe XXI and Fe XXII

In our CR model, radiative transition probabilities and energy levels are basically calculated by using HULLAC code [13]. For radiative transition probabilities of some dipole transitions among  $n = 2$  and 3 the data from the NIST database [20] are used. The rate coefficients of electron-impact collisional processes are calculated by using HULLAC code. We also use the effective collision strengths of electron-impact excitation calculated with an *R*-matrix code by Badnell and Griffin [21] for Fe XXI and by Badnell et al. [22] for Fe XXII (called RmaX data hereafter) for transitions among  $n = 2$  and 3. The resonance effects which usually become important at low temperatures are taken into account in the *R*-matrix method. However, the HULLAC code cannot take into account resonance effects since HULLAC uses a distorted wave method.

In addition, proton-impact excitation and de-excitation are included in our CR model. The rate coefficients are evaluated by Skobelev et al. [23, 17]. The proton-impact excitation process is important for transitions among the ground state fine-structure levels, i.e.,  $2s^22p^2^3P_J$  (Fe XXI) and  $2s^22p^2^3P_J$  (Fe XXII) and the metastable levels  $2s2p^2^4P_J$  (FeXXII) when proton

and electron temperature are higher than about 1keV. In our CR model we assume the proton temperature is equal to the electron temperature. The proton density is assumed as equal to the electron density ( $n_p/n_e=1$  case) or 0 ( $n_p/n_e=0$  case).

#### 4. PLASMA DIAGNOSTICS BY THE INTENSITY RATIOS

##### 4.1. Fe XIII

The intensity ratio of the Fe XIII line at 20.38 nm ( $3s^2 2p^2 \ ^3P_2 - 3s^2 3p3d \ ^3D_2, \ ^3D_3$ ) to the Fe XIII line at 20.20 nm ( $3s^2 2p^2 \ ^3P_0 - 3s^2 3p3d \ ^3P_1$ ) is used as a density diagnostic for the solar transient region [8]. The calculated ratios based on the three models for the electron temperature ( $T_e$ ) at 137 eV are shown in Fig. 3 along with the measured ratios. The ratios using the HULLAC data and the Aggarwal & Keenan data agree well at densities below  $5 \times 10^9 \text{ cm}^{-3}$ . Their predictions disagree in the high density limit by 10%. The ratio by CHIANTI is in very good agreement with that by the Aggarwal & Keenan model. The ratio from LHD is slightly smaller and does not overlap with either of our models and CHIANTI. These discrepancies might be due to the blend of O V lines at around 20.20nm and 20.38 nm from LHD plasma. The O V line intensities from LHD seem to depend on the experimental shots. The observed intensity ratios of  $I(20.38 \text{ nm})/I(20.20 \text{ nm})$  changed from 2.6 to 5.3 for different shots.

The density dependence of the  $I(20.38 \text{ nm})/I(20.20 \text{ nm})$  ratio arises because of an increase in the population of the higher-lying fine structure levels as the density increases. Proton excitation as well as electron excitation can contribute to collisional rearrangement between fine structure levels, which may matter, in principle, in the Sun as well as in LHD plasma. However, the temperature range of interest is about 130 – 140 eV, where proton excitation is not strong. Proton excitation becomes comparable to electron excitation only for an electron temperature higher than 200 eV.

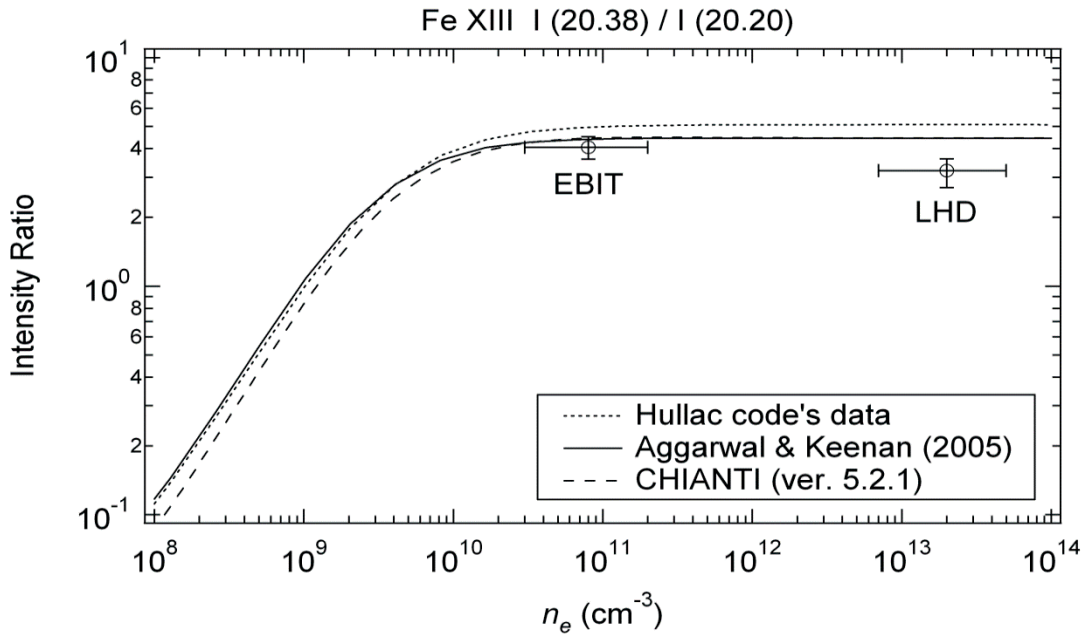


FIG. 3. Fe XIII intensity ratio of  $I(20.38 \text{ nm})/I(20.20 \text{ nm})$  as a function of electron density. Electron temperature is assumed to be 137 eV (corresponding to temperature of Fe XIII maximum emissivity). Solid, dotted, and dashed lines are by data of Aggarwal & Keenan (2005), HULLAC code, and CHIANTI code. Effects of proton collision are included in our calculations. Open circles are experimental data by EBIT-II [5] and LHD experiments (#66810) [5].

## 4.2. Fe XXI and Fe XXII

We studied the density dependences of the two intensity ratios of Fe XXII 11.4412 nm ( $2s^2 2p^2 P_{3/2} - 2s2p^2 P_{3/2}$ ) to 11.7144 nm ( $2s^2 2p^2 P_{1/2} - 2s2p^2 P_{1/2}$ ) and Fe XXI 12.1201 nm ( $2s^2 2p^2 P_2 - 2s2p^3 P_2$ ) to 12.8755 nm ( $2s^2 2p^2 P_0 - 2s2p^3 D_1$ ). Figs. 4 and 5 show the calculated line intensity ratios of Fe XXII  $I(11.4412\text{nm})/I(11.7144\text{nm})$  and Fe XXI  $I(12.1201\text{nm})/I(12.8755\text{nm})$  for  $T_e = 1$  keV with measured ratios, respectively. Ratios calculated by the CR model using two different data sets are shown, i.e., the model with excitation rate coefficients calculated by HULLAC (indicated as HULLAC) and the model with the effective collision strengths calculated by the *R*-matrix method (indicated as RmaX). Two cases with  $n_p/n_e=1$  and 0 are also shown for both models where  $n_p$  and  $n_e$  indicate the proton and electron density, respectively.

For Fe XXII, the calculated intensity ratio,  $I(11.4412\text{nm})/I(11.7144\text{nm})$  shows the electron density dependence for the electron density  $10^{11} - 10^{16} \text{ cm}^{-3}$  range as seen in Fig. 4. The calculated ratio with the RmaX data is larger than that with the HULLAC data by about 16% at most. The ratio with  $n_p/n_e=1$  is larger than that with  $n_p/n_e=0$  for both models, as seen in Fig. 4. The difference between the RmaX model and the HULLAC model is due to the different effective collision strength for the transition between the fine structure levels of the ground state configuration from  $2s^2 2p^2 P_{1/2}$  to  $P_{3/2}$ . The RmaX data for this transition is larger than the HULLAC data because of the resonance effect as seen in Fig. 6. The effect of proton-impact excitation is significant for this intensity ratio at 1 keV. The measured intensity ratios of the LHD plasma (#64921) for different exposure frames are located between the values of the  $n_p/n_e=1$  and the  $n_p/n_e=0$  case of the RmaX model. More detailed analysis is carried out by Sakaue et al. [6].

For Fe XXI, the calculated intensity ratio,  $I(12.1201\text{nm})/I(12.8755\text{nm})$  shows strong electron density dependence in the range  $10^9 - 10^{15} \text{ cm}^{-3}$  as seen in Fig. 7. Similarly to the Fe XXII ratio, the calculated ratios with the RmaX model are larger than those with the HULLAC model, and the ratios with  $n_p/n_e=1$  are larger than those with  $n_p/n_e=0$  for both models. The difference between the RmaX model and the HULLAC model is due to the different effective collision strength for  $2s^2 2p^2 P_0 - P_2$  and  $2s^2 2p^2 P_0 - 2s2p^3 P_2$  transitions. The RmaX data are larger than the HULLAC data as seen in Fig. 7, because of the resonance effect. The electron-impact excitation effective collision strengths for the  $2s^2 2p^2 P_0 - 2s2p^3 P_0$  and  $2s^2 2p^2 P_0 - 2s2p^3 P_2$  transitions by the RmaX model and by the HULLAC model are almost the same. The proton-impact excitation effective collision strength for the transition  $2s^2 2p^2 P_0 - P_2$  becomes larger than that by electron-impact for higher proton and electron temperature than around 1keV. This also affects the intensity ratio. The measured intensity ratios of the LHD plasma (#64921) are spread widely around the values of the  $n_p/n_e=1$  and the  $n_p/n_e=0$  case predicted by the RmaX model.

It will be possible to diagnose electron and proton densities by using many line pairs such as these two line pairs of Fe XXII and Fe XXI with more precise measurement of spectral lines.

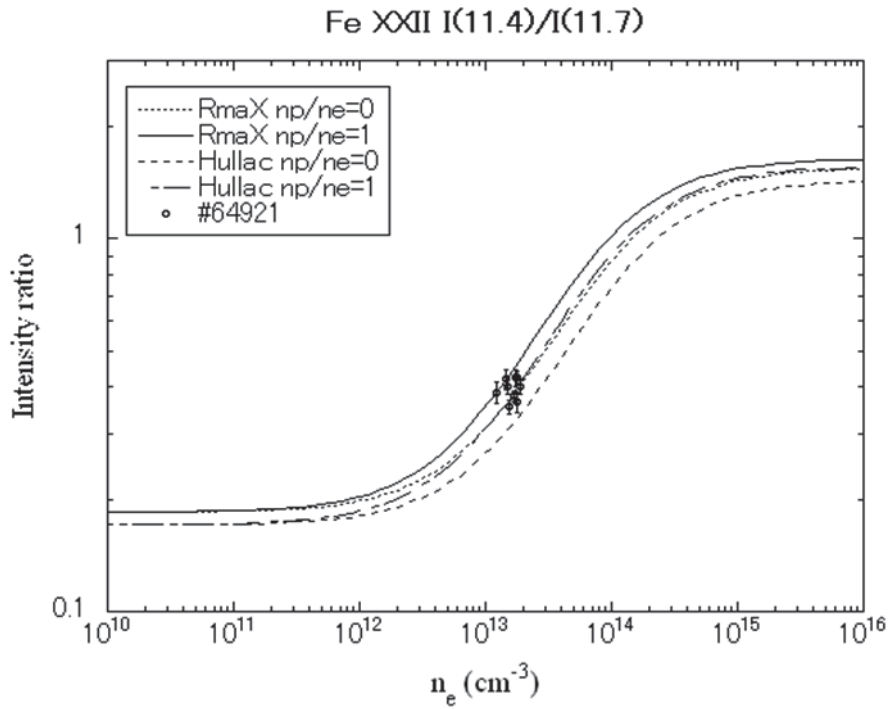


FIG. 4. Fe XXII intensity ratio of  $I(11.4412\text{nm})/I(11.7144\text{nm})$  as a function of electron density. Calculated ratios for the  $n_p/n_e=0$  (dotted line) and  $n_p/n_e=1$  (solid line) cases of the RmaX model, the  $n_p/n_e=0$  (dashed line), and  $n_p/n_e=1$  (long dashed line) cases of the HULLAC model are shown with measured ratio of the LHD plasma #64921.

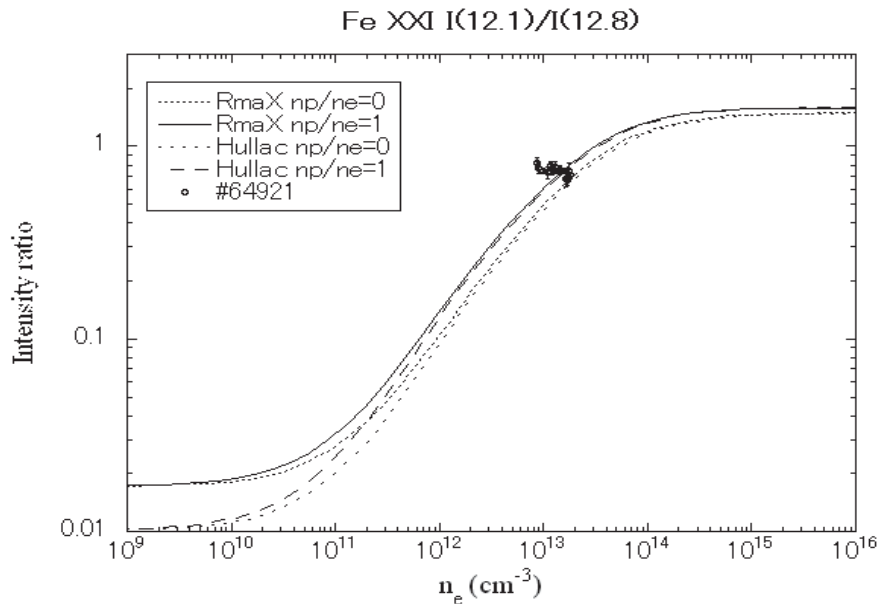


FIG. 5. Fe XXI intensity ratio of  $I(12.1201\text{nm})/I(12.8755\text{nm})$  as a function of electron density. Calculated ratios for the  $n_p/n_e=0$  (dotted line) and  $n_p/n_e=1$  (solid line) cases of the RmaX model, and the  $n_p/n_e=0$  (dashed line) and  $n_p/n_e=1$  (long dashed line) cases of the HULLAC model are shown with measured ratio of the LHD plasma #64921.

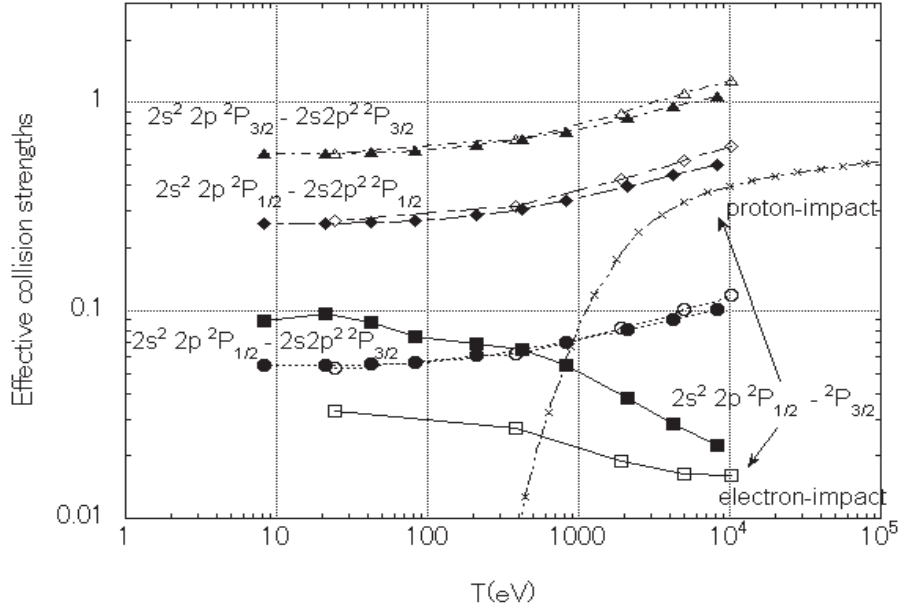


FIG. 6. Effective collision strengths of some Fe XXII transitions as a function of electron temperature. Filled symbols are Rmax data and open symbols are HULLAC data for the  $2s^2 2p^2 P_{3/2} - 2s2p^2^2 P_{3/2}$  (triangle),  $2s^2 2p^2 P_{1/2} - 2s2p^2^2 P_{1/2}$  (diamond),  $2s^2 2p^2 P_{1/2} - 2s2p^2^2 P_{3/2}$  (circle), and  $2s^2 2p^2 P_{1/2} - ^2P_{3/2}$  (square) transitions. The proton-impact excitation data of the  $2s^2 2p^2 P_{1/2} - ^2P_{3/2}$  transition (cross) are plotted for comparison. The proton temperature is assumed to be equal to the electron temperature.

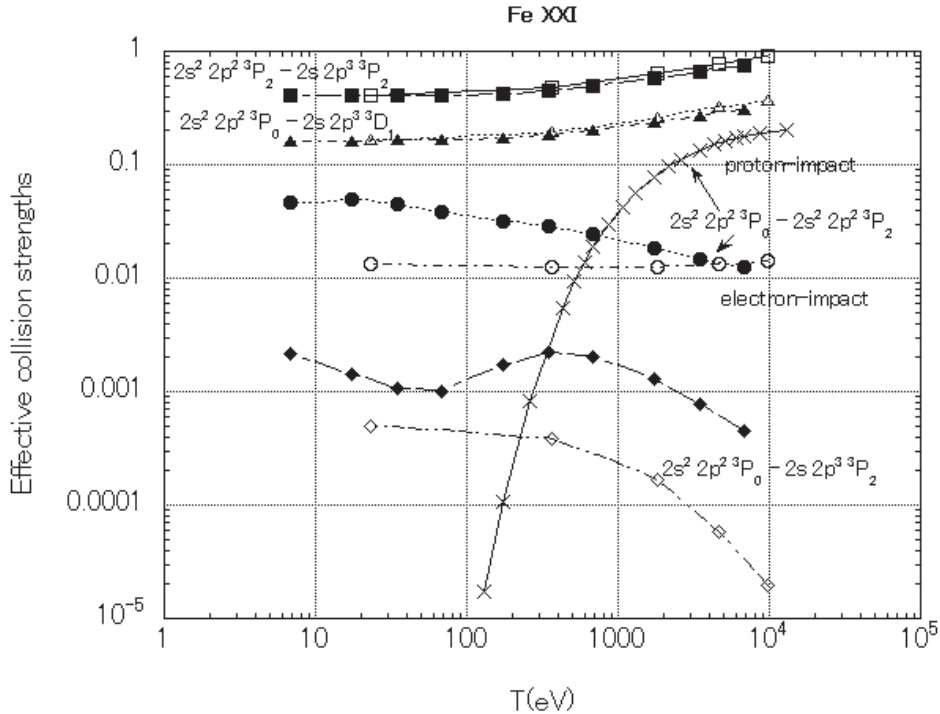


FIG. 7. Effective collision strengths of some Fe XXI transitions as a function of electron temperature. Filled symbols are Rmax data and open symbols are HULLAC data for the  $2s^2 2p^2 ^3P_2 - 2s2p^3^3 P_2$  (square),  $2s^2 2p^2 ^3P_0 - 2s2p^3^3 D_1$  (triangle),  $2s^2 2p^2 ^3P_0 - 2s2p^3^3 P_2$  (diamond), and  $2s^2 2p^2 ^3P_0 - 2s2p^3^3 P_2$  (circle) transitions. The proton-impact excitation data of the  $2s^2 2p^2 ^3P_0 - 2s2p^3^3 P_2$  transition (cross) are plotted for comparison. The proton temperature is assumed to be equal to the electron temperature.

## 5. RECOMMENDED EXCITATION RATE COEFFICIENTS FOR Fe IONS

As we have discussed in the previous sections, the atomic data are indispensable to interpret the measured spectra for plasma diagnostics. The excitation rate coefficients are especially important for the line intensities. We evaluate the effective collision strengths in this section.

### 5.1. Electron-Impact

Reliable atomic data for electron-impact excitation rates of Fe ions are important for population kinetic models for plasma diagnostics. These data mostly rely on theoretical calculations, and the development of computer power and atomic codes over the last decades has made it possible to obtain more detailed calculations. After an assessment meeting in 1992 [9], Pradhan & Zhang [10] reviewed available atomic data of electron-impact excitation published by 1999 and gave recommended data for Fe I, II, III, IV, V, X, XII, XIV, XVI, XVII, XVIII, XXI, XXII, XXIII, XXIV, and XXVI. The rate coefficients of electron-impact excitation for 12 ions among the above 16 ions have been calculated using several *R*-matrix methods, mostly provided by the Iron Project [24]. The Iron Project has provided extensive atomic data for energy levels, transition probabilities, and electron-impact excitation rates for ions important for astrophysical plasmas, and much data for Fe ions has been published. During the decade since the review of Pradhan & Zhang, new data were calculated with using various *R*-matrix methods and we assess the available information for electron-impact excitation rates for Fe ions.

Table 1 gives a list of recommended data for electron-impact excitation effective collision strengths, which are obtained by averaging the collision strengths with Maxwellian distribution for electron velocity. We select the data (1) calculated with an *R*-matrix method, (2) with many levels included, and (3) checking treatment of configuration interaction, partial waves, relativistic effects, and energy range of calculations. As for a relativistic effect, Berrington et al. [25] compared the effective collision strengths of Fe<sup>14+</sup> calculated by Breit-Pauli *R*-matrix method and Dirac *R*-matrix method with the same number of target states and the same energy mesh which gives very fine resolution to resolve the resonances. The results by both methods agree well and the average difference between the effective collision strengths is about 6%. This means that the difference in relativity treatment is not important for moderately ionized iron if all other conditions are the same.

There exist updated data for most of Fe ions produced since the review of Pradhan and Zhang, as seen in Table 1. The number of levels included in the calculations is increased for many ions. Important trends since 2000 are that the collision cross-sections are calculated by (1) Breit-Pauli *R*-matrix method (BPRM), (2) Dirac *R*-matrix method (DARC), or (3) intermediate-coupling frame transformation (ICFT) *R*-matrix method [26]. The third method is equivalent to the full Breit-Pauli *R*-matrix approach and computationally less demanding, so large calculations with many levels can be performed. The relativistic effects are included as the mass velocity, spin-orbit, and Darwin relativistic collections. All of the ICFT *R*-matrix calculations listed in Table 1 performed the exchange calculations only for lower angular momentum partial waves, and not for higher partial waves.

Most of the data listed in Table 1 are available electronically via internet, as indicated in column 6. The references for recommended data are shown by bold-face in the text below. We show some of the new recommended data in figures. Other data than the recommended data are also shown in figures for comparison.

#### Fe I

There is no updated data for Fe I since 1999 and the same data by Pelan and Berrington [27] are recommended as Pradhan and Zhang did in [10]. Ten fine-structure levels of  $3d^6 4s^2$  <sup>5</sup>D and  $3d^7 4s$  <sup>5</sup>F states are considered.

#### Fe II

Ramsbottom et al. [28] performed the calculation with 262 levels using the Breit-Pauli  $R$ -matrix method and gave more accurate data for transitions among the lowest 16 fine-structure levels of  $3d^6 4s$  and  $3d^7$  states than those of Zhang and Pradhan (1995) [29]. Fig. 8 compares the effective collision strengths of the  $3d^6(^5D)4s\ ^6D_{2/3} - 3d^6(^5D)4s\ ^6D_{7/2}$  and the  $3d^6(^5D)4s\ ^6D_{2/3} - 3d^6(^5D)4s\ ^6D_{5/2}$  transitions obtained by Zhang and Pradhan [29] and Ramsbottom et al. [28].

### Fe III

Zhang [30] gave the data for transitions among 219 levels. McLaughlin et al. [31] also calculated the effective collision strengths using the parallel  $R$ -matrix code PRMAT with 3 configurations ( $3d^6$ ,  $3d^5 4s$ , and  $3d^5 4p$ ) and 136  $LS$  terms considered, as Zhang did, but not for fine structure level transitions. They published data only for forbidden transitions.

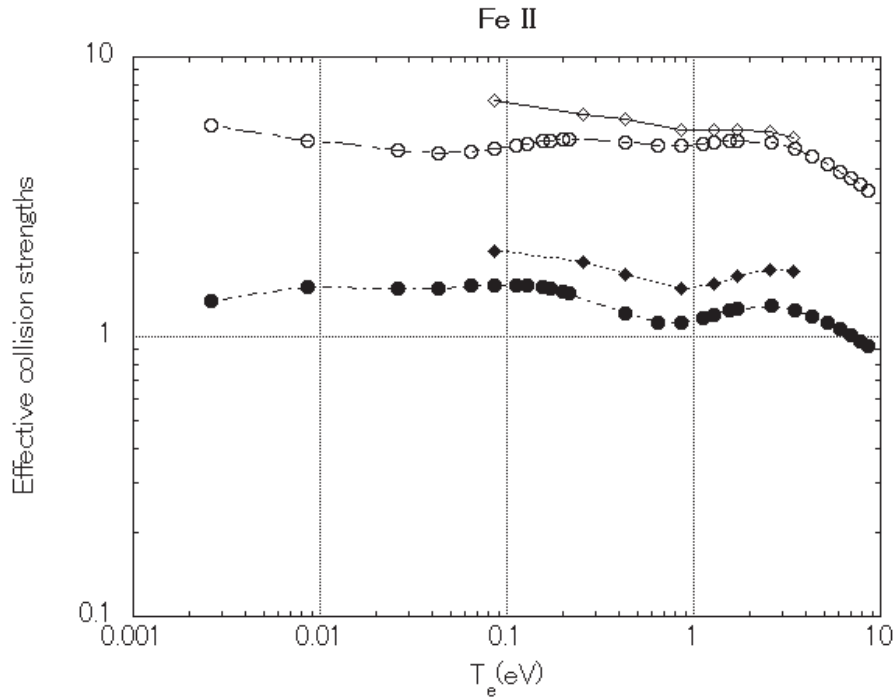


FIG. 8. Effective collision strengths of the Fe II  $3d^6(^5D)4s\ ^6D_{2/3} - 3d^6(^5D)4s\ ^6D_{7/2}$  (open symbols) and the  $3d^6(^5D)4s\ ^6D_{2/3} - 3d^6(^5D)4s\ ^6D_{5/2}$  (filled symbols) transitions obtained by Zhang and Pradhan (1995) [29] (diamonds) and Ramsbottom et al. (2007) [28] (circles) as a function of electron temperature.

### Fe IV

Zhang and Pradhan [32] gave the data for transitions among 140 levels (49  $LS$  terms) obtained by non-relativistic  $R$ -matrix code. They compared their results with ones obtained using the Breit-Pauli  $R$ -matrix code for lowest 16 levels and found good agreement. McLaughlin et al. [33] performed calculations with 108  $LS$  terms (no fine-structure levels) using the PRMAT code and published data for forbidden transitions between the lowest 16 levels and the other higher levels.

### Fe V

Ballance and Griffin [34] published data for transitions among 182 fine-structure levels with 3 configurations ( $3d^4$ ,  $3d^3 4s$ , and  $3d^3 4p$ ), but the calculations were done with 359 levels. Fig. 9 compares the effective collision strengths of the  $3d^4\ ^5D_0 - 3d^4\ ^5D_1$  and  $3d^4\ ^5D_0 - 3d^4\ ^5D_2$  transitions obtained by Berrington (1995) [35] and Ballance and Griffin.

### Fe VI

Ballance and Griffin [36] calculated the collision cross-sections by using Dirac  $R$ -matrix method including 1728 levels but published the effective collision strengths for transitions among 96 fine-structure levels with 3 configurations ( $3d^3$ ,  $3d^24s$ , and  $3d^24p$ ). Fig. 10 compares the effective collision strengths of the  $3d^3\ ^4F_{3/2} - 3d^3\ ^4F_{5/2}$  and  $3d^3\ ^4F_{3/2} - 3d^3\ ^4F_{7/2}$  transitions obtained by Chen and Pradhan (1999) [37] and Ballance and Griffin.

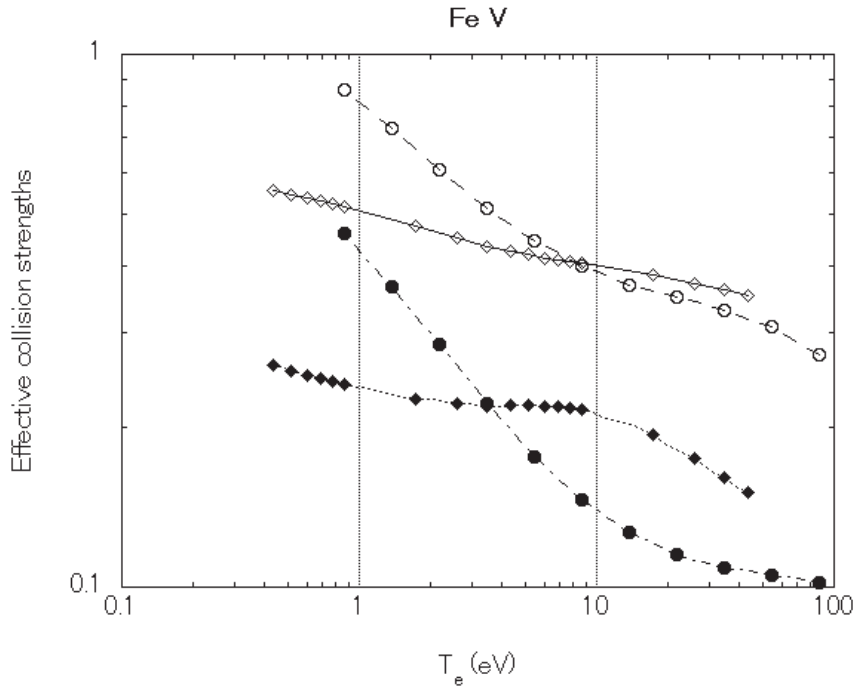


FIG. 9. Effective collision strengths of the Fe V  $3d^4\ ^5D_0 - 3d^4\ ^5D_1$  (open symbols) and the  $3d^4\ ^5D_0 - 3d^4\ ^5D_2$  (filled symbols) transitions obtained by Berrington (1995) [35] (circles) and Ballance and Griffin (2007) [34] (diamonds) as a function of electron temperature.

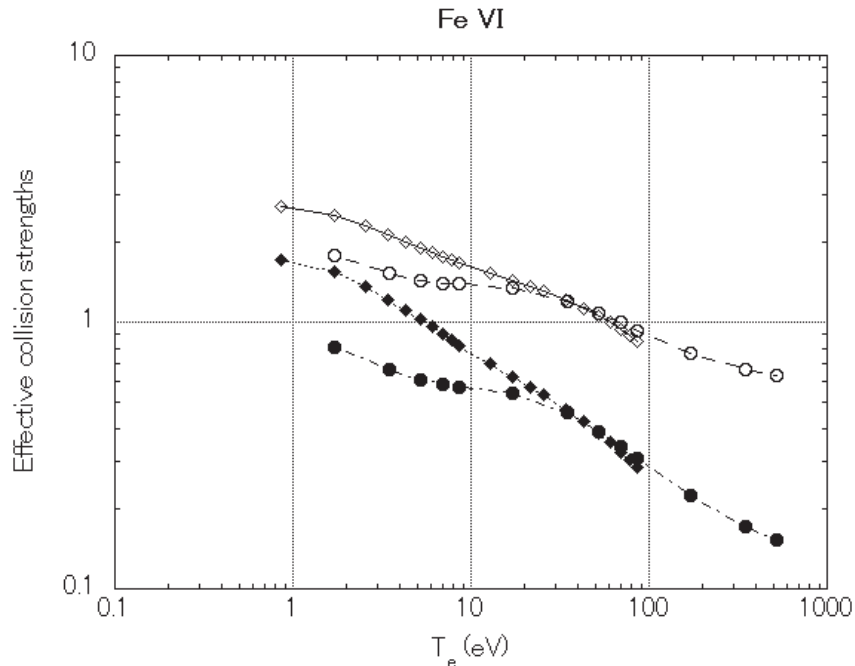


FIG. 10. Effective collision strengths of the Fe VI  $3d^3\ ^4F_{3/2} - 3d^3\ ^4F_{5/2}$  (open symbols) and the  $3d^3\ ^4F_{3/2} - 3d^3\ ^4F_{7/2}$  (filled symbols) transitions obtained by Chen and Pradhan (1999) [37] (diamonds) and Ballance and Griffin (2008) [36] (circles) as a function of electron temperature.

## Fe VII

Witthoef and Badnell [38] obtained the effective collision strengths using ICFT  $R$ -matrix method for transitions among 189 levels with 40 configurations ( $n=3, 4,$  and  $5$ ). Fig. 11 compares the effective collision strengths of the  $3d^2\ ^3F_2 - 3d^2\ ^3F_3$  and  $3d^2\ ^3F_2 - 3d^2\ ^3F_4$  transitions obtained by Berrington et al. (2000) [39], who considered only 9 levels, and Witthoef and Badnell for a comparison.

## Fe VIII

Griffin et al. [40] obtained the effective collision strengths using ICFT  $R$ -matrix method for transitions among 77 levels with 7 configurations ( $n=3$  and  $4$ ). There is no other data published for the effective collision strengths. Fig. 12 shows the  $3d\ ^2D_{3/2} - 3d\ ^2D_{5/2}$  and the  $3p^6 3d\ ^2D_{3/2} - 3p^5 3d^2\ ^4D_{1/2}$  transitions by Griffin et al.

## Fe IX

There is only one paper by Storey et al. [41] who calculated the effective collision strength with the  $R$ -matrix method. But they only published their data for transitions among the lowest 16 levels. The data table in the CHIANTI database [18] does not include all transitions, either. The CHIANTI provides only the spline fitting coefficients of the effective collision strengths, and the fitting functions described by Burgess and Tully [42] are used. Fig. 13 shows the effective collision strengths of the  $3p^6\ ^1S_0 - 3p^5 3d\ ^3P_0$  and the  $3p^6\ ^1S_0 - 3p^5 3d\ ^3P_1$  transitions obtained by Fawcett and Mason [43] with using a distorted wave method and Storey et al.

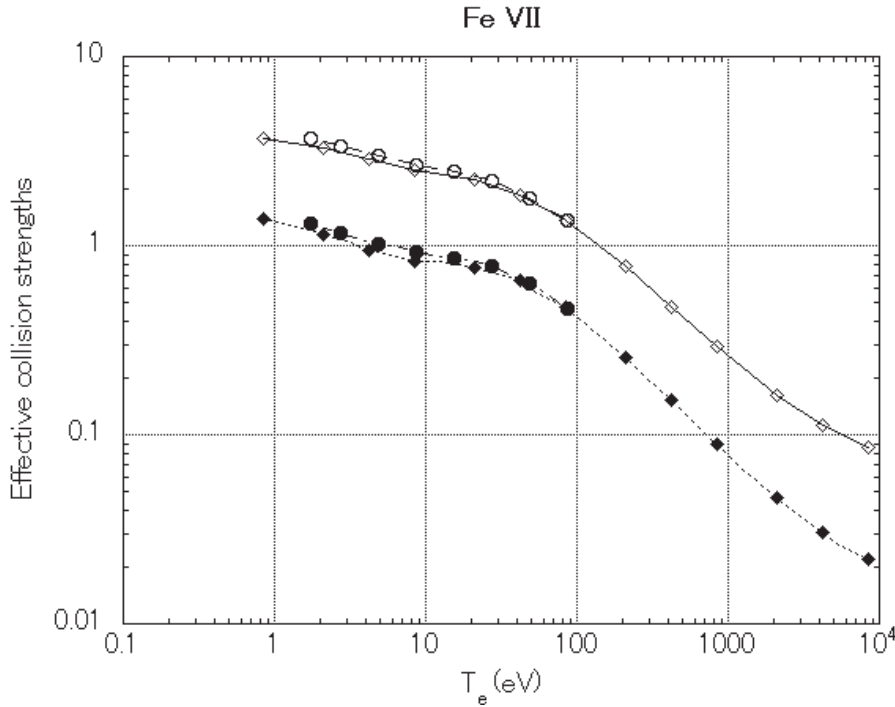


FIG. 11. Effective collision strengths of the Fe VII  $3d^2\ ^3F_2 - 3d^2\ ^3F_3$  (open symbols) and the  $3d^2\ ^3F_2 - 3d^2\ ^3F_4$  (filled symbols) transitions obtained by Berrington et al. (2000) [39] (circles) and Witthoef and Badnell (2008) [38] (diamonds) as a function of electron temperature.

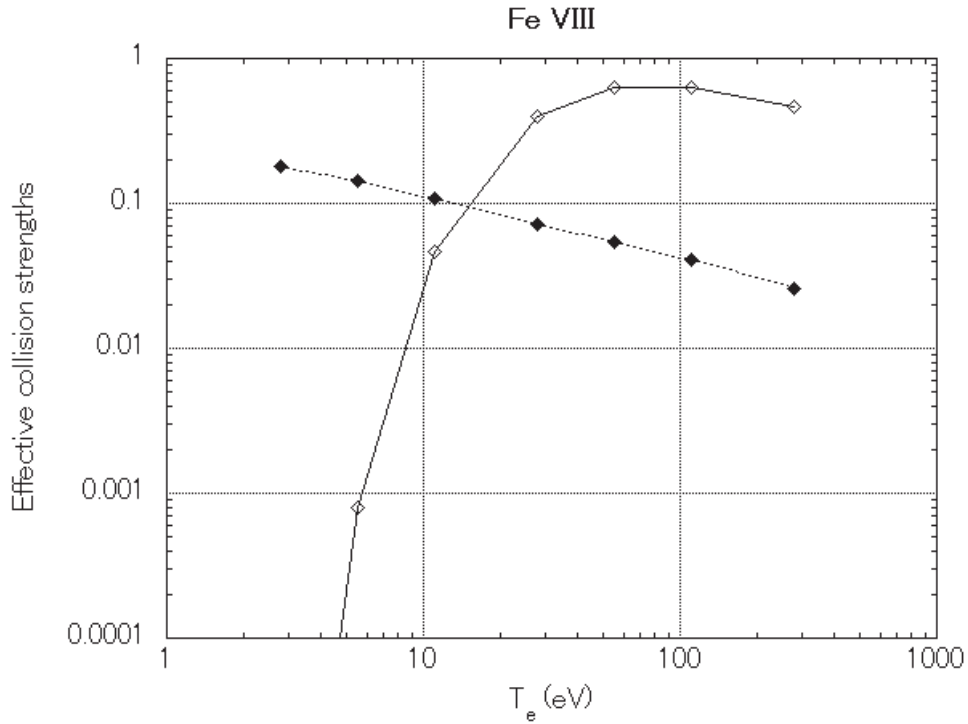


FIG. 12. Effective collision strengths of the Fe VIII  $3d^2D_{3/2} - 3d^2D_{5/2}$  (open symbols) and the  $3p^6 3d^2D_{3/2} - 3p^5 3d^2^4D_{1/2}$  (filled symbols) transitions obtained by Griffin et al. (2000) [40] (diamonds) as a function of electron temperature.

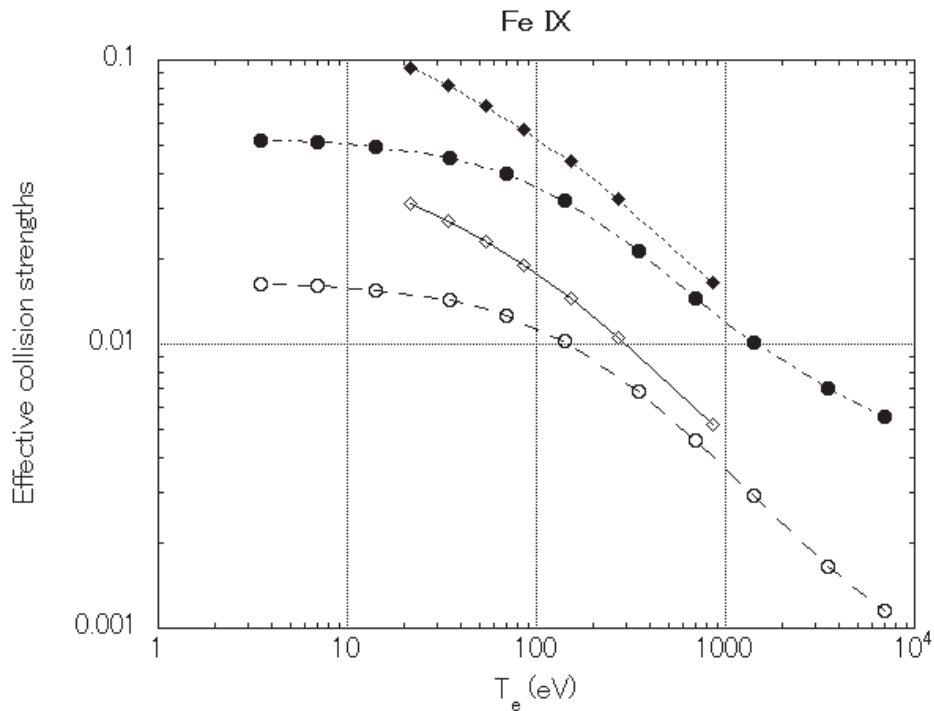


FIG. 13. Effective collision strengths of the Fe IX  $3p^6 ^1S_0 - 3p^5 3d^3P_0$  (open symbols) and the  $3p^6 ^1S_0 - 3p^5 3d^3P_1$  (filled symbols) transitions obtained by Fawcett and Mason (1991) [43] (circles) with a distorted wave method and Storey et al. (2002) [41] (diamonds) with an R-matrix method as a function of electron temperature.

## Fe X

Aggarwal and Keenan [44] calculated the effective collision strengths among 90 levels (5 configurations;  $n=3$ ) using Dirac  $R$ -matrix method. Del Zenna et al. [45] calculated the effective collision strengths with 180 levels (5 configurations;  $n=3$ ) using full Breit-Pauli  $R$ -matrix method, but they only published their data for transitions among 31 levels. Fig. 14 compares the effective collision strengths of the  $3s^23p^5\ ^2P_{3/2} - 3s^23p^5\ ^2P_{1/2}$  and  $3s^23p^5\ ^2P_{3/2} - 3s3p^6\ ^2S_{1/2}$  transitions obtained by Pelan and Berrington (1995) [46] calculated with 2 levels, Tayal (2001) [47] calculated with 49 levels, Pelan and Berrington (2001) [48] calculated with 31 levels, Del Zenna et al. [45], and Aggarwal and Keenan (2005) [44].

## Fe XI

Aggarwal and Keenan [49] calculated the effective collision strengths among 48 levels with 4 configurations ( $n=3$ ) using Dirac  $R$ -matrix method. Gupta and Tayal (1999) [50] and Tayal (2000) [51] calculated the effective collision strengths among 38 levels using semi-relativistic  $R$ -matrix method and Breit-Pauli  $R$ -matrix method, respectively. Fig. 15 compares the effective collision strengths of the  $3s^23p^4\ ^3P_2 - 3s^23p^4\ ^3P_1$  and  $3s^23p^4\ ^3P_2 - 3s^23p^4\ ^3P_0$  transitions by [49], [50], and [51].

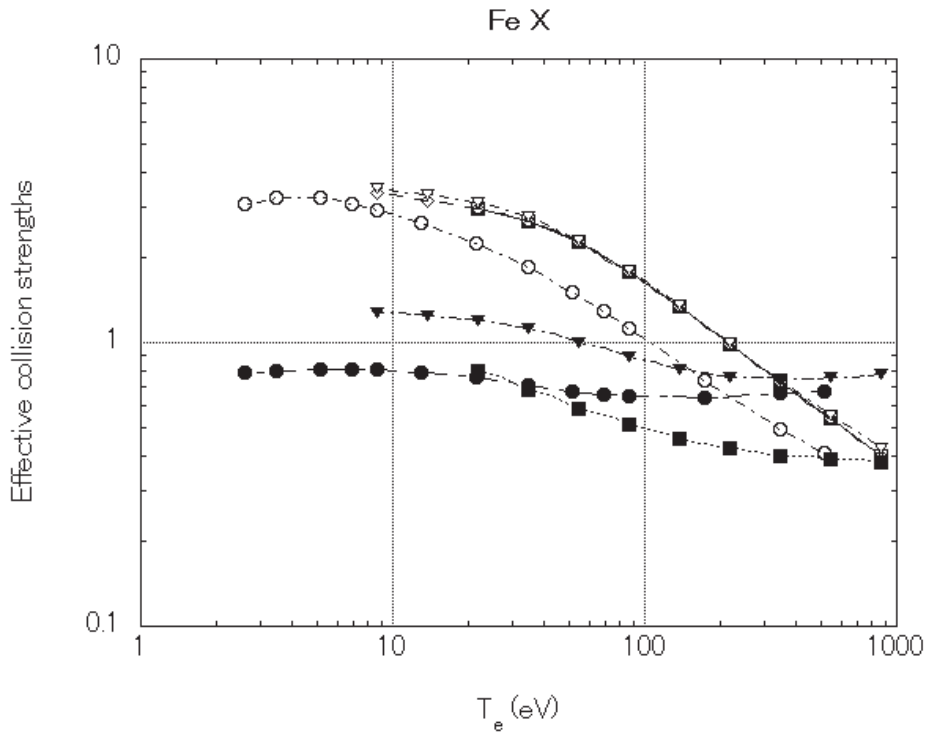


FIG. 14. Effective collision strengths of the Fe X  $3s^23p^5\ ^2P_{3/2} - 3s^23p^5\ ^2P_{1/2}$  (open symbols) and the  $3s^23p^5\ ^2P_{3/2} - 3s3p^6\ ^2S_{1/2}$  (filled symbols) transitions obtained by Pelan and Berrington (1995) [46] (diamonds), Tayal (2001) [47] (circles), Pelan and Berrington (2001) [48] (squares), Del Zenna et al. (2004) [45] (diamonds), and Aggarwal and Keenan (2005) [44] (triangles) as a function of electron temperature.

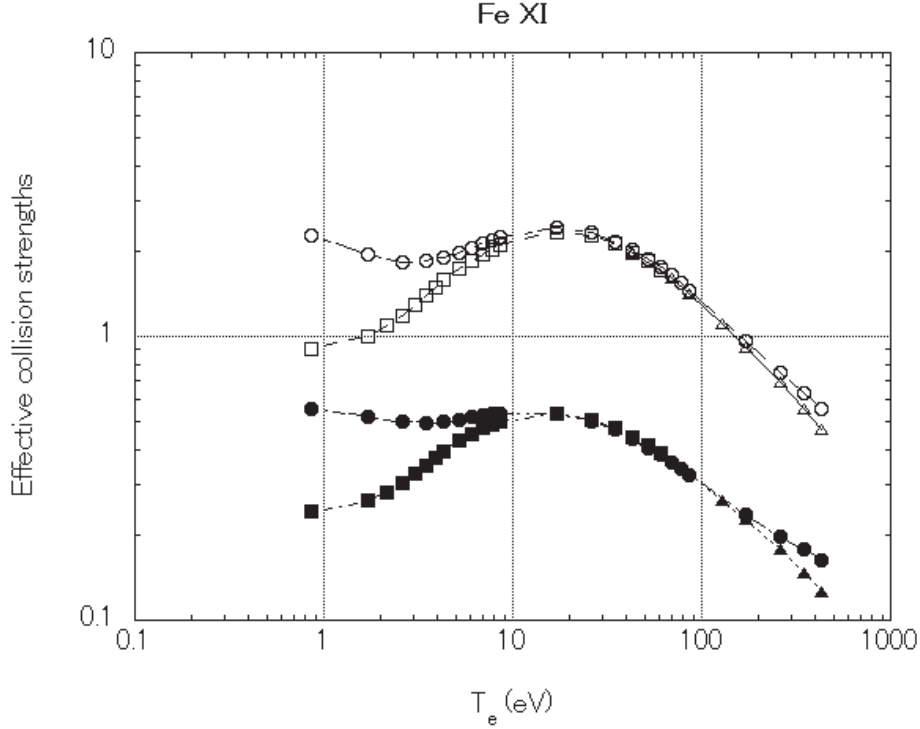


FIG. 15. Effective collision strengths of the Fe XI  $3s^2 3p^4 \ ^3P_2 - 3s^2 3p^4 \ ^3P_1$  (open symbols) and the  $3s^2 3p^4 \ ^3P_2 - 3s^2 3p^4 \ ^3P_0$  (filled symbols) transitions obtained by Gupta and Tayal (1999) [50] (triangles), Tayal (2000) [51] (squares), and Aggarwal and Keenan (2003) [49] (circles) as a function of electron temperature.

### Fe XII

Storey et al. [52] performed the calculation with 143 fine-structure levels (6 configurations with  $n=3$ ), but published a part of the data, and the data file in the CHIANTI database does not include the effective collision strengths for all transitions, either. Binello et al. [53] performed the calculation with 41 levels (3 configurations) and published the effective collision strengths among 5 fine-structure levels of the ground state. Fig. 16 compares the effective collision strengths of the Fe XII  $3s^2 3p^3 \ ^4S_{3/2} - 3s^2 3p^3 \ ^2D_{3/2}$  and the  $3s^2 3p^3 \ ^4S_{3/2} - 3s^2 3p^3 \ ^2D_{5/2}$  transitions.

### Fe XIII

Aggarwal and Keenan [54] calculated the effective collision strengths among 97 levels (6 configurations with  $n=3$ ) using Dirac  $R$ -matrix method. Gupta and Tayal [55] and Tayal [51] calculated the effective collision strengths among 26 levels using a semi-relativistic  $R$ -matrix method and Breit-Pauli  $R$ -matrix method, respectively. Fig. 17 compares the effective collision strengths of the  $3s^2 3p^2 \ ^3P_0 - 3s^2 3p^2 \ ^3P_1$  and  $3s^2 3p^2 \ ^3P_0 - 3s^2 3p^2 \ ^3P_2$  transitions.

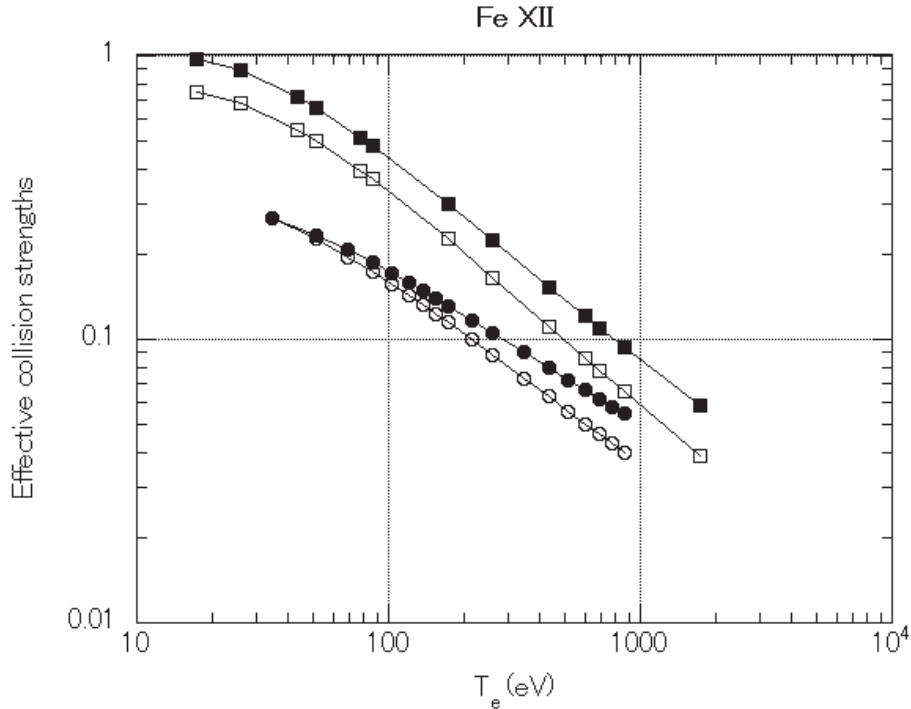


FIG. 16. Effective collision strengths of the Fe XII  $3s^23p^3\ ^4S_{3/2} - 3s^23p^3\ ^2D_{3/2}$  (open symbols) and the  $3s^23p^3\ ^4S_{3/2} - 3s^23p^3\ ^2D_{5/2}$  (filled symbols) transitions obtained by Binello et al. (1998) [53] (circles) and Storey et al. (2005) [52] (squares) as a function of electron temperature.

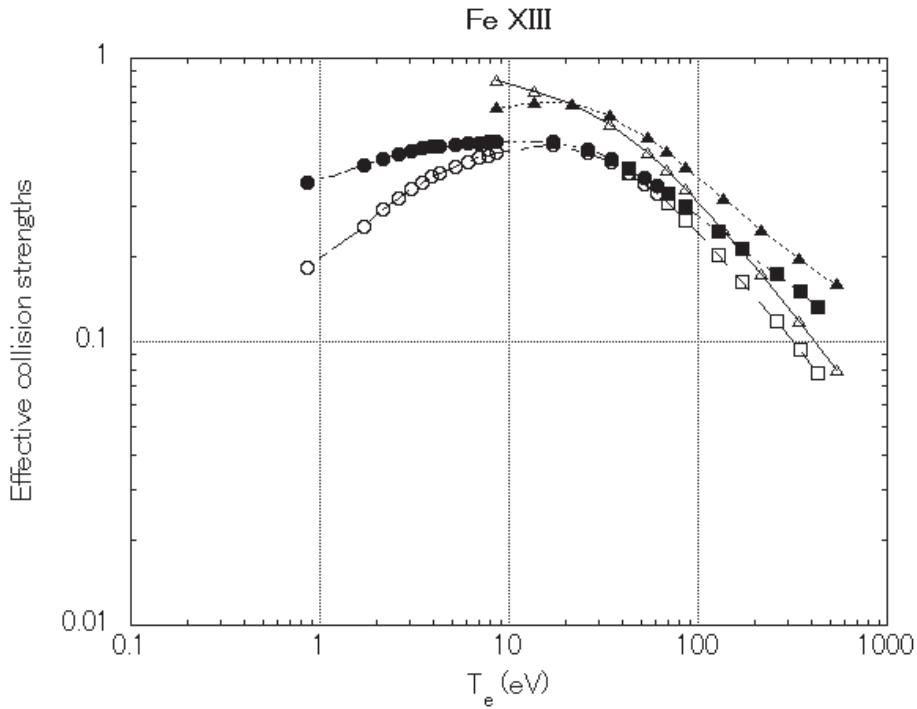


FIG. 17. Effective collision strengths of the Fe XIII  $3s^23p^2\ ^3P_0 - 3s^23p^2\ ^3P_1$  (open symbols) and the  $3s^23p^2\ ^3P_0 - 3s^23p^2\ ^3P_2$  (filled symbols) transitions obtained by Gupta and Tayal (1998) [55] (squares), Tayal (2000) [51] (circles), and Aggarwal and Keenan (2005) [54] (triangles) as a function of electron temperature.

## Fe XIV

Tayal [56] calculated the effective collision strengths with 135 levels from 11 configurations ( $n = 3$  and 4) using Breit-Pauli  $R$ -matrix code, but only a part of the data for transitions among the first 13 levels and transitions from these levels to the next 46 levels are published. Fig. 18 shows the effective collision strengths of the  $3s^23p\ ^2P_{1/2} - 3s^23p\ ^2P_{3/2}$  and  $3s^23p\ ^2P_{1/2} - 3s3p^2\ ^4P_{1/2}$  transitions obtained by Storey et al. (1996) [57] calculated among the 2 fine-structure levels of the ground state, by Storey et al. (2000) [58] calculated with 40 levels, and by Tayal for a comparison. Recently Aggarwal et al. [59] are calculating the effective collision strengths with 136 levels using both the Dirac  $R$ -matrix Code and the relativistic distorted wave method (the FAC code [60]).

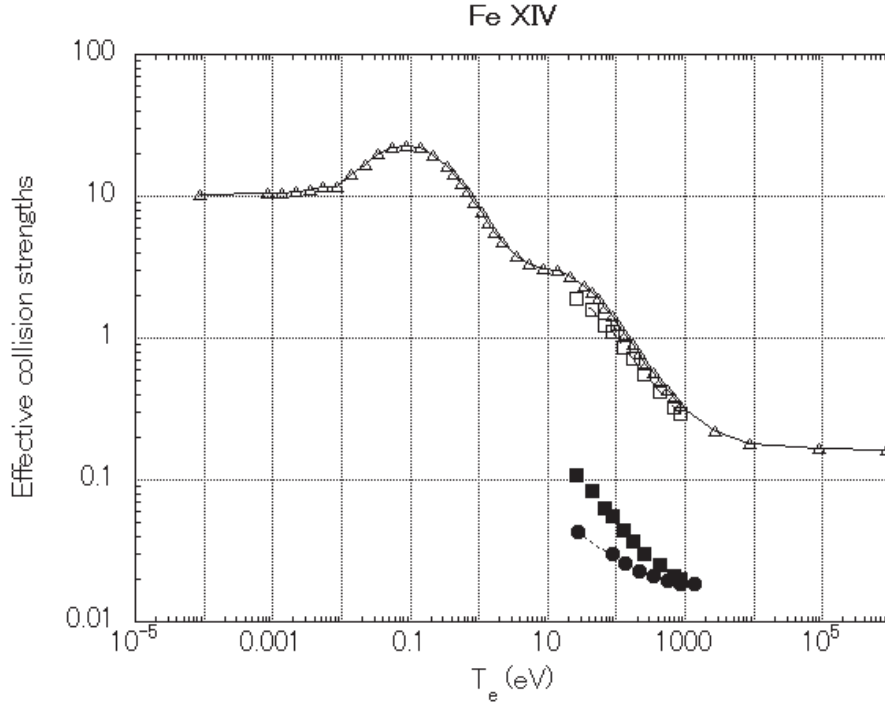


FIG. 18. Effective collision strengths of the Fe XIV  $3s^23p\ ^2P_{1/2} - 3s^23p\ ^2P_{3/2}$  (open symbols) and the  $3s^23p\ ^2P_{1/2} - 3s3p^2\ ^4P_{1/2}$  (filled symbols) transitions obtained by Storey et al. (1996) [57] (triangles), Storey et al. (2000) [58] (circles), and Tayal (2008) [56] (squares) as a function of electron temperature.

## Fe XV

Aggarwal et al. [61] calculated the effective collision strengths with 53 levels from 11 configurations ( $n = 3$  and 4) using Dirac  $R$ -matrix Code, and Berrington et al. [62] also calculated the effective collision strengths with 45 levels ( $n = 3$  and 4) using Breit-Pauli  $R$ -matrix code. Because the number of levels included to the calculation is slightly larger and higher partial waves are included for the calculation by Aggarwal et al., their data are recommended and listed in the Table 1. Fig. 19 compares the effective collision strengths of the  $3s^2\ ^1S_0 - 3s3p\ ^3P_0$  and  $3s^2\ ^1S_0 - 3s3p\ ^3P_1$  transitions obtained by Griffin et al. (1999) [63] calculated with 45 levels using Breit-Pauli  $R$ -matrix method and with the ICFT  $R$ -matrix method, by Eissner et al. (1999) [64] calculated with 35 levels ( $n = 3$ ) using Breit-Pauli  $R$ -matrix method, by Aggarwal et al. [61], and by Berrington et al. [62].

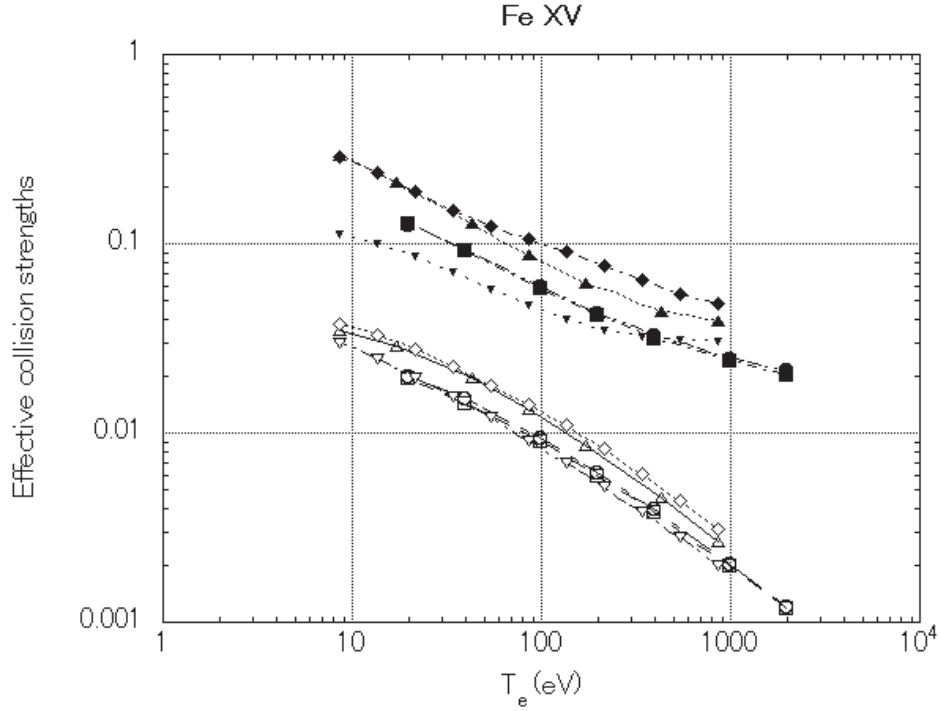


FIG. 19. Effective collision strengths of the Fe XV  $3s^2\ ^1S_0 - 3s3p\ ^3P_0$  (open symbols) and the  $3s^2\ ^1S_0 - 3s3p\ ^3P_1$  (filled symbols) transitions obtained by Griffin *et al.* (1999) [63] with Breit-Pauli *R*-matrix method (circles) and with ICFT *R*-matrix method (squares), Eissner *et al.* (1999) [64] (down triangles), Aggarwal *et al.* (2003) [61] (diamonds), and Berrington *et al.* (2005) [62] (triangles) as a function of electron temperature.

### Fe XVI

Aggarwal and Keenan [65] included 39 levels with  $n=3-7$  and calculated the effective collision strengths using Dirac *R*-matrix Code. Fig. 20 shows the effective collision strengths of the  $3s\ ^2S_{1/2} - 3p\ ^2P_{1/2}$  and  $3s\ ^2S_{1/2} - 3p\ ^2P_{3/2}$  transitions obtained by Eissner *et al.* (1999) [66] calculated with 12 levels ( $n=3$  and 4) and by Aggarwal and Keenan [65] for a comparison. Aggarwal and Keenan [67] and Liang *et al.* [68] both calculated the effective collision strengths for inner-shell transitions with 134 levels. Aggarwal and Keenan [67] used Dirac *R*-matrix code, and Liang *et al.* [68] used the ICFT *R*-matrix code with including Auger and radiation damping effects. Liang *et al.* concluded that the effective collision strengths of Aggarwal and Keenan [67] for inner-shell transitions are overestimated due to their omission of Auger and radiation damping.

### Fe XVII

Loch *et al.* [69] calculated the effective collision strengths using Dirac *R*-matrix code including 139 levels with  $n=2-5$ . Fig. 21 compares the effective collision strengths of the  $2p^6\ ^1S_0 - 2p^53s\ ^3P_0$  and  $2p^6\ ^1S_0 - 2p^53s\ ^3P_1$  transitions obtained by Landi and Gu (2006) [70] calculated with 267 levels ( $n=2-7$ ) using relativistic distorted-wave method (the FAC code) and by Loch *et al.*

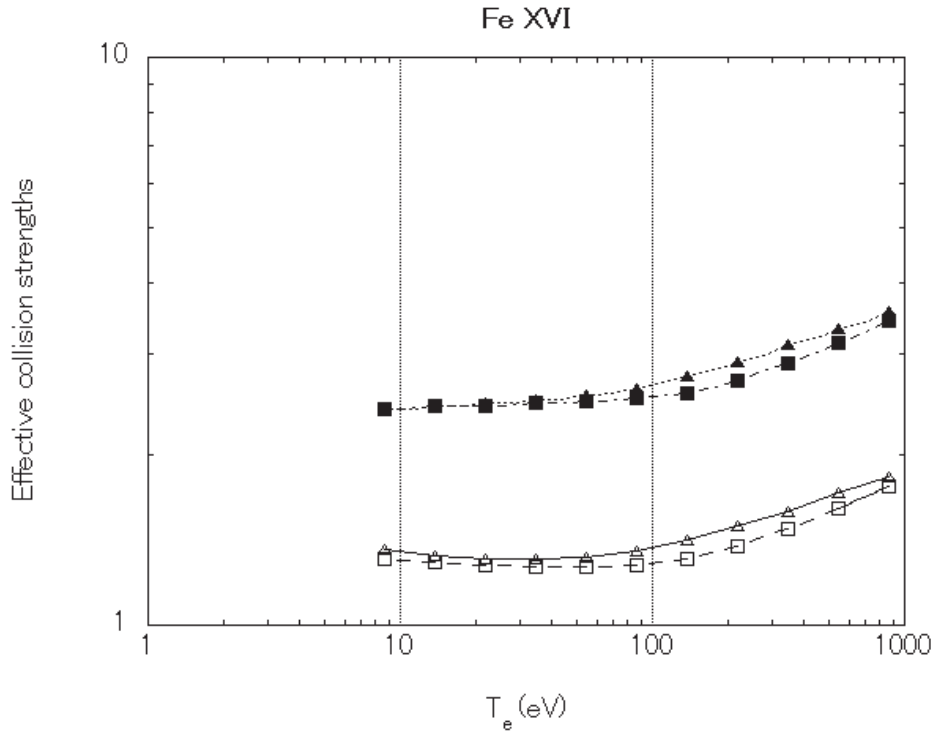


FIG. 20. Effective collision strengths of the Fe XVI  $3s^2S_{1/2} - 3p^2P_{1/2}$  (open symbols) and the  $3s^2S_{1/2} - 3p^2P_{3/2}$  (filled symbols) transitions obtained by Eissner et al. (1999) [66] (squares) and Aggarwal and Keenan (2006) [65] (triangles) as a function of electron temperature.

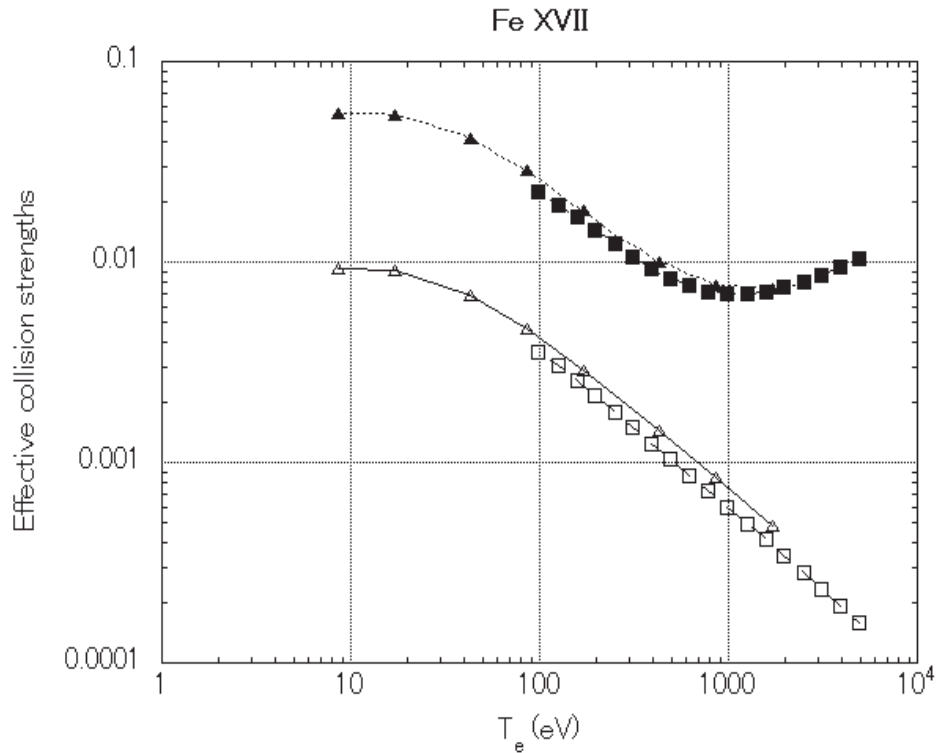


FIG. 21. Effective collision strengths of the Fe XVII  $2p^6^1S_0 - 2p^53s^3P_0$  (open symbols) and the  $2p^6^1S_0 - 2p^53s^3P_1$  (filled symbols) transitions obtained by Landi and Gu (2006) [70] (squares) and Loch et al. (2006) [69] (triangles) as a function of electron temperature.

### Fe XVIII

Witthoef et al. [71] calculated the effective collision strengths using the ICFT  $R$ -matrix method including 279 levels with  $n=2-4$ . Fig. 22 compares the effective collision strengths of the  $2s^22p^5\ ^2P_{3/2} - 2s^22p^5\ ^2P_{1/2}$  and  $2s^22p^6\ ^2P_{3/2} - 2s2p^6\ ^2S_{1/2}$  transitions obtained by Berrington et al. (1998) [72] calculated with 20  $LS$  terms, by Witthoef et al. [71] with 279 levels, and by Witthoef et al. (2007) [73] with 195 levels.

### Fe XIX

Butler and Badnell [74] calculated the effective collision strengths using ICFT  $R$ -matrix method including 342 levels ( $n$  up to 4). Butler and Zeippen [75] performed full relativistic Breit-Pauli  $R$ -matrix calculation with 92 levels included ( $n=2$  and 3). Fig. 23 compared the data by Butler and Badnell [74] with [75].

### Fe XX

Witthoef et al. [76] calculated the effective collision strengths using ICFT  $R$ -matrix method including 302 levels ( $n$  up to 4). Butler and Zeippen [77] performed full relativistic Breit-Pauli  $R$ -matrix calculation with 86 levels ( $n=2$  and 3). Fig. 24 compared the data by Butler and Zeippen (2001), and MacLaughlin and Kirby (2001) [78] who included 23 levels ( $n=2$  and 3) for semi-relativistic Breit-Pauli  $R$ -matrix calculation with [76].

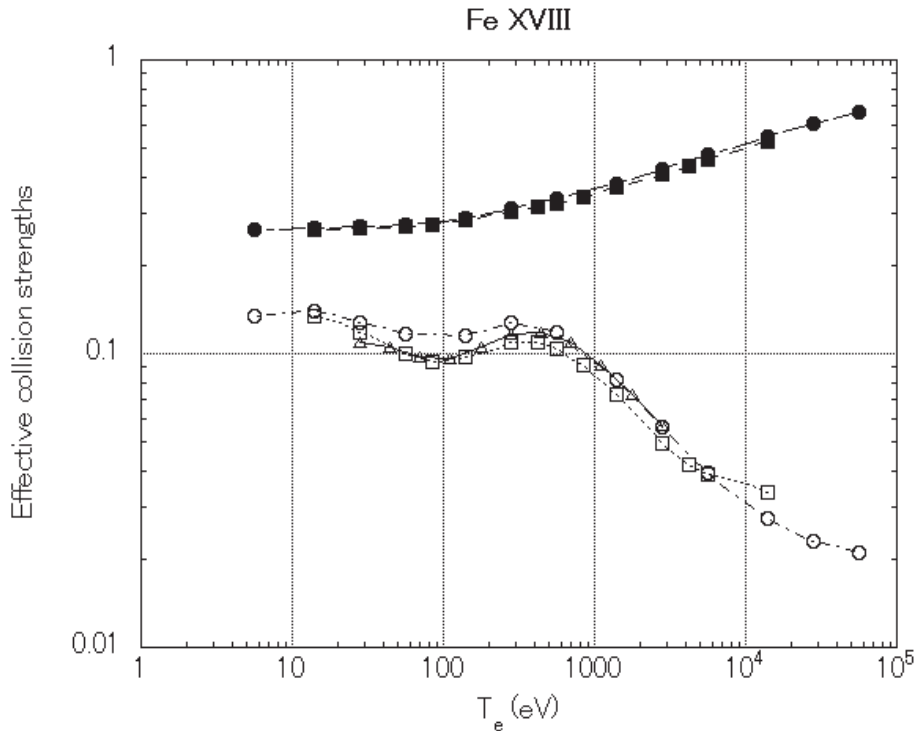


FIG. 22. Effective collision strengths of the Fe XVIII  $2s^22p^5\ ^2P_{3/2} - 2s^22p^5\ ^2P_{1/2}$  (open symbols) and the  $2s^22p^6\ ^2P_{3/2} - 2s2p^6\ ^2S_{1/2}$  (filled symbols) transitions obtained by Berrington et al. (1998) [72] (triangles), Witthoef et al. (2006) [71] with 279 levels (squares), and Witthoef et al. (2007) [73] with 195 levels (circles) as a function of electron temperature.

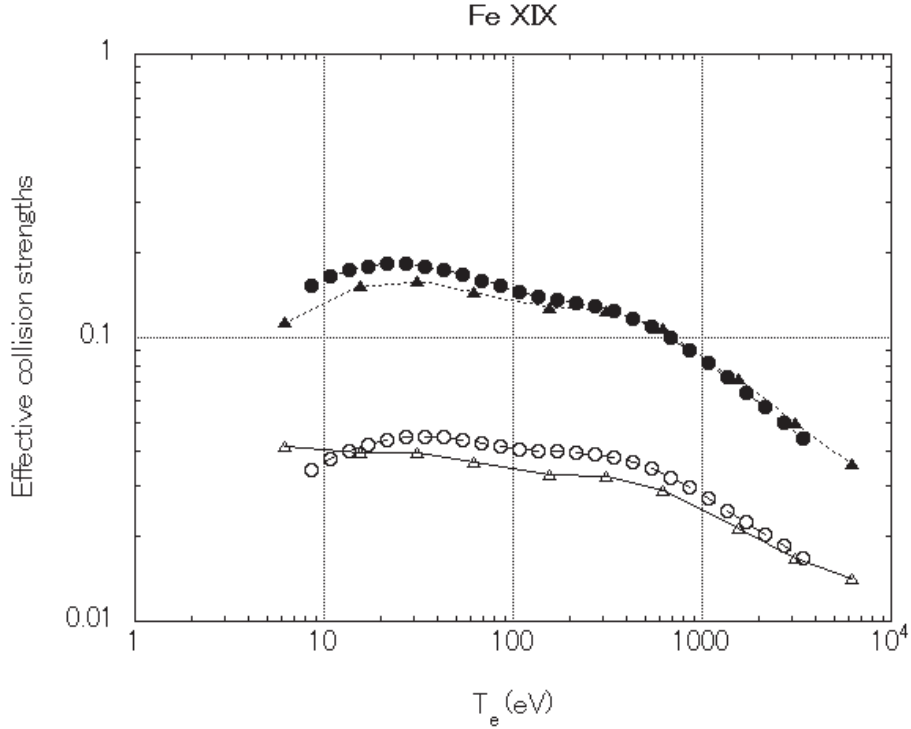


FIG. 23. Effective collision strengths of the Fe XIX  $2s^22p^4\ ^3P_2 - 2s^22p^4\ ^3P_0$  (open symbols) and the  $2s^22p^4\ ^3P_2 - 2s^22p^4\ ^3P_1$  (filled symbols) transitions obtained by Butler and Zeippen (2001) [75] (triangles) and Butler and Badnell (2008) [74] (circles) as a function of electron temperature.

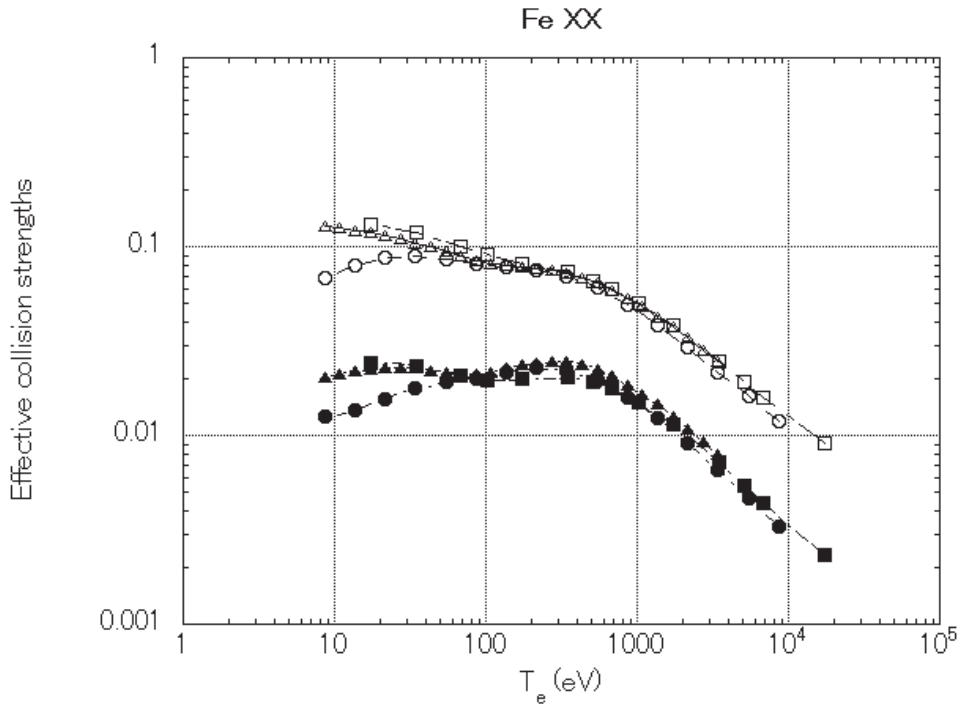


FIG. 24. Effective collision strengths of the Fe XX  $2s^22p^3\ ^4S_{3/2} - 2s^22p^3\ ^2D_{1/2}$  (open symbols) and the  $2s^22p^3\ ^4S_{3/2} - 2s^22p^3\ ^2P_{1/2}$  (filled symbols) transitions obtained by Butler and Zeippen (2001) [77] (triangles), McLaughlin and Kirby (2001) [78] (circles), and Witthoef et al. (2007) [76] (squares) as a function of electron temperature.

## Fe XXI

Badnell and Griffin [21] calculated the effective collision strengths using ICFT  $R$ -matrix method including 200 levels ( $n$  up to 4). Aggarwal and Keenan [79, 80] performed fully relativistic Dirac  $R$ -matrix calculations with 46 levels ( $n = 2$  and 3) including partial waves with  $J$  up to 36.5. On the other hand, Butler and Zeippen [81] performed Breit-Pauli  $R$ -matrix calculations with 52 levels ( $n = 2$  and 3) including partial waves with  $J$  up to 28.5. Both relativistic results reasonably agreed. Bautista et al. [82] calculated the effective collision strengths for inner-shell transitions using Breit-Pauli  $R$ -matrix method. Landi and Gu [70] calculated the data by FAC code including levels with  $n$  up to 5. Fig. 25 compared the data by [21], [81], [79, 80] and [70].

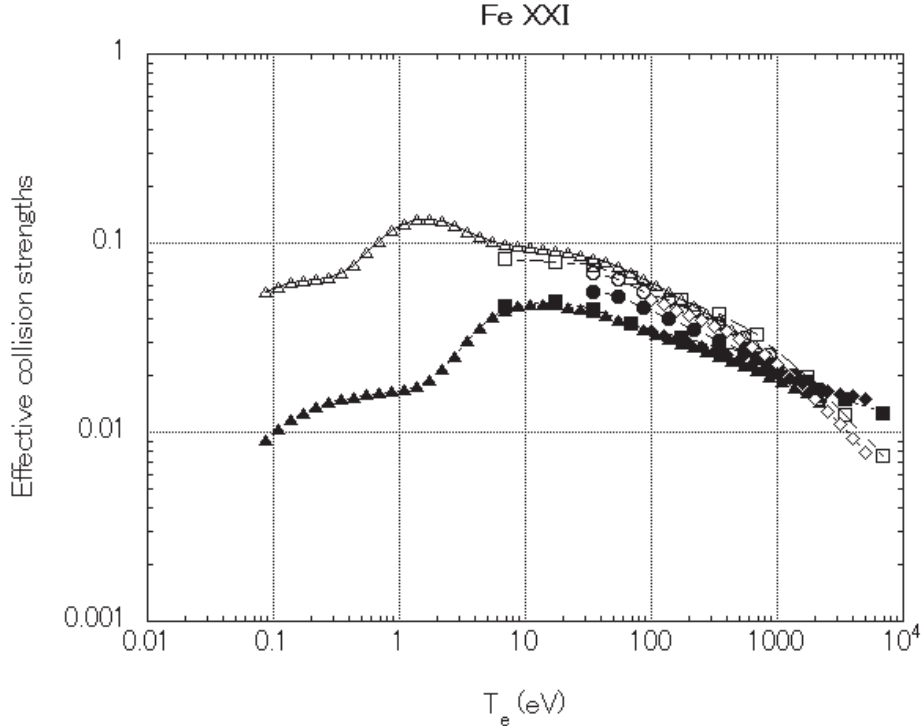


FIG. 25. Effective collision strengths of the Fe XXI  $2s^2 2p^2 \ ^3P_0 - 2s^2 2p^2 \ ^3P_1$  (open symbols) and the  $2s^2 2p^2 \ ^3P_0 - 2s^2 2p^2 \ ^3P_2$  (filled symbols) transitions obtained by Butler and Zeippen (2000) [81] (triangles), Aggarwal and Keenan (2001) [80] (circles), Badnell and Griffin (2001) [21] (squares), and Landi and Gu (2006) [70] (diamonds) as a function of electron temperature.

## Fe XXII

Badnell et al. [22] calculated the effective collision strengths using ICFT  $R$ -matrix method including 204 levels ( $n$  up to 4). Fig. 26 compared the data obtained by Zhang and Pradhan (1997) [83] including 45 levels ( $n = 2$  and 3) using Breit-Pauli  $R$ -matrix method, by Landi and Gu [70] using the FAC code including levels with  $n$  up to 5, and by [22].

## Fe XXIII

Chidichimo et al. [84] calculated the effective collision strengths using ICFT  $R$ -matrix method including 98 levels ( $n$  up to 4). Fig. 27 compared the data by [84] and by the FAC code [70] including levels with  $n$  up to 5.

## Fe XXIV

Whiteford et al. [85] calculated the effective collision strengths using ICFT  $R$ -matrix method including 106 levels ( $1s^2 nl$  with  $n$  up to 5 and  $1s2ln'l'$  with  $n'$  up to 3), including radiation and Auger damping effects. They included inner-shell transitions. Fig. 28 compared the data by [85] and those obtained by Berrington and Tully (1997) [86] including 15 levels with  $n$  up to 4 using Breit-Pauli  $R$ -matrix method.

### Fe XXV

Whiteford et al. [87] calculated the effective collision strengths using ICFT  $R$ -matrix method for 49 levels with  $n$  up to 5, including radiation and damping effects. Fig. 29 compared the data by [87] and by Kimura et al. (2000) [88] including 31 levels with  $n$  up to 4 using Dirac  $R$ -matrix method.

### Fe XXVI

Aggarwal et al. [89] calculated the effective collision strengths using Dirac  $R$ -matrix code including 25 levels ( $n$  up to 5). Ballance et al. [90] also calculated the effective collision strengths for Fe XXVI using Breit-Pauli  $R$ -matrix method including 25 levels for the electron temperature range  $10^6 - 10^{8.5}$  K. Most of both results agree well, but there were found large discrepancies in the effective collision strengths for some transitions. The reasons for the discrepancies are discussed in the paper of Aggarwal et al. [89] and one of the reasons is the different energy mesh for integration to obtain the effective collision strengths from the cross-sections. Fig. 30 compared the data obtained by [89], [90], and Kisielius et al. (1996) [91] including 25 levels with  $n$  up to 5 using Dirac  $R$ -matrix method.

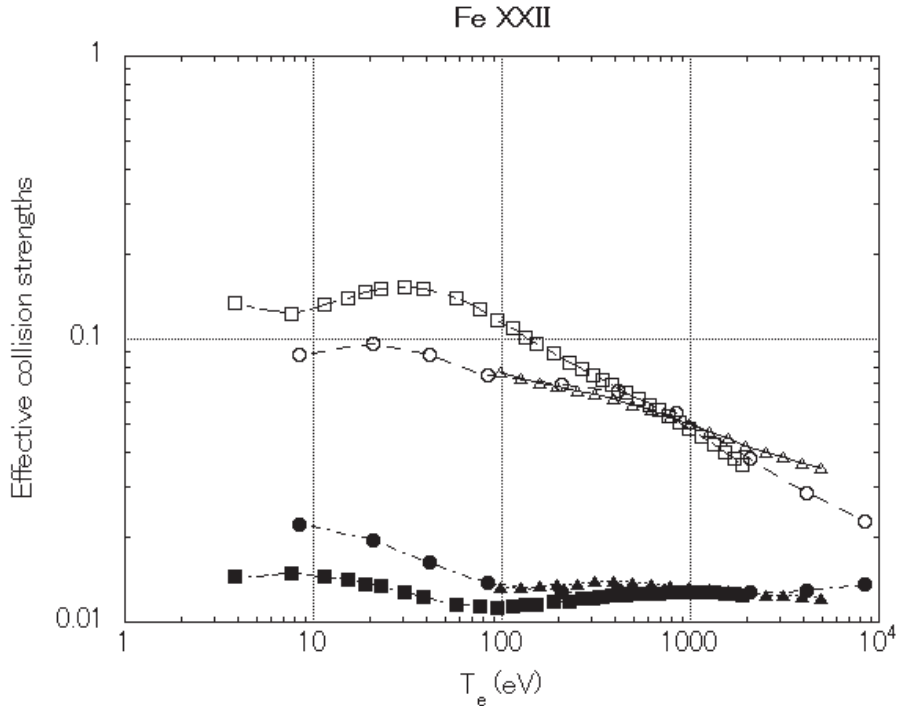


FIG. 26. Effective collision strengths of the Fe XXII  $2s^2 2p^2 P_{1/2} - 2s^2 2p^2 P_{3/2}$  (open symbols) and the  $2s^2 2p^2 P_{1/2} - 2s^2 2p^2 P_{1/2}$  (filled symbols) transitions obtained by Zhang and Pradhan (1997) [83] (squares), Budnell et al. (2001) [22] (circles), and Landi and Gu (2006) [70] (triangles) as a function of electron temperature.

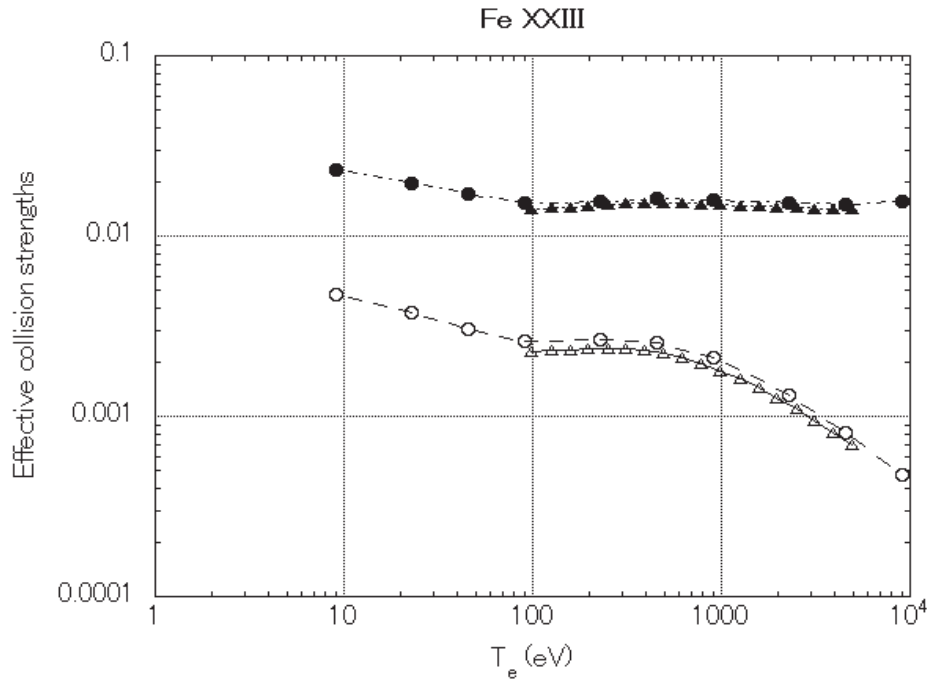


FIG. 27. Effective collision strengths of the Fe XXIII  $2s^2\ ^1S_0 - 2s2p\ ^3P_0$  (open symbols) and the  $2s^2\ ^1S_0 - 2s2p\ ^3P_1$  (filled symbols) transitions obtained by Chidichimo et al. (2005) [84] (circles), and Landi and Gu (2006) [70] (triangles) as a function of electron temperature.

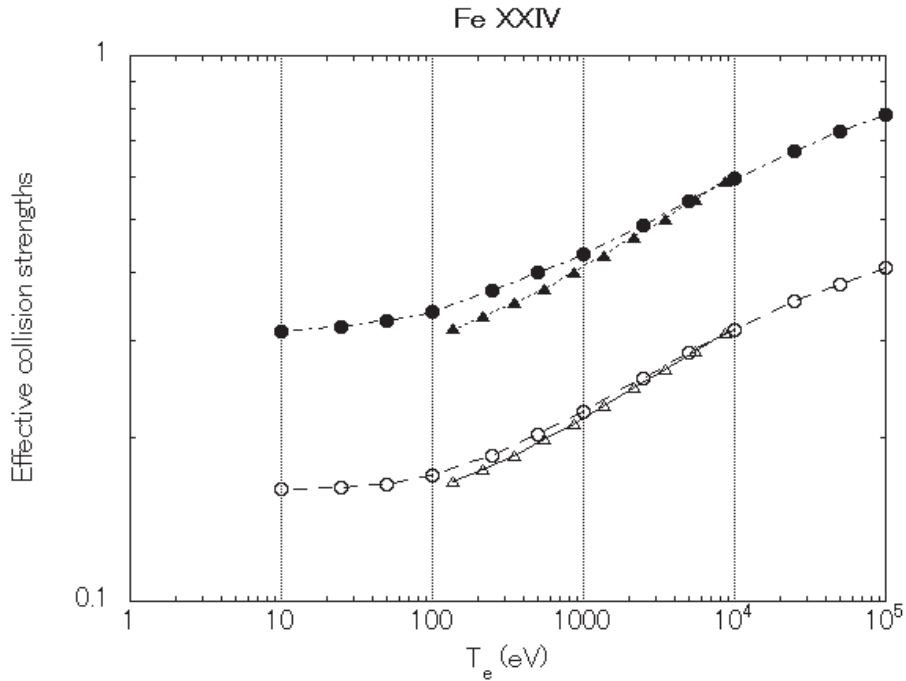


FIG. 28. Effective collision strengths of the Fe XXIV  $2s\ ^2S_{1/2} - 2p\ ^2P_{1/2}$  (open symbols) and the  $2s\ ^2S_{1/2} - 2p\ ^2P_{3/2}$  (filled symbols) transitions obtained by Berrington and Tully (1997) [86] (triangles) and Whiteford et al. (2002) [85] (circles) as a function of electron temperature.

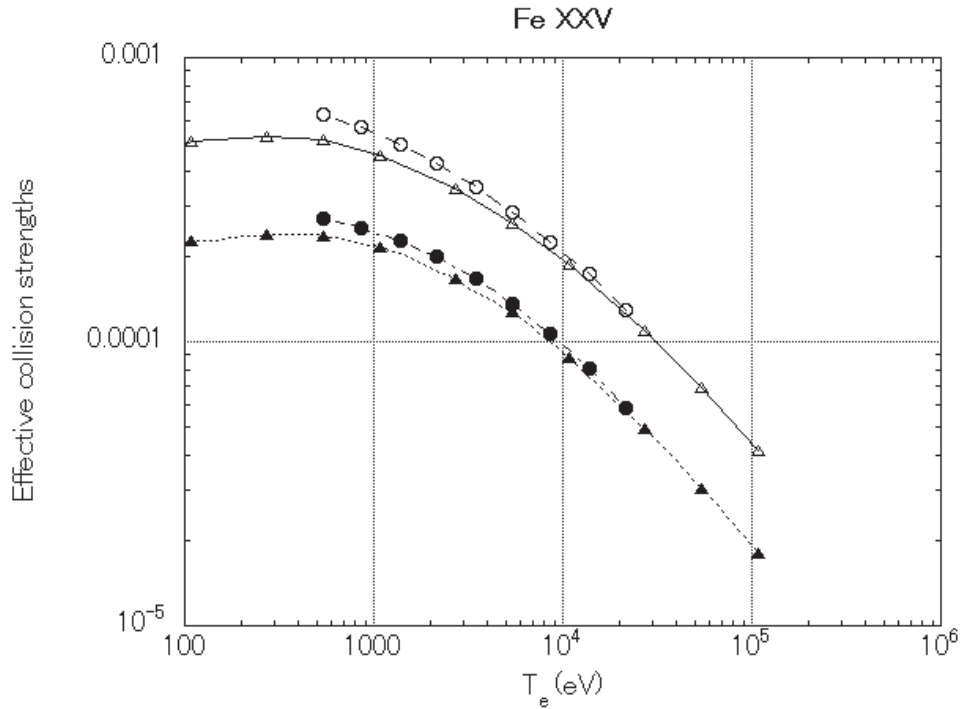


FIG. 29. Effective collision strengths of the Fe XXV  $1s^2\ ^1S_0 - 1s2s\ ^3S_1$  (open symbols) and the  $1s^2\ ^1S_0 - 1s2p\ ^3P_0$  (filled symbols) transitions obtained by Kimura et al. (2000) [88] (circles) and Whiteford et al. (2001) [87] (triangles) as a function of electron temperature.

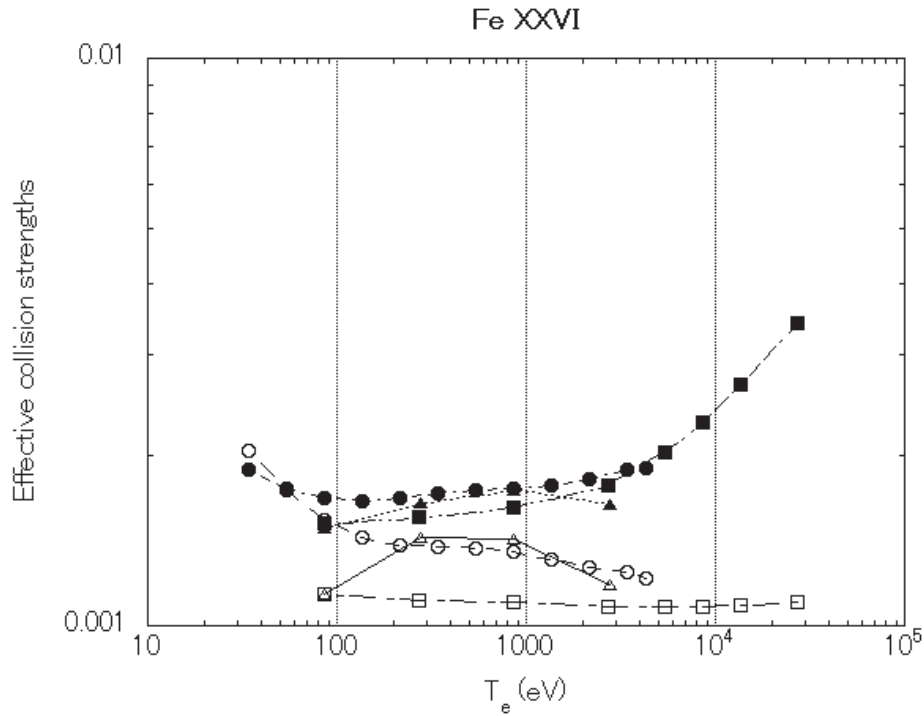


FIG. 30. Effective collision strengths of the Fe XXVI  $1s^2\ ^2S_{1/2} - 2s^2\ ^2S_{1/2}$  (open symbols) and the  $1s^2\ ^2S_{1/2} - 2p^2\ ^2P_{1/2}$  (filled symbols) transitions obtained by Kisielius et al. (1996) [91] (triangles), Balance et al. (2002) [90] (squares), and Aggarwal et al. (2008) [89] (circles) as a function of electron temperature.

TABLE 1. RECOMMENDED DATA OF EFFECTIVE COLLISION STRENGTHS FOR ELECTRON-IMPACT EXCITATION FOR Fe IONS

Ion	Method <sup>a</sup>	Number of levels included	Principal quantum number of levels	Log (K)	T <sub>e</sub>	Data file	Reference
Fe I	BPRM	10	4	2.0 – 3.6		Pradhan's homepage <sup>b</sup>	[27] *
Fe II	BPRM	16 (262)	3, 4	1.5 – 5		CDS <sup>c</sup>	[28]
Fe III	BPRM	219	3, 4	3.5 – 5		CDS	[30] *
Fe IV	NRRM	140	3, 4	3.3 – 5.7		CDS	[32] *
Fe V	RMPS	182 (359)	3, 4	4.6 – 5.6		ORNL <sup>d</sup>	[34]
Fe VI	DARC	96 (1728)	3, 4	4.3 – 6.8		ORNL	[36]
Fe VII	ICFTR	189	3 – 5	5.0 – 8.0		ORNL	[38]
Fe VIII	ICFTR	77	3, 4	4.5 – 6.5		CDS	[39]
Fe IX	RM	140	3, 4	5.4 – 7.0		CHIANTI <sup>e</sup>	[41]
Fe X	DARC	90	3	5.0 – 7.0		CDS	[44]
Fe XI	DARC	48	3	4.0 – 6.7		AA electronic journal	[49]
Fe XII	RM	143	3	5.0 – 8.0		CHIANTI	[52]
Fe XIII	DARC	97	3	5.0 – 6.8		CDS	[54]
Fe XIV	BPRM	135	3, 4	5.5 – 7.0		ApJS electronic journal	[56]
Fe XV	DARC	53	3, 4	5.0 – 7.0		CDS	[61]
Fe XVI	DARC	39	3 – 7	5.0 – 7.0		CDS	[65]
Fe XVII	DARC	139	2 – 5	5.0 – 7.0		ORNL	[69]
Fe XVIII	ICFTR	279	2 – 4	5.2 – 8.2		OPEN-ADAS <sup>f</sup> Flike_mcw05#fe17.dat	[71]
Fe XIX	ICFTR	342	2 – 4	4.9 – 7.9		ORNL / CDS	[74]
Fe XX	ICFTR	302	2 – 4	5.3 – 8.3		ORNL / CDS	[76]
Fe XXI	ICFTR	200	2 – 4	4.9 – 7.9		ORNL	[21]
Fe XXII	ICFTR	204	2 – 4	5.0 – 8.0		ORNL	[22]
Fe XXIII	ICFTR	98	2 – 4	6.3 – 8.1		ORNL / CDS	[84]
Fe XXIV	ICFTR	106	2 – 5	6.2 – 8.0		ORNL	[85]
Fe XXV	ICFTR	49	2 – 5	6.0 – 9.0		ORNL	[87]
Fe XXVI	DARC	25	2 – 5	5.6 – 7.7		CDS	[89]

\*same as the recommendation by Pradhan and Zhang [10]

<sup>a</sup>Method

BPRM: Breit-Pauli R-Matrix

NRRM: Non-relativistic R-matrix

RMPS: R-matrix with pseudo-state

PRMAT: Parallel R-matrix

DARC: Dirac Atomic R-matrix Code

ICFTR: ICFT R-matrix

<sup>b</sup><http://www.astronomy.ohio-state.edu/~pradhan/atomic.html>

<sup>c</sup>CDS: <http://cdsweb.u-strasbg.fr/>

<sup>d</sup>ORNL: <http://www-cfadc.phy.ornl.gov/>

<sup>e</sup>CHIANTI: <http://wwwsolar.nrl.navy.mil/chianti.html>

<sup>f</sup>OPEN-ADAS: <http://open.adas.ac.uk/>

## 5.2. Proton-Impact

The proton – ion collisions are important for excitation and de-excitation of the fine structure levels of Fe ions in high temperature plasmas as shown in the previous sections and in Figs. 6 and 7. The proton excitation/de-excitation between the fine structure levels involving ground or low-lying metastable states are of primary interest. We have evaluated the excitation rate coefficients by proton-impact for Fe X - Fe XV ions [16, 17] and for Fe XVII - Fe XXIII ions [23, 17]. In these reports, the evaluated rate coefficients are expressed by a simple analytical formula with 7 parameters.

## 6. CONCLUSIONS

EUV spectral lines of Fe XIII, Fe XXI, and Fe XXII measured from LHD are identified and the intensity ratios are studied for density diagnostics. The theoretical calculations of the line intensity ratios by a CR model of each ion species as a function of the electron density are compared with measured intensity ratios. For Fe XXI and XXII ions, the proton-impact excitation is important for the intensity ratios in fusion plasmas.

The recent data for excitation rate coefficients by electron-impact are surveyed and evaluated for all Fe ions and atom. Information for the recommended data is listed in a Table. Most of the data are available electronically via internet.

## ACKNOWLEDGMENTS

This work was partly supported by the research collaboration program in NIFS. The authors would like to thank the LHD experiment group for their support.

## REFERENCES

- [1] BROWN, C.M., FELDMAN, U., SEELY, J.F., KORENDYKE, C.M., HARA, H., Wavelengths and intensities of spectral lines in the 171-211 and 245-291 Å ranges from five solar regions recorded by the extreme-ultraviolet imaging spectrometer (EIS) on *Hinode*, *Astrophys. J. Suppl.* **176** (2008) 511.
- [2] FOURNIER, K.B., FINKENTHAL, M., PACELLA, D., MAY, M.J., LEIGHEB, M., SOUKHANOVSKII, V., GOLDSTEIN, W.H., Measurement of *M*-shell iron ionization balance in a tokamak plasma, *Astrophys. J.* **550** (2001) L117.
- [3] MASAI, K., KATO, T., Electron density diagnostics by Fe XXII line intensity ratio, *Physics Letters A* **123** (1987) 405.
- [4] BEIERSDORFER, P., Laboratory X-Ray Astrophysics, *Ann. Rev. Astronom. & Astrophys.* **41** (2003) 343.
- [5] YAMAMOTO, N., KATO, T., FUNABA, H., SATO, K., TAMURA, N., SUDO, S., BEIERSDORFER, P., LEPSON, J.K., Measurement and modeling of density-sensitive lines of Fe XIII in the extreme ultraviolet, *Astrophys. J.* **689** (2008) 646.
- [6] SAKAUE, H.A., YAMAMOTO, N., MORITA, S., NAKAMUR, N., CHEN, C., KATO, D., KIKUCHI, H., MURAKAMI, I., OHTANI, S., TANUMA, H., WATANABE, T., TAWARA, H., Electron density dependence of intensity ratio for FeXXII extreme ultraviolet emission lines arising from different ground levels in electron beam ion trap and large helical device”, *J. Appl. Phys.* 109 (2011) 073304.
- [7] YOUNG, P.R., Radiative data for Fe XIII, *Astron. & Astrophys.* **417** (2004) 785.
- [8] WATANABE, T., HARA, H., YAMAMOTO, N., KATO, D., SAKAUE, H.A., MURAKAMI, I., KATO, T., NAKAMURA, N., YOUNG, P.R., Fe XIII density diagnostics in the EIS observing wavelengths, *Astrophys. J.* **692** (2009) 1294.
- [9] LANG, J., The atomic data assessment meeting, abingdon, March 1992, *Atomic Data and Nucl. Data Tables* **57** (1994) 1.

- [10] PRADHAN, A.K., ZHANG, H.L., Photon and Electron Interactions with Atoms, Molecules and Ions, Landolt-Beornstein New Series I/17B, Ed. Y. Itikawa (Springer-Verlag, 2001), p.3-1.
- [11] SCHWOB, J.L., WOUTERS, A.W., SUCKEWER, S., FINKENTHAL, M., High-resolution duo-multichannel soft x-ray spectrometer for tokamak plasma diagnostics, *Rev. Sci. Instrum.* **58** (1987) 1601.
- [12] CHOWDHURI, M.B., MORITA, S., GOTO, M., NISHIMURA, H., NAGAI, K., FUJIOKA, S., Spectroscopic comparison between 1200 grooves/mm ruled and holographic gratings of a flat-field spectrometer and its absolute sensitivity calibration using bremsstrahlung continuum, *Rev. Sci. Instrum.* **78** (2007) 023501.
- [13] BAR-SHALOM, A., KLAPISCH, M., OREG, J., HULLAC, an integrated computer package for atomic processes in plasmas, *J. Quant. Spectr. Rad. Transf.* **71** (2001) 169.
- [14] AGGARWAL, K.M., KEENAN, F.P., Effective collision strengths for transitions in Fe XIII, *Astron. Astrophys.* **429** (2005) 1117.
- [15] SKOBELEV, I., (2009) excitation fitting, NIFS-DATA-104.
- [16] SKOBELEV, I., et al., (2006) NIFS-DATA-95.
- [17] SKOBELEV, I., MURAKAMI, I., KATO, I., Recommended data on proton-ion collision rate coefficients for Fe X – Fe XXIII ions, *Astron. & Astrophys.* **511** (2010) A60.
- [18] DERE, K.P., LANDI, E., MASON, H.E., MONSIGNORI FOSSI, B.C., YOUNG, P.R., CHIANTI - an atomic database for emission lines, *Astron. & Astrophys. Suppl.* **125** (1997) 149.
- [19] LANDI, E., DEL ZANNA, G., YOUNG, P.R., DERE, K.P., MASON, H.E., LANDINI, M., CHIANTI—an atomic database for emission lines. VII. new data for x-rays and other improvements, *Astrophys. J. (Suppl.)* **162** (2006) 261.
- [20] RALCHENKO, YU. et al., <http://physics.nist.gov/asd3> (2008).
- [21] BADNELL, N.R., GRIFFIN, D.C., Electron-impact excitation of Fe<sup>20+</sup>, including  $n = 4$  levels, *J. Phys. B* **34** (2001) 681.
- [22] BADNELL, N.R., GRIFFIN, D.C., MITNIK, D.M., Electron-impact excitation of Fe<sup>21+</sup>, including  $n = 4$  levels, *J. Phys. B* **34** (2001) 5071.
- [23] SKOBELEV, I., et al., NIFS-DATA-99 (2007).
- [24] HUMMER, D.G., BERRINGTON, K.A., EISSNER, W., PRADHAN, A.K., SARAPH, H.E., TULLY, J.A., Atomic data from the Iron Project I. goals and methos, *Astron. & Astrophys.* **279** (1993) 298.
- [25] BERRINGTON, K.A., BALLANCE, C.P., GRIFFIN, D.C., BADNELL, N.R., The agreement of Breit–Pauli and Dirac  $R$ -matrix collision strengths for iron peak elements : an Fe<sup>14+</sup> case study, *J. Phys. B* **38** (2005) 1667.
- [26] GRIFFIN, D.C., BADNELL, N.R., PINDZOLA, M.S.,  $R$ -matrix electron-impact excitation cross-sections in intermediate coupling: an MQDT transformation approach, *J. Phys. B* **31** (1998) 3713.
- [27] PELAN, J., BERRINGTON, K.A., Atomic data from the Iron Project XXI. Electron excitation of fine-structure transitions involving the  $3d^6 4s^2 \ ^5D$  ground state and the  $3d^7 4s \ ^5F$  metastable state of Fe I, *Astron. & Astrophys. Suppl.* **122** (1997) 177.
- [28] RAMSBOTTOM, C.A., HUDSON, C.E., NORRINGTON, P.H., SCOTT, M.P., Electron-impact excitation of Fe II Collision strengths and effective collision strengths for low-lying fine-structure forbidden transitions, *Astron. & Astrophys.* **475** (2007) 765.
- [29] ZHANG, H.L., PRADHAN, A.K., Atomic data from the Iron Project VI. Collision strength and rate coefficients for Fe II, *Astron. Astrophys.* **293** (1995) 953.
- [30] ZHANG, H.L., Atomic data from the Iron Project. XVIII. Electron-impact excitation collision strengths and rate coefficients for Fe III, *Astron. Astrophys. Suppl.* **119** (1996) 523.
- [31] McLAUGHLIN, B.M., SCOTT, M.P., SUNDERLAND, A.G., NOBLE, C.J., BURKE, V.M., RAMSBOTTOM, C.A., REID, R.H.G., HIBBERT, A., BELL, K.L., BURKE, P.G., Electron collisions with Fe-peak elements: Forbidden transitions between the low

- lying valence states  $3d^6$ ,  $3d^5 4s$ , and  $3d^5 4p$  of Fe III, *Atomic Data and Nucl. Data Tables* **93** (2007) 55.
- [32] ZHANG, H.L., PRADHAN, A.K., Atomic data from the Iron Project XXVII. Electron-impact excitation collision strengths and rate coefficients for Fe IV, *Astron. Astrophys. Suppl.* **126** (1997) 373.
- [33] McLAUGHLIN, B.M., HIBBERT, A., SCOTT, M.P., NOBLE, C.J., BURKE, V.M., BURKE, P.G., Electron collisions with Fe-peak elements: Fe IV I. Forbidden transitions:  $3d^5$ - $3d^4 4s$  and  $3d^5$ - $3d^4 4p$  manifolds, *Astron. Astrophys.* **446** (2006) 1185.
- [34] BALLANCE, C.P., GRIFFIN, D.C., McLAUGHLIN, B.M., Electron-impact excitation of  $Fe^{4+}$ : an intermediate-coupling *R*-matrix calculation, *J. Phys. B* **40** (2007) F327.
- [35] BERRINGTON, K.A., Atomic data from the Iron Project. VIII. Electron excitation of the  $3d^4 \ ^5D_J$  ground state fine-structure transitions in Ti-like ions V II, Cr III, Mn IV, Fe V, Co VI and Ni VII, *Astron. Astrophys. Suppl.* **109** (1995) 193.
- [36] BALLANCE, C.P., GRIFFIN, D.C., Intermediate-coupling *R*-matrix calculations of electron-impact excitation of  $Fe^{5+}$ , *J. Phys. B* **41** (2008) 195205.
- [37] CHEN, G.X., PRADHAN, A.K., Atomic data from the Iron Project XXXVII. Electron-impact excitation collision strengths and rate coefficients for Fe VI, *Astron. Astrophys. Suppl.* **136** (1999) 395.
- [38] WITTHOEFT, M.C., BADNELL, N.R., Atomic data from the Iron Project LXV. Electron-impact excitation of  $Fe^{6+}$ , *Astron. & Astrophys.* **481** (2008) 543.
- [39] BERRINGTON, K.A., NAKAZAKI, S., NORRINGTON, P.H., Atomic data from the Iron Project XLI. Electron excitation rates among the  $3d^2$  fine-structure levels of Ca-like Fe VII, *Astron. Astrophys. Suppl.* **142** (2000) 313.
- [40] GRIFFIN, D.C., PINDZOLA, M.S., BADNELL, N.R., Electron-impact excitation of  $Fe^{7+}$ , *Astron. Astrophys. Suppl.* **142** (2000) 317.
- [41] STOREY, P.J., ZEIPPEN, C.J., LE DOURNEUF, M., Atomic data from the Iron Project LI. Electron-impact excitation of Fe IX, *Astron. Astrophys.* **394** (2002) 753.
- [42] BURGESS, A., TULLY, J.A., On the analysis of collision strengths and rate coefficients, *Astron. Astrophys.* **254** (1992) 436.
- [43] FAWCETT, B.C., MASON, H.E., Collision strengths and oscillator strengths for Fe IX, *Atomic Data and Nucl. Data Tables* **47** (1991) 17.
- [44] AGGARWAL, K.M., KEENAN, F.P., Effective collision strengths for transitions in Fe X, *Astron. & Astrophys.* **439** (2005) 1215.
- [45] DEL ZANNA, G., BERRINGTON, K.A., MASON, H.E., Benchmarking atomic data for astrophysics: Fe X, *Astron. Astrophys.* **422** (2004) 731.
- [46] PELAN, J., BERRINGTON, K.A., Atomic data from the Iron Project. IX. Electron excitation of the  $^2P^o_{3/2}$ - $^2P^o_{1/2}$  fine-structure transition in chlorine-like ions, from Ar II to Ni XII, *Astron. Astrophys., Suppl.* **110** (1995) 209.
- [47] TAYAL, S.S., Electron-impact excitation collision strengths for Fe X, *Astrophys. J. Suppl.* **132** (2001) 117.
- [48] PELAN, J.C., BERRINGTON, K.A., Atomic data from the Iron Project XLVI. Electron excitation of  $3s3p^6$  and  $3s^2 3p^4 3d$  fine-structure transitions in Fe X, *Astron. & Astrophys* **365** (2001) 258.
- [49] AGGARWAL, K.M., KEENAN, F.P., Effective collision strengths for transitions in Fe XI, *A&A* **399** (2003) 799.
- [50] GUPTA, G.P., TAYAL, S.S., Effective collision strengths for electron-impact excitation of fine-structure levels in Fe XI, *Astrophys. J.* **510** (1999) 1078.
- [51] TAYAL, S.S., Effective collision strengths of fine-structure transitions in Fe X, Fe XI, and Fe XIII, *Astrophys. J.* **544** (2000) 575.
- [52] STOREY, P.J., DEL ZANNA, G., MASON, H.E., ZEIPPEN, C.J., Atomic data from the Iron Project LVIII. Electron-impact excitation of Fe XII, *Astron. & Astrophys.* **433** (2005) 717.
- [53] BINELLO, A.M., Mason, H.E., Storey, P.J., Atomic data from the Iron Project XXV. Electron-impact excitation of fine-structure transitions in the ground configuration of Fe XII, *Astron. Astrophys. Suppl.* **127** (1998) 545.

- [54] AGGARWAL, K.M., KEENAN, F.P., Effective collision strengths for transitions in Fe XIII, *Astron. & Astrophys.* **429** (2005) 1117.
- [55] GUPTA, G.P, TAYAL, S.S., Collision strengths for electron-impact excitation of fine-structure levels in Fe XIII, *Astrophys. J.* **506** (1998) 464.
- [56] TAYAL, S.S., Transition probabilities and electron excitation rates for Fe XIV, *Astrophys. J. Suppl.* **178** (2008) 359.
- [57] STOREY, P.J., MASON, H.E., SARAPH, H.E., Atomic data from the Iron Project XIV. Electron-impact excitation of the Fe XIV fine-structure transition  ${}^2P^o_{1/2} \rightarrow {}^2P^o_{3/2}$ , *Astron. & Astrophys.* **309** (1996) 677.
- [58] STOREY, P.J., MASON, H.E., YOUNG, P.R., Atomic data from the Iron Project XL. Electron-impact excitation of the Fe XIV EUV transitions, *Astron. Astrophys. Suppl.* **141** (2000) 285.
- [59] AGGARWAL, K. KEENAN, F.P., Energy levels, radiative rates and electron impact excitation rates for transitions in Fe XIV, *Mon. Not. Roy. Astron. Soc.* **445** (2014) 2015.
- [60] GU, M.F., Indirect x-ray line-formation processes in iron *L*-shell ions, *Astrophys. J.* **582** (2003) 1241.
- [61] AGGARWAL, K.M., KEENAN, F.P., MSEZANE, A.Z., Effective collision strengths for transitions in Fe XV, *Astron. & Astrophys.* **410** (2003) 349.
- [62] BERRINGTON, K.A., BALLANCE, C.P., GRIFFIN, D.C., BADNELL, N.R., The agreement of Breit–Pauli and Dirac *R*-matrix collision strengths for iron peak elements: an Fe<sup>14+</sup> case study, *J. Phys. B* **38** (2005) 1667.
- [63] GRIFFIN, D.C., BADNELL, N.R., PINDZOLA, M.S., SHAW, J.A., Electron-impact excitation of Mg-like ions, *J. Phys. B* **32** (1999) 2139.
- [64] EISSNER, W., GALAVÍS, M.E., MENDOZA, C., ZEIPPEN, C.J., Atomic data from the Iron Project XXXVIII. Electron-impact excitation of the fine-structure transitions in the *n*=3 complex of Fe XV, *Astron. Astrophys. Suppl.* **137** (1999) 165.
- [65] AGGARWAL, K.M., KEENAN, F.P., Electron-impact excitation of Fe XVI: radiative and excitation rates, *Astron. & Astrophys.* **450** (2006) 1249.
- [66] EISSNER, W., GALAVÍS, M.E., MENDOZA, C., ZEIPPEN, C.J., Atomic data from the Iron Project XXXIV. Electron-impact excitation of Fe XVI, *Astron. Astrophys. Suppl.* **136** (1999) 385.
- [67] AGGARWAL, K.M., KEENAN, F.P., Effective collision strengths for inner shell transitions of Fe XVI, *J. Phys. B* **41** (2008) 015701.
- [68] LIANG, G.Y., WHITEFORD, A.D., BADNELL, N.R., *R*-matrix inner-shell electron-impact excitation of Fe<sup>15+</sup> including Auger-plus-radiation damping, *J. Phys. B* **41** (2008) 235203.
- [69] LOCH, S.D., PINDZOLA, M.S., BALLANCE, C.P., GRIFFIN, D.C., The effects of radiative cascades on the x-ray diagnostic lines of Fe<sup>16+</sup>, *J. Phys. B* **39** (2006) 85.
- [70] LANDI, E., GU, M.F., Atomic data for high-energy configurations in Fe XVII–XXIII, *Astrophys. J.* **640** (2006) 1171.
- [71] WITTHOEFT, M.C., BADNELL, N.R., DEL ZANNA, G., BERRINGTON, K.A., PELAN, J.C., Atomic data from the Iron project-LX. Electron-impact excitation of *n*=3, 4 levels of Fe<sup>17+</sup>, *Astronomy & Astrophysics* **446** (2006) 361.
- [72] BERRINGTON, K.A., SARAPH, H.E., TULLY, J.A., Atomic data from the Iron Project XXVIII. Electron excitation of the  ${}^2P^o_{3/2} \rightarrow {}^2P^o_{1/2}$  fine structure transition in fluorine-like ions at higher temperatures, *Astron. Astrophys. Suppl.* **129** (1998) 161.
- [73] WITTHOEFT, M.C., WHITEFORD, A.D., BADNELL, N.R., *R*-matrix electron-impact excitation calculations along the F-like iso-electronic sequence, *J. Phys. B* **40** (2007) 2969.
- [74] BUTLER, K., BADNELL, N.R., Atomic data from the Iron Project LXVI. Electron-impact excitation of Fe<sup>18+</sup>, *Astron. & Astrophys.* **489** (2008) 1369.
- [75] BUTLER, K., ZEIPPEN, C.J., Atomic data from the Iron Project-XLIX. Electron-impact excitation of Fe XX, *Astronomy & Astrophysics* **372** (2001) 1078
- [76] WITTHOEFT, M.C., DEL ZANNA, G., BADNELL, N.R., Atomic data from the Iron Project LXIII. Electron-impact excitation of Fe<sup>19+</sup> up to *n* = 4, *Astron. & Astrophys.*

- 466 (2007) 763.
- [77] BUTLER, K., ZEIPPEN, C.J., Atomic data from the Iron Project XLIX. Electron-impact excitation of Fe XX, *Astron. & Astrophys.* **372** (2001) 1078.
  - [78] McLAUGHLIN, B.M., KIRBY, K.P., Electron collisional excitation of the  $1s^2 2s^2 2p^3$  ( $^4S^o_{3/2}$ ,  $^2D^o_{5/2, 3/2}$ ,  $^2P^o_{3/2, 1/2}$ ) fine-structure levels in Fe<sup>19+</sup> ions, *J. Phys. B* **34** (2001) 2255.
  - [79] AGGARWAL, K.M., KEENAN, F.P., Electron-impact excitation of carbon-like iron, *J. Phys. B* **32** (1999) 3585.
  - [80] AGGARWAL, K.M., KEENAN, F.P., Effective collision strengths for transitions within the ground configuration of Fe XXI, *Phys. Scr.* **64** (2001) 439.
  - [81] BUTLER, K., ZEIPPEN, C.J., Atomic data from the Iron Project XLII. Electron-impact excitation of Fe XXI, *Astron. Astrophys. Suppl.* **143** (2000) 483.
  - [82] BAUTISTA, M.A., MENDOZA, C., KALLMAN, T.R., PALMERI, P., *K*-shell photoionization and electron-impact excitation of Fe XVII-Fe XXIII, *Astron. & Astrophys.* **418** (2004) 1171.
  - [83] ZHANG, H.L., PRADHAN, A.K., Atomic data from the Iron Project XXIII. Relativistic excitation rate coefficients for Fe XXII with inclusion of radiation damping, *Astron. Astrophys. Suppl.* **123** (1997) 575.
  - [84] CHIDICHIMO, M.C., DEL ZANNA, G., MASON, H.E., BADNELL, N.R., TULLY, J.A., BERRINGTON, K.A., Atomic data from the Iron Project LVI. Electron excitation of Be-like Fe XXIII for the  $n = 2, 3, 4$  configurations, *Astron. & Astrophys.* **430** (2005) 331.
  - [85] WHITEFORD, A.D., BADNELL, N.R., BALLANCE, C.P., LOCH, S.D., O'MULLANE, M.G., SUMMERS, H.P., Excitation of Ar<sup>15+</sup> and Fe<sup>23+</sup> for diagnostic application to fusion and astrophysical plasmas, *J. Phys. B* **35** (2002) 3729.
  - [86] BERRINGTON, K.A., TULLY, J.A., Atomic data from the Iron Project XXIV. Electron excitation of Li-like Fe XXIV between the  $n = 2$  and  $n' = 2, 3, 4$  fine-structure levels, *Astron. Astrophys. Suppl.* **126** (1997) 105.
  - [87] WHITEFORD, A.D., BADNELL, N.R., BALLANCE, C.P., O'MULLANE, M.G., SUMMERS, H.P., THOMAS, A.L., A radiation-damped *R*-matrix approach to the electron-impact excitation of helium-like ions for diagnostic application to fusion and astrophysical plasmas, *J. Phys. B* **34** (2001) 3179.
  - [88] KIMURA, E., NAKAZAKI, S., BERRINGTON, K.A., NORRINGTON, P.H., Rate coefficients for electron-impact excitation of helium-like ions within the Dirac *R*-matrix approach, *J. Phys. B* **33** (2000) 3449.
  - [89] AGGARWAL, K.M., HAMADA, K., IGARASHI, A., JONAUSKAS, V., KEENAN, F.P., NAKAZAKI, S., Radiative rates and electron-impact excitation rates for H-like Fe XXVI, *Astron. & Astrophys.* **484** (2008) 879.
  - [90] BALLANCE, C.P., Badnell, N.R., Berrington, K.A., Electron-impact excitation of H-like Fe at high temperatures, *J. Phys. B* **35** (2002) 1095.
  - [91] KISIELIUS, R., BERRINGTON, K.A., NORRINGTON, P.H., Atomic data from the Iron Project. XV. Electron excitation of the fine-structure transitions in hydrogen-like ions He II and Fe XXVI, *Astron. Astrophys. Suppl.* **118** (1996) 157.



# EUV SPECTRA OF HIGH Z IMPURITIES FROM LARGE HELICAL DEVICE AND ATOMIC DATA

T. KATO<sup>1</sup>, G. O'SULLIVAN<sup>2</sup>, C. SUZUKI<sup>1</sup>, C. HARTE<sup>2</sup>, J. WHITE<sup>2</sup>, R. D'ARCY<sup>2</sup>,  
H. FUNABA<sup>1</sup>, K. SATO<sup>1</sup>, H. TANUMA<sup>3</sup>, I. MURAKAMI<sup>1</sup>, D. KATO<sup>1</sup>, H.  
SAKAUE<sup>1</sup>, N. NAKAMURA<sup>4</sup>

<sup>1</sup> National Institute for Fusion Science, Toki, Gifu, Japan

<sup>2</sup> University College Dublin, Dublin, Ireland

<sup>3</sup> Tokyo Metropolitan University, Tokyo, Japan

<sup>4</sup> Electro Communication University, Chofu, Japan

## Abstract

The results of experiments on high Z impurity injection in the Large Helical Device at the National Institute for Fusion Science are described. Spectra from Xe, Sn and W ions were recorded in the extreme ultraviolet spectral region. Two different situations were observed in the case of Xe and Sn, depending on whether or not the plasma underwent radiative collapse. If the plasma was stable, the spectrum consisted of a number of strong lines and in both cases the strongest contribution was from  $4p - 4d$  transitions of Cu-like ions. If the plasma underwent radiative collapse in each case it was dominated by an intense unresolved transition array with some strong lines overlapping it resulting from  $4p^6 4d^m - 4p^5 4d^{m+1} + 4p^6 4d^{m-1} 4f$  transitions. For tungsten, radiative collapse was not observed though the spectrum here was dominated by the same array which lies between 4.5 and 7 nm with some additional contribution at the same wavelength from  $4d^{10} 4f^m - 4d^9 4f^{m+1}$  and  $4d^{10} 4f^m - 4d^{10} 4f^{m-1} 5d$  transitions in lower stages also. From observation and comparison with other sources, it is shown that the spectra are dominated by resonance transitions to the ground state of the emitting ions, in marked contrast to results from charge exchange spectra that had been recorded to assist with ion stage separation. In the case of tungsten, no sharp lines are seen though the profile of the unresolved array structure changes with plasma temperature and the origin of these changes can be traced to differences in the populations of contributing ions. New assignments for lines of Xe XVIII, Sn XIX and Sn XVII of  $4p - 4d$  transitions are listed in Tables. Strong lines of W, Xe and Sn ions in EUV range are also tabulated.

## 1. INTRODUCTION

In the next generation fusion reactor, ITER, the material of the plasma facing components (PFC) must be capable of tolerating large thermal loads, have a low erosion rate and low cross-section for tritium assimilation. For this reason, tungsten has become the standby material for use as a divertor coating if carbon generated from the carbon fibre composite tiles at the strike zones leads to unacceptable levels of tritium capture, and will be used for the divertor baffles and dome [1]. To investigate the effect of having tungsten ions present in a fusion plasma, studies are already underway at a number of major locations worldwide, for example, at JET, where tungsten erosion rates and the impact of an all tungsten divertor are being studied and at the ASDEX Upgrade Tokamak in Garching where interior regions have been coated with tungsten to study the effects of tungsten impurities on the plasma dynamics and on the spectral emission from tungsten ions [2, 3]. The spectra are dominated by intense unresolved transition array (UTA) emission in the 4.5 – 7 nm region which a simple plot of  $\sqrt{E}$  vs.  $Z$  ( $E$  is the transition energy,  $Z$  the atomic number) shows to have a common origin with the UTA observed and studied in considerable detail in studies of extreme ultraviolet lithography (EUVL) source plasmas in Sn and Xe spectra and primarily arise from the  $4p^6 4d^m - 4p^6 4d^{m-1} 4f$  component of  $4p^6 4d^m - 4p^5 4d^{m+1} + 4p^6 4d^{m-1} 4f$  transition arrays [4]. Thus the large body of work performed on EUVL sources has relevance also to fusion science.

From work performed in the late 1970s at ORMAK, the Oak Ridge Tokamak it was found that radiation from tungsten ions sputtered into the plasma radiated very strongly between 4.5 and 7 nm where a structured quasicontinuum overlaid by a few strong lines was observed. The radiation was shown to primarily originate from  $4d^{10}4f-4d^94f^2$  and  $4d^{10}4f-4d^{10}5d$  transitions in the Ag-like W XXVIII spectrum [5]. Subsequently features in the 4-7 nm region resulting from groups of unresolved  $4d - 4f$ ,  $5p$  and  $4f - 5d$ ,  $5g$  transitions in W XXII through XXVI were identified in spectra from the TEXT tokamak [6]. Later Sugar, Kaufman and Rowan succeeded in identifying the strongest  $4d - 4f$  lines in Ag-like W XXVIII, Pd-like W XXIX and Rh-like W XXX spectra from TEXT data [7–9].

At the plasma temperatures typically attained in a tokamak or stellarator, tungsten ions will not be fully stripped and this will give rise to intense line emission in the EUV and x-ray spectral regions (20 eV – 10 keV). In the hot plasma core, under conditions as envisaged for ITER, one expects to have F-like  $W^{65+}$  to Cl-like  $W^{57+}$  ions and the spectra should then be dominated by K and L shell emission whereas towards the wall, one will encounter intense M and N shell emission as the average degree of ionisation decreases. While such emission is an unwanted source of energy loss it also provides a useful diagnostic tool so there is a major interest worldwide in the spectra of tungsten ions. High power radiation near the edge can protect the wall from damage by high energy particles from the plasma. Also in the 1970s, it was found that the emission from laser generated plasmas of tungsten produced broad-band EUV continuum radiation overlaid with very few lines in the 3-20 nm spectral region with some unresolved intense structure in the 4.5-7 nm region associated again with  $4d-4f$  transitions in stages lower than W XVII [10]. The only discrete lines observed were from W VI and VII [11, 12]. The absence of strong emission or absorption lines in higher stages was attributed to the near degeneracy of  $5p$  and  $4f$  binding energies past  $W^{5+}$  which in the most extreme cases gives rise to thousands of closely spaced lines from strongly interacting configurations based on configurations with open  $5p$  and  $4f$  subshells [13]. In extreme cases, the number of lines that may be emitted is so great that the average line separation will be less than the individual linewidths. The resulting extremely weak lines are then submerged in the background recombination continuum to give essentially a spectrum that appears as a line-free continuum. When the  $5p$  subshell empties at W XIII, the  $4f$  and  $5s$  binding energies are so close that again the existence of low excited configurations with differing numbers of  $4f$  and  $5s$  electrons inhibits strong line emission so no strong lines are found in spectra from W VIII ( $5p^5$ ) to W XIV ( $5s$ ). For ion stages possessing open  $4d$  subshell configurations, i.e. resonance transitions in W XXIX ( $4d^{10}$ ) through W XXXVII ( $4d^2$ ), the spectrum will be dominated by a UTA exactly analogous to that observed in Sn and Xe. Furthermore, for transitions of the type  $4p^64d^m - 4p^54d^{m+1} + 4p^64d^{m-1}4f$ , final state configuration interaction causes the lines in adjacent ion stages to almost completely overlap [14–16]. From experiments at the Berlin EBIT it was verified that this was indeed the case [17]. Again for the most part, these spectra contain strong, generally unresolved, line emission in the 4.5–7 nm range. However, spectra from an EBIT are usually quite different in appearance from either pinched or laser plasmas as they are excited by a monoenergetic electron beam at low electron densities in an optically thin regime. In particular, the width and consequently the profile of the UTAs resulting from ions with open  $4p$ ,  $4d$  and  $4f$  subshells are known to be different. Indeed, Radke et al. [17] using detailed calculations based on a collisional-radiative model succeeded in showing that the UTA observed in their experiments were narrower than predicted and also the intensity weighted mean wavelength deviated from the simple gA weighted mean of the arrays. Consequently, there is a need to obtain data from other sources for further comparison with theory.

The plasma temperatures obtaining in ASDEX-Upgrade and JT60U [18, 19] are higher than in the earlier devices, moreover, there is continuous injection of tungsten from the walls so that it is always present. Under these conditions, higher ion stages are observed and open  $4p$ ,  $4s$  and  $3d$  subshell spectra have been recorded in stages from W XXXIX to W LI and confirmed by EBIT data. Additional data from Berlin, LLNL and NIST [20–22] have resulted in the identification of lines in ion stages all the way to Ne-like W LXV, many of

which have potential for use as temporal and spatial diagnostics in ITER. A comprehensive compilation of available spectroscopic data has been published by Kramida and Shirai [23].

In recent years there has been considerable interest in the extreme ultraviolet (EUV) spectra of a number of intermediate and high  $Z$  ions for applications ranging from EUV lithography (EUVL) to plasma diagnostics for fusion. For the former, the operating wavelength, 13.5 nm, is set by the availability of multilayer Mo/Si mirrors that have peak reflectivities of approximately 70% and are efficient reflectors within a 2% bandwidth at this wavelength [24]. Plasmas of two elements have been studied intensively, xenon, which has strong emission from  $4p^6 4d^9 - 4p^6 4d^8 5p$  transitions in Xe X at this wavelength [25] and tin, whose EUV spectrum is dominated by an intense UTA due to  $4p^6 4d^m - 4p^5 4d^{m+1} + 4p^6 4d^{m-1} 4f$  transitions, in stages from IX to XIV, in the 13 - 14 nm region [26]. All of the strongest lines from these ion stages have been identified in high resolution spectra by Churilov and Ryabtsev [27]. In Xe, the same UTA appears at lower wavelengths in the 11 nm region and is significantly brighter than the Xe X 4d-5p emission [28]. Indeed, because of the greater brightness associated with the UTA emission, Sn plasma sources will be used in high volume manufacturing tools.

In plasmas produced in EUV sources, such as the laser produced or discharge plasmas, emission from many stages is produced simultaneously. Because they typically possess electron and ion densities in the  $10^{17} - 10^{21} \text{ cm}^{-3}$  range opacity effects can dramatically alter the ratio of intensity of high to low oscillator strength lines, making intensity comparisons between theory and experiment extremely difficult. So for these plasmas, unambiguous line identification is almost impossible in the majority of cases especially in regions of high line density, such as regions where  $4p^6 4d^m - 4p^5 4d^{m+1} + 4p^6 4d^{m-1} 4f$  transitions overlap in energy. For these spectra, ion separation techniques are an essential prerequisite to any analysis. Such ion stage specific spectra of the emission contributing to both Sn and Xe UTAs have been obtained with the charge exchange method by Tanuma et al. [29, 30]. In these experiments multiply charged ions were produced in the 14.25 GHz ECR ion source at Tokyo Metropolitan University [31]. Xenon gas or tin oxide was inserted into the plasma chamber and charge state specific ions were selected from the ECR source output beam and allowed to collide with rare gas target atoms at a sufficiently low pressure such that single electron capture was strongly favoured.

In this paper we report on the results of tin, xenon and tungsten, injection experiments in the Large Helical Device (LHD) at the National Institute for Fusion Science (NIFS) at Toki. In all cases the spectra are dominated by  $4p^6 4d^m - 4p^5 4d^{m+1} + 4p^6 4d^{m-1} 4f$  transitions. For Xe and Sn we look at the differences between spectra obtained at the LHD and those from charge exchange experiments. In the case of tungsten, we show that the spectra obtained at different plasma conditions can be explained by varying contributions from open 4f, 4d and 4p subshell ions. The ion stage identification is made possible both by comparison with previously published work and new atomic structure calculations.

## 2. EXPERIMENT

### 2.1. Experimental Method

The LHD is one of the world's largest stellarators for fusion research with two superconducting helical coils and six superconducting poloidal (vertical field) coils. The plasma size is 3.9 m in major radius and 0.6 m in minor radius. The helical coils produce a magnetic field up to 3 tesla. The plasma density ( $\leq 10^{14} \text{ cm}^{-3}$ ), its spatial profile and electron temperature were measured by a Thomson scattering diagnostic system [32]. Solid tin and tungsten were introduced by a tracer encapsulated solid pellet (TESPEL) [33] injected into the background hydrogen plasma, while a gas puff injection setup was used for xenon injection. The EUV spectra were recorded by a grazing incidence spectrometer SOXMOS [34] whose groove density and focal length were  $600 \text{ mm}^{-1}$  and 1 m, respectively. The spectrometer contains two microchannel plates coupled via a phosphor to silicon photodiode detectors thus permitting the simultaneous recording of spectra from two different spectral regions. The

integration time of the detector was typically 200 ms. The overall spectral resolution was about 0.01 nm. The optical axis of the spectrometer could be slightly tilted to permit viewing either directly through the plasma core or between the core and the edge. For the tungsten injection, for a given set of plasma conditions, no differences were noted as the line of view was varied, though, interestingly in the case of the lower temperature emission a central accumulation was observed essentially as seen in the PLT Tokamak [35] where the core plasma cooling also led to an emission dominated by W XXVIII – XXX. It should be noted that in LHD experiments with Xe and Sn injection, such strong emission from open 4d subshell ions was always accompanied by plasma collapse [36, 37]. The spectrometer was carefully calibrated by observing iron, neon, carbon and boron ion lines whose wavelengths are known and the absolute wavelength was determined within an accuracy of  $\pm 0.01$  nm.

## 2.2. Experimental Results for Xenon

As stated in the introduction, there has been a considerable interest in the extreme ultraviolet (EUV) spectra of xenon ions due to the importance of xenon plasmas as potential sources for high intensity operation at  $\lambda = 13.5$  nm for EUV lithography (EUVL) and also as lower power metrology sources at this wavelength. Indeed, the two  $\alpha$ -tools shipped in 2005 by ASML initially used high power Xe-based plasma discharge sources developed by Philips [38]. While the EUVL relevant spectral lines have been recently identified [25], lines at other wavelengths have been identified by a number of authors and a compilation of this work up to 2003 may be found in the review by Saloman [39].

While Churilov and co-workers [40, 41] succeeded in analysing the 4–4 transition groups ( $n = 4 - n = 4$  transition where  $n$  is a principle quantum number) on the low energy side of the array for Xe X and Xe XI, ion stage specific spectra of the emission contributing to the UTA itself is required for any further analysis. The relative contributions of the different ion stages to the UTA were illustrated by the charge exchange (CX) data [29–31]. A detailed theoretical study of the effects of configuration interaction (CI) in xenon and the influence of satellite lines on the overall UTA emission profile showed that while CI effects produce a strong spectral narrowing, the presence of satellite emission causes the UTA to broaden and leads to the appearance of structure on the long wavelength side of the UTA, especially at higher densities [42, 43]. EUV radiation from very highly charged xenon ions has been observed in EBIT spectra where again some degree of charge state selection is possible [44–46].

In performing the LHD experiments, a small puff of xenon gas was injected. In some cases, the plasmas maintained a high temperature until plasma heating stopped because the plasma heating proceeded evenly, while on many other occasions the plasma underwent a very abrupt radiation collapse [36]. The term ‘radiation collapse’ is used to describe the phenomenon when a plasma decays rapidly together with a large cooling rate from radiation [47]. A typical example of each is given in Fig. 1. The main component of the plasma is hydrogen and hydrogen gas is puffed into the plasma constantly. A small amount of xenon gas was puffed at 1 s after the initiation of the discharge. For stable sustained heating the spectrum obtained is presented in Fig. 1(a), the stored energy increased to a value of  $\sim 245$  kJ after a heating time of approximately 0.66 s and remained close to this value for a further 2.14 s. The neutral beam injection (NBI) for plasma heating continued during this time.

The line-averaged electron density was seen to rise steadily at first, reaching a value of  $\sim 2 \times 10^{13}$  cm $^{-3}$  after 1 s and a maximum of  $2.26 \times 10^{13}$  cm $^{-3}$  after a further 1.36 s. The radiated power essentially followed the electron density curve but was seen to peak abruptly during the cooling phase when a maximum value of 0.782 MW was emitted 3.0 s after the initiation of the discharge. For a radiation collapse case typified by spectrum (b), the total heating time by NBI was 2.83 s and a peak-stored energy of 268.9 kJ was attained after approximately 1 s. The maximum line-averaged electron density,  $3.7 \times 10^{13}$  cm $^{-3}$ , was reached just as the stored energy dropped to zero. The radiated power attained a maximum of 1.03 MW just prior to this after 1.409 s.

It was possible to record spectra from both the centre of the discharge and also close to the edge or 24 cm from the centre. An example is shown in Fig. 2 for a 10 – 12 nm range. Generally, the line of sight of the measurement was fixed through the centre of the plasma. It included the region from the lower temperature edge to the high temperature core. For spectra recorded during the heating phase in the wavelength range from 10–12 nm through both paths the only major difference was in intensity. While emission from the UTA completely dominated both sets of spectra, some strong individual lines resulting from 4p–4d lines in ionization stages from Xe<sup>17+</sup> to Xe<sup>23+</sup> were observed. At wavelengths longer than the UTA position, lines of higher ionization stage Xe<sup>25+</sup> are observed. In the wavelength range from 12 to 16.5 nm, 4p – 4d transition lines of Xe XXIV - Xe XXVI are observed. The intensities of these lines are almost the same in both cases. For the uncollapsed plasma, the most intense lines observed are the Cu-like Xe XXVI 4p <sup>2</sup>P<sub>1/2</sub>–4d <sup>2</sup>D<sub>3/2</sub> and Zn-like Xe XXV 4s<sup>2</sup> <sup>1</sup>S – 4s4p <sup>1</sup>P. The measured intensity of 4s<sup>2</sup> – 4s4p Xe XXV line through 24 cm is higher than through the centre due to the smaller excitation energy. The comparison of the intensities indicates that the dominant emitting ions are not in the centre but in the periphery.

From a comparison of these data with the results of the CX experiments it was possible to tentatively identify a number of lines in the open 4d subshell spectra of Xe XXVII and Xe XXVIII [36] with the aid of atomic structure calculations using the Cowan code [48] and the relativistic GRASP code [49]. The results of the Cowan code calculations are more accurate here as the Slater Condon parameters were scaled to give agreement between theoretical and experimental values. The scaling allows for interactions with high lying configurations not explicitly included in the calculations and also for the effects of term dependence which are particularly important for the more intense 4d – 4f transitions. For intermediate charge states, the radius of the 4f electron in an average energy of configuration calculation tends to be underestimated which leads to values of direct and exchange integrals which are 10-20% too large and scaling adjusts for this. The calculations from the GRASP code are *ab initio* with no scaling of parameters and consequently less accurate. The results of the former calculation are also indicated in Fig. 1(b). The new assignment for 4p – 4d transitions of Xe XXVIII are listed in Table 1 [36]. The CX spectra measured of Xe ions by Tanuma et al. [29] are shown in Fig. 3. The gA values in Table 1 is multiplication of g and A where g is the statistical weight of the upper levels and A is the transition probability from the upper state to the lower state.

### 2.3. Experimental Results for Tin

The LHD spectra of Sn may be categorized into two types depending on the discharge conditions, examples of which are shown in Fig 4. Discharges were initiated by electron cyclotron heating (ECH) followed by three NBI heating beams. When the pellet was injected at 1.3 s, the total radiated power rapidly increased and the stored energy began to decrease simultaneously due to radiative cooling. The cooling process is apparently faster in case (a) than in case (b) as observed in the waveforms of the stored energy which showed that the plasma underwent radiative collapse and the total radiated power increased rapidly at the end of the integration time in case (a), while it remained stable during the integration time in the case (b). The line-averaged electron density was about  $3 \times 10^{13} \text{ cm}^{-3}$  in both cases. The electron temperature in case (b) is higher than that in case (a). Spectrum (a) is dominated by the 4 – 4 UTA near 13.5 nm, by stages from around Sn<sup>8+</sup> - Sn<sup>13+</sup> while in spectrum (b) which is dominated by several discrete lines the contribution from these stages is quite weak. The charge states responsible for spectrum (a) would be dominant when the electron temperature is around 50 eV assuming coronal ionization equilibrium. However, the actual electron temperature near the point of the pellet ablation is much higher (300–400 eV), which implies that the plasma lies far from ionization equilibrium due to the effects of radial transport of tin ions. It indicates the ions are in the plasma ionizing phase; the electron temperature is higher than the ionization temperature. The sharp discrete lines in the 13.9–14.7 nm region are relatively more intense in case (b), and while 4d-5p or 4d-4f lines of charge states lower than Sn<sup>11+</sup> would appear in this wavelength range, the dominant charge states are expected to be

higher than that in case (a) considering the difference in the speed of radiative cooling. The most intense line in this spectrum once more is the Cu-like  $4p\ ^2P_{1/2} - 4d\ ^2D_{3/2}$  transition that occurs in Sn XXII at 14.602 nm [50]. It and several other discrete lines appear in both spectra. From Cowan code calculations it was possible to identify the strongest of these as the highest gA- value  $4p - 4d$  transitions in Sn XIX and the assignments are presented in Table 2. The gA- values for  $4p - 4d$  transitions are shown in Fig.4 with the measured spectra.

It is interesting also to note that although the Cu-like Sn XXII line originates as a transition between excited states, apart from this particular stage strong lines that did not involve resonance transitions to the ground state were not observed for other ion stages. Indeed, a search for the  $4s4p - 4s4d$ ,  $4s4p - 4p^2$  and  $4s4d - 4s4f$  transitions in Zn-like Sn XXI failed to identify any of the known lines [51]. This is in marked contrast to the situation for the CX spectra where it was shown that the spectra in stages from Sn XV ( $4p^6$ ) – Sn XVIII ( $4p^3$ ) are completely dominated by the transitions between excited states  $\delta n = 0$ ,  $n = 4 - n = 4$ . The CX spectra measured by Tanuma [29] are shown in Fig. 5. The strongest lines arise from  $4s^24p^{m-1}4d - 4s^24p^{m-1}4f + 4s^24p^{m-2}4d^2$  transitions and it was found that in interpreting this spectrum it was necessary to allow for  $4p^{m-1}4f + 4p^{m-2}4d^2 + 4s4p^m4d$  CI (Fig.6). The effects are particularly dramatic here and lead, as in open 4d subshell spectra, to a dramatic spectral narrowing. Also the  $4s - 4p$  low energy component essentially loses its oscillator strength to the higher energy zone of the combined array (Fig. 6). Indeed, such interactions, already known to dominate open 4d subshell spectra appear to be a universal feature associated with  $\delta n = 0$ ,  $4 - 4$  excitation. The comparison between theoretical prediction and observation permitted identification of all of the strongest lines in the spectra of Sn XV to Sn XVIII [52]. Examples of the comparison between theory and experiment for Sn XV and Sn XVI are shown in Fig. 7.

#### 2.4. Experimental Results for Tungsten

In the case of tungsten, spectra were recorded with the SOXMOS spectrometer in two different wavelength bands, and those simultaneously covered were 4.1 – 6.8 and 16.4 – 21.3 nm at a lower plasma core temperature of approximately 1.5 keV while simultaneous settings of 2.0 – 4.1 and 12.7 – 17.1 nm and 4.1 – 6.8 and 25.4 – 31.3 nm were investigated at identical higher temperature conditions (core temperature approximately 3 keV). The spectra recorded in the 4.1 – 6.8 nm region are presented in Fig. 8. Similar spectra have been previously measured in the LHD [53]. The spectrum (a) was recorded at a lower core temperature and is expected to contain lower ionization stages. Indeed, the strong line group evident between 4.9 and 5.1 nm can be attributed to the previously identified  $4d - 4f$  resonance lines of Ag- to Rh-like W XXVIII, W XXIX and W XXX [6–9, 54]. The strong isolated line at 4.895 nm in the spectra is identified as the  $4d^{10}\ ^1S_0 - 4d^94f\ ^1P_1$  of W XXIX. Based on the Sn results it is expected that the majority of transitions giving rise to these spectra result from resonance transitions to the ground state. However, the strong  $4p-4d$  Cu-like transitions that dominated both Sn and Xe plasmas and that occur in W XLVI (Ionization potential 2.4 keV [20]) at 4.9603 and 7.1976 nm [55] are absent here. Moreover, some differences between the spectra of Fig. 8 are apparent, most noticeably the short wavelength structure in the 4.5 – 4.8 nm region is absent at lower temperature (case (a)) while the structure appearing in the 5.5 – 6.5 nm region is quite different in both cases. From earlier data it is possible to associate the mean peak lying between 4.9 and 5.5 nm with transitions from open 4d subshell ions, i.e. W XXIX – XXXVIII [17, 56], while the open 4p subshell ions W XXXIX - WXLIV are known to give rise to two line groups centred near 4.6 and 6.4 nm respectively [3, 4, 56]. Open 4f subshell ions can give rise to  $4d - 4f$  transitions at wavelengths below 5 nm [6, 17],  $4f - 5d$  transitions that move towards shorter wavelength with increasing charge eventually ending at with the Ag-like W XXVIII  $4f - 5d$  doublet near 4.4 nm [5] and  $4d - 5p$  and  $4f - 5g$  transitions that also move towards shorter wavelengths with increasing charge and should give rise to well-defined UTAs in the 2.5 – 4 nm region [6]. These latter features were absent in the case of the higher temperature spectrum in the

LHD which therefore must contain little or no contribution from stages lower than W XXVIII.

It is thus possible to attribute the main peak in the higher temperature spectrum (case (b)) to  $4d - 4f$  and  $4p^6 4d^m - 4p^5 4d^{m+1} + 4p^6 4d^{m-1} 4f$  transitions in W XXVIII ( $4d^{10} 4f$ ) - W XXXVIII ( $4d$ ). Because of the different rates for valence and subvalence excitation, the dominant emission will be from the  $4p^6 4d^m - 4p^6 4d^{m-1} 4f$  transitions [57]. The UTA structure in the 4.5 – 4.8 and 5.5 – 6.5 nm region arises mainly from  $4p - 4d$  transitions in W XXXIX ( $4p^6$ ) – W XLV ( $4s^2$ ). For the lower temperature spectrum (case (a)), the main peak is a mixture of  $4d^{10} 4f^m - 4d^9 4f^{m+1}$  and,  $4d - 4f$  and  $4p^6 4d^m - 4p^5 4d^{m+1} + 4p^6 4d^{m-1} 4f$ , transitions in stages lower than W XXXVIII. Cowan code calculations show the UTA structure in the 5.5 – 7 nm region arises from  $4f - 5d$  transitions in W XXII – XXIV and possibly to some contribution from  $4f - 5g$  transitions in W XIX – XXI as will be discussed in the following section.

### 3. THEORETICAL RESULTS FOR TUNGSTEN

To further investigate the contribution of different transitions to the 5-7 nm structure, detailed calculations were performed with the Hartree Fock with Configuration Interaction suite of codes written by Cowan [46]. For transitions from stages with an open 4d subshell CI effects have already been shown to be very important [25] because of the proximity of  $4p - 4d$  and  $4d - 4f$  excitation energies. Thus in the calculations for W XXX ( $4d^9$ ) to W XXXVIII ( $4d$ ) excited state CI of the form  $4p^5 4d^{m+1} + 4p^6 4d^{m-1} 4f$  ( $1 \leq m \leq 9$ ) was included. From these data the corresponding line distributions were parameterized in terms of their various moments according to the UTA model in order to get the mean position and widths of the different arrays [58–62] and the results are shown in Fig. 9.

For those ions with an open 4f subshell, i.e. W XV ( $4f^{14}$ ) - W XXVIII ( $4f$ ), the dominant transitions are  $4d - 4f$  (from W XVI onwards),  $4d - 5p$ ,  $4f - 5d$  and  $4f - 5g$ . Some examples of the results of the calculations are shown in Fig. 10, which show the line distributions of  $4d-4f$  transitions in W XXII to XXVII as well as the result of convoluting each line with a Gaussian broadening function with a width of 0.02 nm to replicate the effects of instrumental broadening. Since the  $4d^{10} 4f^m - 4d^9 4f^{m+1}$  and  $4d^{10} 4f^m - 4d^{10} 4f^{m-1} 5d$  transitions overlap in energy between W XXII and W XXVIII, the effects of CI were investigated and found to be negligible in all cases except for W XXVI, where there is a slight modification to the UTA near 5 nm. Because of the limited effects of CI the transitions can be essentially treated as independent. For the  $4f - 5g$  transitions, because of the large centrifugal repulsion experienced by the 5g electron, the 4f and 5g wavefunction overlap is initially quite small. With increasing ionisation, the increased importance of the Coulomb term causes the mean 5g radius to decrease and the intensity of the  $4f - 5g$  array increases. However, as far as  $\delta n = 1$  transitions are concerned, the  $4f - 5g$  intensity is everywhere predicted to be greater than the  $4f - 5d$ . From our calculations W XVI and W XVII spectra contain  $4f - 5g$  arrays centred near 6 and 5.5 nm respectively on the low energy side of the main peak while line groups from W XIX onwards are predicted to give rise to features on the higher energy side. The main contribution from  $4f - 5d$  transitions is on the low energy side, in particular W XXII – W XXV are expected to give rise to structure in the 5.5 – 7 nm region.

In W XXIX ( $4d^{10}$ ) the dominant transitions are  $4d - 4f$  and  $4d - 5p$ . For ions with an open 4d subshell, i.e. W XXX ( $4d^9$ ) – W XXXV ( $4d^4$ ), the dominant transitions become  $4p^6 4d^m - 4p^5 4d^{m+1} + 4p^6 4d^{m-1} 4f$  and  $4p^6 4d^m - 4p^6 4d^{m-1} 5p$ . In Fig. 11 plots for W XXXI ( $4d^8$ ) - XXXVI ( $4d^3$ ) are presented showing the line by line data and superimposed, as before, plots where each line is given a width of 0.02 nm and the theoretical UTA fits are presented. Note that because of the configuration mixing between  $4p^5 4d^{m+1}$  and  $4p^6 4d^{m-1} 4f$  it is meaningless to treat these as separate arrays and the UTA data refer to the mixed configuration. In these figures, the intensity weighted UTA are seen to give rise to a Gaussian which is peaked towards the lower wavelength end. Note that because of the spin-orbit splitting of the array, the fit to a single curve results in the UTA having a considerable width.

For W XXXIX ( $4p^6$ ), the resonance transitions are  $4s^24p^6 - 4s^24p^54d$  and give rise to lines observed at 4.640 and 6.398 nm in Berlin EBIT data [17]. Many of the lines for the ions from W XL ( $4p^5$ ) – W XLIV ( $4p$ ) have been measured and identified from both EBIT and ASDEX-Upgrade data and will not be considered further here.

#### 4. RADIATIVE AND DIELECTRONIC RECOMBINATION FROM $Xe^{10+}$ TO $Xe^{9+}$

Up to now we have concentrated purely on spectral emission. Finally, to show that other theoretical work performed for the EUVL also has relevance to fusion plasmas we shall consider the case of dielectronic recombination (DR) in high Z plasmas. Recently Song and Kato [63] have calculated the energy levels, radiative transition probabilities, autoionization rates, and radiative recombination cross section for  $Xe^{10+}$  ions using the flexible atomic code (FAC) [64]. Dielectronic recombination rate coefficients to excited states of  $Xe^{9+}$  as well as total rate coefficients from the  $Xe^{10+}$  ions were calculated as well as the related dielectronic satellite lines. The dielectronic satellite lines from the processes  $4d^8 + e \rightarrow 4d^7 4f^1 nl \rightarrow 4d^8 nl + hv$  and the  $4d^8 + e \rightarrow 4d^7 5p^1 nl \rightarrow 4d^8 nl + hv$  were found to make a greater contribution to line intensities at low electron temperature for line intensities than collisional excitation. The radiative recombination rate coefficients were shown to be always smaller than the values of the dielectronic recombination rate coefficient in the temperature region  $1 \leq T_e \leq 1000eV$  (Fig. 12). Moreover, from an investigation of the density effect on the dielectronic recombination rate coefficient, it was found that the dielectronic recombination rate coefficients are larger than radiative recombination rate coefficients for  $n_e < 10^{19} cm^{-3}$ . More recently, the dielectronic recombination rates in  $Sn^{10+}$  ions have been explored making full allowance for CI and once again in open 4d ions it was shown that the DR rate exceeded the direct excitation or three body recombination rates by almost two orders of magnitude [65, 66]. It is planned to repeat these calculations for tungsten ions, where the availability of so many closely spaced levels in low ion stages is expected to lead to a considerable enhancement of the DR, relative to other rates and which in turn should enhance radiative losses and has relevance to calculations of the input powers needed to overcome them.

#### 5. STRONG LINES FOR HIGH Z ELEMENTS IN EUV RANGES

Although the spectra of high Z ions show UTA structure, it is useful to list strong lines of high Z impurities in fusion plasmas for plasma diagnostics and identifications. We list the prominent lines in EUV ranges of Sn, Xe and W ions in Table 4.

#### 6. CONCLUSIONS

In this paper we have summarised the results of a spectroscopic study of high Z impurities, Sn, Xe and W injected into the LHD plasma at NIFS. For plasmas undergoing radiative collapse spectra from open 4d subshell ions dominate the extreme UV emission of Xe and Sn, while at higher temperature, open 4d subshell emission is hardly observed, indicating that the presence of some such species in a localised cool plasma region could be the trigger that produces the plasma collapse. In the case of tungsten, emission from open 4d subshell ions is always present. However, the spectra are for the most part dominated by resonance transitions to the ground states of the constituent ions. We have shown that many of the results, obtained to aid understanding of EUV lithography source plasmas, which are usually at equilibrium with  $30 < T_e < 50 eV$  are relevant to high temperature non-equilibrium tungsten plasmas in fusion devices.

#### ACKNOWLEDGEMENTS

This work was partly supported by the research collaboration program in NIFS. A part of this work was performed under the auspices of Leading Project promoted by MEXT in

Japan. One of the authors (GOS) wishes to acknowledge the UCD President's Research Fellowship Award Scheme and a Science Foundation Ireland STTF08/RFP/PHY1100 award that recently supported his visits to NIFS to participate in this work.

TABLE 1. ASSIGNMENTS OF RB I LIKE LINES IN XE XVIII BASED ON  $4P^64D-4P^54D^2$  TRANSITIONS (UNLESS OTHERWISE STATED).  $\lambda_{\text{COWAN}}$  AND  $\lambda_{\text{GRASP}}$  ARE THE CALCULATED VALUES FROM COWAN'S CODE AND THE GRASP CODE RESPECTIVELY.  $\lambda_{\text{CX}}$  IN THE FOURTH COLUMN IS THE OBSERVED WAVELENGTH FROM A CHARGE EXCHANGE EXPERIMENT.  $\lambda_{\text{LHD}}$  IS THE OBSERVED WAVELENGTH FROM THE LHD [36].

Transition Lower upper	$\lambda_{\text{Cowan}}$ (Å)	$gA \times 10^{10} s^{-1}$	$\lambda_{\text{CX}}$ (Å)	$\lambda_{\text{LHD}}$ (Å)	$\lambda_{\text{Grasp}}$ (Å)	$gA \times 10^{10} s^{-1}$
$^2D_{5/2} - 5p \ ^2P_{3/2}$	80.45	75.40	80.20	-		
$^2D_{3/2} - 5p \ ^2P_{1/2}$	81.70	39.36	81.60	-		
$^2D_{3/2} - ({}^1D) {}^2F_{5/2}$	122.04	4.798		(Shoulder of strong unresolved Xe XII 4d-5p array feature)	123.86	0.99
$^2D_{5/2} - ({}^1G) {}^2G_{7/2}$	122.77	9.071	123.0	-	124.72	9.1
$^2D_{5/2} - ({}^1D) {}^2F_{5/2}$	125.41	8.834	125.80 (shoulder)	125.80	127.43	7.52
$^2D_{5/2} - ({}^1S) {}^2F_{7/2}$	125.72	7.659	126.40	126.4	128.69	17.1
$^2D_{3/2} - ({}^1S) {}^2P_{3/2}$	126.34	1.396	“		127.20	1.36
$^2D_{5/2} - ({}^3F) {}^4G_{7/2}$	127.65	0.744	128.0	128.0	130.647	1.00
$^2D_{3/2} - (P) {}^4D_{1/2}$	128.48	14.90	128.5		130.05	9.96
$^2D_{3/2} - ({}^3F) {}^4F_{5/2}$	129.33	2.739		129.8	132..35	1.41
$^2D_{5/2} - ({}^1S) {}^2P_{3/2}$	129.96	22.85	129.80	129.8	130.98	16.9
$^2D_{5/2} - ({}^3P) {}^2F_{5/2}$	130.69	5.843	131.80		134.19	6.82
$^2D_{5/2} - ({}^3F) {}^4F_{5/2}$	133.12	15.66	133.10	133.1- 133.3(blended with Xe XI line.)	136.44	4.2
$^2D_{3/2} - ({}^3P) {}^2D_{3/2}$	134.21	13.00	134.0	134.0 (Blended with Xe XI line)	136.13	6.7
$^2D_{5/2} - ({}^3F) {}^4D_{7/2}$	135.22	10.41	135.40	135.4 (Blend with Xe XI lines)	137.02	1.35
$^2D_{3/2} - ({}^1G) {}^2F_{5/2}$	136.13	12.80	137.0	136.7-137.0 (Blended with Xe XVII feature)	139.12	2.15
$^2D_{3/2} - ({}^3P) {}^4D_{5/2}$	139.59	2.867	140.60	140.60	143.13	1.70
$^2D_{5/2} - ({}^1G) {}^2F_{5/2}$	140.34	1.614	141.80?	141.80	143.65	0.28
$^2D_{5/2} - ({}^3P) {}^4D_{7/2}$	143.47	3.335	144.60	144.60	146.84	0.15
$^2D_{5/2} - ({}^1D) {}^2F_{7/2}$	145.10	1.980	146.20	146.20 (Blend with Xe XI line)	148.62	1.80
$^2D_{5/2} - ({}^3F) {}^2G_{7/2}$	147.74	0.02	148.80		150.92	0.038
$^2D_{5/2} - ({}^3P) {}^4P_{7/2}$	152.996	0.004	154.80		157.61	0.054
$^2D_{5/2} - ({}^3P) {}^4P_{5/2}$	154.21	0.09	156.2		158.99	0.020
$^2D_{5/2} - ({}^3F) {}^4G_{7/2}$	154.42	0.05	156.2		159.37	0.001

TABLE 2. NEW LINE IDENTIFICATION IN THE SPECTRA OF SN XIX

Ion	Transition	$\lambda_p(\text{\AA})$	$\lambda_{\text{obs}}(\text{\AA})$	Gf
Sn XIX	$4s^24p^2\ ^3P_1 - 4s^24p4d\ ^3P_1$	137.42	138.05?	1.289
	$4s^24p^2\ ^3P_0 - 4s^24p4d\ ^3D_1$	137.56	138.42	2.167
	$4s^24p^2\ ^3P_1 - 4s^24p4d\ ^1D_2$	140.30	141.20 <sup>b</sup>	1.749
	$4s^24p^2\ ^3P_2 - 4s^24p4d\ ^3D_3$	140.45	141.20	5.273
	$4s^24p^2\ ^3P_2 - 4s^24p4d\ ^1D_2$	143.62	144.64	1.434
	$4s^24p^2\ ^1D_2 - 4s^24p4d\ ^1F_3$	145.98	147.03	5.805
	$4s^24p^2\ ^1S_0 - 4s^24p4d\ ^1P_1$	153.03	154.22?	2.256
	$4s^24p^2\ ^3P_1 - 4s^24p4d\ ^3P_2$	153.30	154.22	1.939
	$4s^24p^2\ ^1D_2 - 4s^24p4d\ ^3P_2$	155.61	156.56 <sup>a</sup>	2.701
	$4s^24p^2\ ^3P_2 - 4s^24p4d\ ^3P_2$	157.28	158.41?	1.197

<sup>a</sup> Blended with Sn XXII  $4d\ ^2D_{3/2} - 4f\ ^2F_{5/2}$  observed at 156.518 $\text{\AA}$

<sup>b</sup> Blended

? Uncertain

TABLE 3. CALCULATED AND OBSERVED ENERGIES FOR THE STRONGEST OBSERVED LINES OF THE  $3D^{10} 4S^2 4P^3 4D^1 \rightarrow 4S^2 4P^2 4D^2 + 4S^2 4P^3 4D^0 4F^1$  TRANSITIONS OF SNXVII [52]

Transition	$\lambda_{\text{cowan}}$ (nm)	$\lambda_{\text{ECR}}$ (nm)	gf
$^3P_2 \rightarrow (4d)^3D_3$	13.37 <sup>a</sup>	13.37	8.91
$^3G_5 \rightarrow (4f)^3H_6$	13.40	13.43	17.79
$^1D_2 \rightarrow (4d)^1F_3$	13.46 <sup>b</sup>	13.47	10.82
$^1G_4 \rightarrow (4d)^3G_5$	13.51	13.50	10.47
$^3F_4 \rightarrow (4d)^1H_5$	13.54		5.78
$^3P_0 \rightarrow (4d)^3D_1$	13.55	13.55	3.69
$^3G_4 \rightarrow (4f)^3G_5$	13.57		7.26
$^5D_3 \rightarrow (4d)^5P_3$	13.58	13.59	5.17
$^3P_2 \rightarrow (4f)^3D_3$	13.59		3.72
$^5D_4 \rightarrow (4f)^5F_5$	13.64	13.65	10.25
$^3F_4 \rightarrow (4d)^3F_4$	13.65		6.05
$^5D_4 \rightarrow (4d)^5D_4$	13.69	13.72	7.58
$^3D_3 \rightarrow (4d)^3F_4$	13.74		19.81
$^1F_3 \rightarrow (4d)^1G_4$	13.82	13.82	25.43
$^3D_1 \rightarrow (4f)^3F_2$	13.93		13.41
$^3F_4 \rightarrow (4f)^3G_5$	13.94	13.95	13.70
$^1D_2 \rightarrow (4f)^1F_3$	13.95		13.20
$^3P_2 \rightarrow (4f)^3D_3$	14.00	13.99	10.32
$^1D_2 \rightarrow (4d)^1D_2$	14.23	14.23	5.74
$^1P_1 \rightarrow (4f)^1D_2$	14.29	14.29	11.35
$^1F_3 \rightarrow (4d)^1F_3$	14.46	14.43	7.25

\* a, b are calculated resonance lines

TABLE 4. STRONG LINES FROM HIGH Z ELEMENTS OF W, XE AND SN IONS IN EUV REGION. THEY ARE LISTED ACCORDING TO ISO ELECTRONIC SEQUENCES. NOTE THAT THE GROUND STATE CONFIGURATION OF AG-LIKE FOR W XXVIII ( $4D^{10}4F$ ) AND FOR XE VIII ( $4D^{10}5S$ ) AND SN IV ( $4D^{10}5S$ ) ARE DIFFERENT. [ ] INDICATES A REFERENCE NUMBER. < > INDICATES THE EXPERIMENTAL MEAN WAVELENGTH.

Transitions Lower -Upper	W (Z=74) Wavelength (nm)	Xe (Z =54) Wavelength (nm)	Sn (Z = 50) Wavelength (nm)
<b>Cu -like [3d<sup>10</sup>4s]</b>	<b>W XLVI (45+)</b>	<b>Xe XXVI (25+)</b>	<b>Sn XXII (21+)</b>
4p <sup>2</sup> P <sub>3/2</sub> - 4d <sup>2</sup> D <sub>5/2</sub>	7.1976 [23]	13.839 [40]	16.4360 [50], 16.441 [70]
4p <sup>2</sup> P <sub>1/2</sub> - 4d <sup>2</sup> D <sub>3/2</sub>	4.9208 [23]	11.8935 [40]	14.602 [50], 14.596 [708]
4s <sup>2</sup> S <sub>1/2</sub> - 4p <sup>2</sup> P <sub>3/2</sub>	6.217 [17,2], 6.2336 [23]	17.3938 [40]	21.8978 [50], 21.89 [70]
4s <sup>2</sup> S <sub>1/2</sub> - 4p <sup>2</sup> P <sub>1/2</sub>	12.6998 [23]	23.3959 [40]	27.6065 [50], 27.61 [70]
4d <sup>2</sup> D <sub>3/2</sub> - 4f <sup>2</sup> F <sub>5/2</sub>	6.7852 [23]	13.0428 [39]	15.6518 [50], 15.646 [70]
4d <sup>2</sup> D <sub>5/2</sub> - 4f <sup>2</sup> F <sub>7/2</sub>	7.4426 [23]	13.4852 [39]	16.0563 [50], 16.055 [70]
<b>Zn-like [3d<sup>10</sup>4s<sup>2</sup>]</b>	<b>W XLV (44+)</b>	<b>Xe XXV (24+)</b>	<b>Sn XXI (20+)</b>
4s <sup>2</sup> <sup>1</sup> S <sub>0</sub> - 4s4p <sup>1</sup> P <sub>1</sub>	6.087 [17,2], 6.09 [51,54]	16.4412 [39] 16.4398 [51]	20.4798 [67], 20.47 [69,70] 20.481 [51]
4s <sup>2</sup> <sup>1</sup> S <sub>0</sub> - 4s4p <sup>3</sup> P <sub>1</sub>	13.275 [17,2]	25.2473 [39,51]	30.1679 [68] 30.1713 [51]
4s4p <sup>1</sup> P <sub>1</sub> - 4p <sup>2</sup> <sup>1</sup> S <sub>0</sub>	6.186 [51]	17.3322 [51]	21.8829 [51]
4s4p <sup>3</sup> P <sub>1</sub> - 4p <sup>2</sup> <sup>1</sup> D <sub>2</sub>	6.2106 [51]	17.0630 [51]	21.3629 [51]
4s4p <sup>3</sup> P <sub>0</sub> - 4p <sup>2</sup> <sup>3</sup> P <sub>1</sub>	6.0581 [51]	16.5739 [51]	20.7957 [51]
4s4p <sup>3</sup> P <sub>1</sub> - 4p <sup>2</sup> <sup>3</sup> P <sub>2</sub>	4.8604 [51]	13.8694 [51]	18.0412 [51]
4s4p <sup>3</sup> P <sub>2</sub> - 4p <sup>2</sup> <sup>3</sup> P <sub>2</sub>	7.6516 [51]	16.6514 [51]	20.8320 [51]
4s4p <sup>3</sup> P <sub>2</sub> - 4s4d <sup>3</sup> D <sub>3</sub>	6.8995 [51]	13.2459 [45b] 13.2537 [51]	15.7638 [51] 15.764[70]
4s4p <sup>3</sup> P <sub>0</sub> - 4s4d <sup>3</sup> D <sub>1</sub>	4.7900 [51]	11.4985 [51]	14.1073 [51]
4s4p <sup>3</sup> P <sub>1</sub> - 4s4d <sup>3</sup> D <sub>1</sub>	4.9369 [51]	11.8208 [51]	14.4704 [51]
4s4p <sup>1</sup> P <sub>1</sub> - 4s4d <sup>3</sup> D <sub>2</sub>	7.3840 [51]	15.5431 [51]	18.5065 [51]
4s4p <sup>1</sup> P <sub>1</sub> - 4s4d <sup>1</sup> D <sub>2</sub>	6.3706 [51]	13.6169[45b], 13.6311 [51]	16.2737 [51] 16.274[70]
4p <sup>2</sup> <sup>3</sup> P <sub>2</sub> - 4s4f <sup>3</sup> F <sub>3</sub>	6.0529 [51]	10.9111 [51]	12.5998 [51]
4s4d <sup>3</sup> D <sub>3</sub> - 4s4f <sup>3</sup> F <sub>4</sub>	6.4042 [51]	13.0220 [51]	15.5791 [51]
4s4d <sup>3</sup> D <sub>1</sub> - 4s4f <sup>3</sup> F <sub>2</sub>		12.6690 [51]	15.2479 [51]
4s4d <sup>1</sup> D <sub>2</sub> - 4s4f <sup>1</sup> F <sub>3</sub>	6.8114 [51]	13.2380 [51]	15.8646 [51]
<b>Ga like [4s<sup>2</sup>4p]</b>	<b>W XLIV (43+)</b>	<b>Xe XXIV (23+)</b>	<b>Sn XX (19+)</b>
4s <sup>2</sup> 4p <sup>2</sup> P <sub>1/2</sub> - 4s <sup>2</sup> 4d <sup>2</sup> P <sub>3/2</sub>	4.769 [17], 4.78 [54]		

$4s^2 4p^2 P_{1/2} - 4s^2 4d^2 P_{1/2}$	6.061 [17,2]		
$4s^2 4p^2 P_{1/2} - 4s^2 4d^2 D_{3/2}$	6.129 [17,2]		13.999 [70]
$4s^2 4p^2 P_{1/2} - 4s 4p^2 P_{1/2}$	6.0616 [23]		
$4s^2 4p^2 P_{1/2} - 4s 4p^2 D_{3/2}$	6.1334 [23]		
$4s^2 4p_{1/2} - 4s^2 4d_{3/2}$		11.359 [45a]	
$4s^2 4p_{3/2} - 4s^2 4d_{5/2}$		13.055 [45b]	15.593 [70]
$4s^2 4p_{3/2} - 4s^2 4d_{3/2}$		13.4948 [45b]	
$4s^2 4p_{3/2} J=3/2 - 4s 4p^2_{3/2} J=3/2$		16.0503 [45a]	
$4s^2 4p_{3/2} J=3/2 - 4s 4p_{1/2} 4p_{3/2} J=1/2$		16.247 [45a]	
$4s^2 4p_{1/2} J=1/2 - 4s 4p_{1/2} 4p_{3/2} J=1/2$			20.21 [69]
$4s^2 4p_{1/2} J=1/2 - 4s 4p_{1/2} 4p_{3/2} J=3/2$			21.68 [69]
<b>Ge-like <math>[4s^2 4p^2]</math></b>	<b>W XLIII (42+)</b>	<b>Xe XXIII (22+)</b>	<b>Sn XIX (18+)</b>
$4s^2 4p^2 P_0 - 4s 4p^3 D_1$	6.130 [17,2]		
$4s^2 4p^2 P_0 - 4s^2 4p 4d^3 D_1$	4.697 [17,2]	11.238 [45a]	13.843 [70]
$4s^2 4p^2 P_2 - 4s^2 4p 4d^3 D_3$			14.120 [70]
$4s^2 4p^2 P_2 - 4s^2 4p 4d^1 D_2$			14.760 [70]
$4s^2 4p^2 D_2 - 4s^2 4p 4d^1 F_3$			14.698 [70]
$4s^2 4p^2 J=2 - 4s 4p^3 J=1$			19.78 [69]
$4s^2 4p^2 J=0 - 4s 4p^3 J=1$			22.09 [69]
$4s^2 4p^3 D_{3/2} - 4p^2 4d_{3/2}$	4.716 [17]		
$4s^2 4p^3 D_{3/2} - 4p^2 4d_{5/2}$	7.015 [17]		
$4s^2 4p^3 D_{3/2} - 4s 4p^4 J=3/2$	6.071 [17]		
$4s^2 4p^3 D_{3/2} - 4s 4p^4 J=5/2$	6.482 [17]		
$4s^2 4p^2 4p_{1/2}[3/2] - 4s^2 4p_{1/2} 4p_{3/2} 4d_{3/2}[1/2, 3/2]$		11.1715 [45a]	
$4s^2 4p^2 4p_{1/2}[3/2] - 4s^2 4p_{1/2} 4p_{3/2} 4d_{3/2}[5/2]$		11.2775 [45a]	
<b>Se-like <math>[4p^4]</math></b>	<b>W XLI (40+)</b>	<b>Xe XXI (20+)</b>	<b>Sn XVII (16+)</b>
$4s^2 4p^4 P_2 - 4s 4p^5 D_2$	6.260 [17]		
$4p^4 - 4p^3 4d_{3,2,1}$	4.688 [17]		
$4p^4 J=2 - 4p^3 4d_{5/2} J=3$	6.581 [17]		
$4p^4 J=2 - [4p_{1/2} 4p^2_{3/2}(2)](3/2) 4d_{3/2}[3]$		10.8565 [45a]	
<b>Br-like <math>[4p^5]</math></b>	<b>W XL (39+)</b>	<b>Xe XX (19+)</b>	<b>Sn XVI (15+)</b>
$4p^5 P_{3/2} - 4p^4 4d(2,3/2)$	4.681 [17]		
$4p^5 P_{3/2} - 4p^4 4d(2,3/2)_{1/2}$	4.6827 [23]		
$4p^5 P_{3/2} - 4p^4 4d(2,5/2)_{5/2}$	6.4661 [23], 6.474 [17]		

$4p^5 \ ^2P_{3/2} - 4p^4 \ 4d \ (2,5/2)_{3/2}$	6.5658 [23], 6.576 [17]		
$4p^5 \ ^3P_{3/2} - 4p^4 \ 4d \ ^5S_{3/2}$		10.8845 [45a]	
<b>Kr-like [4p<sup>6</sup>]</b>	<b>W XXXIX (38+)</b>	<b>Xe XIX (18+)</b>	<b>Sn XV (14+)</b>
$4p^6 \ ^1S_0 - 4p^5 4d(1/2,32)_1$	4.640 [17] 4.6670 [23]		13.2463 [27],
$4p^6 \ ^1S_0 - 4p^5 4d(3/2,52)_1$	6.398 [17]		
$4p^6 \ ^1S_0 - 4p^5 4d \ ^1P_1$		10.8409 [40]	
$4p^6 \ ^1S_0 - 4p^5 4d \ ^3D_1$		13.1740 [40]	
<b>Rb-like [4d]</b>	<b>W XXXVIII (37+)</b>	<b>Xe XVIII (17+)</b>	<b>Sn XIV (13+)</b>
$4p^6 4d \ ^2D_{3/2} - (4p^5 \ ^3P_{3/2} 4d \ ^3D_{3/2})_3 \ 4d_{5/2} \ J = 3/2$	6.387 [17]		
$4p^6 4d \ ^2D_{3/2} - 4p^5 (^2P_{1/2} 4d \ ^2D_{3/2})_{(1/2,2)} \ J = 3/2$	4.5781 [23]		13.1358 [27],
$4p^6 4d \ ^2D_{3/2} - 4p^5 4f_{5/2} \ J = 5/2$	5.686 [17]		
$4p^6 4d \ ^2D_{3/2} - 4p^5 (^2P_{3/2} 4d \ ^2F_4)_{(3/2,4)} \ J = 5/2$	5.7755 [23]		
$4p^6 4d \ ^2D_{3/2} - 4p^5 4f \ (0,5/2)_{5/2}$	5.6880 [23]		
$4p^6 4d \ ^2D_{3/2} - 4p^5 (^2P_{1/2} 4d \ ^2F_2)_{(1/2,2)} \ J = 5/2$	4.9641 [23], 4.952 [17]		
$4p^6 4d \ ^2D_{5/2} - 4p^5 4d^2 \ ^2F_{5/2}$		10.9521 [40]	
$4p^6 4d \ ^2D_{3/2} - 4p^5 4d^2 \ ^2F_{7/2}$		10.7224 [40]	
$4p^6 4d \ ^2D_{5/2} - 4p^5 4d^2 \ ^2D_{5/2}$		10.8005 [40]	13.3102 [27]
<b>Sr-like [4d<sup>2</sup>]</b>	<b>W XXXVII (36+)</b>	<b>Xe XVII (16+)</b>	<b>Sn XIII (12+)</b>
$4d^2 \ ^3F_2 \ J = 2 - 4d_{3/2} 4f_{5/2} \ J = 3$	5.414 [17]		
$4p^6 4d^2 \ ^3F_2 - 4p^5 4d^3 \ (^4F)^3F_2$			13.3800 [27]
$4d^2 \ ^3F_2 - 4d 4f \ (^1S)^3G_3$			13.4943 [27]
<b>Y-like [4d<sup>3</sup>]</b>	<b>W XXXVI (35+)</b>	<b>Xe XVI (15+)</b>	<b>Sn XII (11+)</b>
	<5.37> [17]		
$4d^3 \ ^4F_{3/2} - 4d^2 4f \ (^3F)^4D_{1/2}$			13.4457 [27]
$4d^3 \ ^4F_{3/2} - 4d^2 4f \ (^3F)^4G_{5/2}$			13.5339 [27]
<b>Zr-like [4d<sup>4</sup>]</b>	<b>W XXXV (34+)</b>	<b>Xe XV (14+)</b>	<b>Sn XI (10+)</b>
	<5.32> [17]		
$4d^4 \ ^5D_1 - 4d^3 4f \ (^4F)^5F_2$			13.6435 [27]
$4d^4 \ ^5D_0 - 4d^3 4f \ (^4F)^5D_1$			13.7881 [27]
<b>Nb-like [4d<sup>5</sup>]</b>	<b>W XXXIV (33+)</b>	<b>Xe XIV (13+)</b>	<b>Sn X (9+)</b>
	<5.27> [17]		
$4d^5 \ ^6S_{5/2} - 4d^4 4f \ (^5D)^6P_{5/2}$			13.8441 [27]

$4d^5\ ^6S_{5/2} - 4d^44f\ (^5D)^6P_{3/2}$			13.8598 [27]
<b>Mo-like [4d<sup>6</sup>]</b>	<b>W XXXIII (32+)</b>	<b>Xe XIII (12+)</b>	<b>Sn IX (8+)</b>
	<5.22> [17]		
$4p^64d^6\ ^5D_4 - 4p^54d^7\ (^4F)^5D_4$			14.1060 [27]
$4d^6\ ^5D_4 - 4d^54f\ (^6S)^5F_5$			14.6850 [27]
<b>Tc-like [4d<sup>7</sup>]</b>	<b>W XXXII (31+)</b>	<b>Xe XII (11+)</b>	<b>Sn VIII (7+)</b>
	<5.19> [17]		
$4d^7 - 4d^65p^2H_{9/2}$			22.6271 [72]
$4d^7 - 4d^65p^4F_{9/2}$			22.6288 [72]
$4d^7 - 4d^65p^2H_{9/2}$			22.7083 [72]
<b>Ru-like [4d<sup>8</sup>]</b>	<b>W XXXI (30+)</b>	<b>Xe XI (10+)</b>	<b>Sn VII (6+)</b>
	<5.15> [17]		
$4d^8\ ^1D, ^3F - 4d^75p$		13.5334 [40, 45a]	
$4d^8\ ^3F_4 - 4d^74f$		11.2055 [40]	
$4d^8\ ^3F_4 - 4d^75p_5$		13.5072 [40]	
$4d^8 - (4d^74f + 4p^54d^9)$			15.7902, 15.8266, 15.8437, 16.3298 [72,72]
<b>Rh-like [4d<sup>9</sup>]</b>	<b>W XXX (29+)</b>	<b>Xe X (9+)</b>	<b>Sn VI (5+)</b>
$4d^9\ ^2D_{3/2} - 4d^8\ 4f\ ^2F_{7/2}$	4.9785 [9]		
$4d^9\ ^2D_{3/2} - 4d^8\ 4f\ ^2F_{5/2}$	4.9856 [9]		
$4d^9\ ^2D_{5/2} - 4d^8\ 4f\ ^2P_{3/2}$	4.9938 [9]		
$4d^9\ ^2D_{5/2} - 4d^8\ 4f\ ^2D_{5/2}$	5.0265 [9]		
$4d^9\ ^2D_{3/2, 5/2} - 4d^8\ 4f\ ^2D_{5/2, 7/2}$		11.4880 [39]	
$4d^9\ ^2D_{3/2} - 4d^8\ 5p\ ^3/2,$		15.0089 [39]	
$4d^9\ ^2D_{3/2} - 4d^8\ 5p\ ^5/2,$		15.0124 [39]	
$4d^9\ ^2D_{5/2} - 4d^8\ 6p\ ^5/2, 7/2$			19.1554 [73]
$4d^9\ ^2D_{5/2} - 4d^8\ 4f\ ^7/2$			19.3096 [73]
<b>Pd-like [4d<sup>10</sup>]</b>	<b>W XXIX(28+)</b>	<b>Xe IX (8+)</b>	<b>Sn V (4+)</b>
$4d^{10}\ ^1S_0 - 4d^94f\ ^1P_1$	4.8948 [8], 4.89 [54]	12.0133 [40]	22.4040 [71]
$4d^{10}\ ^1S_0 - 4d^94f\ ^3D_1$	5.9852 [8]		23.6199 [71]
$4d^{10}\ ^1S_0 - 4d^94f\ ^3P_1$			24.2532 [71]
$4d^{10}\ ^1S_0 - 4d^95p\ ^3D_1$		16.1742 [40]	35.5138 [71]
$4d^{10}\ ^1S_0 - 4d^95p\ ^1P_1$	2.951 [53]	16.5322 [40]	36.1010 [71]
$4d^{10}\ ^1S_0 - 4d^95p\ ^3P_1$			37.2551 [71]
<b>Ag-like</b>	<b>W XXVIII (27+)</b> <b>[4d<sup>10</sup>4f]</b>	<b>Xe VIII (7+)</b> <b>[4d<sup>10</sup>5s]</b>	<b>Sn IV (3+)</b>
$4d^{10}4f\ ^2F_{5/2} - 4d^94f^2\ ^2F_{5/2}$	4.8729 [7]		
$4d^{10}4f\ ^2F_{5/2} - 4d^94f^2\ ^2D_{3/2}$	4.9403 [7]		
$4d^{10}4f\ ^2F_{7/2} - 4d^94f^2\ ^2G_{9/2}$	5.0895 [7]		

$4d^{10}4f - 4d^{10}5d$	$\sim 4.4$ [13]	21.222 [40]	
$4d^{10}5s^2S_{1/2} -$ $4d^95s5p(^1P_1) (2/5, ^1P_1) J =$ $3/2$		17.0856[39]	



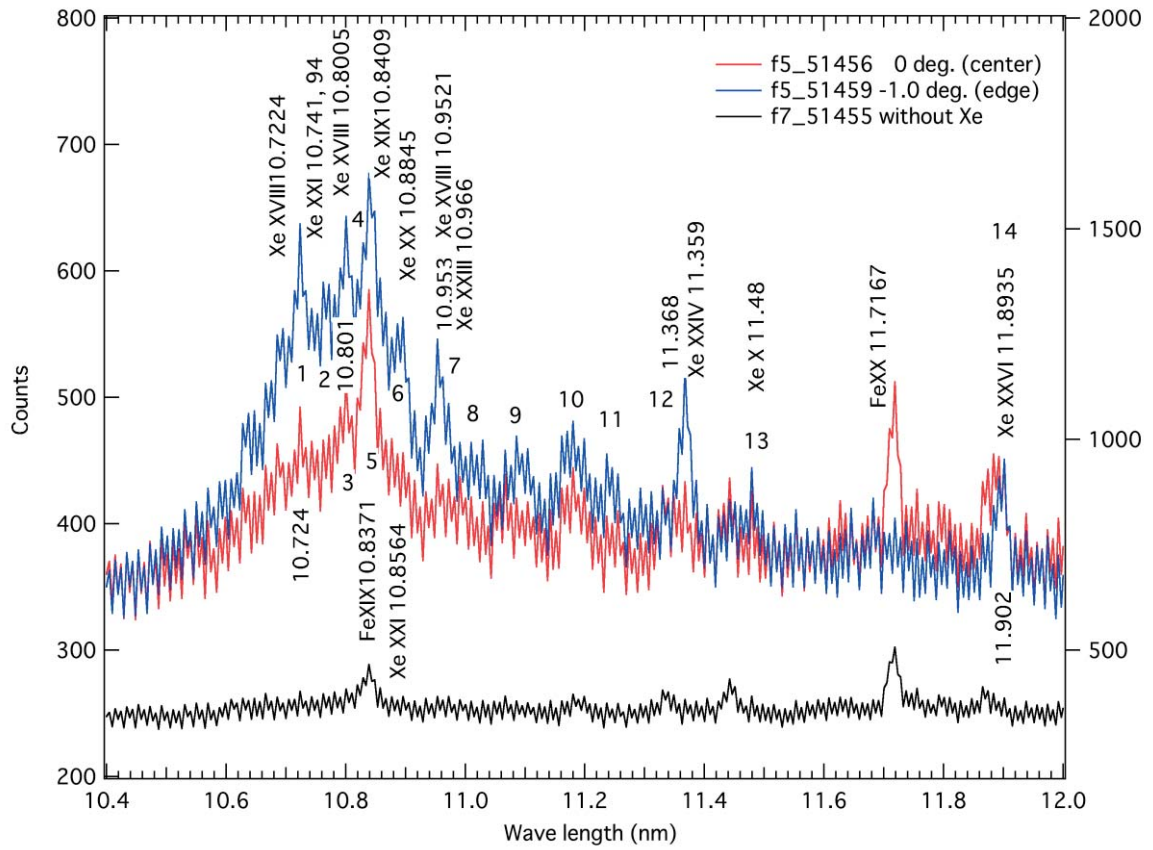


FIG. 2. Spectra recorded during the heating phase through the centre of the plasma (red) and through a line 24 cm away from the centre (blue) for the 10 – 12 nm. A background spectrum showing the presence of Fe impurity ions is also shown (black). Note that the emission of Fe is particularly strong at the centre.

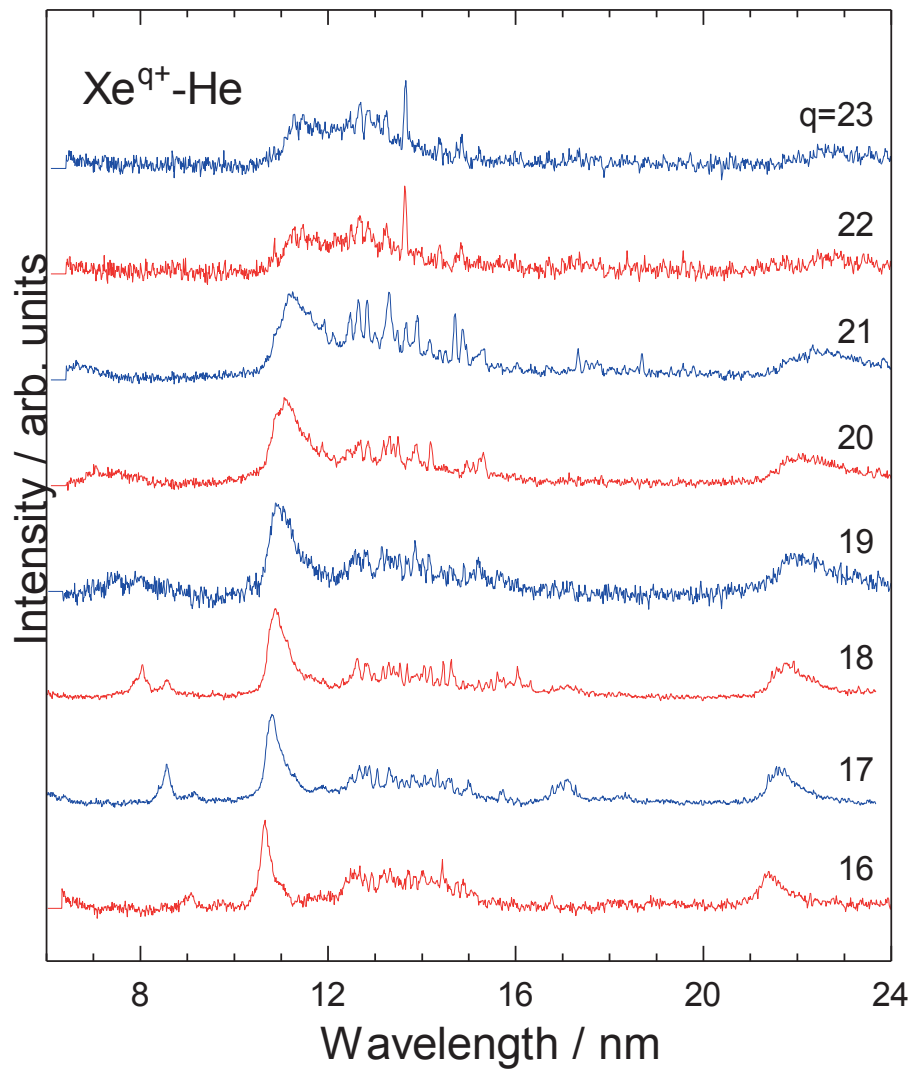


FIG. 3. The charge exchange EUV spectra for  $Xe^{q+} + He \rightarrow Xe^{(q-1)+}$  [29].

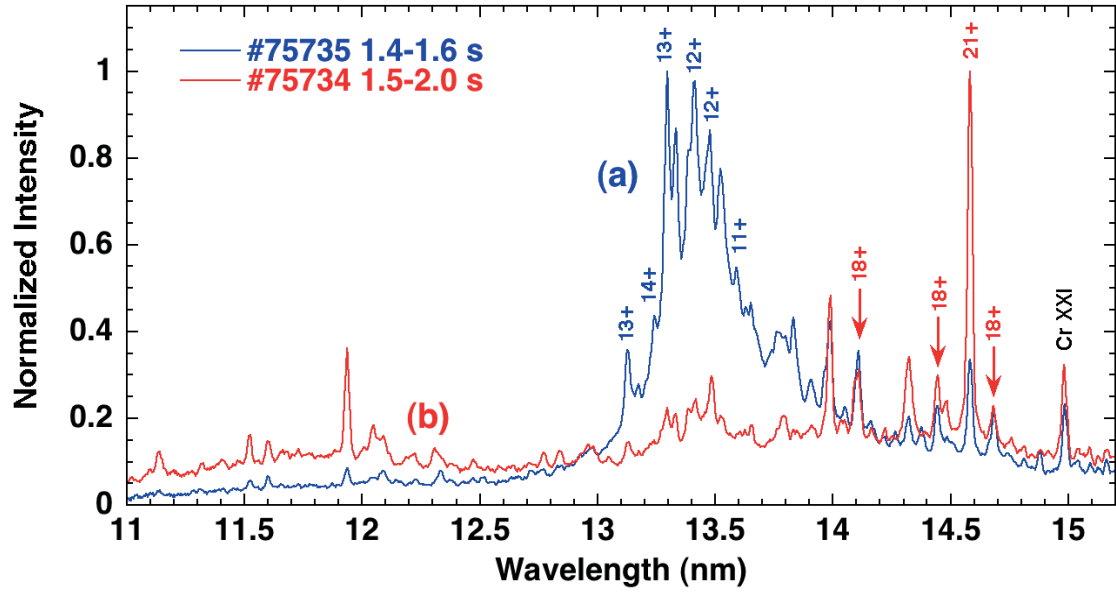


FIG. 4. Spectrum of Sn (a) Plasma collapse case, (b) steady state, no collapse. The strongest line is Cu-like Sn XXII. The majority of the other lines indicated by arrows originate from 4p - 4d resonance transitions in Sn XIX. The theoretical  $gA$ -values for Sn XIX are also indicated.

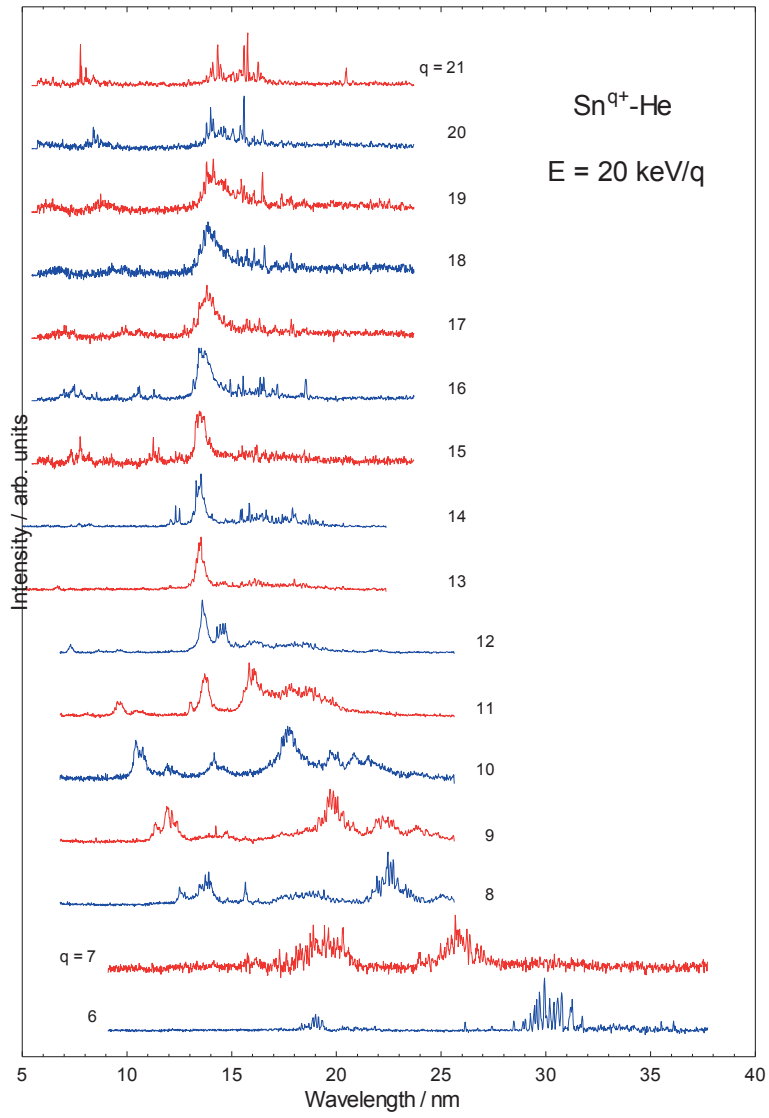


FIG. 5. The charge exchange spectra for  $\text{Sn}^{q+} + \text{He} \rightarrow \text{Sn}^{(q-1)+}$  [29]

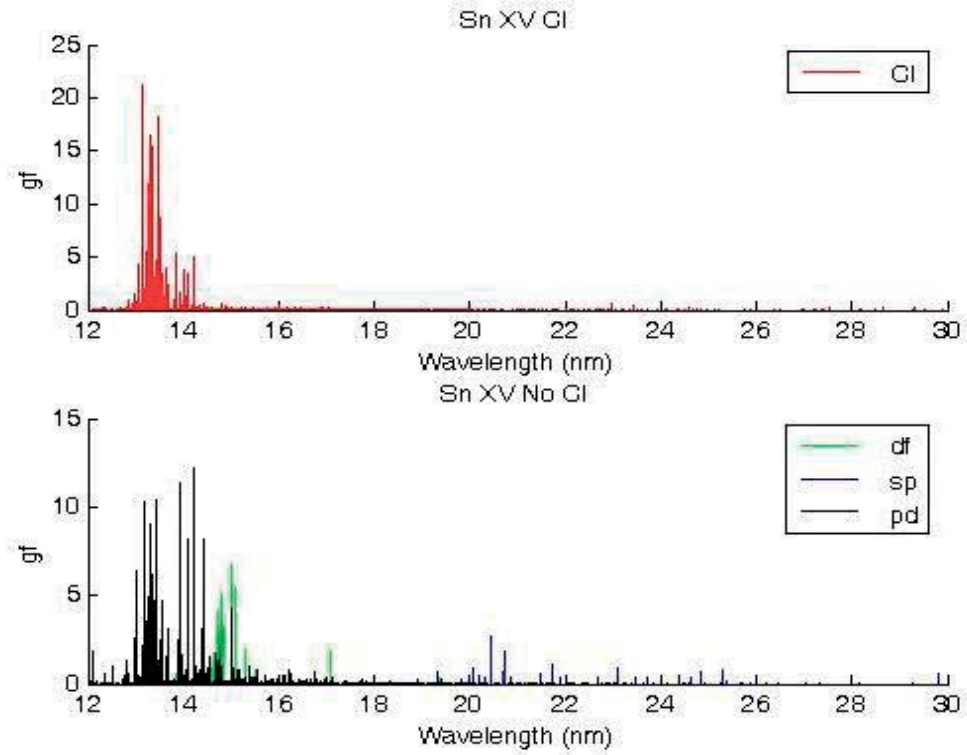


FIG. 6. The effects of configuration interaction in the  $4s^24p^54d - 4s^24p^54f + 4s^24p^34d^2 + 4s4p^64d$  excited to excited state transitions in Sn XV. The top spectrum shows the results of a full CI calculation while the bottom shows the contributions of  $4s^24p^54d - 4s^24p^54f$  (green),  $4s^24p^54d - 4s^24p^34d^2$  (black) and  $4s^24p^54d - 4s4p^64d$  (blue) in the absence of any interactions.

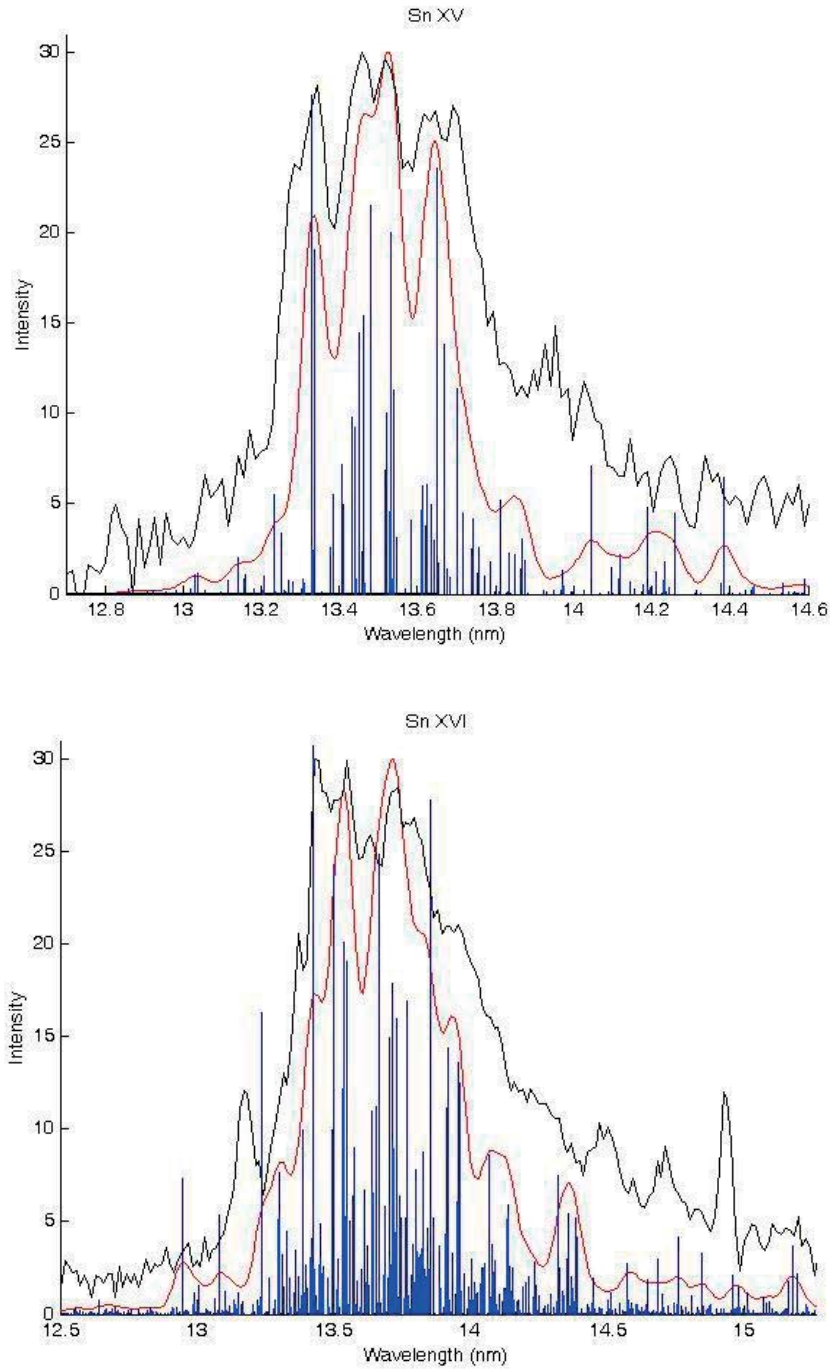


FIG. 7. Comparison between a theoretical spectrum for Sn XV (top) and XVI (bottom) convolved with a Gaussian instrumental function and experimental spectrum obtained from CX spectroscopy with the Tokyo Metropolitan University ECR source [9]. The theoretical data are also presented in the form of stick plots of height equal to the  $gf$ -value.

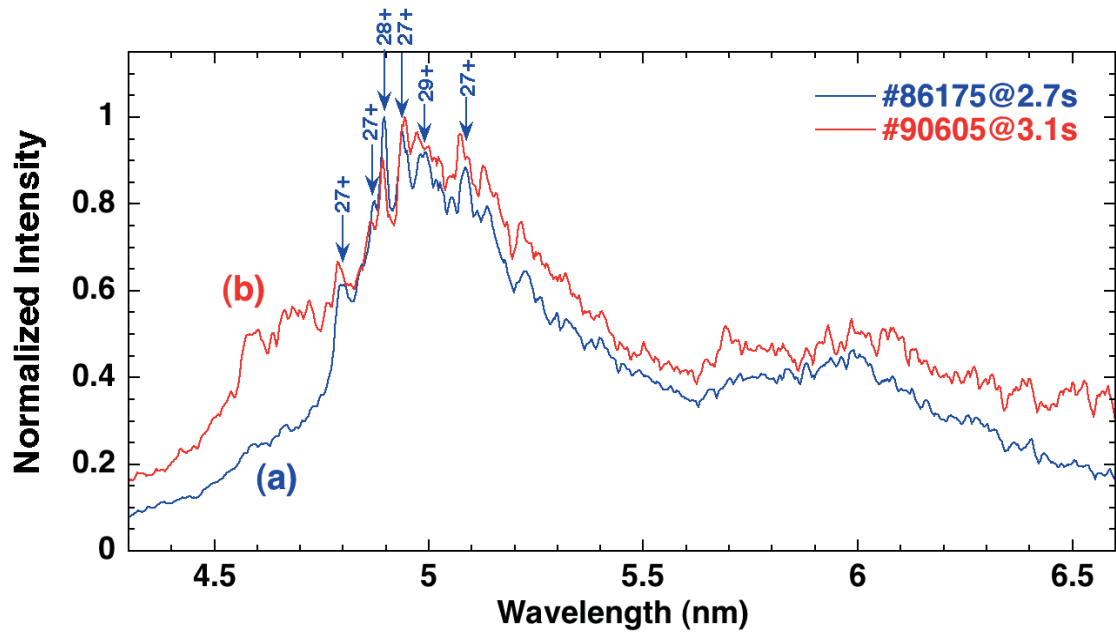


FIG. 8. LHD spectrum of tungsten following TESPEL injection in (a) low temperature (approx. 1.5 keV) plasma, and (b) higher temperature (approx. 3keV) plasma.

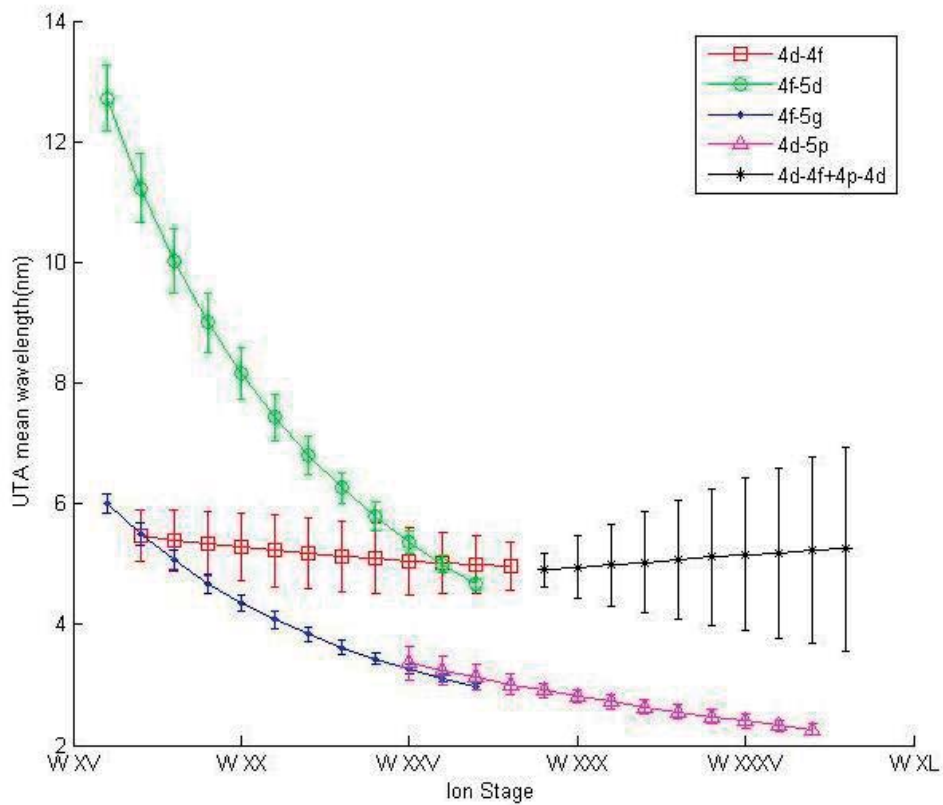


FIG. 9. Calculated mean wavelength and width of the different transition groups for W XVI – W XXXVIII. The 4-4 arrays are broader than the 4-5 ones.

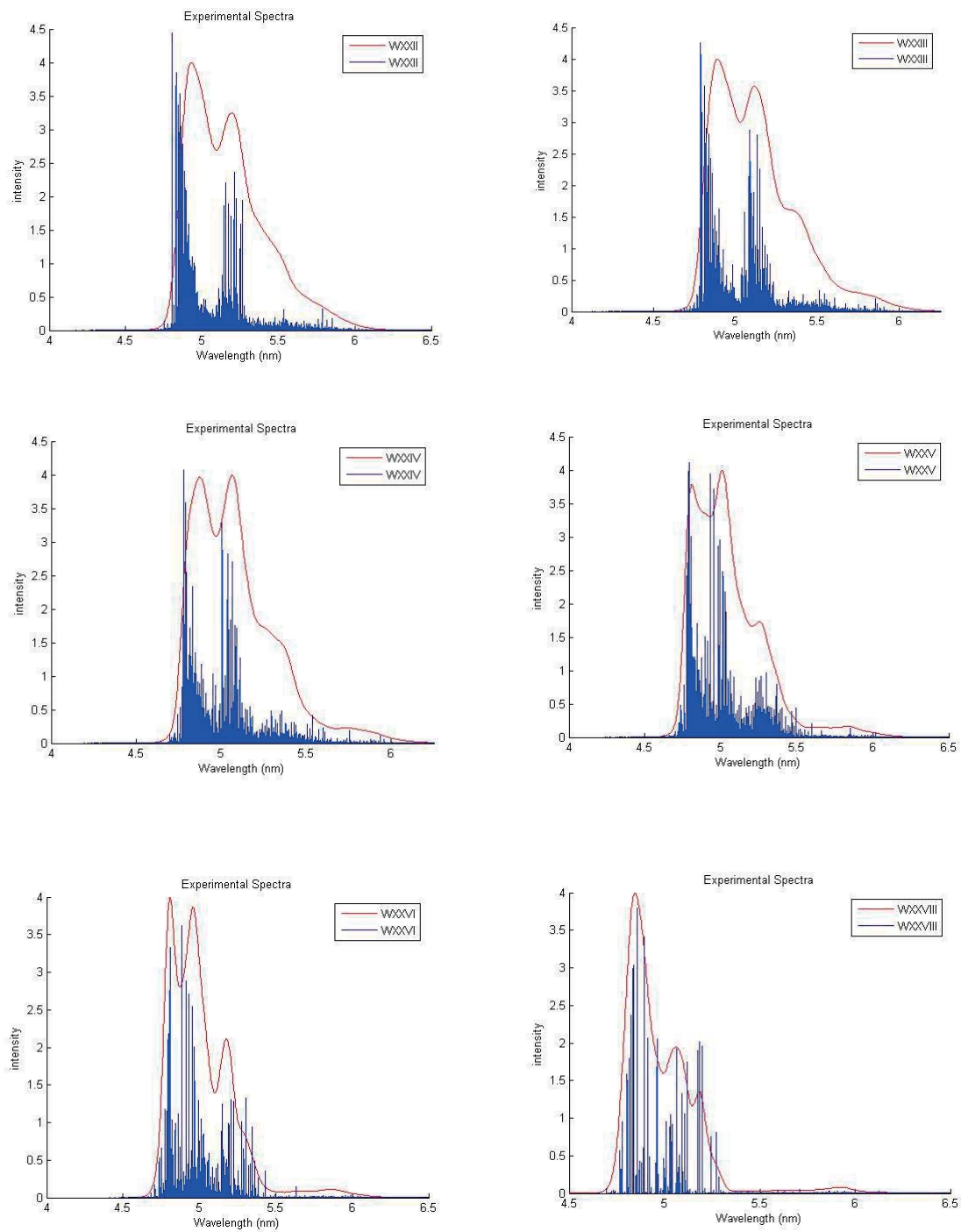


FIG. 10. Calculated spectra for  $4d - 4f$  transitions in  $W\ XXII - W\ XXVII$ . The red curve is the result of convoluting the line by line spectra with a Gaussian function of linewidth 0.02 nm.

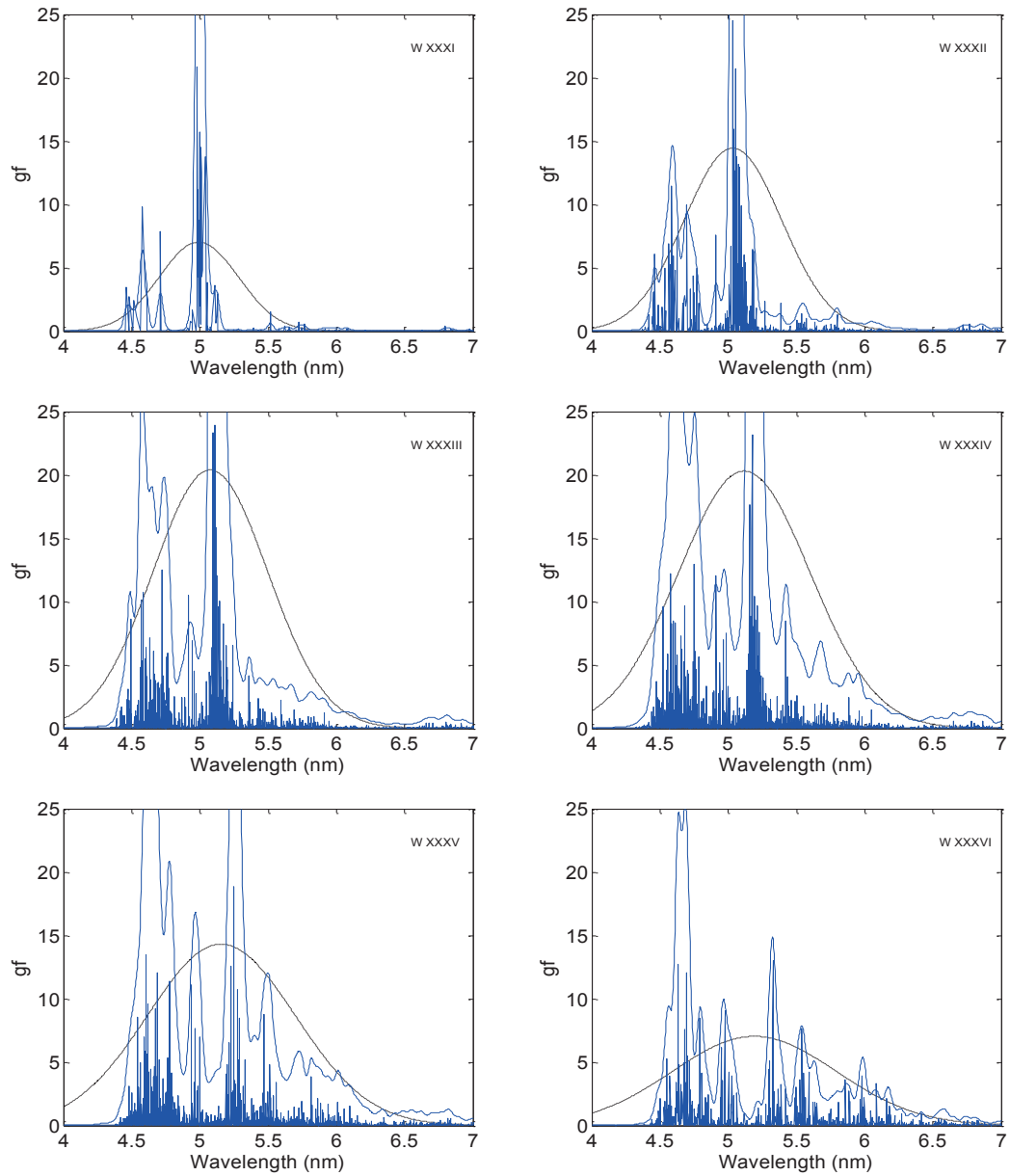


FIG. 11. Calculated spectra for  $4d - 4f$  transitions in  $W\ XXXI - W\ XXXVI$ . The blue curve is the result of convoluting the line by line spectra with a Gaussian function of linewidth 0.02 nm. The red curve is the UTA fit to the data.

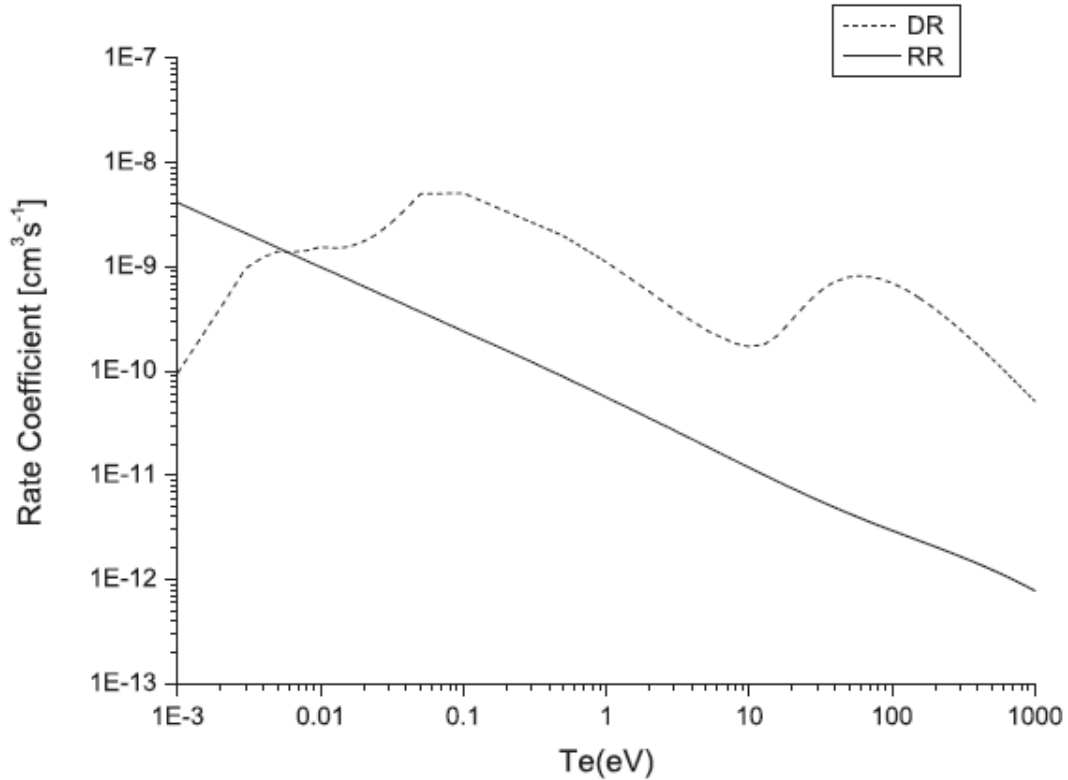


FIG. 12. Comparison of total dielectronic recombination (DR) rate coefficient and the total radiative recombination (RR) rate coefficient from  $Xe^{10+}$  to  $Xe^{9+}$  ions.

## REFERENCES

- [1] MATTHEWS, G.F., EDWARDS, P., HIRAI, T., KEAR, M., LIOURE, A., LOMAS, P., LOVING, A., LUNGU, C., MAIER, H., METENS, P., NIELSON, D., NEU, R., PAMELA, J., PHILIPPS, J., PIAZZA, G., RICCARDO, V., RUBEL, M., RUSSET, C., VILLEDIEU, E., WAY, M., on behalf of the ITER-like Wall Project Team, Overview of the ITER-like wall project, *Phys. Scr.* **T128** (2007) 137.
- [2] PÜTTERICH, T., NEU, R., BIEDERMANN, C., RADKE, R. and the ASDEX Upgrade Team, Disentangling the emissions of highly ionized tungsten in the range 4–14 nm, *J. Phys. B: Atom. Mol. Opt. Phys.* **38** (2005) 3071.
- [3] PÜTTERICH, T., NEU, R., DUX, R., WHITEFORD, A.D., O’MULLANE, M.G., the ASDEX Upgrade Team, Modelling of measured tungsten spectra from ASDEX Upgrade and predictions for ITER, *Plasma Phys. Control. Fusion* **50** (2008) 085016.
- [4] OHASHI, H., HIGASHIGUCHI, T., SUZUKI, Y., ARAI, G., OTANI, Y., YATAGAI, T., LI, B., DUNNE, P., O’SULLIVAN, G., JIANG, W., ENDO, E., SAKAUE, H. A., KATO, D., MURAKAMI, I., TAMURA, N., SUDO, S., KOIKE, F., SUZUKI, C. Quasi-Moseley’s law for strong narrow bandwidth soft x-ray sources containing higher charge state ion. *Appl. Phys. Lett.* **104** (2014) 234107.
- [5] SUGAR, J., KAUFMAN, V., Tokamak-generated tungsten radiation identified in Ag I isoelectronic sequence (W XXVIII), *Phys. Rev. A* **21** (1980) 2096.
- [6] FINKENTHAL, M., HUANG, L.K., LIPPMAN, S., MOOS, H.W., MANDELBAUM, P., SCHWOB, J.L., KLAPISCH, M., the TEXT Group, Soft X-ray bands of highly ionized tungsten, gold and lead emitted by the TEXT tokamak plasma, *Phys. Lett. A* **127** (1988) 255.

- [7] SUGAR, J., KAUFMAN, V., ROWAN, W.L., Spectra of Ag I isoelectronic sequence observed from Er<sup>21+</sup> to Au<sup>32+</sup>, *J. Opt. Soc. Am. B* **10** (1993) 1321.
- [8] SUGAR, J., KAUFMAN, V., ROWAN, W.L., Observation of Pd-like resonance lines through Pt<sup>32+</sup> and Zn-like resonance lines of Er<sup>38+</sup> and Hf<sup>42+</sup>, *J. Opt. Soc. Am. B* **10** (1993) 799.
- [9] SUGAR, J., KAUFMAN, V., ROWAN, W.L., Rh I isoelectronic sequence observed from Er<sup>23+</sup> to Pt<sup>33+</sup>, *J. Opt. Soc. Am. B* **10** (1993) 1977.
- [10] CARROLL, P.K., O'SULLIVAN, G., Ground-state configurations of ionic species I through XVI for  $Z=57-74$  and the interpretation of  $4d-4f$  emission resonances in laser-produced plasmas, *Phys. Rev. A* **25** (1982) 275.
- [11] SUGAR, J., KAUFMAN, V., Seventh spectrum of tungsten (W VII); resonance lines of Hf V, *Phys. Rev. A* **12** (1975) 994.
- [12] SUGAR, J., KAUFMAN, V., Identification of 5g and 6g terms and revised ionization energies in the Yb II  $4f^{14}n l$  isoelectronic sequence, *J. Opt. Soc. Am.* **69** (1979) 141.
- [13] O'SULLIVAN, G., CARROLL, P.K., DUNNE, P., FAULKNER, R., MCGUINNESS, C., MURPHY, N., Supercomplex spectra and continuum emission from rare-earth ions: Sm, a case study, *J. Phys. B: At. Mol. Opt. Phys.* **32** (1999) 1893.
- [14] KOIKE, F., FRITZSCHE, S., NISHIHARA, K., SASAKI, A., KAGAWA, T., NISHIKAWA, T., FUJIMA, K., KAWAMURA, T., FURUKAWA, H., Precise and accurate calculations of electronic transitions in heavy atomic ions relevant to extreme ultra-violet light sources, *J. Plasma. Fusion. Res.* **7** (2006) 253.
- [15] MANDELBAUM, P., FINKENTHAL, M., SCHWOB, J.L., KLAPISCH, M., Interpretation of the quasicontinuum band emitted by highly ionized rare-earth elements in the 70–100-Å range, *Phys. Rev. A* **35** (1987) 5051.
- [16] SVENDSEN, W., O'SULLIVAN, G., Statistics and characteristics of xuv transition arrays from laser-produced plasmas of the elements tin through iodine, *Phys. Rev. A* **50** (1994) 3710.
- [17] RADKE, R., BIEDERMANN, C., SCHWOB, J.L., MANDELBAUM, P., DORON, R., Line and band emission from tungsten ions with charge 21+ to 45+ in the 45–70-Å range, *Phys. Rev. A* **64** (2001) 012720.
- [18] BIEDERMANN, C., RADKE, R., SEIDEL, R. and PÜTTERICH, T., Spectroscopy of highly charged tungsten ions relevant to fusion plasmas *Phys. Scr.* **T134** (2009) 014026
- [19] NAKANO, T., ASAKURA, N., KUBO, H., YANAGIBAYASHI, J., UEDA, Y., Tungsten accumulation in H-mode plasmas of JT-60U, *Nuclear Fusion* **49** (2009) 115024.
- [20] UTTER, S.B., BIEDERDORFER, P., TRÄBERT, E., Electron-beam ion-trap spectra of tungsten in the EUV, *Can. J. Phys.* **80** (2002) 1503.
- [21] RALCHENKO, YU., READER, J., POMEROY, J.M., TAN, J.N., GILLASPY, J.D., Spectra of W<sup>39+</sup>–W<sup>47+</sup> in the 12–20 nm region observed with an EBIT light source, *J. Phys. B: At. Mol. Opt. Phys.* **40** (2007) 3861.
- [22] RALCHENKO, YU., DRAGANIC, I.N., TAN, J.N., GILLASPY, J.D., POMEROY, J.M., READER, J., FELDMAN, U., HOLLAND, G.E., EUV spectra of highly-charged ions W<sup>54+</sup>–W<sup>63+</sup> relevant to ITER diagnostics, *J. Phys. B: At. Mol. Opt. Phys.* **41** (2008) 021003.
- [23] KRAMIDA, A.E., SHIRAI, T., Energy levels and spectral lines of tungsten, W III through W LXXIV, *At. Data and Nuc. Data Tables* **95** (2009) 305.
- [24] ATTWOOD, D.T., *Soft X-rays and Extreme Ultraviolet Radiation: Principles and Applications*, Publ. Cambridge University Press (2000).
- [25] CHURILOV, S.S., JOSHI, Y.N., READER, J., High-resolution spectrum of xenon ions at 13.4 nm, *J. Opt. Lett.* **28** (2003) 1478.
- [26] O'SULLIVAN, G.D., FAULKNER, R., Tunable narrowband soft x-ray source for projection lithography, *Opt. Eng.* **33** (1994) 3978.
- [27] CHURILOV, S.S., RYABTSEV A.N., Analyses of the Sn IX–Sn XII spectra in the EUV region, *Phys. Scr.* **73** (2006) 614.

- [28] FAHY, K., DUNNE, P., MCKINNEY, L., O'SULLIVAN, G., SOKELL, E., WHITE, J., AGUILAR, A., POMEROY, J.M., TAN, J.N., BLAGEJOVIĆ, B., Le BIGOT, E.-O., GILLASPY, J.D., UTA versus line emission for EUVL: studies on xenon emission at the NIST EBIT, *J. Phys. D: Appl. Phys.* **37** (2004) 3225.
- [29] TANUMA, H., OHASHI, H., FUJIOKA, S., NISHIMURA, H., SASAKI, A., NISHIHARA, K., 4d-4f unresolved transition arrays of xenon and tin ions in charge exchange collisions, *J. Phys. Conf. Ser.* **58** (2007) 231.
- [30] NISHIHARA, K., SUNAHARA, A., SASAKI, A., NUNAMI, M., TANUMA, H., FUJIOKA, S., SHIMADA, Y., FUJIMA, K., FURUKAWA, H., KATO, T., KOIKE, F., MORE, R., MURUKAMI, M., NISHIKAWA, T., ZHAKOVSKII, V., GAMATA, K., TAKATA, A., UEDA, H., NISHIMURA, H., IZAWA, Y., MIYANAGA, N., MIMA, K., Plasma physics and radiation hydrodynamics in developing an extreme ultraviolet light source for lithography, *Phys. Plasmas* **15** (2005) 056708.
- [31] TANUMA, H., OHASHI, H., SHIBUYA, E., KOBAYASHI, N., OKUNO, T., FUJIOKA, S., NISHIMURA, H., NISHIHARA, K., EUV emission spectra from excited multiply charged xenon ions produced in charge-transfer collisions, *Nucl. Instrum. Meth. B* **235** (2005) 331.
- [32] NARIHARA, K., YAMADA, I., HAYASHI, H., YAMAUCHI, K., Design and performance of the Thomson scattering diagnostic on LHD, *Review of Scientific Instruments* **72** (2001) 1122.
- [33] SUDO, S., Diagnostics of particle transport by double-layer pellet, *J. Plasma Fusion Res.* **69** (1993) 1349.
- [34] SCHWOB, J.L., WOUTERS, A.W., SUCKEWER, S., FINKENTHAL, M., High - resolution duo - multichannel soft x - ray spectrometer for tokamak plasma diagnostics, *Rev. Sci. Instrum.* **58** (1987) 1601.
- [35] NEU, R., High-Z plasma facing components in fusion devices: boundary conditions and operational experiences, *Phys. Scr.* **T123** (2006) 33.
- [36] KATO, T., FUNABA, H., SATO, K., KATO, D., SONG, M.-Y., YAMAMOTO, N., TANUMA, H., OHASHI, H., SASAKI, A., KOIKE, F., NISHIHARA, K., FAHY, K., O'SULLIVAN, G., EUV spectroscopy of Xe ions from the large helical device at the National Institute for Fusion Science for stable plasmas and plasmas undergoing radiation collapse, *J. Phys. B: At. Mol. Opt. Phys.* **41** (2008) 035703.
- [37] SUZUKI, C., KATO, T., SATO, K., TAMURA, N., KATO, D., SUDO, S., YAMAMOTO, N., TANUMA, H., OHASHI, H., SUDA, S., O'SULLIVAN, G., SASAKI, A., EUV spectra from highly charged tin ions observed in low density plasmas in LHD, In *Journal of Physics: Conference Series*, **163** (2009) 012019.
- [38] CARTHOUT, M., APETZ, R., BERGMANN, K., DERRA, G., JONKERS, J., PANKERT, J., ZINK, P., Proc. 5th Int. SEMATECH EUVL Symp. (Barcelona, 18–24 Oct. 2006).
- [39] SALOMON, E.B., Energy levels and observed spectral lines of xenon, Xe I through Xe LIV, *J. Phys. Chem. Ref. Data* **33** (2004) 765.
- [40] CHURILOV, S.S., JOSHI, Y.N., READER, J., KILDIYAROVA, R.R.,  $4p^64d^8-(4d^75p+4d^74f+4p^54d^9)$  transitions in Xe XI, *Phys. Scr.* **70** (2004) 126.
- [41] CHURILOV, S.S., JOSHI, Y.N., Analysis of the  $4p^64d^84f$  and  $4p^54d^{10}$  configurations of Xe X and some highly excited levels of Xe VIII and Xe IX ions, *Phys. Scr.* **65** (2002) 40.
- [42] De GAUFRIDY De DORTAN, F., Influence of configuration interaction on satellite lines of xenon and tin in the EUV region, *J. Phys. B: At. Mol. Opt. Phys.* **40** (2007) 599.
- [43] SASAKI, A., NISHIHARA, K., KOIKE, F., KAGAWA, T., NISHIKAWA, T., FUJIMA, K., KAWAMURA, T., FURUKAWA, H., Simulation of the EUV spectrum of Xe and Sn plasmas, *IEEE J. Quantum Electron* **10** (2004) 1307.
- [44] TRÄBERT, E., BEIERSDORFER, P., LEPSON, J.K., CHEN, H., Extreme ultraviolet spectra of highly charged Xe ions, *Phys. Rev. A* **68** (2003) 042501.

- [45] 45a, BIEDERMANN, C., RADKE, R., FUSSMANN, G., SCHWOB, J.L., MANDELBAUM, P., EUV spectroscopy of highly charged xenon ions, Nucl. Instrum. Methods Phys. Res. B **235** (2005) 126, 45b, RADKE, R., BIEDERMANN, C., MANDELBAUM, P., SCHWOB, J.L., private communication (2009).
- [46] FAHY, K., SOKELL, E.J., O'SULLIVAN, G., AGUILAR, A., POMEROY, J.M., TAN, J.N., GILLASPY, J.D., Extreme-ultraviolet spectroscopy of highly charged xenon ions created using an electron-beam ion trap, Phys. Rev. A **75** (2007) 032520.
- [47] PETERSON, B.J., et al., Characteristics of radiating collapse at the density limit in the large helical device, Plasma Fusion Res. **1** (2006) 45.
- [48] COWAN, R.D., The Theory of Atomic Structure and Spectra (University of California Press, Berkeley) (1991).
- [49] DYALL, K.G., GRANT, I.P., JOHNSON, C.T., PARPIA, F.H., PLUMMER, E.P., GRASP: A general-purpose relativistic atomic structure program, Comput. Phys. Commun. **55** (1989) 425.
- [50] READER, J., ACQUISTA, N., COOPER, D., Spectra and energy levels of ions in the copper isoelectronic sequence from Ru<sup>15+</sup> to Sn<sup>21+</sup>, J. Opt. Soc. Am. **73** (1983) 1765.
- [51] BROWN, C.M., SEELY, J.F., KANIA, D.R., HAMMEL, B.A., BACK, C.A., LEE, R.W., BARSHALOM, A., BEHRING, W.E., Wavelengths and energy levels for the Zn I isoelectronic sequence Sn<sup>20+</sup> through U<sup>62+</sup>, At. Data Nucl. Data Tables **58** (1994) 203.
- [52] D'ARCY, R., OHASHI, H., SUDA, S., TANUMA, H., FUJIOKA, S., NISHIMURA, H., NISHIHARA, K., SUZUKI, C., KATO, T., KOIKE, F., WHITE, J., O'SULLIVAN, G., Transitions and the effects of configuration interaction in the spectra of Sn XV–Sn XVIII, Phys. Rev. A, **79** (2009) 042509.
- [53] CHOWDHURI, M.B., MORITA, S., GOTO, M., NISHIMURA, H., NAGAI, K., FUJIOKA, S., Line analysis of EUV spectra from molybdenum and tungsten injected with impurity pellets in LHD, Plasma and Fusion Research, **2** (2007) S1060
- [54] ASMUSSEN, K., FOURNIER, K.B., LAMING, J.M., NEU, R., SEELY, J.F., DUX, R., ENGELHARDT, W., FUCHS, J.C., the ASDEX Upgrade Team, Spectroscopic investigations of tungsten in the EUV region and the determination of its concentration in tokamaks, Nucl. Fusion, **38** (1998) 967
- [55] SEELY, J.F., BROWN, C.M., BEHRING, W.E., Transitions in Fe-, Co-, Cu-, and Zn-like ions of W and Re, J. Opt. Soc. Am. B **6** (1989) 3.
- [56] HARTE, C. S., SUZUKI, C., KATO, T., SUKAUE, H. A., KATO, D., SATO, K., TAMURA, N., SUDO, S., D'ARCY, R., SOKELL, E., WHITE, J., O'SULLIVAN, G., Tungsten spectra recorded at the LHD and comparison with calculations. J. Phys. B: Atom. Molec. Opt. Phys. **43** (2010) 205004
- [57] WU T., HIGASHIGUCHI, T., LI, B., ARAI, G., HARA, H., KONDO, Y., MIYAZAKI, T., DINH, T.-H., DUNNE, P., O'REILLY, F., SOKELL, E., O'SULLIVAN, G., Spectral investigation of highly ionized bismuth plasmas produced by subnanosecond Nd:YAG pulses. J. Phys. B: Atom. Molec. Opt. Phys. **49**, (2016) 035001.
- [58] BAUCHE-ARNOULT, C., BAUCHE, J., KLAPISCH, M., Mean wavelength and spectral width of transition arrays in x-uv atomic spectra, J. Opt. Soc. Am. **68** (1978) 1136.
- [59] BAUCHE-ARNOULT, C., BAUCHE, J., KLAPISCH, M., Variance of the distributions of energy levels and of the transition arrays in atomic spectra, Phys. Rev. A **20** (1979) 2424.
- [60] BAUCHE-ARNOULT, C., BAUCHE, J., KLAPISCH, M., Variance of the distributions of energy levels and of the transition arrays in atomic spectra. II. Configurations with more than two open subshells, Phys. Rev. A **25** (1982) 2641.
- [61] BAUCHE-ARNOULT, C., BAUCHE, J., KLAPISCH, M., Asymmetry of  $l^{N+1} - l^N l'$  transition-array patterns in ionic spectra, Phys. Rev. A **30** (1984) 3026.
- [62] BAUCHE-ARNOULT, C., BAUCHE, J., KLAPISCH, M., Variance of the distributions of energy levels and of the transition arrays in atomic spectra. III. Case of spin-orbit-split arrays, Phys. Rev. A **31** (1985) 2248.

- [63] SONG, M.-Y., KATO, T., Dielectronic Recombination processes of  $Xe^{10+}$  ions, J. Phys. Conf. Ser. **72** (2007) 012019.
- [64] GU, M.F., Dielectronic recombination rate coefficients for H-like through Ne-like isosequences of Mg, Si, S, Ar, Ca, Fe, and Ni, Astrophys. J. **590** (2003) 1131.
- [65] Fu, Y.B., Dong, C.Z, Su, M.G, O'Sullivan, G., Dielectronic recombination of  $Sn^{10+}$  ions and related satellite spectra, Chinese Physics Letters **25** (2008) 927.
- [66] FU, Y.B., SU, M.G., DONG, C.Z., KOIKE, F., O'SULLIVAN, G., Theoretical investigation of dielectronic recombination of  $Sn^{12+}$  ions, Phys. Rev. A **83**(2011) 062708
- [67] ACQUISTA, N., READER, J.,  $4s^2\ ^1S_0-4s4p\ ^1P_1$  transitions in zinc-like ions, J. Opt. Soc. Am. B **1** (1984) 649.
- [68] CHURILOV, S.S., RYABTSEV, A.N., WYART, J.-F, Identification of  $n = 4$ ,  $\Delta n = 0$  transitions in the spectra of nickel-like and zinc-like ions through tin, Phys. Scr. **38** (1988) 326.
- [69] NAKAMURA, N., 3rd workshop on Physics at EBITs and Advanced Research Light Sources (PEARL2009), May 6th to May 9th 2009, Dublin City University.
- [70] SUZUKI, C., KATO, T., SAKAUE, H.A., KATO, D., SATO, K., TAMURA, N., SUDO, S., YAMAMOTO, N., TANUMA, H., OHASHI, H., D'AREY, R. D., O'SULLIVAN, G., Analysis of EUV spectra of Sn XIX – XXII observed in low-density plasmas in the Large Helical Device, J. Physics B, **43** (2010) 074027
- [71] CHURILOV, S.S., JOSHI, Y.N., RYABTSEV, A.N., The  $4d^{10}\ ^1S_0-4d^9(np+n'f)$  transitions in the Pd I isoelectronic sequence from Cd III to Cs X, J. Phys. B: At. Mol. Opt. Phys. **27** (1994) 5485.
- [72] AZAROV, V.I., JOSHI, Y.N., Analysis of the  $4d^7-4d^65p$  transition array of the eighth spectrum of tin: Sn VIII, J. Phys. B: At. Mol. Opt. Phys. **26** (1993) 3495.
- [73] CHURILOV, S.S., KILDIYAROVA, R.R., RYABTSEV, A.N., KRAMIDA, A., JOSHI, Y.N., Analysis of the  $4d^9-4d^8(4f+6p)$  transition array of Sn VI, Phys. Scr. **50** (1994) 463.
- [74] AZAROV, V.I., JOSHI, Y.N., CHURILOV, S.S., RYABTSEV, A.N., Analysis of the  $4d^7(4f+6p)$  and  $4p^54d^9$  configurations of Sn VII, Sb VIII and Te IX, Phys. Scr. **50** (1994) 642.
- [75] VAN HET HOF, G.J, JOSHI, Y.N., The analysis of the  $4d^8$ ,  $4d^75s$  and  $4d^75p$  configurations of six-times ionized tin: Sn VII, Phys. Scr. **48** (1993) 714.

# CONVERGENT CLOSE-COUPPLING CALCULATIONS OF ELECTRON-IMPACT IONIZATION OF INTERMEDIATE AND HIGHLY CHARGED IONS

I. BRAY, C. J. BOSTOCK, D. V. FURSA, A. C. RENWICK

ARC Centre for Antimatter-Matter Studies,  
Curtin University of Technology,  
GPO Box U1987 Perth, WA 6845, Australia

## Abstract

The convergent close-coupling (CCC) method is applied to the calculation of electron-impact total ionisation cross-sections for H-, Na- and Mg-like ions. For low to intermediate charges the non-relativistic CCC method is used. For higher charges a relativistic CCC implementation has been applied with a Breit or a Møller correction. Comparisons with the distorted wave Born approximations (DWBA) are often very good, even when electron exchange is very important.

## 1. INTRODUCTION

The convergent close-coupling (CCC) method was initially developed for calculating electron-hydrogen scattering by Bray and Stelbovics [1]. The method is underpinned by the usage of a complete Laguerre basis. This basis is used to diagonalise the target Hamiltonian, which results in a finite discretisation of the target negative- and positive-energy spectrum. The resulting target states are all square-integrable and are used to expand the total wavefunction of the electron-target system, and thereby define the close-coupling equations. The usage of a complete basis ensures that as the basis size is increased the expansion becomes more complete. In the CCC approach the equations take the form of momentum-space coupled Lippmann-Schwinger equations. These are solved upon partial-wave expansion.

Though historically close-coupling methods were designed for the treatment of excitation processes at low energies, the application of the CCC method to total e-H ionisation [2] showed that the method was much more general. By summing the cross-sections for excitation of the positive-energy states excellent agreement with experiment for total ionisation cross-sections was achieved from near threshold to very high energies. In fact, more recently the method has been shown to yield excellent fully differential ionisation cross-sections [3].

Following the success of the CCC method for atomic hydrogen it was extended to alkali targets [4]. Here the core electrons are treated by the Hartree-Fock approximation together with core-polarisation potentials. The method has also been extended to helium [5] and alkaline earth [6] targets. Here the Laguerre basis is used to construct two-electron target states.

Consequently, the CCC method is very well established for providing accurate ionisation cross-sections for quasi one- and two-electron targets. The purpose of this manuscript is to report on the calculations performed during the coordinated research project (CRP) on "Atomic Data for Heavy Element Impurities in Fusion Reactors".

## 2. QUASI ONE-ELECTRON TARGETS

Throughout the CRP our goal has been to provide the requested data for electron-impact ionisation (and excitation) of Na- and Mg-like ions, as well as develop further functionality to enable the treatment of very heavy targets. We begin with the consideration of the H-like sequence where, in addition to such targets being the foundation of the Na-like sequence, we have also developed a relativistic CCC (RCCC) method for dealing with particularly heavy and highly charged species.

### 2.1. H-like targets

We begin with the consideration of one-electron targets from neutral hydrogen through to (H-like)  $U^{91+}$ . In Fig. 1 we present comparison of experiment with the CCC-calculated e-H total ionisation cross-sections. Also presented are the individual total spin  $S$  components. We present the latter because we shall see that the qualitative relationship between the two components, with the  $S = 0$  cross-section being the more dominant, stays remarkably similar even when the ionic charge is substantially increased. We see that there is good agreement between theory and experiment, and this result heralded the CCC theory as a particularly successful approach to the problem [2].

We next consider the  $e-B^{4+}$  system presented in Fig. 2. Here comparison with experiment is again excellent as is with the distorted wave Born approximation (DWBA). Note the dominance of the  $S = 0$  component even out to relatively large energies.

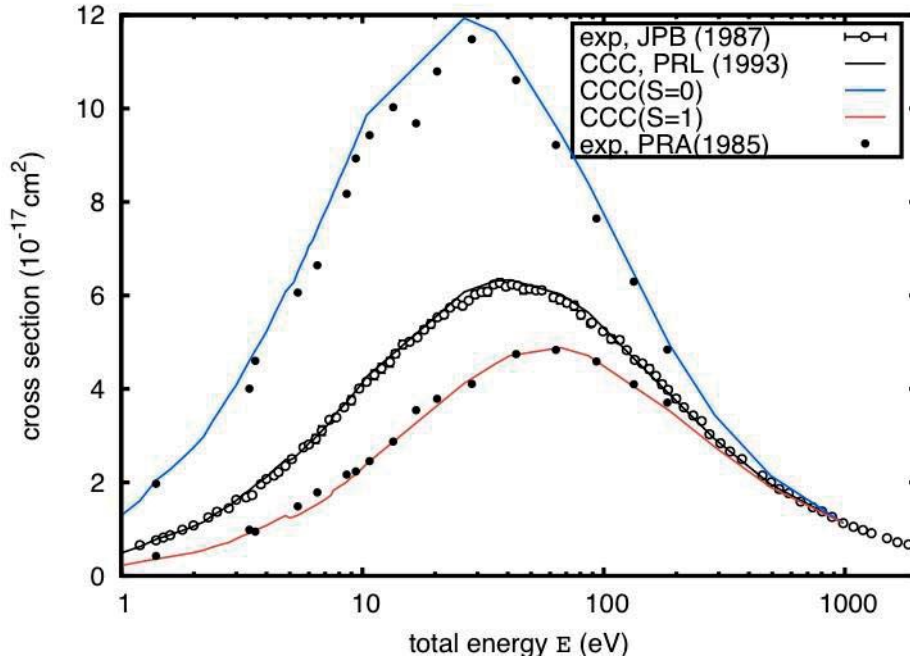


FIG. 1. The total e-H ionisation cross-section. The total ionisation measurements of Shah *et al.* [7] have been combined with the spin asymmetries of Fletcher *et al.* [8] to yield the individual contributions for the two total spins  $S$ . The CCC calculations are from Ref. [2].

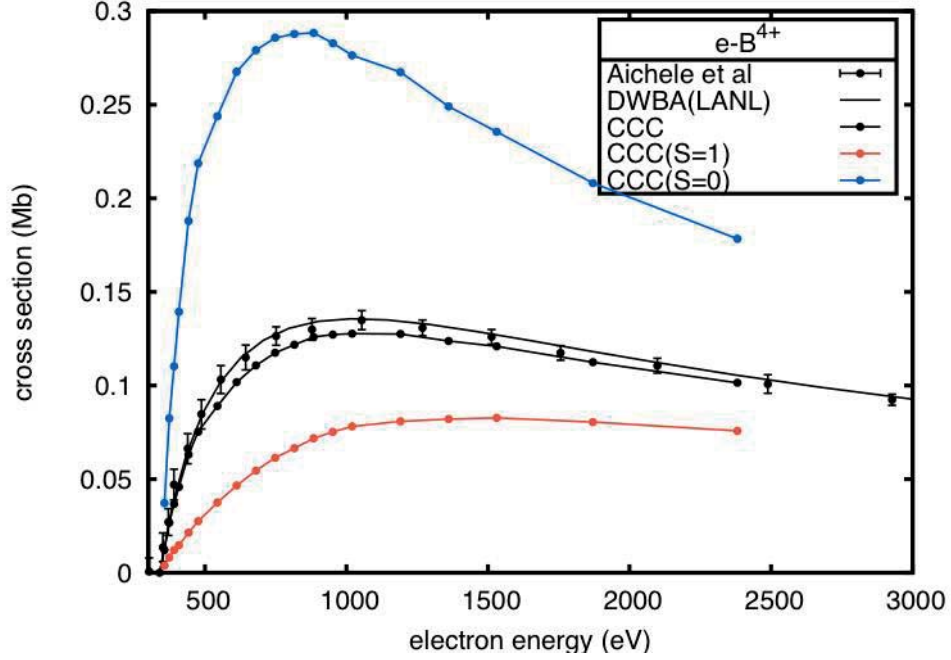


FIG. 2. The total  $e-B^{4+}$  ionisation cross-section. The measurements are due to Aichele et al. [11]. The present CCC calculations have been given together with their individual total spin  $S$  components. The DWBA calculations were obtained from <http://aphysics2.lanl.gov/tempweb>.

The  $e-Zn^{29+}$  total ionisation cross-sections are presented in Fig. 3. Here we present the results of the RCCC calculations and find that they agree well with the CCC and DWBA results. The spin-dependent behaviour is still much the same.

In Fig. 4 we consider the  $e-W^{73+}$  total ionisation cross-sections, with W ions being considered a major source of heavy ion impurities. For such heavy highly charged systems we check the effect of the Breit correction in the relativistic formalism. We see that it has the effect of increasing the cross-sections by around 20%. The more computationally demanding Møller correction yields much the same results.

The most highly charged ionic species considered is  $U^{91+}$ . Here we have one experimental point and several other calculations with which we can compare, and therefore validate our treatment of highly charged targets. The  $e-U^{91+}$  total ionisation cross-sections are given in Fig. 5. At such high energies the RCCC calculations reduce to the Coulomb-Born results, which additionally require the Breit or Møller interaction to be added. We find good agreement with the calculations of Fontes et al. [9] and the experiment of Marrs et al. [10].

This concludes our consideration of H-like ions. We have established the validity of the CCC and RCCC methods to the treatment of such targets.

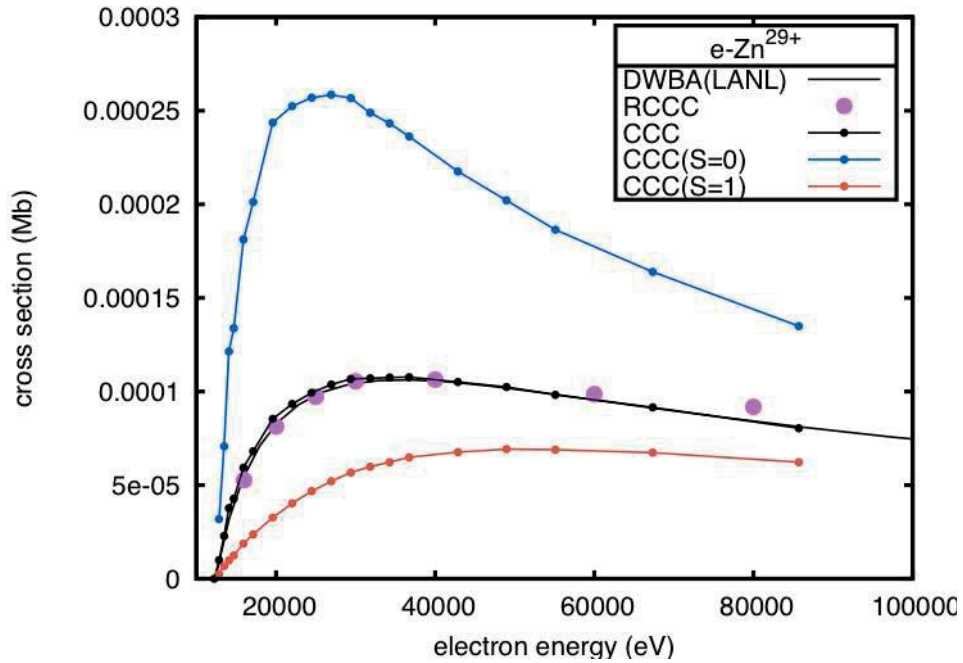


FIG. 3. The total  $e\text{-Zn}^{29+}$  ionisation cross-section. The present CCC calculations have been given together with their individual total spin  $S$  components. The present RCCC calculations have been performed at the indicated energies. The DWBA calculations were obtained from <http://aphysics2.lanl.gov/tempweb>.

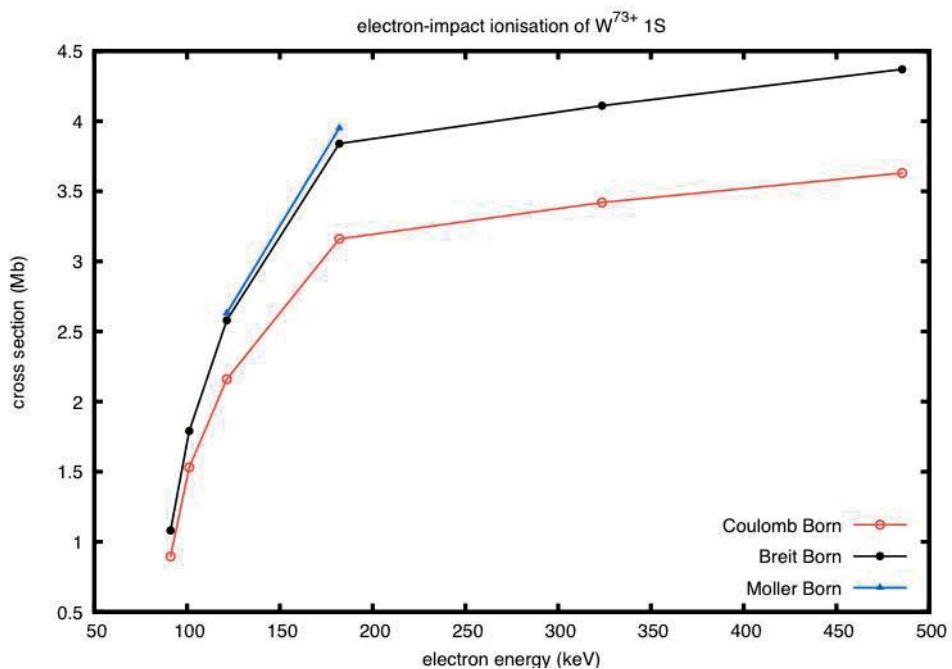


FIG. 4. The total  $e\text{-W}^{73+}$  ionisation cross-section calculated in a relativistic Born approximation, and with Born and Møller correction.

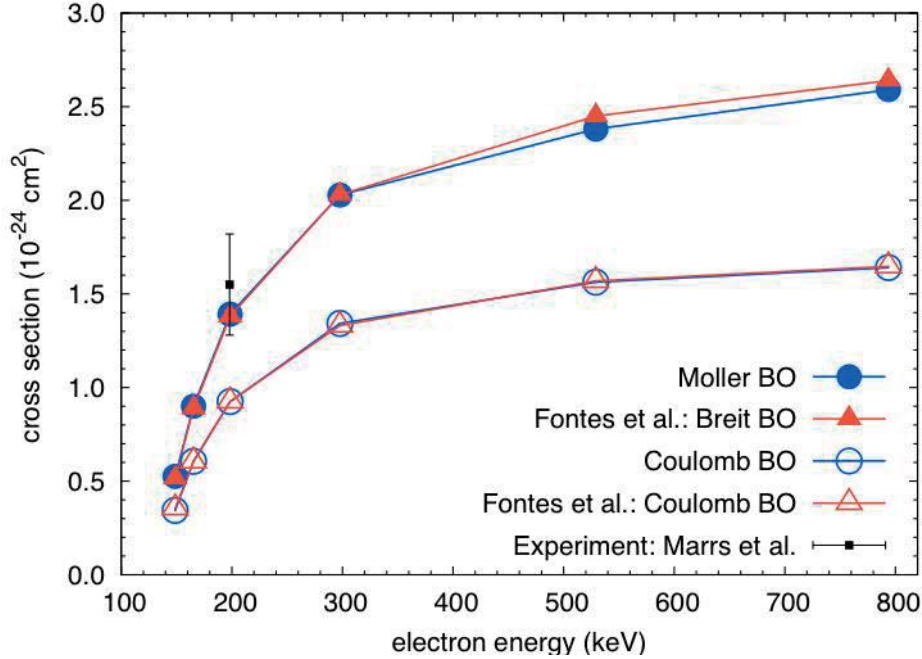


FIG. 5. The total  $e-U^{p1+}$  ionisation cross-section. The present calculations are compared with the experiment is of MARRS et al. [10] and the calculations of Fontes et al. [9]

## 2.2. Na-like targets

The extension of the CCC method for e-H scattering [1] to Na-like targets has been given by Bray [4]. The major difference is that the pure Coulomb core potential is replaced with a Hartree-Fock potential that collectively treats the relatively inert Ne-like core.

The first target considered is the  $\text{Si}^{3+}$  ion, with the results presented in Fig. 6. While there is good agreement between the CCC and DWBA calculations we see that experiment continues to rise away from theory above 100 eV. This is due to the highly energetic incident electrons being able to eject some of the Ne-like core electrons. Reasonably accurate estimates for such contributions may be obtained utilising the Born approximation. Note once more how the  $S = 0$  contribution dominates.

Fig. 7 presents the data for electron-impact ionisation of Na-like  $\text{Cl}^{6+}$ . Once more the agreement between the DWBA and CCC calculations is very good and the spin-resolved contributions are as previously observed.

The last requested Na-like target was  $\text{Ar}^{7+}$ , for which the electron-impact total ionisation cross-sections are presented in Fig. 8. As above, there is good agreement between the two theories and the dominance of the  $S = 0$  component remains. The DWBA results of Loch et al. [12] are similar to those presented here.

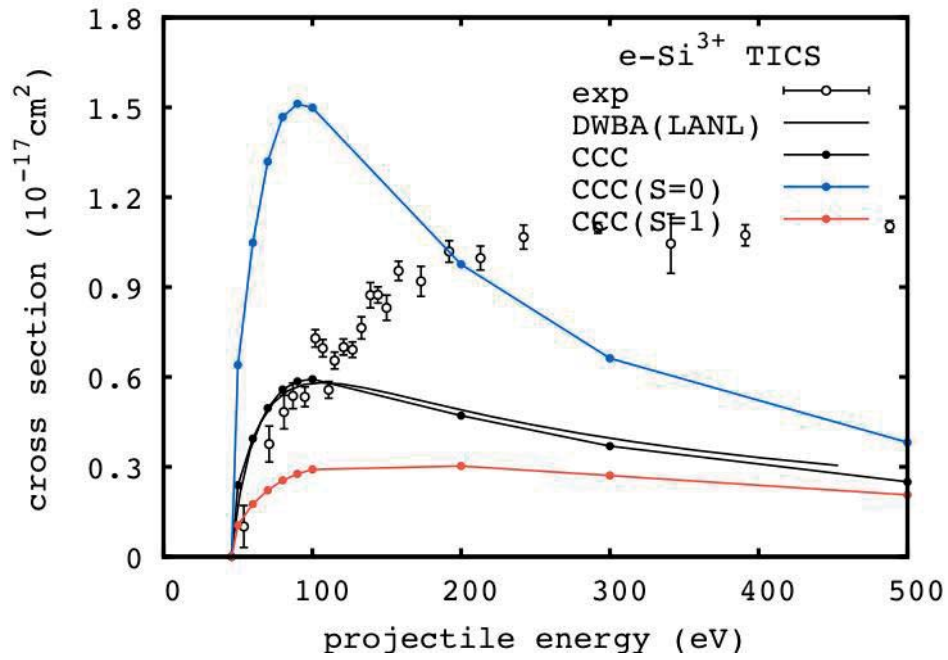


FIG. 6. The total  $e\text{-Si}^{3+}$  ionisation cross-section. The present CCC calculations for direct ionisation have been given together with their individual total spin  $S$  components. The DWBA calculations were obtained from <http://aphysics2.lanl.gov/tempweb>. The experiment is due to Crandall et al. [13] and includes core-ionisation contributions above 100 eV.

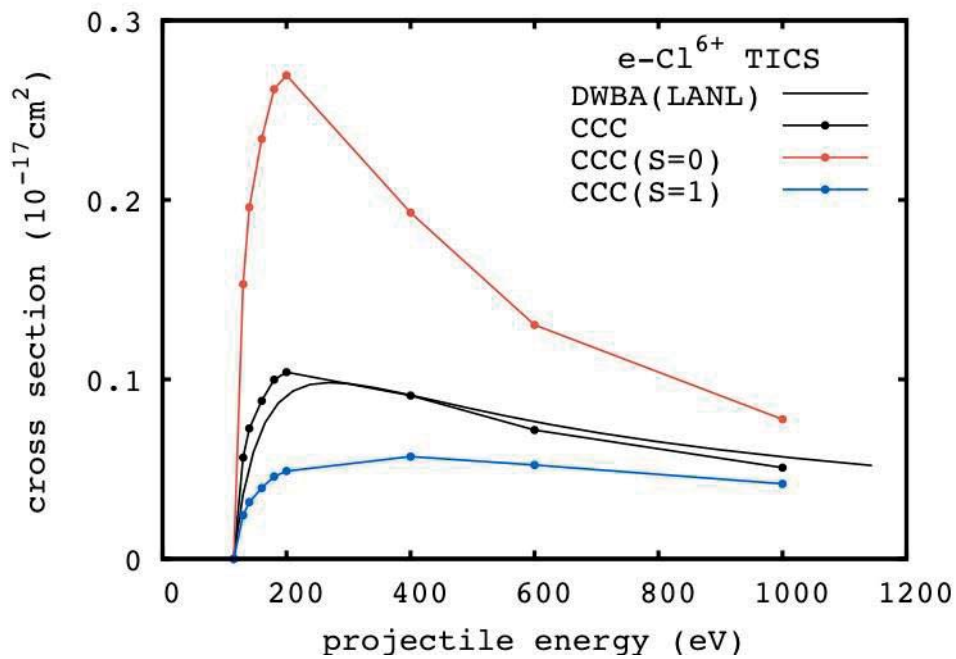


FIG. 7. The total  $e\text{-Cl}^{6+}$  ionisation cross-section. The DWBA calculations were obtained from <http://aphysics2.lanl.gov/tempweb>.

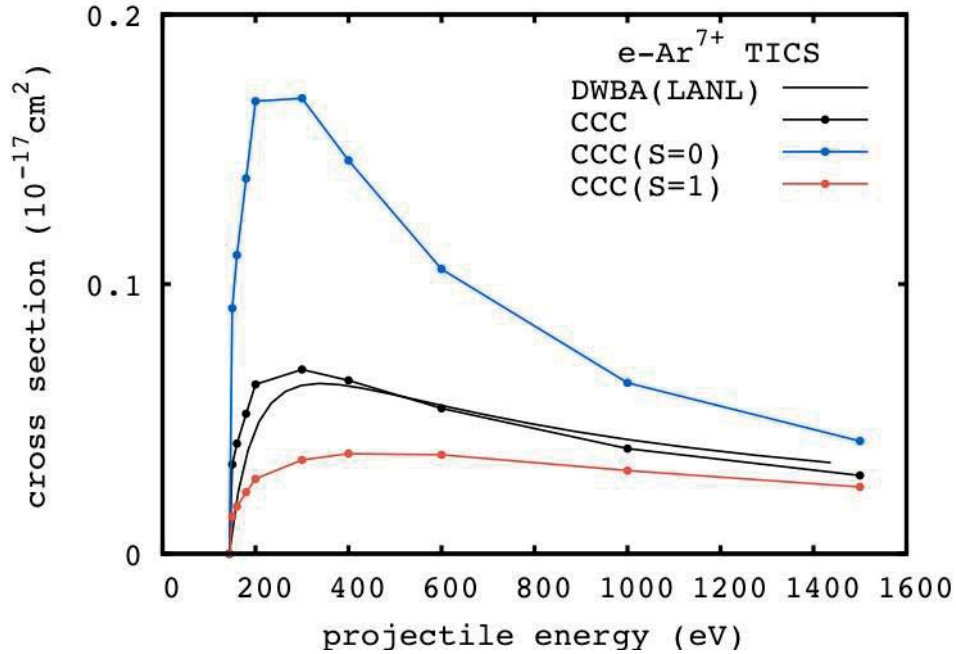


FIG. 8. The total  $e\text{-Ar}^{7+}$  ionisation cross-section. The DWBA calculations were obtained from <http://aphysics2.lanl.gov/tempweb>

### 3. QUASI TWO-ELECTRON TARGETS

The CRP also requested CCC calculations for Mg-Like Si, Cl, and Ar. These are presented in Figs. 9, 10 and 11, respectively. Here the initial state is a singlet state and hence there is only a total spin  $S = 1/2$  cross-section. Comparison of the presented CCC and DWBA calculations shows a small, but a systematic difference between the two calculations. Soon after threshold the DWBA calculations are a little larger than the CCC calculations. We are not certain as to why this is the case, and this is currently under investigation. Howald et al. [14] measured the total ionization cross-section for both  $\text{Cl}^{5+}$  and  $\text{Ar}^{6+}$ . In both cases the agreement is excellent near threshold (not shown), but due to the ejection of the core electrons, generally such experiments yield cross-sections that are much larger than the calculated direct ionization cross-sections, making comparison problematic.

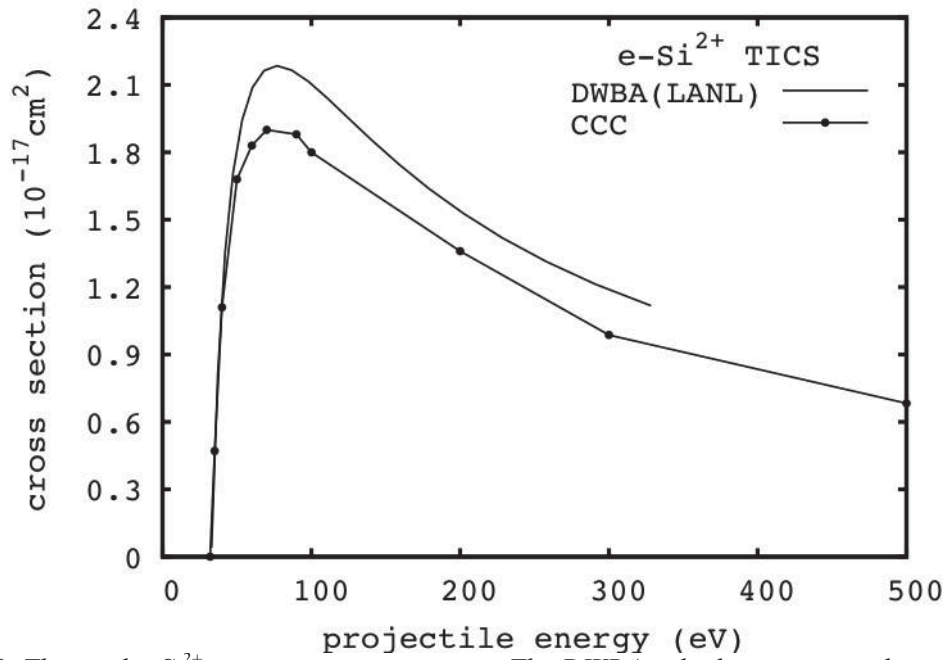


FIG. 9. The total  $e\text{-Si}^{2+}$  ionisation cross-section. The DWBA calculations were obtained from <http://aphysics2.lanl.gov/tempweb>.

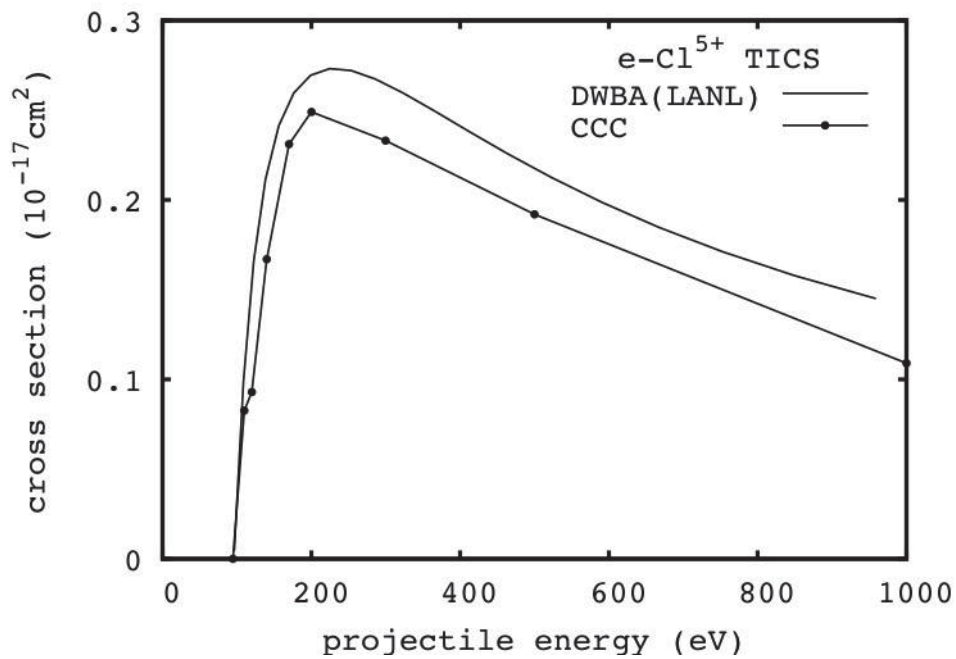


FIG. 10. The total  $e\text{-Cl}^{5+}$  ionisation cross-section. The DWBA calculations were obtained from <http://aphysics2.lanl.gov/tempweb>.

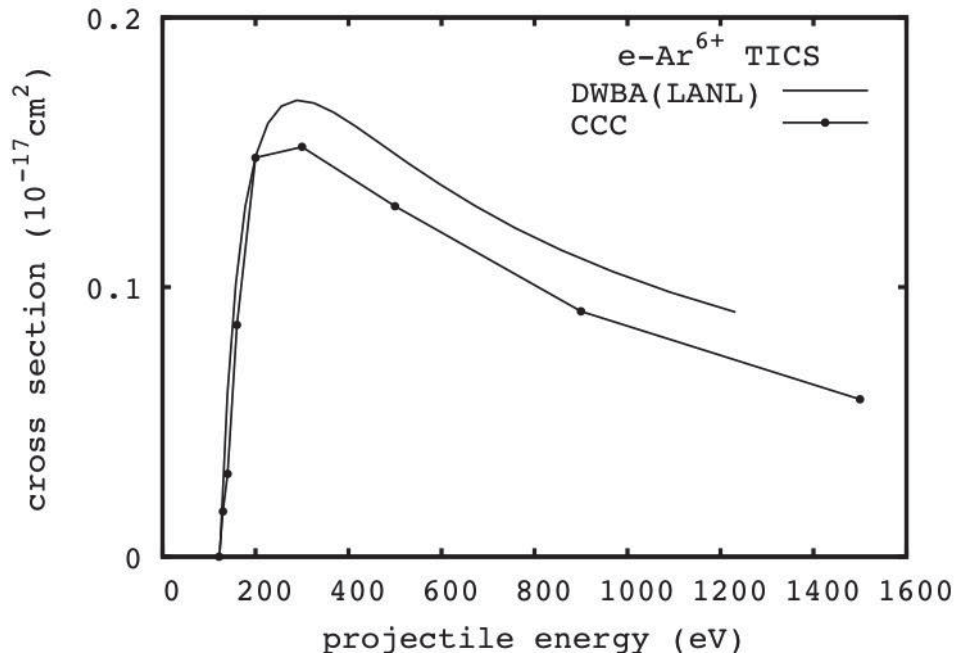


FIG. 11. The total  $e\text{-Ar}^{6+}$  ionisation cross-section. The DWBA calculations were obtained from <http://aphysics2.lanl.gov/tempweb>.

#### 4. CONCLUSIONS

We have carried out all of the requested calculations for the Na-like and Mg-like Si, Cl and Ar. Additionally, we have extended the capability of the CCC method to include a relativistic treatment with Breit and Møller corrections. We have attempted to validate our results by comparison with other theory and experiment, and generally found very good agreement with the DWBA calculations. A few minor discrepancies have been identified, and we look forward to their resolution. Finally, a surprising result from this systematic study is that in the case of scattering on a doublet state the total spin  $S = 0$  contribution to the total ionisation cross-section is by far the most dominant, and this relationship seems independent of the magnitude of the ionic charge.

#### ACKNOWLEDGMENTS

This work was supported by the Australian Research Council. We are grateful for access to the Australian National Computing Infrastructure Facility and its Western Australian node iVEC.

#### REFERENCES

- [1] BRAY, I., STELBOVICS, A.T., Convergent close-coupling calculations of electron-hydrogen scattering, *Phys. Rev. A* **46** (1992) 6995.
- [2] BRAY, I., STELBOVICS, A.T., Calculation of the total ionization cross-section and spin asymmetry in electron-hydrogen scattering from threshold to 500 eV, *Phys. Rev. Lett.* **70** (1993) 746.
- [3] BRAY, I., Close-coupling approach to coulomb three-body problems, *Phys. Rev. Lett.* **89** (2002) 273201.
- [4] BRAY, I., Convergent close-coupling method for the calculation of electron scattering on hydrogen-like targets, *Phys. Rev. A* **49** (1994) 1066.

- [5] FURSA, D.V., BRAY, I., Calculation of electron-helium scattering, *Phys. Rev. A* **52** (1995) 1279.
- [6] FURSA, D.V., BRAY, I., Convergent close-coupling calculations of electron scattering on helium-like atoms and ions: electron - beryllium scattering, *J. Phys. B* **30** (1997) 5895.
- [7] SHAH, M.B., ELLIOT, D.S., GILBODY, H.B., Pulsed crossed-beam study of the ionisation of atomic hydrogen by electron-impact, *J. Phys. B* **20** (1987) 3501.
- [8] FLETCHER, G.D., ALGUARD, M.J., GAY, T.J., HUGHES, V.W., WAINWRIGHT, P.F., LUBELL, M.S., RAITH, W., Experimental study of spin-exchange effects in elastic and ionizing collisions of polarized electrons with polarized hydrogen atoms, *Phys. Rev. A* **31** (1985) 2854.
- [9] FONTES, C.J., SAMPSON, D.H., ZHANG, H.L., Fully relativistic calculations of and fits to  $1s$  ionization cross-sections, *Phys. Rev. A* **59** (1999) 1329.
- [10] MARRS, R.E., ELLIOTT, S.R., KNAPP, D.A., Production and trapping of hydrogen-like and bare uranium ions in an electron beam ion trap, *Phys. Rev. Lett.* **72** (1994) 4082.
- [11] AICHELE, K., HARTENFELLER, U., HATHIRAMANI, D., HOFMANN, G., SCHÄFER, V., STEIDL, M., STENKE, M., SALZBORN, E., PATTARD, T., ROST, J.M., Electron-impact ionization of the hydrogen-like ions  $B^{4+}$ ,  $C^{5+}$ ,  $N^{6+}$  and  $O^{7+}$ , *J. Phys. B* **31** (1998) 2369.
- [12] LOCH, S.D., ABDEL-NABY, S.A., BALLANCE, C.P., PINDZOLA, M.S., Electron-impact ionization and recombination of  $M$ -shell atomic ions in the argon isonuclear sequence, *Phys. Rev. A* **76** (2007) 022706.
- [13] CRANDALL, D.H., PHANEUF, R.A., FALK, R.A., BELIĆ, D.S., DUNN, G.H., Absolute cross-section measurements for electron-impact ionization of Na-like ions— $Mg^+$ ,  $Al^{2+}$ , and  $Si^{3+}$ , *Phys. Rev. A* **25** (1982) 143.
- [14] HOWALD, A.M., GREGORY, D.C., MEYER, F.W., PHANEUF, R.A., MÜLLER, A., DJURIC, N., DUNN, G.H., Electron-impact ionization of Mg-like ions:  $S^{4+}$ ,  $Cl^{5+}$ , and  $Ar^{6+}$ , *Phys. Rev. A* **33** (1986) 3779.



## ORDERING LOCALLY

In the following countries, IAEA priced publications may be purchased from the sources listed below or from major local booksellers.

Orders for unpriced publications should be made directly to the IAEA. The contact details are given at the end of this list.

### CANADA

***Renouf Publishing Co. Ltd***

22-1010 Polytek Street, Ottawa, ON K1J 9J1, CANADA  
Telephone: +1 613 745 2665 • Fax: +1 643 745 7660  
Email: [order@renoufbooks.com](mailto:order@renoufbooks.com) • Web site: [www.renoufbooks.com](http://www.renoufbooks.com)

***Bernan / Rowman & Littlefield***

15200 NBN Way, Blue Ridge Summit, PA 17214, USA  
Tel: +1 800 462 6420 • Fax: +1 800 338 4550  
Email: [orders@rowman.com](mailto:orders@rowman.com) Web site: [www.rowman.com/bernan](http://www.rowman.com/bernan)

### CZECH REPUBLIC

***Suweco CZ, s.r.o.***

Sestupná 153/11, 162 00 Prague 6, CZECH REPUBLIC  
Telephone: +420 242 459 205 • Fax: +420 284 821 646  
Email: [nakup@suweco.cz](mailto:nakup@suweco.cz) • Web site: [www.suweco.cz](http://www.suweco.cz)

### FRANCE

***Form-Edit***

5 rue Janssen, PO Box 25, 75921 Paris CEDEX, FRANCE  
Telephone: +33 1 42 01 49 49 • Fax: +33 1 42 01 90 90  
Email: [formedit@formedit.fr](mailto:formedit@formedit.fr) • Web site: [www.form-edit.com](http://www.form-edit.com)

### GERMANY

***Goethe Buchhandlung Teubig GmbH***

Schweitzer Fachinformationen  
Willstätterstrasse 15, 40549 Düsseldorf, GERMANY  
Telephone: +49 (0) 211 49 874 015 • Fax: +49 (0) 211 49 874 28  
Email: [kundenbetreuung.goethe@schweitzer-online.de](mailto:kundenbetreuung.goethe@schweitzer-online.de) • Web site: [www.goethebuch.de](http://www.goethebuch.de)

### INDIA

***Allied Publishers***

1st Floor, Dubash House, 15, J.N. Heredi Marg, Ballard Estate, Mumbai 400001, INDIA  
Telephone: +91 22 4212 6930/31/69 • Fax: +91 22 2261 7928  
Email: [alliedpl@vsnl.com](mailto:alliedpl@vsnl.com) • Web site: [www.alliedpublishers.com](http://www.alliedpublishers.com)

***Bookwell***

3/79 Nirankari, Delhi 110009, INDIA  
Telephone: +91 11 2760 1283/4536  
Email: [bkwell@nde.vsnl.net.in](mailto:bkwell@nde.vsnl.net.in) • Web site: [www.bookwellindia.com](http://www.bookwellindia.com)

## **ITALY**

### ***Libreria Scientifica "AEIOU"***

Via Vincenzo Maria Coronelli 6, 20146 Milan, ITALY  
Telephone: +39 02 48 95 45 52 • Fax: +39 02 48 95 45 48  
Email: [info@libreriaaeiou.eu](mailto:info@libreriaaeiou.eu) • Web site: [www.libreriaaeiou.eu](http://www.libreriaaeiou.eu)

## **JAPAN**

### ***Maruzen-Yushodo Co., Ltd***

10-10 Yotsuyasakamachi, Shinjuku-ku, Tokyo 160-0002, JAPAN  
Telephone: +81 3 4335 9312 • Fax: +81 3 4335 9364  
Email: [bookimport@maruzen.co.jp](mailto:bookimport@maruzen.co.jp) • Web site: [www.maruzen.co.jp](http://www.maruzen.co.jp)

## **RUSSIAN FEDERATION**

### ***Scientific and Engineering Centre for Nuclear and Radiation Safety***

107140, Moscow, Malaya Krasnoselskaya st. 2/8, bld. 5, RUSSIAN FEDERATION  
Telephone: +7 499 264 00 03 • Fax: +7 499 264 28 59  
Email: [secnrs@secnrs.ru](mailto:secnrs@secnrs.ru) • Web site: [www.secnrs.ru](http://www.secnrs.ru)

## **UNITED STATES OF AMERICA**

### ***Bernan / Rowman & Littlefield***

15200 NBN Way, Blue Ridge Summit, PA 17214, USA  
Tel: +1 800 462 6420 • Fax: +1 800 338 4550  
Email: [orders@rowman.com](mailto:orders@rowman.com) • Web site: [www.rowman.com/bernan](http://www.rowman.com/bernan)

### ***Renouf Publishing Co. Ltd***

812 Proctor Avenue, Ogdensburg, NY 13669-2205, USA  
Telephone: +1 888 551 7470 • Fax: +1 888 551 7471  
Email: [orders@renoufbooks.com](mailto:orders@renoufbooks.com) • Web site: [www.renoufbooks.com](http://www.renoufbooks.com)

## **Orders for both priced and unpriced publications may be addressed directly to:**

Marketing and Sales Unit  
International Atomic Energy Agency  
Vienna International Centre, PO Box 100, 1400 Vienna, Austria  
Telephone: +43 1 2600 22529 or 22530 • Fax: +43 1 2600 29302 or +43 1 26007 22529  
Email: [sales.publications@iaea.org](mailto:sales.publications@iaea.org) • Web site: [www.iaea.org/books](http://www.iaea.org/books)

ISBN 978-92-0-105817-1  
ISSN 1018-5577